DESIGN OF AN OPTIMAL PENDULUM-TUNED MASS DAMPER APPLIED TO OFFSHORE WIND TURBINES

Gino Bertollucci Colherinhas

Relatório de Doutorado
Ciências Mecânicas

UNIVERSIDADE DE BRASÍLIA

Faculdade de Tecnologia
Departamento de Engenharia Mecânica

UNIVERSIDADE DE BRASÍLIA
FACULDADE DE TECNOLOGIA
DEPARTAMENTO DE ENGENHARIA MECÂNICA

DESIGN OF AN OPTIMAL PENDULUM-TUNED MASS DAMPER APPLIED TO OFFSHORE WIND TURBINES

Gino Bertollucci Colherinhas

Orientador: Marcela Rodrigues Machado, PhD (ENM/ UnB)

RELATÓRIO DE DOUTORADO

PUBLICAÇÃO: ENM.DM -

BRASÍLIA/DF: 10 de novembro de 2020

UNIVERSIDADE DE BRASÍLIA
FACULDADE DE TECNOLOGIA
DEPARTAMENTO DE ENGENHARIA MECÂNICA

Design of an optimal pendulum-tuned mass damper applied to offshore wind turbines

Gino Bertollucci Colherinhas

DISSERTAÇÃO DE DOUTORADO SUBMETIDA AO DEPARTAMENTO DE ENGENHARIA MECÂNICA DA FACULDADE DE TECNOLOGIA DA UNIVERSIDADE DE BRASÍLIA COMO PARTE DOS REQUISITOS PARCIAIS PARA A OBTENÇÃO DO GRAU DE DOUTOR EM CIÊNCIAS MECÂNICAS.

COMISSÃO EXAMINADORA:

Marcela Rodrigues Machado, PhD (ENM/ UnB)
(Orientadora)

Marcus Vinicius Girão de Morais, PhD (ENM/ UnB)
(Co-orientador)

Éder Lima de Albuquerque, PhD (ENM/ UnB)
(Examinador Interno)

Guilherme Rosa Franzini, PhD (University of São Paulo USP)
(Examinador Externo)

Francesco Petrini, PhD (Sapienza University of Rome)
(Examinador Externo)

Aline Souza de Paula (ENM/ UnB)
(Suplente)

BRASÍLIA/DF, 10 DE NOVEMBRO DE 2020.

FICHA CATALOGRÁFICA

Colherinhas, Gino B.
Design of an optimal pendulum-tuned mass damper applied to offshore wind turbines
[Distrito Federal] 2020.
xviii, 143p. (ENM/FT/UnB, Doutor, Ciências Mecânicas, 2020.
Relatório de Doutorado - Universidade de Brasília.
Faculdade de Tecnologia.
Departamento de Engenharia Mecânica.
Palavras-chave:

1. Offshore Wind Turbine	2. Pendulum Tuned Mass Damper
3. Genetic Algorithm Optimization	4. Structural Control
I. ENM/FT/UnB	II. Título (série)

REFERÊNCIA BIBLIOGRÁFICA

Colherinhas, Gino B.(2020). Design of an optimal pendulum-tuned mass damper applied to offshore wind turbines. Relatório de Doutorado, Publicação ENM.DM - , Departamento de Engenharia Mecânica, Universidade de Brasília, Brasília, Distrito Federal, xviii, 143p.

CESSÃO DE DIREITOS

NOME DO AUTOR: Gino Bertollucci Colherinhas.

TÍTULO DA DISSERTAÇÃO DE DOUTORADO: Design of an optimal pendulum-tuned mass damper applied to offshore wind turbines.

GRAU / ANO: DOUTOR / 2020

Gino Bertollucci Colherinhas

Abstract

DESIGN OF AN OPTIMAL PENDULUM-TUNED MASS DAMPER APPLIED TO OFFSHORE WIND TURBINES

Author: Gino Bertollucci Colherinhas

Supervisor: Marcela Rodrigues Machado, PhD (ENM/ UnB)

Ph.D. in Mechanical Sciences

Brasília, 2020

Offshore Wind Turbines (OWT) may experience excessive vibration levels caused by the actions of wind, waves, rotor torque, and seismic loads. To suppress the vibrations of these primary structures, the Tuned Mass Damper (TMD) is a widely used passive control alternative. Briefly, it is a damper that transfers the kinetic energy from the main structure to a secondary mass usually attached to the hub. These devices need to be finely tuned with a target self-vibration mode of the primary structure to work as dampers, otherwise, they could amplify structural vibrations. This thesis presents optimal parameters of a Pendulum-TMD (PTMD) to mitigates structural vibrations of OWTs levels. The PTMD is examined on a National Renewable Energy Lab (NREL) monopile 5 MW baseline wind turbine model using analytical and numerical procedures, such as a 2-degree-of-freedom (2DOF), spectral elements (SEM), and finite elements (FEM). Following design standards of OWTs structures wind and wave spectra computation, as well as the evaluation of the hydrodynamic and aerodynamic loads by computing the resultant peak displacement response at the OWT hub by a Power Spectral Density (PSD) analysis. In the validation of the OWT models, a result comparison is made with the NREL OpenFAST, finding good matching between the results. An in-house built Genetic Algorithm (GA) toolbox, coded in MATLAB®, is used then to optimally design parameters of a PTMD attached to the OWT. The chosen GA fitness function targets a minimization of the peak responses. The design parameters of the PTMD are the flexural rigidity and damping, the mass ratio, and the pendulum length.

Key-words: Offshore Wind Turbine; Pendulum Tuned Mass Damper; Genetic Algorithm Optimization; Structural Control; Power Spectral Density analysis.

Summary

List of Figures

List of Tables

List of Algorithms

Nomenclature

Abbreviations

2DOF 2-Degrees-Of-Freedom

3d-PTMD 3D - Pendulum Tuned Mass Damper

ABNT Associação Brasileira de Normas Técnicas

CNR Consiglio Nazionale delle Ricerche

DC Design Case

DFT discrete Fourier transform

DNV Det Norske Veritas

DV Design Variables set

ECD Extreme Coherent gust with Direction change

EDC Extreme Direction Change

EOG Extreme Operating Gust

ETM Extreme Turbulence Model

EWM Extreme Wind speed Model

EWS Extreme Wind Shear

FA fore-aft direction

FRF Frequency Responses Functions

HAWT Horizontal-Axis Wind Turbine

IEC International Electrotechnical Commission

JONSWAP Joint North Sea Wave Project

LC load case

MDOF Multi-Degree-Of-Freedom

MSL Mean Sea Level

NREL National Renewable Energy Laboratory

NWP Normal Wind Profile

OC3 Offshore Code Comparison Collaboration 3

OWT Offshore Wind Turbine

PM Pierson-Moskowitz

PSD Power Spectral Density

PTMD Pendulum Tuned Mass Damper

SDOF single-degree-of-freedom system

SEM Spectral Element Method

SS side-to-side direction

SWL Still Water Level

SWL Still Water Level

Greek characters

α angle of attack $= \phi - \beta$

α generalized Phillips' constant

α wind shear; power law exponent

β local blade twist

β_1 direction of propagation

Δr magnitude of the projection of the separation vector between the two points on to a plane normal to the average wind direction

Δ non-dimensional roughness

η surface elevation

γ peak-enhancement factor or overshoot parameter

$\Gamma()$ gamma function

γ_f partial safety factors for loads

κ wavenumber

$\kappa_u(\tau)$ autocorrelation function for the along wind turbulent fluctuations at a fixed point in space from the corresponding power spectrum

$\kappa_u(r)$ cross-correlation function between the turbulence component k at two points separated longitudinally by a distance r

$\kappa_u^o(r,\tau)$ autocorrelation function for a point on the rotating blade at a radius r

Λ turbulence scale parameter

λ tip speed ratio

μ ratio between the element radius and the total radius of the blade

μ ratio mass between the pendulum and system

μ viscosity

μ_w shallow water parameter

ν kinematic viscosity of the fluid

Ω rotational speed of rotor (rad/s)

ω wave frequency

ω_d dependent-depth frequency of the depth z

Φ velocity potential

ϕ flow angle

Φ_k transformation factor

ψ_n phase angle of the nth harmonic force

ρ air/water density

$\rho_u^o(r,\tau)$ Rotationally normalized autocorrelation function

$\sigma(r)$ solidity

σ_1 hub-height longitudinal wind velocity standard deviation

σ_2 hub-height lateral wind velocity standard deviation

σ_3 hub-height upward wind velocity standard deviation

σ_M standard deviation of the blade root bending moment

σ_u standard deviation of fluctuating component of wind in along-wind direction

σ_u standard deviation of particle velocity u

σ_v standard deviation of wind speed in across-wind direction

Latin characters

$\bar{U}$ mean wind velocity in the along-wind direction (typically taken over a period of 10 min)

$\hat{\mathbf{i}}$ unitary versor of x axis

$\hat{\mathbf{j}}$ unitary versor of y axis

$\hat{\mathbf{k}}$ unitary versor of z axis

A cross-sectional area

a axial flow induction factor

a' tangential flow induction factor

A_D actuator disk area

c chord length of the aerofoil

c phase velocity

c site-dependent scale parameter

$C(\Delta r, n)$ coherence function

$C(\gamma)$ normalizing factor

c_b velocity of the breaking wave

C_D drag constant relationship

c_d drag or resistance coefficient

C_I inertial constant relationship

c_i inertial coefficient

C_L lift coefficient

c_l^n lift coefficient for the nth harmonic

c_m added mass coefficient

c_m added mass coefficient

C_p damping of the pendulum

C_p power coefficient

C_T coefficient of thrust

C_z decay coefficient

D diameter

d water depth

$F(U)$ hourly mean wind speed variation about the annual mean

f_{fitness} fitness function

F_B fluctuating buoyancy force

F_D drag forces

F_f tip loss factor

F_I inertial forces

F_L lift force

F_X out-of-plane force per unit length

F_Y in-plane force per unit length

$F_{\bar{U}_{\text{max,1year}}}$ cumulative distribution function of the annual maximum value of 10-minute mean wind speed

$F_{H_S}(h)$ significant wave height

f_{vs} frequency of vortex shedding

H hub height above the MSL

H wave height

h mean water depth

h_0 reference depth for wind-generated current (typically 50m)

$H_\theta(\omega)$ pendulum response in the frequency domain

H_s significance wave height

$H_y(\omega)$ structure response in the frequency domain

H_{10} maximum wave height for a typical wave record of ten minutes in length

I turbulence intensity

I_{ref} turbulence Intensity at 15 m/s

K index referring to the velocity component direction (i.e. 1 = longitudinal, 2 = lateral, 3 = upward)

k height-dependent shape parameter

k surface roughness

K_C Keulegan-Carpenter number

K_p stiffness of the pendulum

K_s system stiffness

K_ν modified Bessel function of the second kind and order ν

L_c coherence scale parameter

L_k integral length scale for the along wind turbulence component measured in the direction k

L_p pendulum length

M_p pendulum mass

M_s system mass

n frequency (Hz)

N_{dec} step of generation for the occurrence of decimation

N_{gen} number of generations

N_{ind} number of individuals of the population

$n_k(z_j)$ non-dimensional height frequency

n_p frequency corresponding to maximum energy density given by the PM spectrum

P power developed by the rotor

p pressure

p_{c} crossover probability

p_{dec} decimation probabilit

p_{elit} elitism probability

p_{m} mutation probability

Q torque developed by the rotor

R blade length or rotor radius

$R_u^o(r,n)$ rotationally sampled power spectral density function

Re Reynolds number

S power Spectrum

s separation distance between a position fixed B and a position seen by a point A at a radius r (or two radius) on the rotating blade

S_F wave force PSD

$S_M(n)$ power spectrum of the blade root bending moment

$S_u^o(n_k)$ rotationally sampled spectrum at the frequencies n_k

S_w wave steepness parameter

$S_{jk}(n)$ cross spectrum of longitudinal wind-speed fluctuations, u, at points j and k (single-sided)

S_{JS} JONSWAP spectrum

S_{PM} Pierson-Moskowitz spectrum

$S_u(n)$ single-sided power spectrum of longitudinal wind-speed fluctuations, u, at a fixed point

$S_v(n)$ single-sided power spectrum of lateral wind-speed fluctuations, v, at a fixed point

$S_w(n)$ single-sided power spectrum of vertical wind-speed fluctuations, w, at a fixed point

St Strouhal number

T return period

T wave period

T' rotational integral length scale

T_p peak period

T_Z zero-upcrossing period

u,$\dot{u}$ horizontal velocity and acceleration of the particle

U' atmospheric turbulence component wind speed in the along-wind direction

U_1' longitudinhal component of turbulence (along x)

U_2' lateral component of turbulence (along y)

U_3' vertical component of turbulence (along z)

U_r Ursell parameter

U_r rated wind speed

U_{ave} annual average wind speed at hub height

U_{hub} mean wind speed at hub height

U_{ref} reference wind speed defined as 10 min mean wind speed at hub height with 50 year return period

U_{e1} extreme wind speed with a recurrence period of 1 year

U_{e50} extreme wind speed with a recurrence period of 50 years

V characteristic velocity of the flow

$v(z)$ current velocity

V_b forward velocity of particle water

V_g wind velocity in free atmosphere

V_m maximum horizontal water-particle velocity

V_N nominal lifetime

V_{in} cut-in wind speed

V_{out} cut-out wind speed

v_{tide} velocities generated by the tide

v_{wind} velocities generated by the wind

w,$\dot{w}$ vertical velocity and acceleration of the particle

z^* corrected height above ground for an obstacle z'

z_0 roughness length

Z_g height of atmospheric boundary layer

z_r reference height above ground

1 General Introduction

The current chapter gives an overview of the motivation, objectives, and scope of the work. The remaining chapters are related to:

- Chapter 2: The background of numerical modeling of Offshore Wind Turbine (OWT), the demanding environment, load actions due to rotating blades, the dynamic structural response procedure, and design loads.
- Chapter 3 The NREL 5-MW monopile OWT and the theory concerning the vibration control of OWTs, focusing on the Pendulum-Tuned-Mass-Damper (PTMD) type design used in this work. The analytical and numerical procedures for the PTMD coupled at the OWT hub using the 2-Degrees-Of-Freedom (2DOF), Spectral Element (SEM), and Finite Element (FEM) techniques.
- Chapter B Concepts of optimization and Genetic Algorithm (GA), as well as the home-made genetic optimization toolbox, used to search optimum PTMD designs.
- Chapter 4 Results from the case studies.
- Chapter 5 Conclusions from the case studies and suggestions for further work.

Appendix A present the author's list of publications, Appendix B presents a brief theory concerning the genetic algorithms optimization, and Appendix C is devoted to the Multi-degree-of-freedom (MDOF) reduction model.

1.1 Motivation

Wind energy is one of the renewable sources in fast development and implementation all over the world. Wind resources can be classified in offshore and onshore that comprehending coastal and inland. The Global Wind Energy Council (1) reports that worldwide installed wind power reached more than 650 GW up to 2019. The increase in worldwide installed wind power was 329% between 2010 and 2019 and 914% from 2000 to 2009 due to a deceleration of coastal wind farm facilities.

OWTs are beneficed from the vaster amount of wind power compared to the onshore. The offshore wind power reached a historical record in 2019 with 6145 MW new installations, and the cumulative capacity was 29136 MW (1).

Structural analysis of Offshore Wind Turbine (OWT) models has been vastly improved with new designs for global deployments in the coming years. These turbines are complex structural systems influenced by non-linearities, uncertainties, and fluid-structure interactions. The OWT design process requires the comprehension of some aspects, such as international standards, the macro/meso/micro-level of the OWT elements that will be analyzed, the costs involved, and the loads provoked by the wind blade rotation (2). The characterization of wind and hydrodynamic actions in analytical and numerical procedures is also fundamentals to comprehend the environmental conditions over an OWT.

To improve the productivity of modern OWTs, support structures significantly increased in slenderness and size, and structural designers are often requested to find their limitations based on the dynamics, structure, and control systems. High vibration levels occur in OWT due to its height, slenderness, and loads caused by its rotor operation and environmental action. As a result, the implementation of structural control is required systems to avoid failure and reduce maintenance costs (3).

Structural control mechanisms for the tower have been developed to balance dynamic forces on OWTs, such as earthquake excitation, wind loads and waves, dissipating energy, and increasing the efficiency in terms of fatigue and stability of the tower.

There are some types of controllers such as Tuned Mass Dampers (TMDs), tuned liquid mass dampers, controllable fluid dampers, etc, that can be used combined or not in different control strategies (passive, active, semi-active) (4) and more details about them are explored in sec. 3.2.1. Several types of vibration control dampers are found in literature and a brief review of its mechanisms and applications are presented in sec. 3.2.2.

Wind turbines with or without vibration control have been modeled by reduced models represented by analytical solutions or with the finite element method (FEM) (5, 6, 7). As an alternative, the SEM is an interesting method for modeling the whole system. The SEM (8, 9) is formulated by the analytical solution of the wave equation in the frequency domain. It implies high accuracy and low computational cost because of the reduction of DOFs to model a structure. It is a meshing method similar to FEM, where the element shape functions are replaced by the exact dynamic shape functions obtained from the analytical solution of governing differential equations. Therefore, a single element is sufficient to model any continuous and uniform part of the structure. The SEM had been used in the structural dynamics analysis including rod, beam, plates, cables, composite structures (10, 11, 12, 13, 14, 15), and ongoing researches is proposing new and improved elements (16, 17).

1.2 Objectives

The main objective of this thesis is to mitigate OWT vibrations with an optimal PTMD design. Two analytical procedures and a finite element case studies are investigated considering the NREL monopile 5-MW baseline OWT (18) as an object OWT reference to be coupled to the PTMD. A consistent OWT model is compared with the NREL OpenFAST software results presenting an alternative modular tool capable to evaluate the power spectrum density of the hydrodynamic and aerodynamic loads considering the parked and operating conditions of the OWT, including its power production. This spectral density is inputted, analytically, on a two-degree-of-freedom and in a spectral element model evaluating the OWT frequency response. A dynamic response is performed on the finite element case study in terms of the mean value of the mean wind and sea current and the standard deviation related to the effects of the turbulent wind and waves.

An in-house built GA toolbox (19) helps to find optimal PTMD parameters (flexural rigidity, damping, mass-ratio, and pendulum length) by setting a fitness function that targets a minimization of the frequency response peaks of the tower.

The case studies include the following research discussions which form the basis of this thesis:

- Numerical modeling of OWTs for response analysis including design load conditions with their respective environment demand and dynamic of rotating blades in operating condition, for both deterministic and stochastic loads.
- Effects of aerodynamic and hydrodynamic power spectral densities on OWTs.
- Analytical modeling of 2DOF and SEM and the numerical modeling of FEM for the NREL monopile 5-MW baseline OWT coupled to the Pendulum Tuned Mass Damper.
- Comparison of the tower-top response of the SEM model of a tower with the finite element, SDOF, and MDOF models, and of the SEM model of a tower coupled to the PTMD with the 2DOF and FEM models.
- Comparison of both SEM and FEM models with the NREL OpenFAST software results.
- Parametric analysis of the pendulum parameters influence for parked and operational conditions of the OWT for the analytical models.
- Optimal PTMD design procedure of the flexural rigidity, damping, mass-ratio, and pendulum length parameters using genetic optimization for all 2DOF, SEM, and FEM models.

- Dynamic structure analysis of the 3D-PTMD coupled to the OWT FEM model evaluating the response displacements and the stresses at the OWT base.
- OWT power production with tip-loss and/or root loss effects.

2 Numerical global modeling of OWTs and of the demanding environment for structural analysis purposes

2.1 Introduction

Historically, the development and advancement of societies have been intimately tied to the members' ability to produce and manipulate structures and materials to fill their needs. The merge of construction techniques with numerical and experimental methods, in last decades, gave rise to complex structures capable to assume the dynamics of nature. The combination of unusual structure shapes with amazing height, length, slenderness, flexibility and lightness can be possible with sophisticated programming methods. The effects of dynamic actions on structures must be evaluated to approximate these methods near to the reality.

The randomness characteristics of dynamics actions, usually termed stochastic excitation, includes seismic ground motions, wind gusts or turbulence in wind and ocean waves, among others. By neglecting the variation of dynamic actions in space, the spatial random field can be simplified as a series of random process with the same statistical characteristics, enabling that, by using a time sequence, one point reflects the effects of random excitation on structures. There are widely used assumptions in the establishment of stochastic excitation models, as the homogeneous and isotropic assumption in which a random field model should be adopted to reflect the spatial dynamic actions; and the stationary assumption in which the variance is a constant and not changing with time. This last assumption is taken to characterize the stationary stochastic processes usually taken in the modeling of the wind turbulence in the atmospheric boundary layer (20).

The phenomenology-based modeling and the physics-based modeling are two methods in the process of modeling stochastic dynamic excitation. The first one used correlation or Power Spectral Density (PSD) functions based on statistical moments. The physics-based modeling focuses on a random function model of dynamic excitation

considering the real physical background. Besides wind and wave, stochastic methods are also capable to describe the operational effects of OWTs due to rotating blades.

In general, the main focus of the structural analysis for PTMD design purposes is the peak or the RMS of the structural response. In order to obtain them, the response is modeled as composed of a mean part, induced by the mean wind and the sea current (eventually including the vortex shedding effects), and by a fluctuating/stochastic part, induced by the wind turbulence and by the sea waves. The first one is obtained by a static analysis, while the second one can be evaluated, in frequency domain, by a PSD analysis. The actions due to the mean wind and the sea current are then modeled by equivalent static forces, while the actions due to turbulent wind and waves are modeled by their power spectrum.

OWTs are located in a complex and high-demanding environment (21) with some non-linear interactions and high variability of loading conditions (6). The scheme of such a complex environment is shown in Figure 2.1.1, as well as the relevant macro-geometric parameters of the problem: the mean water depth (h) under the SWL, the hub height (H_{hub}) above the SWL, the blade length or rotor radius (R), and the bedrock depth (d) (22).

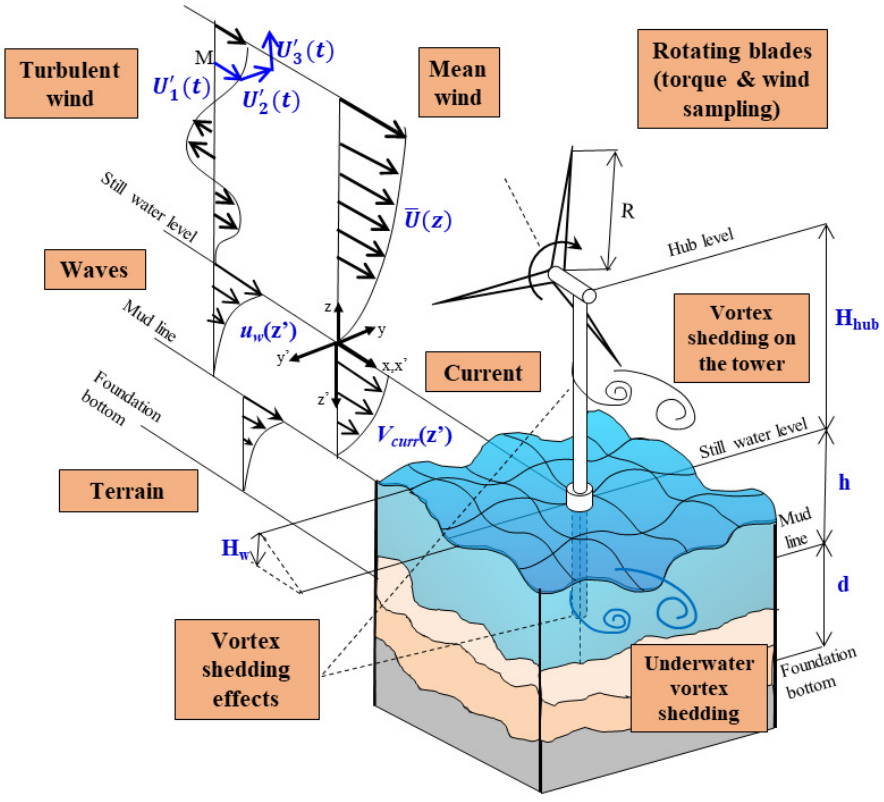

Figure 2.1.1 – Environmental actions over an Offshore Wind Turbine

Beside the wind and waves actions, stochastic models are also capable of describing the wind sampling effects of OWTs due to rotating blades in operating conditions. This is modeled by a rotor torque plus a sampling effect on turbulent wind forces. This section

briefly summarizes the models used for obtaining the peak dynamic response of the turbine under wind-current and wave loads for both parked and operating conditions by the static+PSD analyses.

2.2 Wind field and wind-induced loads

The effects of wind actions on structures are ruled by norms and standards considering specific construction sites, such as the ABNT NBR 6123 (23) in Brasil and the CNR-DT 207/2008 (24) in Italy. While the Brazilian standard ABNT NBR 6123 does not has updates since 1988, the Italian CNR-DT 207/2008 was updated in 2008. Due to the material wealth of the scientific contribution of the CNR-DT 207/2007 and the period spent by this researcher in the University of Rome "Sapienza", the CNR is mainly used in this section for the characterization of the wind.

The CNR-DT 207/2008, of the National Research Council of Italy, specifies limitations and requirements, which includes: civil engineering structures of height not exceeding 200 m, industrial structures, including moving and lifting equipment, and bridges with spans not greater than 200 m, and other specific cases. This norm presents the effects of wind actions on structures and their components, the principles and rules, characterized by (a) the atmospheric characterization over construction site characteristics; (b) wind design velocity and peak velocity pressure; (c) the shape, size and orientation of the structure, the peak aerodynamic actions exerted by the wind on the structure and its components; (d) the mechanical properties of the structure and of its components (if it's considered static actions, dynamic and/or aeroelastic actions and effects caused by vortex shedding, aeroelastic phenomena, such as galloping, flutter, interference).

To show the effects of wind actions on structures, a systematic review about the basic concepts of the wind characterization (sec. 2.2.1), the wind probabilistic characterization (sec. 2.2.2), the effects of turbulence (sec. 2.2.3), and the Aerodynamics of horizontal axis wind turbines (HAWT, sec. 2.2.4) are reported in this section.

2.2.1 Wind characterization

The displacement of air masses provoked by temperature and pressure fields conditioned for the solar radiation, can induce many types of wind circulations. These aeolian phenomena can be classified as primary (trade winds, westerlies, easterlies), secondary circulations (cyclones, anti-cyclones, monsoons), and local winds associated with specific geographic (breezes, Föhn winds, Catabatic winds) or atmospheric conditions (frontal winds, Downbursts, whirlwinds).

There are no mathematical models capable to include all the aeolian phenomena mentioned. But various different partial models are capable to representing single wind

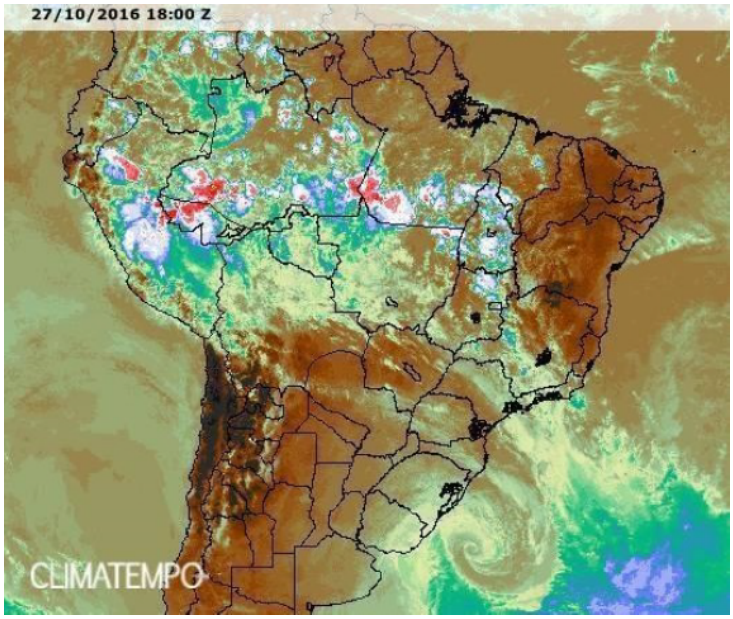

Figure 2.2.1 – Image from Satellite GOES-13

types with varying degrees of confidence. In this thesis the wind representation adopted concerns extratropical cyclones - one of the most severe wind events in terms of probability of occurrence, potentially affecting structures in countries with well behaving climate.

Extratropical cyclones are very common on south coast of Brazil. They are formed from the meeting of cold air carried by the easterlies and hot tropical air carried by the westerlies. The meeting of two air fronts of different temperature causes the phenomenon and also a storm. Figure 2.2.1 shows an extratropical cyclone which affects the coast of Rio Grande do Sul. The bands of the cold front clouds associated with this extratropical cyclone appear between Rio de Janeiro, Minas Gerais and São Paulo south-central.

The wind exerts aerodynamic actions on the whole structure or on individual structural components, due to the oncoming flow and the turbulent wake generated by the bodies. An aeroelastic effect is produced by the interaction between the structure oscillation over the oncoming flow and its aerodynamic actions. Another adjacent structures may also causes an interference phenomena which can reduce or increase actions and effects on the wind dynamics or on individual components.

The wind characteristics at the construction site may be determined by experimental, numerical or analytical methods. The experimental determination can be performed by means of full-scale measurements or wind tunnel testing. The numerical and analytical depends on the terrain roughness and topography surrounding the site, thermal conditions of the atmosphere, and the wind climate of the site.

For climate representation, the Standard International Electrotechnical Commission (IEC) 61400-1 (25) presents a distinction between normal and extreme wind conditions in which a wind turbine shall be design safely. The normal one consider the recurrent structural loading conditions and can determinate the fatigue and extreme loads (by

extrapolating normal operation loads), while the extreme represent rare external design conditions that can lead to extreme loads in the components of the OWT, in the the support and foundation (26).

A simplified procedure to determine wind characteristics can be implemented by computing the mean wind velocity, the turbulence intensity (I), and the peak velocity pressure, based on the following assumptions:

- the designed wind velocity is associated with an extratropical cyclone developed in wide areas and long periods (at least one or two days);
- the wind velocity is high, therefore the atmosphere is neutrally stratified and it is independent of temperature;
- for onshore sites, the terrain roughness is uniform in all directions, the local is flat or includes an isolated topographic of simple shape;
- for offshore sites, sea surface characteristics must be considered (eg. waves).

2.2.2 Wind probabilistic characterization

As environmental conditions have stochastic nature, a certain return period T_R may be defined strategically. The nominal lifetime V_N is defined, for well maintained constructions, as the nominal construction lifetime. It is recommended defines the design reference wind velocity v_r as a function of the design return period T_R to choose the properties and the nominal lifetime of the construction (24). The reference return period $T_{R,0}$ is defined as the larger value between the conventional return period T_0 (tab. 2.2.1) and the nominal lifetime V_N.

$$T_{R,0} = \max\{T_0, V_N\} \tag{2.2.1}$$

Table 2.2.1 – Conventional return period T_0 (24)

Properties of the structure	T_0 (years)
Temporary constructionss, structures under construction or being demolished, provided this condition lasts for less than 1 year. For temporary structures, the overall length of all periods in which the structure is reused shall be less than a year	10
Standard constructions	50
Large important constructions	100
Strategic constructions	200

Low values of T_R means normal wind conditions while high values are associated with extreme conditions. Therefore, this value has a high influence on the design process.

Usually, wind speed variations during the year are characterized in terms of probabilistic distribution, because annual mean wind speeds are hard to predict. For OWTs, in areas where hurricanes do not occur, a Weibull distribution gives a good representation of the variation in hourly mean wind speed over a year at many typical sites (27). For a 10-minute mean wind speed $\bar{U}$, in a given height z above the MSL, the eq. 2.2.2 (from the Det Norske Veritas Offshore Standard DNV-OS-J101 (26)) estimates the fraction of time $F(U)$, for which the hourly mean speed $\bar{U}$ exceeds U.

$$F_{\bar{U}}(U) = 1 - \exp\left[-\left(\frac{U}{c}\right)^k\right] \tag{2.2.2}$$

where the scale and shape parameters, respectively c and k, are site- and height-dependent, which describes the variability about the mean. The annual mean wind speed $\bar{U}$ is related to c by:

$$\bar{U} = c\Gamma(1 + 1/k) \tag{2.2.3}$$

where Γ is the complete gamma function. By differentiating $F(U)$ in terms of U the probability density function can be computed as:

$$f(U) = k\frac{U^{k-1}}{c^k}\exp\left(-\left(\frac{U}{c}\right)^k\right) \tag{2.2.4}$$

The Rayleigh distribution occurs when the Weibull distribution adopts $k = 2$, and this is a fairly typical value for many locations. Higher value of k (eg. 2.5 or 3) indicates a site where the variation of $F(U)$ is small. Lower values of k (eg. 1.2 or 1.5) indicates greater variability about the mean (27).

The wind speed $\bar{U}_{T_R}$, with return period T_R in units of years, is defined as a function of the $(1 - 1/T_R)$ part of the annual maximum 10-minute mean wind speed (Eq. 2.2.5).

$$\bar{U}_{T_R} = \frac{1}{F_{\bar{U}_{\text{max,1year}}}}\left(1 - \frac{1}{T_R}\right) \tag{2.2.5}$$

where $T_R > 1$ year and $F_{\bar{U}_{\text{max,1year}}} = [F_{\bar{U}}(u)]^N$ is the cumulative distribution function of the annual maximum value of 10-minute mean wind speed defined as function of the distribution, $F_{\bar{U}}(u)$, and $N = 52560$ is the number of stationary 10-minute periods in one year.

2.2.3 Turbulence

The effects of turbulence are described as a random function of space and time and are generated mainly by the friction with the earth's surface and by thermal effects which can cause vertical movement of air masses due to temperature variations. Turbulence effects are a complex process and cannot be represented in terms of deterministic equations. For that reason it is generally described in terms of statistical properties.

A detailed representation may consider both mean velocity and turbulent fluctuations. When a long time span are considered and the power spectrum S of the wind velocity is evaluated for a frequency n, a curve is described with two main, well-separated harmonic contents.

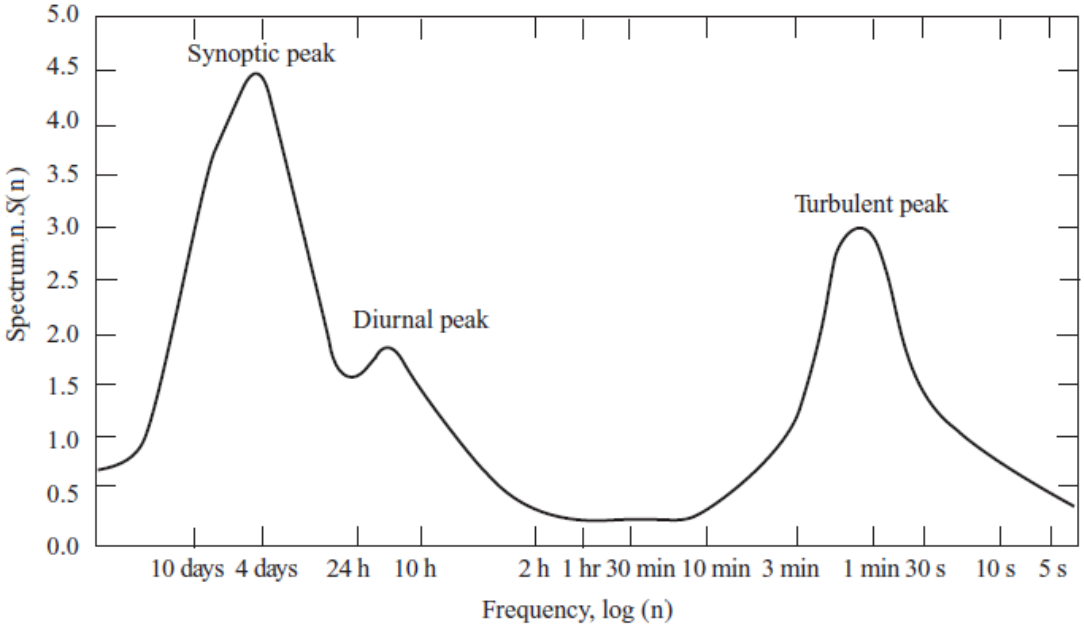

Figure 2.2.2 – Wind spectrum based on work by van de Hoven (27)

In the wind speed spectrum constructed by Van der Hoven (fig. 2.2.2), recorded at Brookhaven, New York, is notable two harmonics behaviors: the first one can be associated with long period aeolian events (between one hour to few months), with two peaks (synoptic and diurnal) which represents the recurrence of aeolian storms; the turbulent peak is associate with short period aeolian events (between few seconds to about ten minutes), representing the turbulent fluctuation of wind speed.

The turbulence intensity is defined as a measure of the overall level of turbulence as (27):

$$I = \sigma/\bar{U} \tag{2.2.6}$$

where σ is the standard deviation of wind speed variations about the mean wind speed $\bar{U}$.

By assuming that, wind turbulence can be represented as a zero-mean Gaussian, stationary, ergodic stochastic process. Wind fluctuations results from a composite of sinusoidally varying winds superimposed on the mean steady wind, and this variations have a variety of frequencies, amplitudes, and phases.

For a Normal Turbulence Model (NTM), the turbulence standard deviation along the direction of the mean wind velocity, $\sigma_k = \sigma_1$ (25) (where $k = 1$ is the along direction), is given by the 90% quantile for a given hub height wind speed (eq. 2.2.7)

$$\sigma_1 = I_{\text{ref}}\,(0.75 U_{\text{hub}} + b)\,; \tag{2.2.7}$$

where $b = 5.6m/s$, and I_{ref} is the reference value of the turbulence intensity defined in tab. 2.2.2.

For wind turbines, the IEC 61400-1 standard (25) defines (tab. 2.2.2) the classes to represent external conditions that cover most applications, in terms of the wind speed and turbulence parameters.

Table 2.2.2 – Basic parameters for wind turbine classes (25, adapted)

	Class I	Class II	Class III
Reference wind speed, U_{ref} (m/s)	50	42.5	37.5
Annual average wind speed, U_{ave} (m/s)	10	8.5	7.5
50-year return gust speed, 1.4 (m/s)	70	59.5	52.5
1-year return gust speed, 1.12 (m/s)	56	47.6	42.0
A, I_{ref} (-)	0.16		
B, I_{ref} (-)	0.14		
C, I_{ref} (-)	0.12		

These parameters are applied at hub height. U_{ref} and U_{ave} are, respectively, the reference wind speed over 10 min and the annual average wind speed, A, B, and C respectively designate the category for higher, medium and lower turbulence characteristics, and I_{ref} is the expected value of the turbulence intensity at 15 m/s. The design values of class S shall be chosen by the designer and lifetime for wind turbine classes I to III shall be at least 20 years (conditions I to III are neither intended to cover tropical storms such as hurricanes, cyclones and typhoons). The 50- and 1-year return gust speed parameters will be used later in other sections.

For extreme wind conditions the shear events, the peak wind speeds due to storms and their rapid changes of direction are also included. The IEC 61400-1 defines the following events for these conditions:

- Extreme Wind speed Model (EWM);
- Extreme Operating Gust (EOG);
- Extreme Turbulence Model (ETM);
- Extreme Direction Change (EDC);
- Extreme Coherent gust with Direction change (ECD);
- Extreme Wind Shear (EWS);

The turbulence standard deviation for extreme conditions is computed by eq. 2.2.8.

$$\sigma_1 = 0.11 U_{\text{hub}} \tag{2.2.8}$$

There are other environmental conditions that can affect the integrity and safety of wind turbines, like thermal, corrosive, mechanical, electrical... that can be found in IEC 61400-1.

2.2.3.1 The boundary layer

Many researchers developed a series of relations which describes the properties of the atmospheric boundary layer, such as turbulence intensities, spectra, length scales and coherence functions.

To represent an extra-tropical cyclone we consider a gradient height Z_g that split the atmospheric boundary and the free atmosphere (fig. 2.2.3). Above that height Z_g (defined, approximately, between 1000 m and 3000 m, depending on the wind velocity and the roughness length) the wind velocity V_g in free atmosphere is constant because there is no influence due to the ground friction force. Below Z_g there is an atmospheric turbulent boundary layer in which the wind velocity is affected by the surface roughness (terrain or sea), the Coriolis effects due to the earth's rotation and thermal effects.

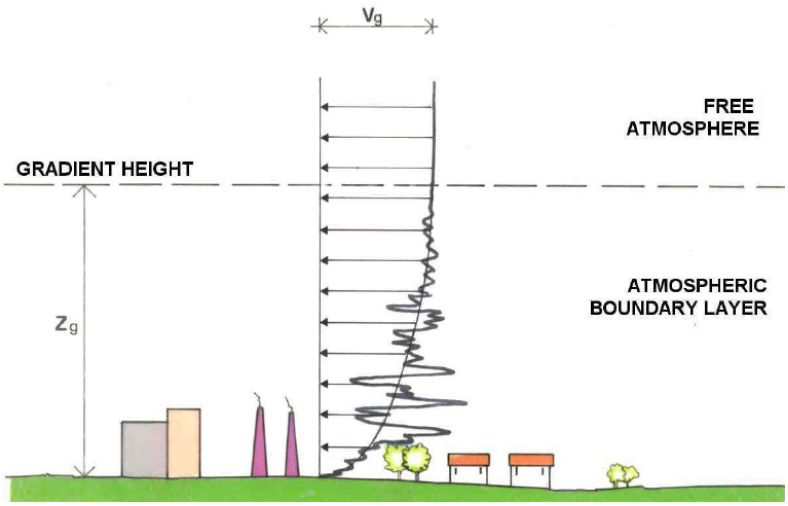

Figure 2.2.3 – Mean wind velocity and atmospheric layer profile on onshore sites (24)

The neutral atmosphere condition of stability are the most important situation when considering the turbulent wind loads on a wind turbine. In the neutral atmosphere the main effects to be considered are the surface roughness and the Coriolis effect. Burton et al. (27) presents some typical surface roughness lengths in tab. 2.2.3.

Table 2.2.3 – Typical surface roughness lengths (27)

Type of Terrain	Roughness length z_o (m)
Cities, forests	0.7
Suburbs, wooded countryside	0.3
Villages, countryside with trees and hedges	0.1
Open farmland, few trees and buildings	0.03
Flat grassy plains	0.01
Flat desert, rough sea	0.001

From the wind shear law, a wind profile can be expressed by the wind speed variation height above ground by a logarithmic (eq. 2.2.9) or a power law profile (eq. 2.2.10).

$$\bar{U}(z) = U(z_r)\frac{\ln(z/z_0)}{\ln(z_r/z_0)} \tag{2.2.9}$$

$$\bar{U}(z) = U(z_r)\left(\frac{z}{z_r}\right)^{\alpha} \tag{2.2.10}$$

where z_r is a reference height above ground used for fitting the profile, z_0 is the roughness length; α is the wind shear (or power law) exponent.

IEC 61400-1 ed. 3 (25) classify specific wind profiles for normal and extreme models. The Normal Wind Profile (NWP) can be computed following the power law of eq. 2.2.11.

$$\bar{U}(z) = U_{\text{hub}}\left(\frac{z}{H}\right)^{\alpha} \tag{2.2.11}$$

where U_{hub} is the wind speed at hub height of the wind turbine, H, and the power law exponent, α, shall be assumed to be 0.2 for normal wind conditions onshore or 0.14 for normal wind conditions offshore locations (25, 28).

For an EWM, the extreme wind speed with a recurrence period of 50 years, U_{e50}, is computed as a function of height z following the eq. 2.2.12.

$$U_{e50}(z) = 1.1U_{\text{ref}}\left(\frac{z}{H}\right)^{\alpha} \tag{2.2.12}$$

where $\alpha = 0.11$. For a recurrence period of 1 year: $U_{e1}(z) = 0.8U_{e50}(z)$.

The mean value of the wind speed over a time period of 10 min is assumed to follow a Rayleigh distribution at hub height given by:

$$P_R(U_{\text{hub}}) = 1 - \exp\left[-\pi\left(\frac{U_{\text{hub}}}{2U_{\text{ave}}}\right)^2\right] \tag{2.2.13}$$

where for standard wind turbine classes $U_{\text{ave}} = 0.2U_{\text{ref}}$.

For a spectral representation, the along-wind velocity U in a generic point in space M, at height z and time t (Eq. 2.2.14) is separated into two contribution: the first one describes the mean wind velocity $\bar{U}$ over 10 minutes in the along-wind direction (Eq. 2.2.15) - characterised by long-term variations; and an atmospheric turbulence U' (Eq. 2.2.16) -

characterised by high frequency fluctuations.

$$U(M;t) = \bar{U}(z) + U'(M;t) \tag{2.2.14}$$

$$U(M) = \hat{\mathbf{i}} \cdot \bar{U}(z) \tag{2.2.15}$$

$$U'(M;t) = \hat{\mathbf{i}} \cdot U_1'(M;t) + \hat{\mathbf{j}} \cdot U_2'(M;t) + \hat{\mathbf{k}} \cdot U_3'(M;t) \tag{2.2.16}$$

where $\hat{\mathbf{i}}$, $\hat{\mathbf{j}}$, $\hat{\mathbf{k}}$ are the versors of x, y, and z axes; $\bar{U}$ is the mean wind velocity at height z in the along-wind direction; U_K' is the component of turbulence which varies in space and time with K referring to the velocity component direction (i.e. 1 = longitudinal, 2 = lateral, 3 = upward).

2.2.3.2 Turbulence spectra

To describe functions of frequency we can use the term spectrum and the function that characterizes turbulence is known as a 'spectral density' function. Power Spectral Densities (PSDs) describes the relation between frequency and power amplitudes of sinusoidally varying signals making up the fluctuating wind speed (29).

The average power in the turbulence over a range of frequencies may be found by integrating the PSD between two frequencies and the integral over all frequencies is equal to the total variance.

PSDs functions are often used in dynamic analysis as models in wind energy engineering when representative turbulence power spectral densities are unavailable from a given site. In 1948, Karman (30) developed extensive series of experiments to create a turbulent homogeneous and isotropic flow regime model in a wind tunnel.

According to the Kolmogorov law, the spectrum must approach an asymptotic limit proportional to $n^{-5/3}$ at high frequency (here n is the frequency in Hz). This represent the decay of turbulent eddies to higher frequencies as turbulent energy is dissipated as heat (27).

To consider the effects of the spatial variation of turbulence in the lateral and vertical direction due to the variation of the wind inside the vertical plan spanned by the moving blades, the spectral description of turbulence must be extended to include information about the cross-correlations between turbulent fluctuations at points separated laterally and vertically. These correlations decrease as the distance separating two points increases and can be described by 'coherence' functions, which describe the correlation as a function of frequency and separation (27). The coherence $C_{jk}(\Delta r, n)$ is defined by:

$$C_{jk}(\Delta r, n) = \frac{|S_{jk}(n)|}{\sqrt{S_{jj}(n) S_{kk}(n)}} \tag{2.2.17}$$

where S_{jk} is the cross-spectrum of variation at two points separated by r, and S_{jj} and S_{kk} are the spectra of variations at each of the points (usually $S_{jj} = S_{kk}$).

Characterizing the turbulent components u and v and neglecting the vertical w, the normalized one-side ESDU PSD (31) can be write as (5, 32):

$$\frac{nS_u(n)}{\sigma_u^2} = \frac{6.868 n_u}{[1 + 10.302\ n_u^2(z_j)]^{5/3}} \tag{2.2.18}$$

$$\frac{nS_v(n)}{\sigma_v^2} = \frac{9.434 n_v}{[1 + 14.151\ n_v^2(z_j)]^{5/3}} \tag{2.2.19}$$

where z_j is the height (in m) of point j, σ_u^2 and σ_v^2 are the variances of the velocity fluctuations, where $\sigma_v/\sigma_u = 0.7$ (5, 32), and $n_k(z_j)$ is a non-dimensional height frequency dependent, given by:

$$n_k(z) = \frac{nL_k(z_j)}{\bar{U}} \tag{2.2.20}$$

It can be see in eq. 2.2.20 a length scale $L_k(z_j)$, where z_j is the height of point j, which can be identified as the integral length scale of the longitudinal component in the longitudinal direction, and defined as $\int_0^\infty \kappa_u(r)dr$ where κ_u is the cross-correlation function between the turbulence component i at two points separated longitudinally by a distance r. The integral scale can be derived for $k = u, v$ according the ESDU (33).

Length scales are dependent on the surface roughness z_0 and the height above ground (z). If there are obstacles on the ground (of height z'), the height above ground should be corrected for assuming an effective ground surface at a height $z^* = z' - 2.5z_0$ (33). Far from the ground the turbulence becomes isotropic.

The out of diagonal terms (cross-spectra) $S_{jk}(n)$ of $[S]_{jk}\,(j, k = 1, 2, \ldots, N)$ are given by:

$$S_{jk}(n) = \sqrt{S_{jj}(n)S_{kk}(n)} \times \exp\left(-F_{jk}(n)\right) \tag{2.2.21}$$

where for vertically aligned points:

$$F_{jk}(n) = \frac{|n|\sqrt{C_z^2(z_j - z_k)^2}}{2\pi(\bar{U}(z_j) + \bar{U}(z_k))} \tag{2.2.22}$$

where C_z represents the *decay coefficient* that is inversely proportional to the spatial correlation of the process. With this model Petrini et al. (5, 22) generates samples of the wind action exerted on each point j of the structure and applied them into an OWT using finite elements.

When site-specific spectral densities of the wind speed process can be determined from available measured wind data, it recommends the use of a spectral density model which fulfils that the spectral density $S(n)$ asymptotically approaches the following form as the frequency f in the inertial subrange increases (26):

$$n\frac{S_k(n)}{\sigma_k^2} = 0.202\left(\frac{L_k}{\bar{U}}\right)^{-2/3} n^{-2/3} \tag{2.2.23}$$

In the OWT context, both IEC 61400-1 and DNV-OS-J101 (26) proposes the use of the Kaimal spectrum (modified Karman's PSD), unless data indicate otherwise, following the Eq. 2.2.24.

$$\frac{nS_k(n)}{\sigma_k^2} = \frac{4nL_k/\bar{U}}{\left(1+6nL_k/\bar{U}\right)^{5/3}} \tag{2.2.24}$$

where the integral scale parameter L_k and the standard deviation σ_k are given in tab. 2.2.4.

Table 2.2.4 – Turbulence spectral parameters for the Kaimal model (25)

Velocity component, K	1	2	3
Standard deviation, σ_k	σ_1	$0.8\sigma_1$	$0.5\sigma_1$
Integral scale, L_k	$8.1\Lambda_1$	$2.7\Lambda_1$	$0.66\Lambda_1$

The longitudinal turbulence scale parameter, Λ_1, at hub height shall be given by:

$$\Lambda_1 = \begin{cases} 0.7z & \text{for } z < 60m \\ 42m & \text{for } z \geq 60m \end{cases} \tag{2.2.25}$$

where z denotes the height above the MSL.

The normalized Kaimal spectrum for $\bar{U} = 12m/s$ is applied to the NREL 5-MW OWT at tower-top $z = 87.6m$ (34) as shown fig. 2.2.4.

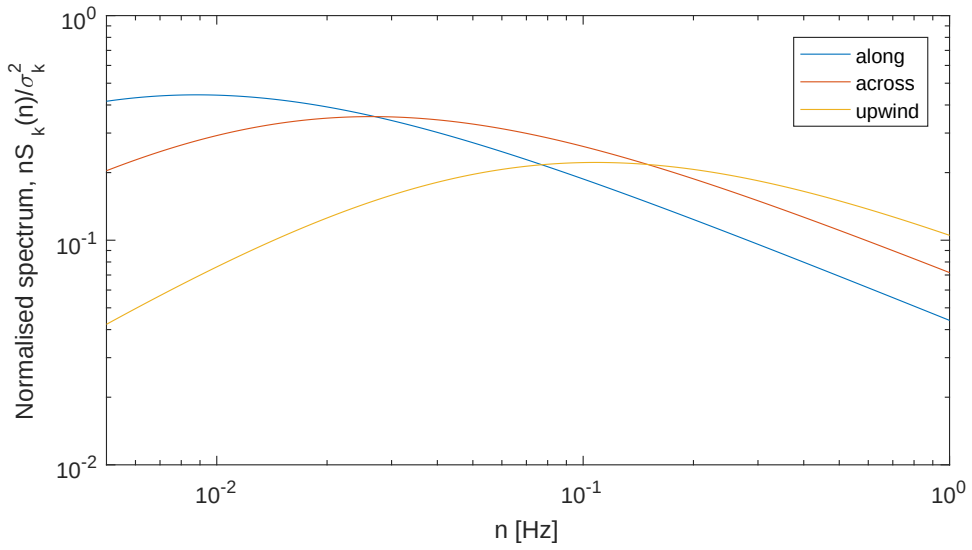

Figure 2.2.4 – Kaimal tower-top wind spectrum in along, across and upwind directions

An exponential coherence model may be used in conjunction with the Kaimal autospectrum to taken into account the spatial correlation in the longitudinal velocity component, defined by (25):

$$C_u(\Delta r, n) = \exp\left[-12\left((n\Delta r/\bar{U})^2 + (0.12\Delta r/L_c)^2\right)^{0.5}\right] \tag{2.2.26}$$

where $C_u(\Delta r, n)$ is the coherence function defined by the complex magnitude of the cross-spectral density of the longitudinal wind velocity components at two spatially separated points divided by the autospectrum function; Δr is the magnitude of the projection of the separation vector between the two points on to a plane normal to the average wind direction; $L_c = 8.1\Lambda_1$ is the coherence scale parameter.

The standard does not specify the coherence of the other two components to be used in conjunction with the Kaimal model, Burton et al. (27) shows that the following expression is often used:

$$C_v(\Delta r, n) = C_w(\Delta r, n) = \exp\left(-12\Delta r \frac{n}{\bar{U}}\right) \tag{2.2.27}$$

2.2.4 Aerodynamics of HAWT

The aim of this section is not to present the entire theory about the aerodynamics of HAWT, but presents a reviewed requirements for its design. To supplement this section two important references must be mentioned: the "Wind energy: handbook" of Burton et al. (27) and the "Aerodynamics of Wind Turbines" from Hansen (35).

2.2.4.1 Simple momentum theory

Burton defines the actuator disc concept, as shown fig. 2.2.5, to describe a simplified mechanism for the extraction of kinetic energy of wind turbines in which D refers to conditions at the disc and W to conditions in the far wake. This actuator disk induces a velocity variation which is superimposed on the free stream velocity U_∞. Then, the net stream-wise velocity is computed as:

$$U_D = U_\infty(1 - a) \tag{2.2.28}$$

where a is called the axial flow induction factor (or inflow factor).

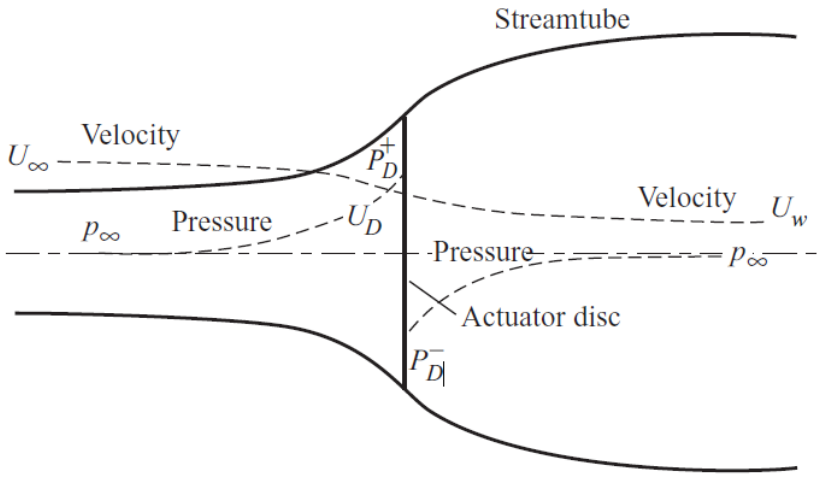

Figure 2.2.5 – An energy extracting actuator disc and stream-tube (27)

By using Bernoulli's equation and assuming the flow to be incompressible ($\rho_\infty = \rho_D$) and horizontal ($h_\infty = h_D$), it can be deducted, by a simple momentum theory, that $U_W = U_\infty(1-2a)$. The power coefficient is then defined as:

$$C_P = \frac{\text{Power}}{\frac{1}{2}\rho U_\infty^3 A_D} = 4a(1-a)^2 \tag{2.2.29}$$

where A_D is the actuator disk area and ρ the air density. The denominator represents the power available in the air without the actuator disc. The maximum value of C_P occurs when $dC_p/da = 0$, i.e. $a = 1/3$, and it is known as the Lanchester-Betz limit. Hence, $C_{p_{max}} = 0.593$.

Other non-dimensional factor which can quantify the actuator disc force caused by the pressure drop is the coefficient of thrust C_T (fig. 2.2.6), defined as:

$$C_T = \frac{\text{Thrust}}{\frac{1}{2}\rho U_\infty^2 A_D} = 4a(1-a) \tag{2.2.30}$$

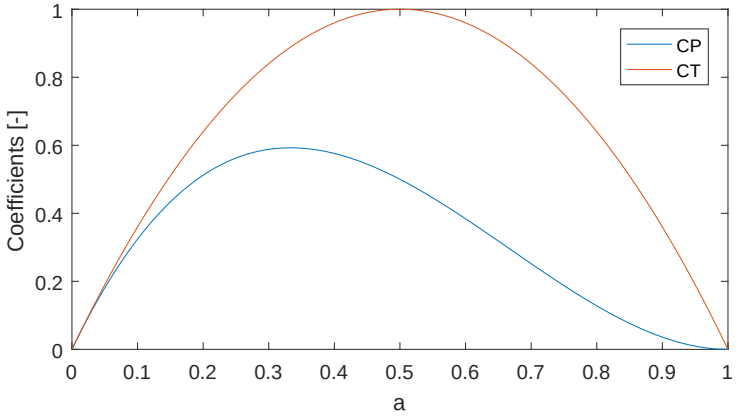

Figure 2.2.6 – C_p and C_t in function of the induction factor a

For values over $a > 1/2$, the wake velocity U_W becomes zero (or negative) and this momentum theory no longer can be applied.

This theory can be expanded adding a tangential component of velocity due to the wake rotation in terms of a tangential flow induction factor a'. Then the actuator disc is swept out by a multiplicity of aerofoil blades each with an uniform bound circulation $\Delta\Gamma$.

2.2.4.2 Blade-element/momentum (BEM) theory

To extend the formulation of the momentum theory, the BEM theory assumes that the forces on a blade element of radius r and length δr (fig. 2.2.7) can be calculated by means of two-dimensional aerofoil characteristics using an estimated angle of attack.

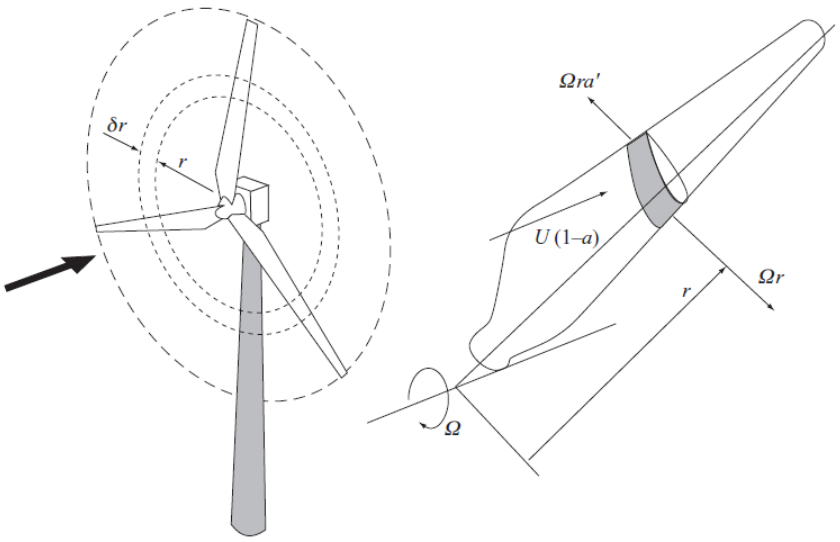

Figure 2.2.7 – Description of a blade element (27)

Figure 2.2.7 shows that the velocity components at a radial position on the blade can be expressed in terms of the wind speed ($U(1-a)$), the flow factors (a and a') and the rotational speed of the rotor (Ωr).

Having information about how the aerofoil characteristic coefficients C_l and C_d vary with the angle of attack, the forces on the blades can be computed in function of a and a'.

The velocities relative to the blade chord line at radius r are shown in fig. 2.2.8. The resultant relative velocity at the blade becomes:

$$W = \sqrt{U_\infty^2(1-a)^2 + r^2\Omega^2(1+a')^2} \tag{2.2.31}$$

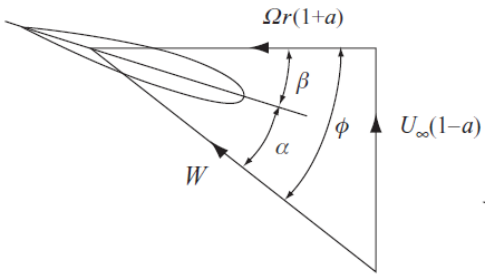

Figure 2.2.8 – Blade element velocities (27)

The angle of attack is given by $\alpha = \phi - \beta$, where ϕ is the inflow angle and β is the local blade twist. Further, it is seen that:

$$\phi = \arctan\left[\frac{U_\infty(1-a)}{r\Omega(1+a')}\right] \tag{2.2.32}$$

The lift and drag force on a span-wise length δr of each blade are computed by eqs. 2.2.33 and 2.2.34, respectively.

$$\delta L = \frac{1}{2}\rho W^2 c C_l \delta r \tag{2.2.33}$$

$$\delta D = \frac{1}{2}\rho W^2 c C_d \delta r \tag{2.2.34}$$

The axial thrust and the torque on an annular ring of the actuator disc are computed by eqs. 2.2.35 and 2.2.36, respectively.

$$\delta T = \frac{1}{2}\rho W^2 B c (C_l \cos(\phi) + C_d \sin(\phi))\delta r \tag{2.2.35}$$

$$\delta Q = \frac{1}{2}\rho W^2 B c (C_l \sin(\phi) - C_d \cos(\phi))\delta r \tag{2.2.36}$$

$$\tag{2.2.37}$$

where B is the number of blades.

The lift and drag projected in the normal and tangential direction of the rotorplane, are convenient described as:

$$p_N = L\cos\phi + D\sin\phi \tag{2.2.38}$$

$$p_T = L\sin\phi - D\cos\phi \tag{2.2.39}$$

These equations are normalized with respect to $(1/2)\rho W^2 c$ (35), yielding:

$$C_n = C_l\cos\phi + C_d\sin\phi \tag{2.2.40}$$

$$C_t = C_l\sin\phi - C_d\cos\phi \tag{2.2.41}$$

A solidity $\sigma(r)$ is defined as the fraction of the annular area by the rotor disc area:

$$\sigma(r) = \frac{c(r)B}{2\pi r} \tag{2.2.42}$$

Then the axial thrust and torque on all blade elements, with the rate of change of axial and angular momentum of the air that passes through the annulus swept by the elements, can be written, respectively, as:

$$\delta T = 2\pi r \delta r \rho U_\infty (1-a) 2a U_\infty \tag{2.2.43}$$

$$\delta Q = 2\pi r \delta r \rho U_\infty (1-a) 2a' r^2 \Omega \tag{2.2.44}$$

From the thrust and torque, the axial and tangential induction factors can be computed, respectively, as:

$$a = \frac{1}{\frac{4\sin^2\phi}{\sigma C_n} + 1} \tag{2.2.45}$$

$$a' = \frac{1}{\frac{4\sin\phi\cos\phi}{\sigma C_t} - 1} \tag{2.2.46}$$

This is the principle of the BEM method. By an initial value of a and a', it is possible estimate the aerodynamic coefficients, inflow angles and angle of attacks for specific elements of a blade. To achieve good results two corrections must be applied: The Prandtl's tip loss factor and the empirical Glauert correction (35).

The Prandtl's tip loss factor corrects the assumption of an infinite number of blades. The vortex system in the wake with finite number of blades is different with a rotor with infinite number of blades. Prandtl derived a correction factor F, from the thrust and torque estimation computed as:

$$F = \frac{2}{\pi} cos^{-1}(e^{-f}) \tag{2.2.47}$$

where:

$$f = \frac{B}{2} \frac{R - r}{r \sin \phi} \tag{2.2.48}$$

where R is the total radius of the rotor.

Then the eqs. 2.2.45 and 2.2.46 becomes:

$$a = \frac{1}{\frac{4F \sin^2 \phi}{\sigma C_n} + 1} \tag{2.2.49}$$

$$a' = \frac{1}{\frac{4F \sin \phi \cos \phi}{\sigma C_t} - 1} \tag{2.2.50}$$

For axial induction factors larger than approximately 0.4, the simple BEM theory don't works anymore. The Glauert correction for high values of a must be applied. Resuming, if $a > a_c$ (with a_c usually taken equals 0.2), the axial induction factor is usually taken as:

$$a = \frac{1}{2} \left[2 + K(1 - 2a_c) - \sqrt{(K(1 - 2a_c) + 2)^2 + 4(Ka_c^2 - 1)} \right] \tag{2.2.51}$$

where:

$$K = \frac{4F \sin^2 \phi}{\sigma C_n} \tag{2.2.52}$$

If $a < a_c$ then a becomes the eq. 2.2.45.

Wilson and Lissaman (36) suggests that the drag coefficient should not be included in the estimation of the induction factors because there is a velocity draft confined in the narrow wake which flows from the the trailing edge of the aerofoil (27).

The BEM theory can be computed using the following algorithm (35):

- **Step 1.** Initialize a and a' (usually taken equals 0);
- **Step 2.** Computes ϕ using eq. 2.2.32, then α;
- **Step 3.** Read off $C_l(\alpha)$ and $C_d(\alpha)$ from the data;

- **Step 4.** Calculate a from eqs. 2.2.49 or 2.2.51 and a' from eq. 2.2.50;
- **Step 5.** If a and a' changed more than a certain tolerance go to **Step 2** or else finish;
- **Step 6.** Compute the local loads on the segment of the blades.

2.2.4.3 Rotor torque and power

After computed the flow induction factors using the BEM theory, the torque developed by the blade element of span wise length δr is

$$\delta Q = 4\pi\rho U_\infty \Omega r a'(1-a) r^2 \delta r \tag{2.2.53}$$

If the drag has been excluded from the determination of the flow induction factors, then

$$\delta Q = 4\pi\rho U_\infty \Omega r a'(1-a) r^2 \delta r - \frac{1}{2}\rho W^2 B c C_d \cos\phi r \delta r \tag{2.2.54}$$

Then the total torque Q developed by the rotor is

$$Q = \frac{1}{2}\rho U_\infty^2 \pi R^3 \lambda \int_0^R \mu^2 \left(8a'(1-a)\mu - \frac{W}{U_\infty}\frac{B\frac{c(r)}{R}}{\pi} C_d (1+a') \right) d\mu \tag{2.2.55}$$

where $\lambda = R\Omega/U_\infty$ is the tip speed ratio and $\mu = r/R$ is the ratio between each element radius and the total radius of the blade.

The power developed by the rotor is

$$P = Q\Omega \tag{2.2.56}$$

And the power coefficient is

$$C_p = \frac{P}{\frac{1}{2}\rho U_\infty^3 \pi R^2} \tag{2.2.57}$$

2.2.4.4 Implementation of BEM theory

In this work the three-blades implemented follows the considerations taken from the three NREL offshore 5-MW baseline wind turbine (34). About the structural properties, each blade follows the 61.5-m-long LM Glasfiber blade adapted from the DOWEC study (37).

The distributed blade aerodynamic properties are shown in tab. 2.2.5, with the blade node locations labeled as “RNodes”, the element lengths as “DRNodes”, the aerodynamic twist as “AeroTwst”, and the Airfoil Table presents eight airfoil-data distributed from

each element (each one have aerodynamic coefficients C_l, C_d, and C_m in function of the angle of attack α, that can be founded in the Jonkman's report annex (34)).

Table 2.2.5 – Distributed Blade Aerodynamic Properties (34)

Node (-)	RNodes (m)	AeroTwst (°)	DRNodes (m)	Chord (m)	Airfoil Table (-)
1	2.8667	13.308	2.7333	3.542	Cylinder1.dat
2	5.6000	13.308	2.7333	3.854	Cylinder1.dat
3	8.3333	13.308	2.7333	4.167	Cylinder2.dat
4	11.7500	13.308	4.1000	4.557	DU40_A17.dat
5	15.8500	11.480	4.1000	4.652	DU35_A17.dat
6	19.9500	10.162	4.1000	4.458	DU35_A17.dat
7	24.0500	9.011	4.1000	4.249	DU30_A17.dat
8	28.1500	7.795	4.1000	4.007	DU25_A17.dat
9	32.2500	6.544	4.1000	3.748	DU25_A17.dat
10	36.3500	5.361	4.1000	3.502	DU21_A17.dat
11	40.4500	4.188	4.1000	3.256	DU21_A17.dat
12	44.5500	3.125	4.1000	3.010	NACA64_A17.dat
13	48.6500	2.319	4.1000	2.764	NACA64_A17.dat
14	52.7500	1.526	4.1000	2.518	NACA64_A17.dat
15	56.1667	0.863	2.7333	2.313	NACA64_A17.dat
16	58.9000	0.370	2.7333	2.086	NACA64_A17.dat
17	61.6333	0.106	2.7333	1.419	NACA64_A17.dat

By applying BEM theory for the three-blade OWT mentioned above, with $U_\infty = 12m/s$ and $\Omega = 12.1rpm$, there are computed the aerodynamic coefficients C_l, C_d, C_m (fig. 2.2.9), the inflow and attack angles (fig. 2.2.10) and the induction factors (fig. 2.2.11).

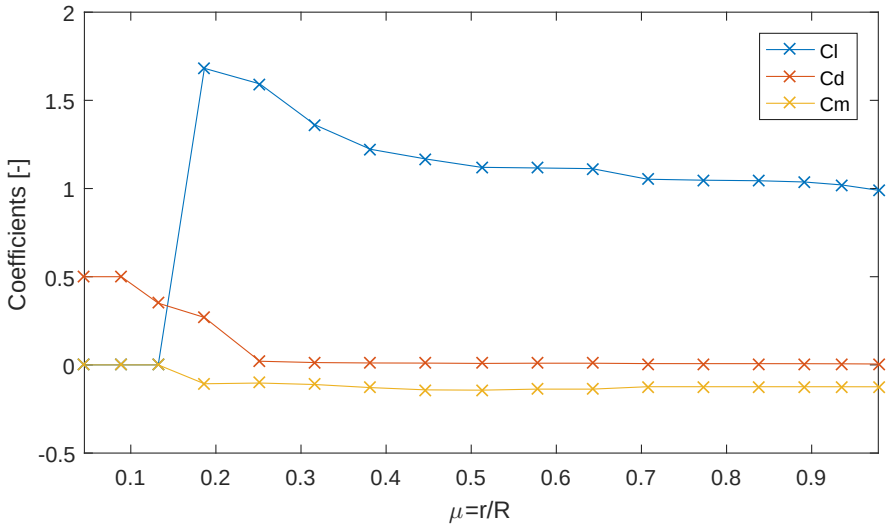

Figure 2.2.9 – Span-wise distribution of the aerodynamic coefficients with blade length

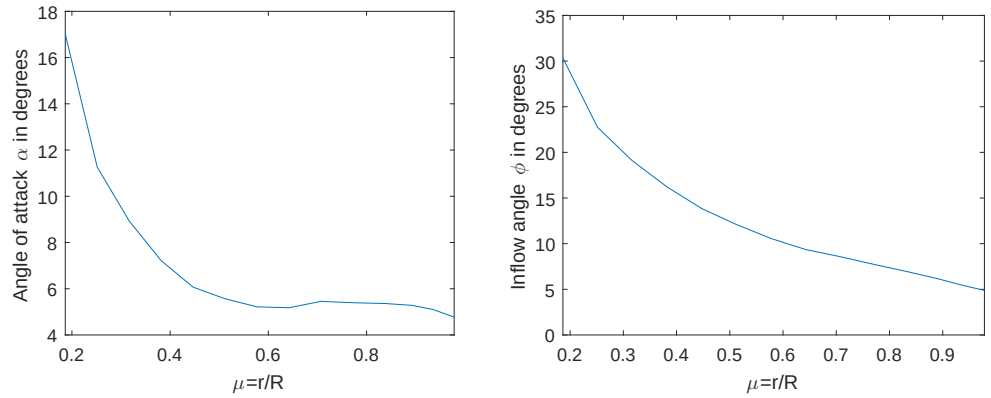

Figure 2.2.10 – Distribution of inflow and attack angles with blade length

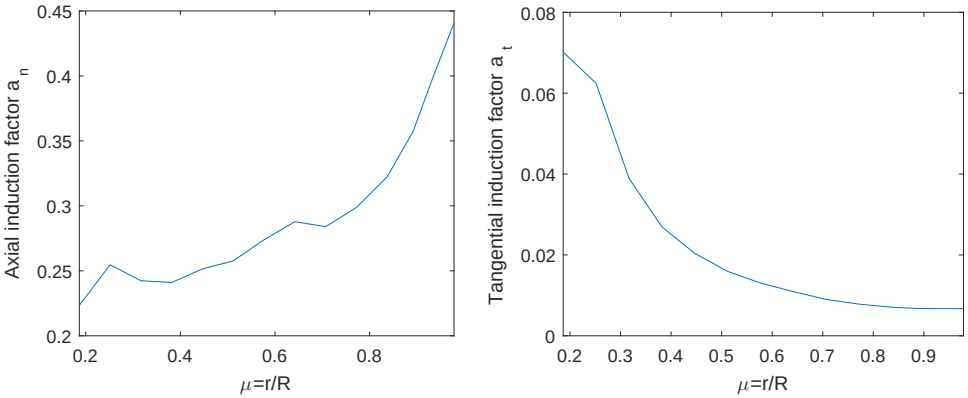

Figure 2.2.11 – Distribution of axial and tangential induction factors with blade length

By extending the BEM theory for other wind speed velocities the performance requirements of this OWT can be estimated. After estimated the total torque (eq. 2.2.55), the power developed by the rotor and the power coefficient in function of the tip speed ratio (eq. 2.2.57) are computed, as shown fig. 2.2.12, for two cases: tip loss (35), and root and tip losses (27). The power coefficient reaches its peak at $\lambda \approx 8$.

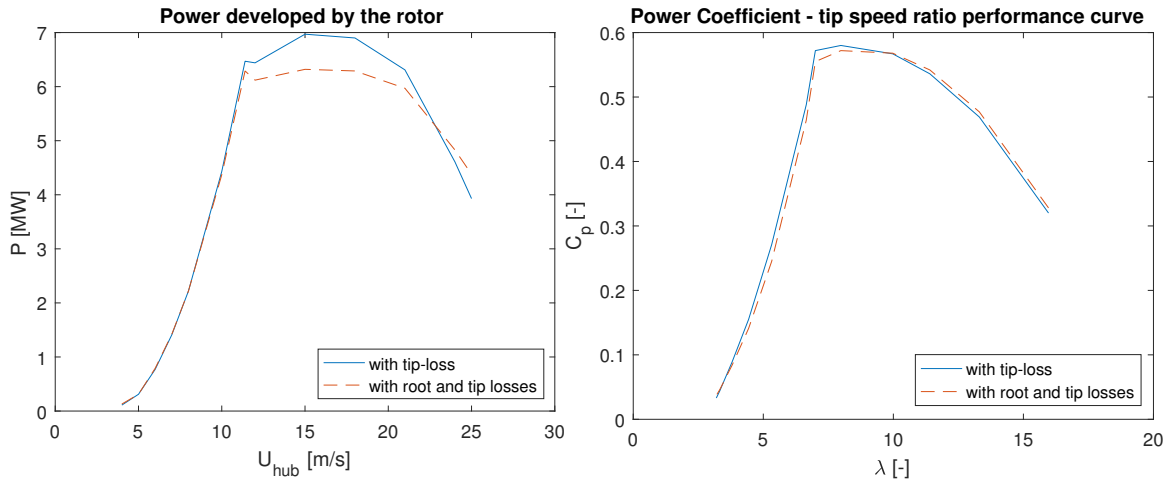

Figure 2.2.12 – Power developed by the rotor and performance curve

2.2.4.5 Aerodynamic loads of blades during operation

Usually there are two representative scales to define the rotating condition of the wind turbine blades. The first one takes its focus exclusively on the blades and the theory behind it is the classical Blade Element Momentum (BEM) method proposed by Glauert in 1935 (38). For time-domain or exclusively blade-only analysis this model can be very helpful, allowing the calculation of the steady loads and thus also the thrust and power for different settings of wind speed, rotational speed and pitch angle (35).

The scale used in this work focuses on the action force produced by the rotor on the tower during the blade operation by interpreting all the dynamic behavior of the blades in a specific vector over a tower, allowing analysis in both time and frequency domain in addition to gravity and inertial loads and also other external forces like wind and wave loading.

By separating out the load components due to the steady wind on the rotating blade (deterministic) and the wind speed fluctuations (stochastic), we can analyze them in different ways (27). The random loading on the blade due to the turbulence of wind speed fluctuations is firstly described in probabilistic terms and, therefore, in a stochastic load component. In order to analyze the response of OWT, the stochastic aerodynamic loads are evaluated in a frequency domain analysis.

2.2.4.6 Deterministic aerodynamic loads

The aerodynamic forces on the blade can be applied at different radii after estimated all the coefficients mentioned in the BEM theory. The forces per unit length on an element perpendicular to the plane of rotation and in the direction of blade motion, known as the

out-of-plane and in-place forces, are computed, respectively, as:

$$F_X = C_n \frac{1}{2} \rho W^2 c = 4\pi\rho U_\infty^2 (1 - aF) a \frac{F}{N} r \tag{2.2.58}$$

$$F_Y = C_t \frac{1}{2} \rho W^2 c = 4\pi\rho U_\infty^2 (1 - aF) a' \frac{F}{N} r^2 \tag{2.2.59}$$

where c is the chord length of the aerofoil and F the Prandlt's tip loss factor.

Figure 2.2.13 shows the deterministic out-of- and in-plane aerodynamic loads for the same defined blade and velocity.

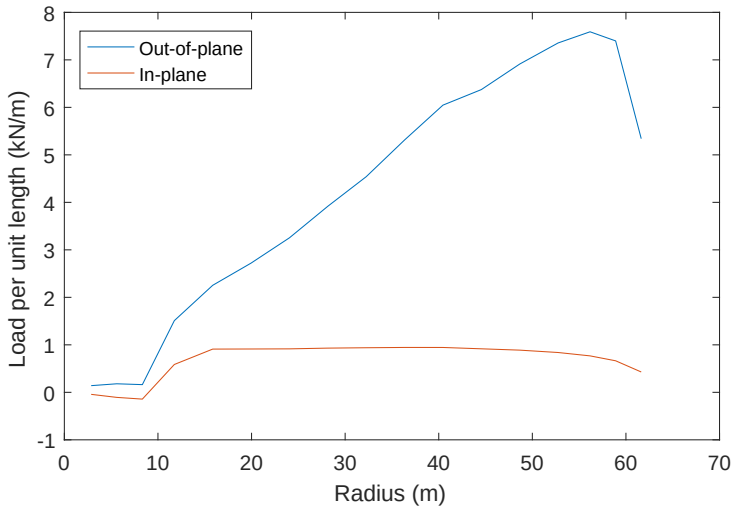

Figure 2.2.13 – Distribution of blade out-of-plane and in-plane aerodynamic loads during operation

The tower shadow effect (the blocking of the air flow by the tower) is not considered in this work.

2.2.4.7 Stochastic aerodynamic loads: frequency domain analysis

To represent the wind speed fluctuations at a fixed point in space there are used a probability distribution (usually a normal one) and a power spectrum which describes how the energy of the fluctuations is distributed in terms of the frequency.

To understand better how to perform a frequency domain analysis of a wind turbine is important have in mind some considerations about the turbulence intensity (already defined in sec. 2.2.2 - see tab. 2.2.2 for intensity references and eq. 2.2.7 to estimate the turbulence standard deviation for a NTM), and its spectra (eqs. 2.2.18 and 2.2.19 for ESDU PSD, and 2.2.24 for Kaimal PSD).

Burton et al. (27) shows that the standard deviation of the blade root bending moment can be computed as:

$$\sigma_M^2 = \left(\frac{1}{2} \rho \Omega \frac{dC_L}{d\alpha} \right)^2 \int_0^R \int_0^R \kappa_u(r_1, r_2, 0) c(r_1) c(r_2) r_1^2 r_2^2 dr_1 dr_2 \tag{2.2.60}$$

where c is the chord length of the aerofoil, C_L is the lift coefficient, α is the angle of attack $= \phi - \beta$ (usually $dC_L/d\alpha = 2\pi$), ϕ is the flow angle, β is the local blade twist, $\kappa_u(r_1, r_2, 0)$ is the cross correlation function $\kappa_u(r_1, r_2, \tau)$ between the wind fluctuations at radii r_1 and r_2 with the time lag τ set to zero, i.e.:

$$\kappa_u(r_1, r_2, 0) = \left[\frac{1}{T}\int_0^T u(r_1, t)u(r_2, t)dt\right] \tag{2.2.61}$$

To find the energy content of the incident wind fluctuations it is necessary to examine some points on the rotating blade at the blade natural frequencies, provided by a rotationally sampled spectrum. The phenomenon 'gust slicing' will enhance the frequency content at the rotational frequency, by an often slice through an individual gust several times.

The **Rotationally sampled spectrum** method can be obtained by deriving the power spectrum of the wind seen by a point on a rotating blade, based on the Fourier transform pair of eqs. 2.2.62 and 2.2.63.

$$S_u(n) = 4\int_0^\infty \kappa_u(\tau)\cos(2\pi n\tau)d\tau \tag{2.2.62}$$

$$\kappa_u = \int_0^\infty S_u(n)\cos(2\pi n\tau)dn \tag{2.2.63}$$

where $S_u(n)$ is the single sided spectrum of wind speed fluctuations in terms of frequency (in Hz) and κ_u the autocorrelation function for the along wind turbulent fluctuations at a fixed point in space from the corresponding spectrum, for an homogeneous and isotropic turbulence, and an incompressible flow.

After found the autocorrelation function, $\kappa_u(\tau)$, the autocorrelation function is computed for a point on the rotating blade at a radius r, $\kappa_u^o(r, \tau)$, by a derivation (the superscript ^{o} denotes a point on a rotating blade - not 'fixed'). This function is transformed to yield the rotationally sampled spectrum. Burton et al. (27) explain this process by following 3 steps:

Step 1: Derivation of the autocorrelation function at a fixed point

In this step, Burton et al. selected the von Karman spectrum (eq. 2.2.24) as input, because it is isotropic and homogeneous.

Using eq. 2.2.63 the expression for the autocorrelation function, for along wind turbulent fluctuations, is estimated by eq. 2.2.64.

$$\kappa_u(\tau) = \frac{2\sigma_u^2}{\Gamma\left(\frac{1}{3}\right)}\left(\frac{\tau/2}{T'}\right)K_{1/3}\left(\frac{\tau}{T'}\right) \tag{2.2.64}$$

where T' has a relation to the turbulence length scale, L, by:

$$T' = \frac{\Gamma\left(\frac{1}{3}\right)}{\Gamma\left(\frac{5}{6}\right)\sqrt{\pi}}\frac{L}{\bar{U}} \approx 1.34\frac{L}{\bar{U}} \tag{2.2.65}$$

where $\Gamma()$ is the gamma function and $K_{1/3}(x)$ is a modified Bessel function (general equation described in eq. 2.2.66) of the second kind and order $\upsilon = 1/3$.

$$K_\upsilon(x) = \frac{\pi}{2\sin\pi\upsilon}\sum_{m=0}^{\infty}\frac{(x/2)^2 m}{m!}\left[\frac{(x/2)^{-\upsilon}}{\Gamma(m-\upsilon+1)} - \frac{(x/2)^{\upsilon}}{\Gamma(m+\upsilon+1)}\right] \tag{2.2.66}$$

Step 2: Derivation of the autocorrelation function at a point on the rotating blade;

This step makes the use of Taylor's 'frozen turbulence' hypothesis - in a time τ the wind speed at C is equal to a point B at a distance $\bar{U}\tau$ at time $t = 0$. From fig. 2.2.14, the autocorrelation function $\kappa_u^o(r,\tau)$ for the along-wind wind fluctuations seen by a point Q at radius r on the rotating blade is equal to the cross correlation function $\kappa_u(\mathbf{s},0)$, between the simultaneous along-wind wind fluctuations at points A and B. A and C are the positions of point Q at the beginning and end of time interval τ, B is $\bar{U}\tau$ upwind of C an $\mathbf{s}$ is the vector BA.

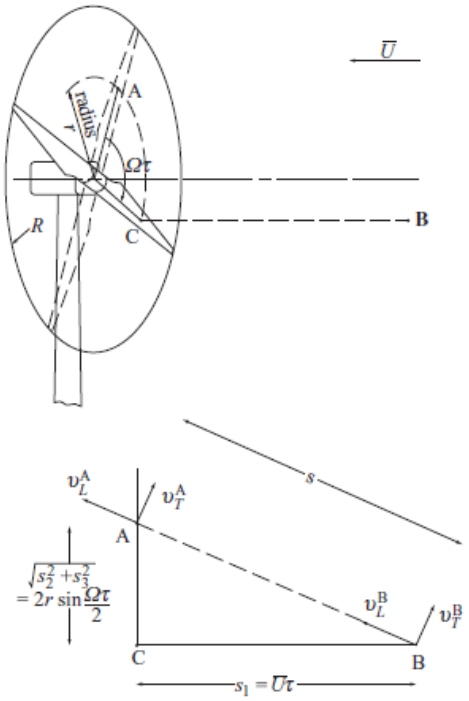

Figure 2.2.14 – Geometry reference for a point on a rotating blade (step 2) (27)

By the theory of homogeneous and isotropic turbulence, Batchelor (39) shown that the cross correlation function $\kappa_u(\mathbf{s},0)$ is given by:

$$\kappa_u(\mathbf{s},0) = (\kappa_L(s) - \kappa_T(s))\left(\frac{s_1}{s}\right)^2 + \kappa_T(s) \tag{2.2.67}$$

where $\kappa_L(s)$ is the cross correlation function between velocity components at points A and B in a direction parallel to AB (v_L^A and v_L^B in fig. 2.2.14), $\kappa_T(s)$ is the function for velocity components in a direction perpendicular to AB (v_T^A and v_T^B), $s_1 = \bar{U}\tau$ is the separation of points A and B in the along wind direction ($\bar{BC}$). By the Pythagorean theorem, the

distance s is calculated by using eq. 2.2.68.

$$s^2 = \bar{U}^2\tau^2 + 4r^2\sin^2(\Omega\tau/2) \tag{2.2.68}$$

where Ω is the rotational speed of rotor.

For incompressible flow:

$$\kappa_T(s) = \kappa_L(s) + \frac{s}{2}\frac{d\kappa_L(s)}{ds} \tag{2.2.69}$$

and substituting eq. 2.2.69 in eq. 2.2.67:

$$\kappa_u(\mathbf{s}, 0) = \kappa_L(s) + \frac{s}{2}\frac{d\kappa_L(s)}{ds}\left(\frac{2r\sin(\Omega\tau/2)}{s}\right)^2 \tag{2.2.70}$$

When the vector $\mathbf{s}$ is in the along-wind direction and using the Taylor's frozen turbulence hypothesis, $\kappa_L(s)$ translates to $\kappa_u(s_1)$ matching with $\kappa_u(\tau)$ from eq. 2.2.64 (with $\tau = s_1/\bar{U}$). By doing this and substituting the result in the eq. 2.2.70, the expression for the autocorrelation function for the along-wind fluctuation at a point at radius r on the rotating blade $[\kappa_u^o(r,\tau) = \kappa_u(\mathbf{s}, 0)]$ is computed in eq. 2.2.71.

$$\kappa_u^o(r,\tau) = \frac{2\sigma_u^2}{\Gamma(1/3)}\left(\frac{s/2}{1.34L}\right)^{1/3} \times \left[K_{1/3}\left(\frac{s}{1.34}\right) - \frac{s}{2(1.34L)}K_{2/3}\left(\frac{s}{1.34L}\right)\left(\frac{2r\sin(\Omega\tau/2)}{s}\right)^2\right] \tag{2.2.71}$$

Step 3: Derivation of the power spectrum seen by a point on the rotating bade.

How the integral of the power spectrum do not have analytical solution, a discrete Fourier transform (DFT) is used to solve it (see Burton et al. (27) notes) and estimate the rotationally sampled spectrum $S_u^o(n_k)$ using eq. 2.2.72.

$$S_u^o(n_k) = 2T\left[\frac{1}{N}\sum_{p=0}^{N-1}\kappa_u^{*o}(r, pT/N)\cos(2\pi kp/N)\right] \tag{2.2.72}$$

where N is the number of points in the time series of $\kappa_u^{*o}(r, pT/N)$, and the PSD is calculated at the frequencies $n_k = k/T$ for $k = 0, 1, 2, \ldots, N-1$. The sum can be evaluated using a fast Fourier transform (FFT) providing for N a value equals to a power of 2.

The selection of $T = 200$ s and $N = 4096$ for the FFT gives useful results up to a frequency of 5 Hz for a interval of 0.005 Hz. These results have been computed following the pre-requisites of IEC 61400-1 Edition 3 (28), with the isotropic integral length scale, L, taken as 3.5 times the turbulence scale parameter, Λ_1. By using the capabilities of MATLAB, for points on a $r = [20; 40; 60]$ m on a blading rotating at $\Omega = 15$ rpm in a mean wind speed of $\bar{U} = 8$ m/s, the rotationally sampled spectrum was generated. Figs. 2.2.15 and 2.2.16 shows, respectively, the generated normalized

autocorrelation function, $\rho_u^o(r,\tau)(=\kappa_u^o(r,\tau)/\sigma_u^2)$, against the number of rotor revolutions and the rotationally sampled power spectral density function, $R_u^o(r,n)(=nS_u^o(r,n)/\sigma_u^2)$, versus the frequency n.

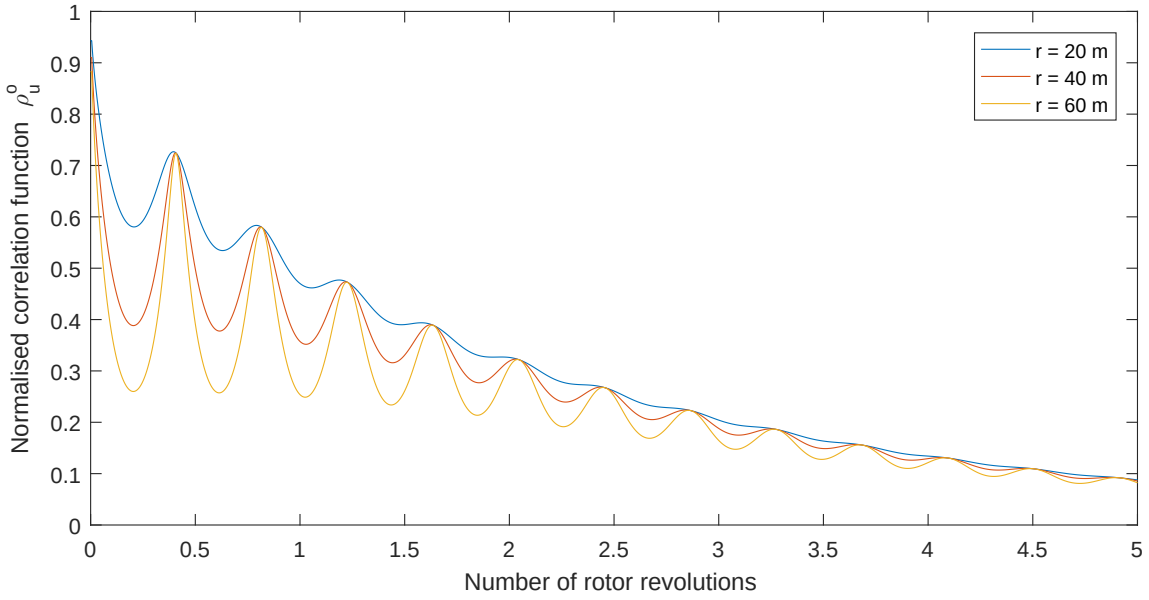

Figure 2.2.15 – Normalized autocorrelation for along-wind wind fluctuations seen by $r = [20, 40, 60]$ m radii on a rotating blade

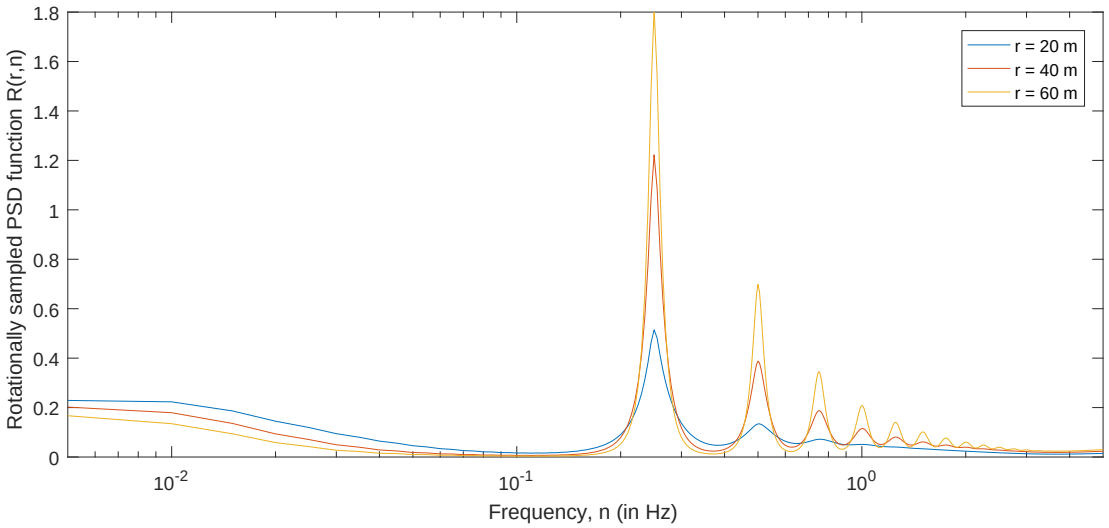

Figure 2.2.16 – Rotationally sampled power spectra of longitudinal wind fluctuations seen by $r = [20, 40, 60]$ m radii on a rotating blade

Figs. 2.2.15 and 2.2.16 present very similar results compared to the reference (27), as expected. Figure 2.2.15 presents curves that display pronounced peaks after each full

revolution (an even more for high values of r). Figure 2.2.16 shows high frequency content of the spectrum to the frequency of rotation in which increases with the radius.

The corresponding cross correlation of the cross spectrum, for a pair of points at radii r_1 and r_2 on a rotating blade, is related with the Fourier transform pair:

$$S_u^o(r_1, r_2, n) = 4 \int_0^\infty \kappa_u^o(r_1, r_2, \tau) \cos 2\pi n\tau d\tau \tag{2.2.73}$$

$$\kappa_u^o = \int_0^\infty S_u^o(r_1, r_2, n) \cos 2\pi n\tau dn \tag{2.2.74}$$

which, setting $\tau = 0$ and substituting into the eq. 2.2.60 of the standard deviation of the blade root bending moment gives:

$$\sigma_M^2 = \left(\frac{1}{2}\rho\Omega\frac{dC_L}{d\alpha}\right)^2 \int_0^R \int_0^R \left[\int_0^\infty S_u^o(r_1, r_2, n)dn\right] c(r_1)c(r_2)r_1^2 r_2^2 dr_1 dr_2 \tag{2.2.75}$$

Then the power spectrum of the blade root bending moment can be computed by eq. 2.2.76.

$$S_M(n) = \left(\frac{1}{2}\rho\Omega\frac{dC_L}{d\alpha}\right)^2 \int_0^R \int_0^R S_u^o(r_1, r_2, n)c(r_1)c(r_2)r_1^2 r_2^2 dr_1 dr_2 \tag{2.2.76}$$

The rotationally sampled cross spectrum, $S_u^o(r_1, r_2, n)$, can be estimated following the same idea presented previously. Burton et al.(27) shows that the separation distance, s, at radii r_1 and r_2 on the rotating blade is now computed by:

$$s^2 = \bar{U}^2\tau^2 + r_1^2 + r_2^2 - 2r_1 r_2 \cos\Omega\tau \tag{2.2.77}$$

The cross correlation thus becomes:

$$\begin{aligned}\kappa_u^o(r_1, r_2, \tau) = \frac{2\sigma_u^2}{\Gamma\left(\frac{1}{3}\right)} \left(\frac{s/2}{1.34L}\right)^{\frac{1}{3}} \times \\ \left[K_{1/3}\left(\frac{s}{1.34L}\right) - \frac{s}{2(1.34L)} K_{2/3}\left(\frac{s}{1.34L}\right) \cdot \left(\frac{r_1^2 + r_2^2 - 2r_1 r_2 \cos\Omega\tau}{s^2}\right)\right]\end{aligned} \tag{2.2.78}$$

Figure 2.2.17 shows the rotationally cross spectrum for $r_1 = 20\ m$ and $r_2 = 40\ m$ compared with the rotationally sampled single autospectra for two cases.

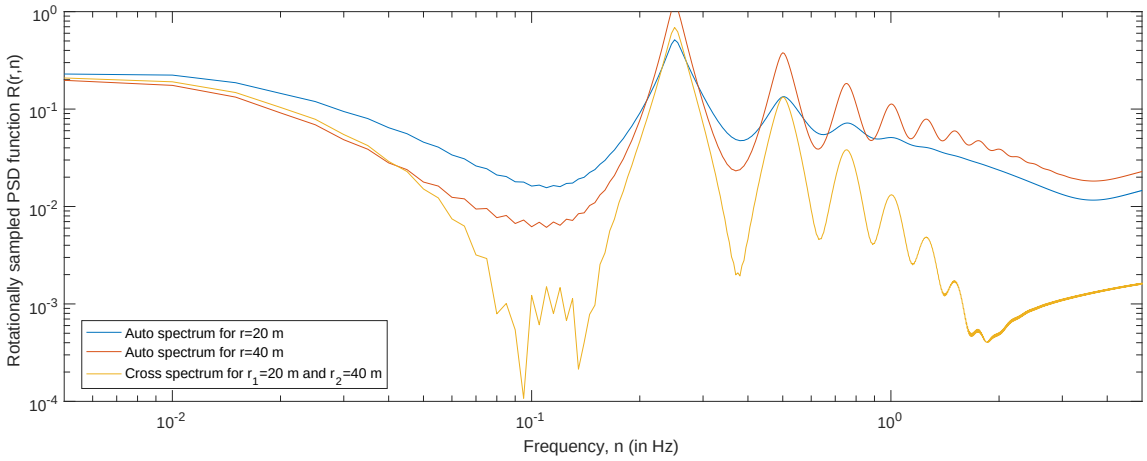

Figure 2.2.17 – Rotationally sampled cross spectrum of longitudinal wind speed fluctuations seen by at $r_1 = 20\ m$ and $r_2 = 40\ m$ radii compared with auto spectra

Burton et al. (27) shows that the power spectrum of the blade root bending moment is computed using summations to approximate to the integrals in eq. 2.2.76, as follows:

$$S_M(n) = \left(\frac{1}{2}\rho\Omega\frac{dC_L}{d\alpha}\right)^2 \sum_j \sum_k S_u^o(r_j, r_k, n)c(r_j)c(r_k)r_j^2 r_k^2(\Delta r)^2 \tag{2.2.79}$$

For the above-mentioned 5-MW NREL OWT the power spectrum of bending root bending moment results in fig. 2.2.18.

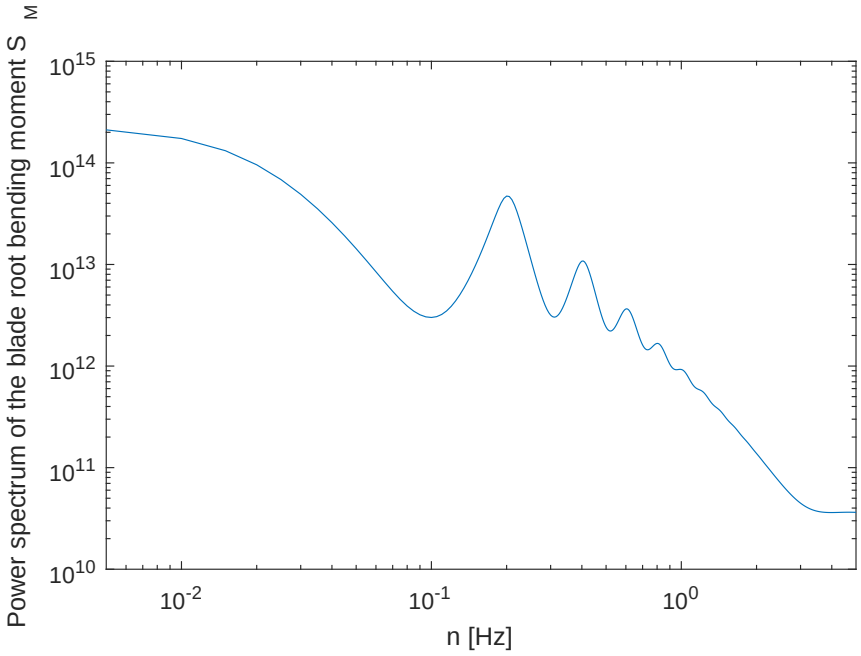

Figure 2.2.18 – Power spectrum of the bending root bending moment

2.2.4.8 Vortex shedding effect on the tower

At certain critical ranges for the flow mean velocities, the frequency of vortex shedding originating around the tower coincides with the first natural (across-wind direction) frequency of the lateral motion of the tower resulting in lock-in vibrations. The lock-in effect can be considered as the applied maximum across-wind displacement $(r^{\mathrm{VS}}_{\mathrm{across}})_{\max}$ given by (40)

$$\left(\frac{r^{\mathrm{VS}}_{\mathrm{across}}}{D}\right)_{\max} = \frac{1.29}{1 + 0.43(2\pi S_t^2 S_c)} \tag{2.2.80}$$

where D is the diameter of the tubular section under wind action and S_t and S_c are the Strouhal and Scruton numbers, respectively (41).

2.3 Wave and sea current dynamics and induced loads

Brebbia and Walker (42) presents two methods for offshore structures analysis which depends of different types of information, the design wave approach and the wave-energy spectrum.

The first is deterministic and requires information about the period and height of the maximum wave occurring for certain environmental condition. The wave-energy spectrum uses a probabilistic theory obtaining results for maximum stresses, displacements, etc., of the structure within a certain confidence level. The probabilistic one is more accurate to define the sea state and allow the use of random vibration theory to analyze the structure.

Important concepts of hydrodynamics of offshore structures on the sea is briefly reviewed in sec. 2.3.1 and wave theories are presented in sec. 2.3.2. These concepts are relevant to interpret oceanographic information to carry out a structural analysis.

Statistical procedures are presented in sec. 2.3.3 for analyzing wave data determining common wave spectrum as the Pierson-Moskowitz and JONSWAP for a wind-generated sea.

In section 2.3.4.1 is presented how the hydrodynamic forces acts on slender members estimating the Morison equation.

2.3.1 Some basic definitions

The motion of an incompressible fluid must be a reasonable consideration for representing the kinematics of waves. For steel offshore structures this can be made by computing the drag forces using the Morison's equation empirical formula.

Assuming an Eulerian velocity vector $\mathbf{v} = (v_x, v_y, v_z)$ with its origin at the SWL with a depth d, consider the Navier-Stokes' eq. 2.3.1 for the motion of an incompressible

fluid.

$$\rho\frac{D\mathbf{v}}{Dt} = \rho\mathbf{F} - \nabla p - \mu\nabla\times\omega \tag{2.3.1}$$

where ρ is the density of the fluid, $D/Dt = \partial/\partial t + \mathbf{v}.\nabla$ is the material derivative, p is the pressure, F is the body force vector, μ is the viscosity and ω is the vorticity field defined by the curl of the velocity vector, i.e. $\omega = \nabla\times\mathbf{v}$, which measure the rotationality of the fluid.

For an irrotationality condition (eq. 2.3.2),

$$\nabla\times\mathbf{v} = \mathbf{0} \tag{2.3.2}$$

it can be assumed a velocity potential $\Phi(x, y, z)$ defined by eq. 2.3.3.

$$\mathbf{v} = \nabla\Phi = \left(\frac{\partial\Phi}{\partial x}, \frac{\partial\Phi}{\partial y}, \frac{\partial\Phi}{\partial z}\right) \tag{2.3.3}$$

The continuity equation is defined by the eq. 2.3.4.

$$\frac{D\rho}{Dt} + \rho\nabla.\mathbf{v} = 0 \tag{2.3.4}$$

if a fluid is incompressible than the density remains constant, i.e. $D\rho/Dt = 0$, consequently $\nabla.\mathbf{v} = 0$ for an incompressible homogeneous fluid. In terms of the potential Φ, the incompressible inviscid fluid is computed by eq. 2.3.5

$$\nabla.\nabla\Phi = \nabla^2\Phi = \frac{\partial^2\Phi}{\partial x^2} + \frac{\partial^2\Phi}{\partial y^2} + \frac{\partial^2\Phi}{\partial z^2} = 0 \tag{2.3.5}$$

Consider now the propagation of a fluid with disturbances of height $\eta(x, y, t)$ above the SWL. Kinematic and pressure conditions occurs at the free surface and a fluid condition at a constant depth.

The kinematic condition: The vertical velocity v_z at the free surface, for smalls slope $\partial\eta$ or horizontal velocity v_x, considering that the surface moves with the fluid, is:

$$v_z \approx \frac{\partial\eta}{\partial t} = \frac{\partial\Phi}{\partial z} \qquad \text{at} \qquad z = \eta \tag{2.3.6}$$

and for small disturbances (by using the Taylor's theorem):

$$\frac{\partial\eta}{\partial t} \approx \frac{\partial\Phi}{\partial z} \qquad \text{at} \qquad z = 0 \tag{2.3.7}$$

The pressure condition: Assuming that the surface has a constant atmospheric pressure, for an irrotational motion, the Bernoulli's equation can be reduced as:

$$P_i - P_o = -\rho\left(\frac{\partial\Phi}{\partial t} + g\eta\right) \tag{2.3.8}$$

where P_i and P_o is the pressure inside and outside the liquid surface, respectively, ρ is the density of the liquid and g is the acceleration due to gravity.

By neglecting the surface-tension effects ($P_i = P_o$), we obtain:

$$\frac{\partial \Phi}{\partial t} = -g\eta \quad \text{at} \quad z = \eta \tag{2.3.9}$$

$$\frac{\partial \Phi}{\partial t} \approx -g\eta \quad \text{at} \quad z = 0 \tag{2.3.10}$$

Combining the kinematic condition, we obtain:

$$\frac{\partial \Phi}{\partial z} = -g\frac{\partial^2 \Phi}{\partial t^2} \quad \text{at} \quad z = 0 \tag{2.3.11}$$

Fluid of constant depth condition: This last condition come from a constant depth $z = -h$, assuming a solid impermeable surface and by neglecting slope. We have no liquid flux at the seabed, so:

$$\frac{\partial \Phi}{\partial z} = 0 \quad \text{at} \quad z = -d \tag{2.3.12}$$

Assuming the real part of the separable solution $\Phi(x, y, z, t) = \phi(x, y) f(z) \exp(i\omega t)$, i.e. $\mathrm{Re}[\exp i\omega t] = \cos \omega t$, and substituting in the continuity equation for an incompressible inviscid fluid of eq. 2.3.5 we obtain that:

$$\nabla^2 \phi f(z) + \phi \frac{\partial^2 f}{\partial z^2} = 0 \tag{2.3.13}$$

which can be rewritten as:

$$\frac{\nabla^2 \phi(x, y)}{\phi(x, y)} = -\frac{\partial^2 f / \partial z^2}{f(z)} \tag{2.3.14}$$

For these functions to be equal for all x, y, and z:

$$\frac{\nabla^2 \phi}{\phi} = -\kappa^2 \tag{2.3.15}$$

$$\frac{\partial^2 f / \partial z^2}{f} = \kappa^2 \tag{2.3.16}$$

where κ^2 is a constant to be determined by using the boundary conditions.

From the eq. 2.3.15 we obtain the Helmholtz equation in two dimensions, i.e.

$$\nabla^2 \phi + \kappa^2 \phi = 0 \tag{2.3.17}$$

where $\phi(x, y)$ is the reduced velocity potential.

From the eq. 2.3.16:

$$\frac{\partial^2 f}{\partial z^2} = \kappa^2 f \tag{2.3.18}$$

By using the initial boundary condition of eq. 2.3.12 and the kinematic condition of eq. 2.3.7, Brebbia and Walker (42) obtain the general solution for a harmonic disturbance (eq. 2.3.19) with where $\phi(x, y)$ is any solution of Helmholtz eq. 2.3.17.

$$\Phi(x, y, z, t) = \phi(x, y) \frac{\cosh[\kappa(z + d)]}{\cosh \kappa d} \exp(-i\omega t) \tag{2.3.19}$$

where $\omega^2 = g\kappa \tanh(\kappa d)$ is the dispersion relation for disturbances traveling on a liquid depth d.

2.3.2 Wave theories

According to Chandrasekaran (43) the particles velocities, accelerations, and dynamic pressure as function of the surface elevation of the waves, can be computed by wave theories. There are different theories such as:

- Linear first-order or Airy theory;
- Stokes fifth-order theory;
- Solitary wave theory;
- Cnoidal theory;
- Dean's stream function theory;
- Numerical theory by Chappelear.

According to Chandrasekaran (43) the particles' velocities, accelerations, and dynamic pressure as function of the surface elevation of the waves, can be computed by a number of wave theories such as the Linear of first-order or Airy theory, Stokes second-, and fifth-order theory, Solitary wave theory, Cnoidal theory, Dean's stream function theory, and the numerical theory by Chappelear.

The linear theory is adequate for slender structures under small-amplitude deep water waves. Other theories such as Stokes's fifth and third-order wave theories can be used for non-linear high waves, as well the stream function theory (numerical methods for a broad range of water depths), while the Boussinesq high-order theory is used for shallow water waves and solitary wave theory for very shallow water.

The most appropriate theory can be found based on the relations between the wave height H_w, wave period T_w, and water depth h (44, 45) as shown fig. 2.3.1. For example, the Airy wave theory can be applied for the light-yellow area of the figure, the light-blue area gives the range of cnoidal wave theory, the blue lines demarcate between the required order in Stokes' wave theory, and for high waves, i.e. $H > 1/4H_{\text{breaking}}$, the light-gray shading gives the range extension by using fifth-order stream-function.

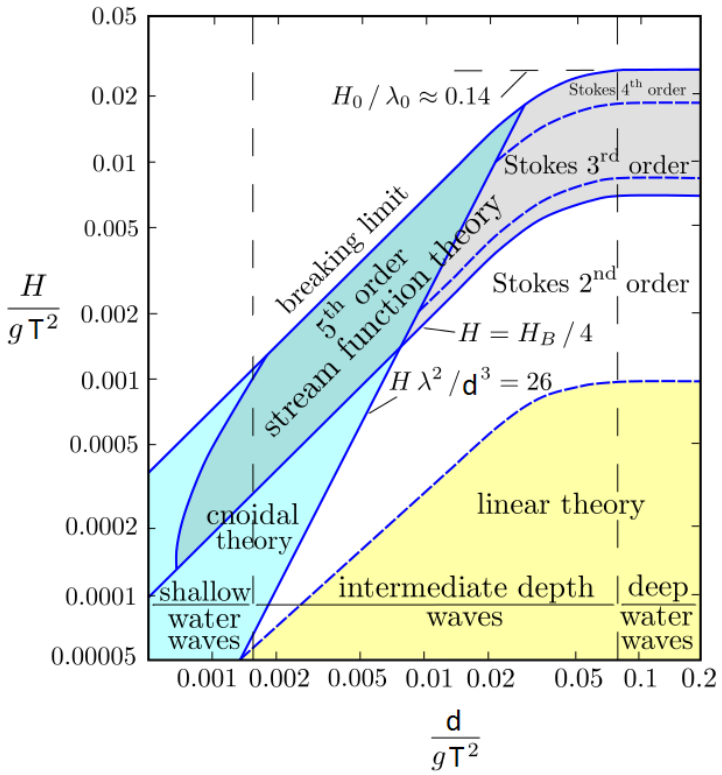

Figure 2.3.1 – Wave theory selection chart (45, adapted)

The DNV-OS-J101 defines three non-dimensional parameters that determine the ranges of validity for different wave theories: the wave steepness parameter, S_w; shallow water parameter, μ_w; and Ursell parameter, U_r. Which are defined in eqs. 2.3.20 to 2.3.22 and have their ranges of application for different wave theories as shows tab. 2.3.1.

$$S_w = 2\pi \frac{H}{gT^2} = \frac{H}{\lambda_0} \tag{2.3.20}$$

$$\mu_w = 2\pi \frac{d}{gT^2} = \frac{d}{\lambda_0} \tag{2.3.21}$$

$$U_r = \frac{H}{k_0^2 d^3} = \frac{S_w}{4\pi^2 \mu_w^3} \tag{2.3.22}$$

Table 2.3.1 – Ranges of application of regular wave theories (26)

Theory	**Depth**	**Approximate range**
Linear (Airy) wave	Deep and shallow	$S_w < 0.006$; $S_w/\mu_w < 0.03$
2^{nd} order Stokes wave	Deep water	$U_r < 0.65$; $S_w < 0.04$
5^{th} order Stokes wave	Deep water	$U_r < 0.65$; $S_w < 0.14$
Cnoidal theory	Shallow water	$U_r > 0.65$; $\mu_w < 0.125$

2.3.2.1 Linear Airy Theory

The wave amplitude can be calculated using eq. 2.3.23 as consequence of the pressure condition of eq. 2.3.10, then the surface elevation becomes

$$\eta(x,y) = +i\frac{\omega}{g}\phi(x,y) \tag{2.3.23}$$

where the wave frequency can be written in function of the period as $\omega = 2\pi/T$.

Consider now the one-dimensional Helmholtz equation of eq. 2.3.24 for a sinusoidal wave of frequency ω of the fig. 2.3.2, then

$$\frac{\partial^2\eta}{\partial\eta^2} + \kappa^2\eta = 0 \tag{2.3.24}$$

The solution η can be computed by using the eq. 2.3.25 as a free surface disturbance as

$$\eta(x,t) = \eta(x)\exp(i\omega t) \tag{2.3.25}$$

The elevation has a harmonic solution (eq. 2.3.26)

$$\eta(x) = a_0\exp(-i\kappa x) \tag{2.3.26}$$

where κ is the wavenumber, $\kappa = 2\pi/\lambda$. Substituting the harmonic solution in the eq. 2.3.25, it is computed the elevation of a linear Airy wave (eq. 2.3.27) of amplitude a_0 with a celerity, or phase velocity, $c = \omega/\kappa$.

$$\eta(x,t) = a_0\exp[-i(\kappa x - \omega t)] \tag{2.3.27}$$

For regular linear waves the wave crest height is equal to the wave trough height, then the wave height is $H = 2a_0$. DNV-OS-J101 defines the surface elevation in terms of x and y as the eq. 2.3.28 (fig. 2.3.2).

$$\eta(x,y,t) = \frac{H}{2}\cos\Theta \tag{2.3.28}$$

where $\Theta = \kappa(x\cos\beta_1 + y\sin\beta_1 - ct)$ and β_1 is the direction of propagation (measure from the positive x-axis). If $\beta_1 = 0°$, $\Theta = \theta = \kappa(x - ct) = \kappa x - \omega t$, with $\omega = 2\pi/T$.

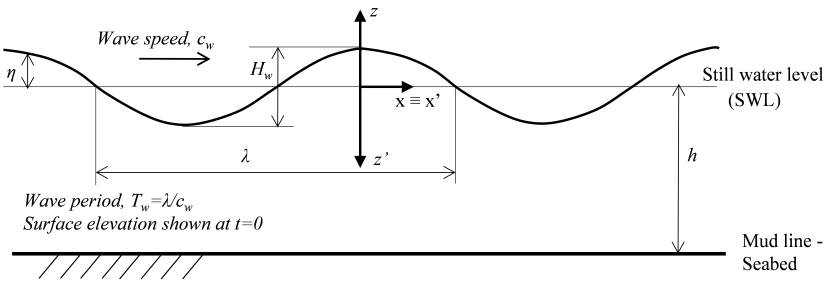

Figure 2.3.2 – Regular traveling properties (46)

The dispersion relationship which determines the wavelength λ is given by eq. 2.3.29.

$$\lambda = \frac{gT^2}{2\pi} \tanh\left(\frac{2\pi d}{\lambda}\right) \tag{2.3.29}$$

that can be approximated as a function of the wave period T by eq. 2.3.30.

$$\lambda = T(gd)^{1/2} \left(\frac{f(\bar{\omega})}{1 + \bar{\omega} f(\bar{\omega})}\right)^{1/2} \tag{2.3.30}$$

where $f(\bar{\omega}) = 1 + \sum_{n=1}^{4} \alpha_n \bar{\omega}^n$, $\bar{\omega} = (4\pi^2 d)/(gT^2)$, $\alpha_1 = 0.666$, $\alpha_2 = 0.445$, $\alpha_3 = -0.105$, $\alpha_4 = 0.272$, and g the gravity.

For linear waves the phase velocity only depends on wave length λ and it is independent of the wave amplitude as:

$$c = \sqrt{\frac{g\lambda}{2\pi} \tanh\left(\frac{2\pi d}{\lambda}\right)} \tag{2.3.31}$$

From eqs. 2.3.30 and 2.3.31 the wave length and phase velocity are shown in fig. 2.3.3 as a function of wave period at various water depths for linear waves.

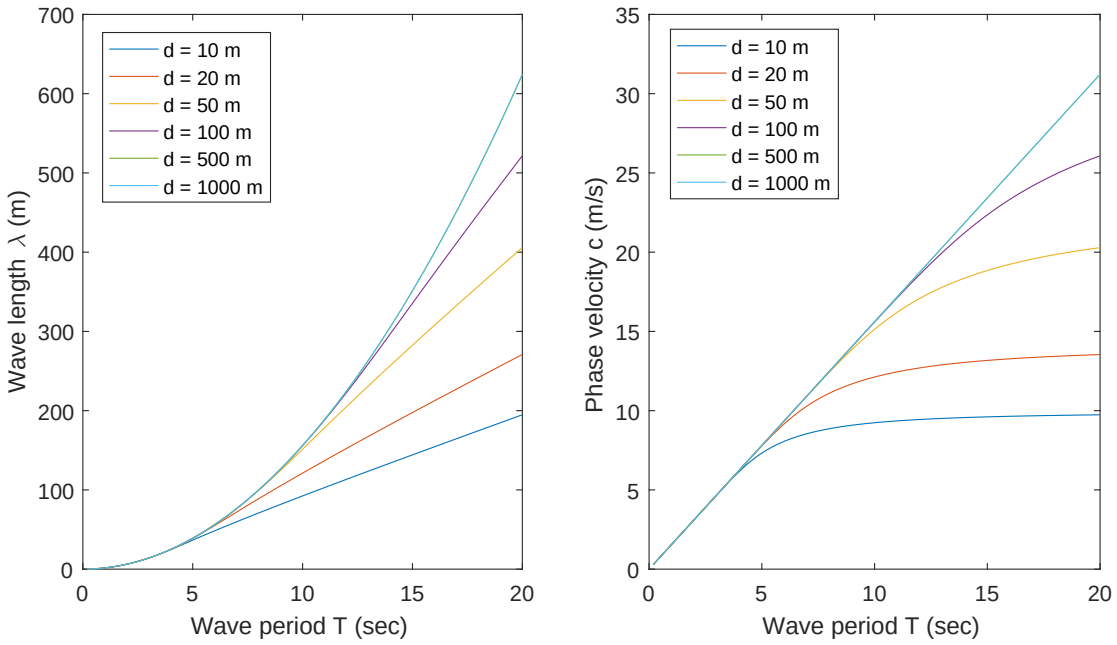

Figure 2.3.3 – Wave length and phase velocity as function of wave period at various water depths

Using again the linearized free-surface boundary conditions, the velocity potential

for the motion is computed by the eq. 2.3.32

$$\begin{aligned}\Phi(x,z,t) &= i\frac{g}{\omega}a_0 \exp\left[-i(\kappa x-\omega t)\right]\frac{\cosh\left[\kappa(z+d)\right]}{\cosh\kappa d}\\ &= \frac{gH}{2\omega}\frac{\cosh\left[\kappa(z+d)\right]}{\cosh\kappa d}\sin\theta\\ &= \frac{\pi H}{\kappa T}\frac{\cosh\left[\kappa(z+d)\right]}{\sinh\kappa d}\sin\theta\end{aligned} \tag{2.3.32}$$

where $\theta = \kappa x - \omega t = \kappa(x-ct)$.

For deep water the component (κd) is large and $\cosh(\kappa d) \approx \exp(\kappa d)/2$ and $\sinh\left[\kappa(z+d)\right] = \cosh\left[\kappa(z+d)\right] \approx \exp\left[\kappa(z+d)\right]/2$, then:

$$\begin{aligned}\Phi(x,z,t) &= i\frac{g}{\omega}a_0 \exp\left[-i(\kappa x-\omega t)\right]\exp(\kappa z)\\ &= \frac{gH}{2\omega}\exp(\kappa z)\sin\theta\\ &= \frac{\pi H}{\kappa T}\exp(\kappa z)\sin\theta\end{aligned} \tag{2.3.33}$$

with dispersion $\omega^2 = g\kappa$ ($\tanh(\kappa d) \approx 1$ for $\kappa d > 2.65$).

As a consequence for $\kappa d > 2.65$, i.e. $d \ll \lambda/2$, we may neglect the effects of smooth variations of the depth d, then $c^2 = g\lambda/2\pi$ or $c = g/\omega$.

2.3.2.2 Second-order Stokes wave theory

The Stokes wave expansion is an extension of the surface elevation in powers of the linear wave (46). While the first-order is identical to a linear (or Airy) wave, the second-order component is smaller than the first-order contribution and provides twice the wave frequency (47).

The surface profile is defined as:

$$\eta = \eta_1 + \frac{\pi H^2}{8\lambda}\frac{\cosh\kappa d}{\sinh^3\kappa d}(2+\cosh 2\kappa d)\cos 2\Theta \tag{2.3.34}$$

where the subscript 1 of η_1 refers to the linear or Airy first-order of eq. 2.3.28.

For deep water:

$$\eta = \eta_1 + \frac{\pi H^2}{4\lambda}\cos 2\Theta \tag{2.3.35}$$

The velocity potential can be computed as

$$\Phi = \phi_1 + \frac{3}{8}\frac{\pi H}{kT}\left(\frac{\pi H}{\lambda}\right)\frac{\cosh[2k(z+d)]\sin 2\theta}{\sinh^4(\kappa d)} \tag{2.3.36}$$

For deep water the Stokes second-order potential is equal to the Airy.

2.3.2.3 Particles velocities, accelerations

For a unidirectional Airy wave, i.e. $n(x) = -i\omega\phi(x)/g = a_0 \exp(-i\kappa x)$, we can express the eq. 2.3.32 as a function of η (eq. 2.3.37)

$$\Phi(x,z,t) = i\frac{g}{\omega}a_0\eta(x)\frac{\cosh\left[\kappa(z+d)\right]}{\cosh\kappa d}\exp(i\omega t) \tag{2.3.37}$$

By deriving the eq 2.3.37, Brebbia and Walker (42) determined the particle velocity components in the x, and z directions (in y direction $v = \dot{v} = 0$), as

$$\begin{aligned} u &= \frac{g}{\omega}\kappa\frac{\cosh\left[\kappa(z+d)\right]}{\cosh\kappa d}\exp(i\omega t)(x) \\ w &= i\frac{g}{\omega}\kappa\frac{\sinh\left[\kappa(z+d)\right]}{\cosh\kappa d}\exp(i\omega t)\eta(x) \end{aligned} \tag{2.3.38}$$

and deriving again the accelerations

$$\begin{aligned} \dot{u} &= ig\kappa\frac{\cosh\left[\kappa(z+d)\right]}{\cosh\kappa d}\exp(i\omega t) \\ \dot{w} &= -g\kappa\frac{\sinh\left[\kappa(z+d)\right]}{\cosh\kappa d}\exp(i\omega t) \end{aligned} \tag{2.3.39}$$

The DNV (46) recommended practice for environmental conditions and environmental loads presents these values tabled as shown tab. 2.3.2.

Table 2.3.2 – Velocities and accelerations of Airy and Stokes second-order wave theory (46, adapted)

Parameter	*Airy wave theory*		*Stokes second-order wave theory*
	General water depth	*Deep water*	
Horizontal particle velocity, u	$\frac{\pi H}{T}\frac{\cosh[k(z+d)]}{\sinh(kd)}\cos\theta$	$\frac{\pi H}{T}e^{kz}\cos\theta$	$u_1 + \frac{3}{4}\frac{\pi H}{T}\left(\frac{\pi H}{\lambda}\right)\frac{\cosh[2k(z+d)]}{\sinh^4(kd)}\cos 2\theta$
Vertical particle velocity, w	$\frac{\pi H}{T}\frac{\sinh[k(z+d)]}{\sinh(kd)}\sin\theta$	$\frac{\pi H}{T}e^{kz}\sin\theta$	$w_1 + \frac{3}{4}\frac{\pi H}{T}\left(\frac{\pi H}{\lambda}\right)\frac{\sinh[2k(z+d)]}{\sinh^4(kd)}\sin 2\theta$
Horizontal particle acceleration, $\dot{u}$	$\frac{2\pi^2 H}{T^2}\frac{\cosh[k(z+d)]}{\sinh(kd)}\sin\theta$	$\frac{2\pi^2 H}{T^2}e^{kz}\sin\theta$	$\dot{u}_1 + \frac{3\pi^2 H}{T^2}\left(\frac{\pi H}{\lambda}\right)\frac{\cosh[2k(z+d)]}{\sinh^4(kd)}\sin 2\theta$
Vertical particle acceleration, $\dot{w}$	$-\frac{2\pi^2 H}{T^2}\frac{\sinh[k(z+d)]}{\sinh(kd)}\cos\theta$	$-\frac{2\pi^2 H}{T^2}e^{kz}\cos\theta$	$\dot{w}_1 - \frac{3\pi^2 H}{T^2}\left(\frac{\pi H}{\lambda}\right)\frac{\sinh[2k(z+d)]}{\sinh^4(kd)}\cos 2\theta$

For a wave height of $H = 6m$ with a peak wave period of $T = 6s$ the velocity and acceleration profile of a water particle are obtained by using the equations presented in tab. 2.3.2, as shown fig. 2.3.4.

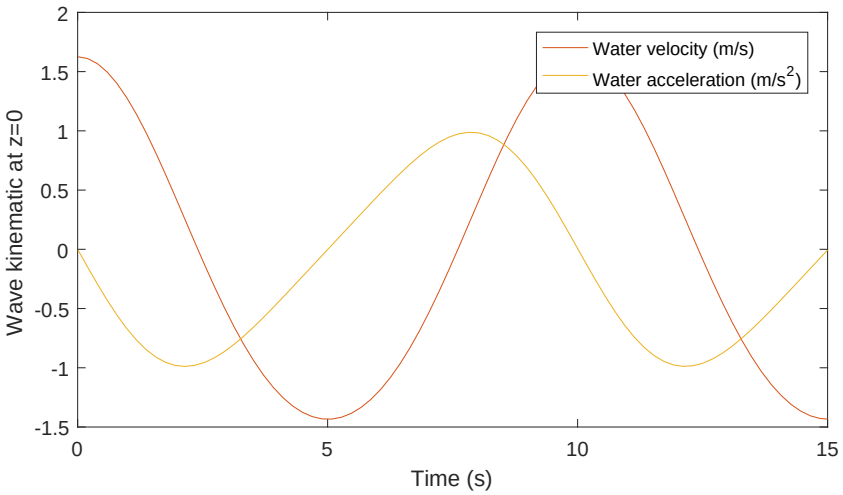

Figure 2.3.4 – Velocity and acceleration of the particle for a second-order wave theory

2.3.3 Wave probabilistic characterization

To get a realistic idea of the wind-generated sea we have to enlarge the discussion not only for waves of constant depth or frequencies. The sea-surface elevation is a time-dependent random variable and must be evaluated using statistical procedures. These methods are usually used to determine the response of offshore structures. For tidal waves, i.e. waves generated by earthquakes, eruptions, etc., there are deterministic methods that must be realized separately because their occurrence is not frequent.

The excitation provoked by the nature have a random variable in function of the surface elevation an can be expressed by an infinite sum of harmonic waves of random phase as

$$\eta(\mathbf{x},\mathbf{t}) = \sum_{i=1}^{\infty} \eta_i(\mathbf{x},t) = \sum_{i=1}^{\infty} a_i(\omega_i,\kappa_i)\cos(\omega_i t - \kappa_\mathbf{i}.\mathbf{x} + \varepsilon_i) \tag{2.3.40}$$

where, for a particular wave, $\mathbf{x} = (x, y)$ is the position vector, κ_i the wavenumber vector, distributed randomly within the storm area, ω_i are the frequencies, ε_i are the random phases distributed uniformly on the interval 0 to 2π, and a_i is the amplitude.

The variable η in the form of eq. 2.3.40 follows the same central theorem described by Rice (48) and the distribution of η is Gaussian. The probability density function of η can be expressed as:

$$p(\eta) = \frac{1}{\sqrt{(2\pi)M_0}} \exp\left(-\frac{\eta^2}{2M_0^2}\right) \tag{2.3.41}$$

where $M_0 = \langle\eta^2\rangle^{1/2}$ is the root mean square value of η and it is assumed that $\langle\eta\rangle = 0$, which means that the surface elevation is measure from the SWL.

For an specific location, it is possible to estimate the significant wave height H_s and the mean zero crossing period T_0 from the local geography and its expected wind velocities.

This values are extensively used for design wave approach. For a spectral approach these parameters can be used to define a spectral form as the Pierson-Moskowitz spectrum and can vary with the sea state.

Brebbia and Walker (42) present three sources to obtain these statistical parameters: oceanographic maps, which computes the probable values of the height of the highest wave in a 50 or 100 year storm, with its most probable zero crossing period; wave scatter diagrams, with the information about different sea states of a certain period; wind roses, which presents the strength, direction and a percentage frequency of the expected winds at the location.

The wave height can be described by the significant wave height H_s and the spectral peak period T_p.

DNV-OS-J101 defines that, unless data indicate otherwise, a 3-parameters Weibull distribution can be assumed for the significant wave height:

$$F_{H_S}(h) = 1 - \exp\left[-\left(\frac{h-\gamma}{\alpha}\right)^{\beta}\right] \tag{2.3.42}$$

The significant wave height with return period T_R in units of years can be computed in a similar way that was defined the wind speed U_{10,T_R} (from Eq. 2.2.5):

$$H_{s,T_R} = F^{-1}_{H_s,\max,1\text{year}}\left(1 - \frac{1}{T_R}\right) \tag{2.3.43}$$

where $T_R > 1$ year, $F_{H_s,\max,1\text{year}}(h) = [F_{H_S}(h)]^N$ represents the maximum annual significant wave height and N is the number of t-hour sea states in one year. For $t = 3$ hours, $N = 2920$. In deep water the wave height can be assumed as a Rayleigh distribution (see DNV-OS-J101).

For a wider frequency range of a narrow-band record, the significant wave height H_s relates to the maximum wave height H_{10}, which occurs a typical wave record of ten minutes in length, by the eq. 2.3.44.

$$H_{10} = 1.6H_s \tag{2.3.44}$$

2.3.4 Wind wave and ocean wave spectrum

2.3.4.1 Hydrodynamic forces on slender members

At this point is important to examine the fluid-structure interaction of slender members to understand the dynamic which involves OWTs. To analyze the stochastic behavior of environmental loads (wind forces, currents, earthquakes, wave loading), a random vibration analysis can handle this approach instead of just statistical procedures.

For forces due to currents and tides their behavior have time period much larger than the resonant period and a vortex shedding is formed around the section of the structure as show fig. 2.3.5.

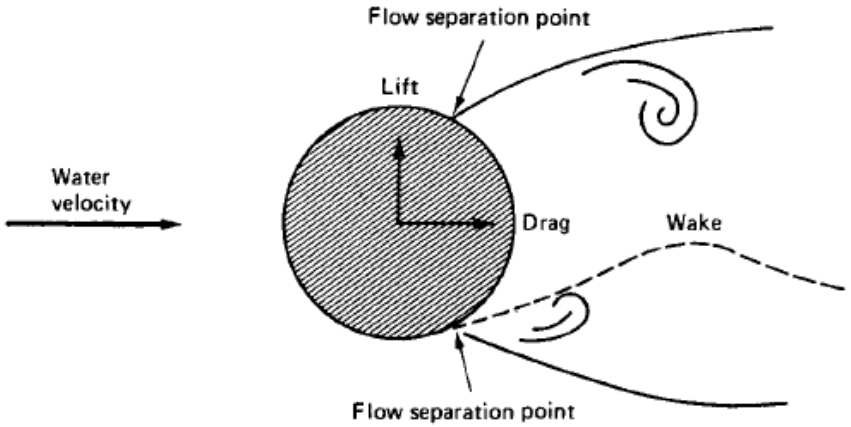

Figure 2.3.5 – Vortex shedding (42)

The effects of this vortex behind the member generates an equal an opposite circulation of the fluid round the cylinder, rising a lift force on it at right angles on the direction of fluid flow. In addiction, currents and tides change the wave field on the surface altering the wave forces provoking a constant drag force due to the viscosity. Brebbia and Walker (42) also says that the designer must take into account other factors as the marine growth, the water-temperature variation and the hydrostatic pressure.

An other important environment loading is the wave motion or the wave loading (fig. 2.3.6).

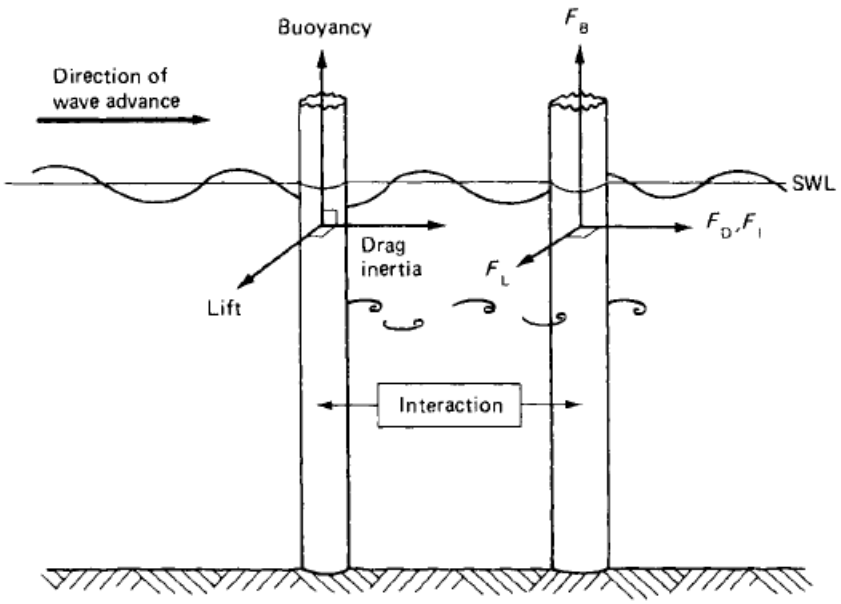

Figure 2.3.6 – Wave loading due to a linear wave (42).

The fig. 2.3.6 shows a fluctuating buoyancy force in the vertical direction resulted

from the varying length of the member immersed. From hydrostatics this force is estimated by eq. 2.3.45

$$F_B = \frac{b\rho g a_0}{\kappa}[\sin(\kappa b - \omega t) + \sin \omega t] \tag{2.3.45}$$

for a sinusoidal Airy wave of amplitude a_0, angular frequency ω, wavenumber κ, and a square-sectioned member of width b. For other shapes must be evaluated the immersed volume of the member at any time during the motion.

For a vertical member 75% of the height of a wave slapping is above SWL as shown in fig. 2.3.7. For this type of members the impact area due to horizontal forces are more important to be considered in the analysis.

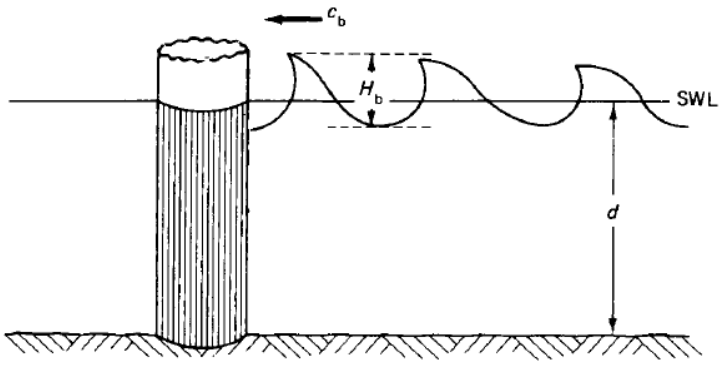

Figure 2.3.7 – Wave slapping on a vertical member (42)

The forward velocity of the water particles:

$$V_b \approx c_b = \sqrt{gd} \tag{2.3.46}$$

where c_b is the velocity of the breaking wave, g the gravity, and d the undisturbed depth of the water.

There are two main wave forces on a supporting member of an offshore structure in the line of the wave direction, the **drag and inertia forces**. The drag force is proportional to the square of the water particle velocity and is associated to the effects of viscosity in the fluid (without vortex shedding effects). The inertia force is independent of any viscosity and is composed of: the virtual mass of the member in motion, which can be an added inertial water mass or a force in opposition to the motion of the member; and the inertia force due to an accelerating fluid.

Morison's equation

For a full analysis, Morison (49) postulated an equation which includes the effects of the drag, lift and inertial forces on a stationary cylinder in accelerating fluid flow (depending of the condition is added a lift component).

His formulation gives inertia and drag forces without considering any modification in the shape of the wave and is valid for a diameter-to-wavelength ratio of less than 0.2.

For a larger diameter the change in the shape of the waves due to diffraction effects must be considered, which means that the inertia effect will be much larger than the drag one and the fluid can be considered inviscid (42).

Considering only the drag and inertia forces and using the Airy wave theory, the force per unit length in the x direction at depth z can be computed using the eq. 2.3.47

$$F_{I+D}(z,t) = F_I + F_D = C_I\dot{u} + C_D u|u| \tag{2.3.47}$$

where the velocities and accelerations u and $\dot{u}$ are evaluated at the cylinder axis.

C_I is an inertia constant which consider an hydrodynamic mass contribution and a variation of the pressure gradient within the accelerating fluid, computed as:

$$C_I = C_M + C_A = c_m\frac{\rho\pi D^2}{4} + \rho A = c_i\frac{\rho\pi D^2}{4} \tag{2.3.48}$$

where $c_i = c_m + 1$ is the inertia coefficient for the section, c_m is the added mass coefficient, and A is the cross-sectional area. For an infinite circular cylinder in an infinite medium $c_m = 1$.

The inertia force on the body then can be written as:

$$F_I(z,t) = C_I\dot{u} = \left(c_m\frac{\rho\pi D^2}{4} + \rho A\right)\dot{u} \tag{2.3.49}$$

The coefficient C_D has the following relation with the drag coefficient c_d:

$$C_D = \frac{1}{2}c_d\rho D \tag{2.3.50}$$

and for a circular cylinder the values of c_d can be computed in function of Reynolds number as shown in fig. 2.3.8. The Reynolds number is defined by:

$$Re = VD/\nu \tag{2.3.51}$$

where D is a typical length associated with the horizontal dimension (in the present context the diameter), V is a characteristic velocity of the flow, and ν is the kinematic viscosity of the fluid.

In order to write the Morison equation properly, a statistical equivalent linearisation of the non-linear drag term of eq. 2.3.50 is carried out to insert the stochastic nature of the process. Brebbia and Walker shows that the linearized drag coefficient $\bar{C_D}$ can be written, after a Gaussian with a zero mean process, as:

$$\bar{C_D} = C_D\sqrt{\frac{8}{\pi}}\sigma_u \tag{2.3.52}$$

where σ_u is the standard deviation of u.

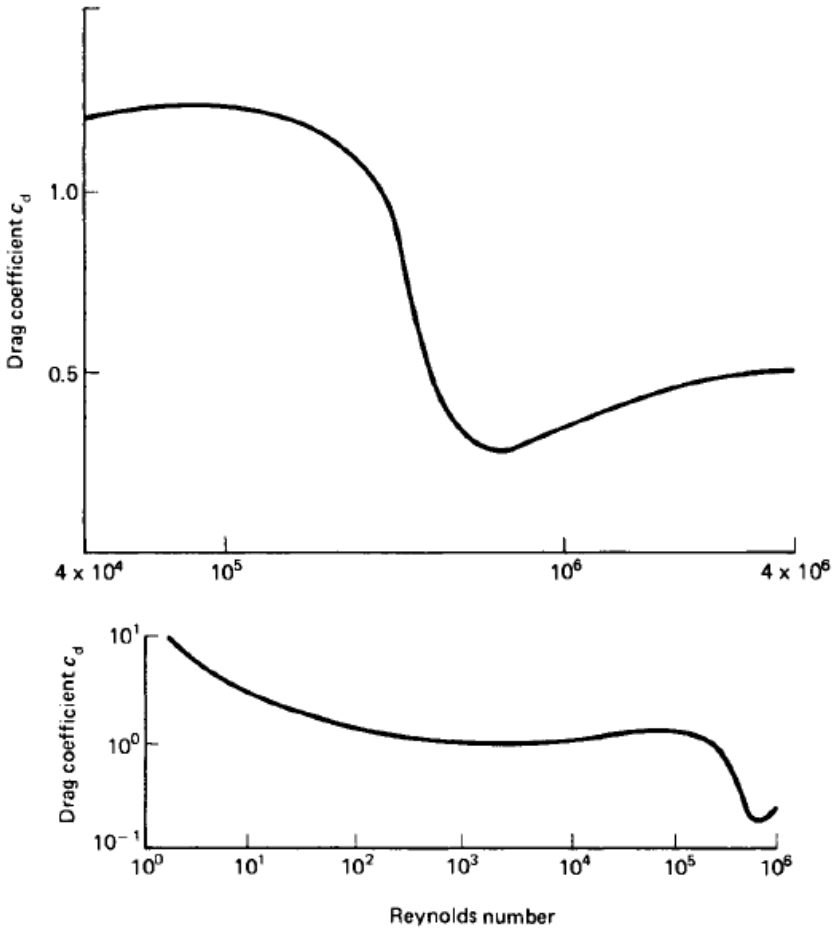

Figure 2.3.8 – Drag coefficient in function of the Reynolds number for a circular cylinder (42).

The linearized Morison equation can now be written as:

$$F_{I+D}(z,t) = C_I \dot{u} + C_D \sqrt{\frac{8}{\pi}} \sigma_u u \tag{2.3.53}$$

Li and Chen (20) introduces

$$H(\omega, z) = \frac{\omega \cosh[\kappa(z+d)]}{\sinh(\kappa d)} \tag{2.3.54}$$

to write the horizontal acceleration and velocity of eqs. 2.3.38 and 2.3.39 as

$$\begin{aligned} u(x,z,t) &= H(\omega,z)\eta(x,t) \\ \dot{u}(u,z,t) &= H(\omega,z)\dot{\eta}(x,t) \end{aligned} \tag{2.3.55}$$

Substituting eqs. 2.3.55 in the linearized Morison eq. 2.3.53 will give

$$F_{I+D}(z,t) = C_I H(\omega,z)\eta(x,t) + C_D \sqrt{\frac{8}{\pi}} \sigma_u H(\omega,z) S_{\eta\eta}(x,t) \tag{2.3.56}$$

If $\eta(t)$ is a stationary stochastic process, from eq. 2.3.56 it is obtained the PSD of the wave force $F(z,t)$ due to the uncorrelated nature of the stationary process and its

derivative

$$S_F(z,\omega) = \left(\frac{8}{\pi}\sigma_u^2 C_D^2 + C_I^2\omega^2\right) H^2(\omega,z) S_\eta(\omega) \tag{2.3.57}$$

Current modeling

The sea currents in shallow water can be characterized by a velocity field whose intensity decreases with depth, when detailed field measurements are not available. DNV-OS-J101 defines the variation in current velocity $v(z)$ with the depth z as:

$$v(z) = v_{\text{tide}}(z) + v_{\text{wind}}(z) \tag{2.3.58}$$

$$v_{\text{tide}}(z) = v_{\text{tide0}}\left(\frac{h+z}{h}\right)^{1/7} \qquad \text{for } z \leq 0 \tag{2.3.59}$$

$$v_{\text{wind}}(z) = v_{\text{wind0}}\left(\frac{h_0+z}{h_0}\right) \quad \text{for } -h_0 \leq z \leq 0 \tag{2.3.60}$$

where $v_{\text{tide}}(z)$ and $v_{\text{wind}}(z)$ are the velocities generated by the tide and wind; v_{tide0} and v_{wind0} are the tidal and wind-generated current at SWL; h_0 is the reference depth for wind-generated current (typically 50m). Unless data indicate otherwise, $v_{\text{wind0}} = kU_0$ with $0.015 \leq k \leq 0.03$.

Lift forces

The motion of fluid on slender members give rise to vortex shedding, which provokes a lift force on the member at a frequency corresponding to the eddy-shedding frequency. For steady flow past a cylinder the Strouhal number St (eq. 2.3.61) can measure the frequency of lift forces.

$$St = \frac{Df_{vs}}{V} \tag{2.3.61}$$

where f_{vs} is the frequency of vortex shedding.

Considering an accelerating flow it is expected for long waves and small cylinder the presence of dynamic lift forces. Keulegan and Carpenter (50) defines a measure in which the coefficients c_i, c_m and c_d depends on the Keulegan-Carpenter number K_C (eq. 2.3.62). For $K_C \geq 15$ Keulegan and Carpenter estimate the occurrence of lift forces.

$$K_C = \frac{V_m T}{D} \tag{2.3.62}$$

where V_m is the maximum horizontal water-particle velocity and T the time period of the wave.

Chakrabarti (51) define the lift force as the eq. 2.3.63.

$$F_L(z,t) = \frac{\rho D V_m^2}{2}\sum_{n=1}^{N} c_l^n \cos\left(n\omega_0 t + \psi_n\right) \tag{2.3.63}$$

where ω_0 is the angular frequency of the incident wave, ψ_n the phase angle of the nth harmonic force, and c_l^n the lift coefficient for the nth harmonic (and a function of K_C).

Hydrodynamic coefficients

The use of Morison equation in the estimation of the hydrodynamic loads on slender member may take into account the variation of the added mass coefficient c_m and the drag coefficient c_d as function of Re (eq. 2.3.51), K_C (eq. 2.3.62) and the non-dimensional roughness Δ, i.e. $c_d = c_d(Re, K_C, \Delta)$ and $c_m = c_m(Re, K_C, \Delta)$ (46).

The non-dimensional roughness parameter is defined as:

$$\Delta = k/D \tag{2.3.64}$$

where k is the surface roughness height and D the diameter of the section.

DNV-GL-RP-C205 (46) suggests the selection of surface roughness presented in tab. 2.3.3 for the estimation of the drag coefficient.

Table 2.3.3 – Typical values of surface roughness

Material	k **(meters)**
Steel, new uncoated	5×10^{-5}
Steel, painted	5×10^{-6}
Steel, highly corroded	3×10^{-3}
Concrete	3×10^{-3}
Marine growth	5×10^{-3} to 5×10^{-2}

For high Reynolds ($Re > 10^6$) a dependence between the drag-coefficient and the roughness may be taken as:

$$c_{DS} = \begin{cases} 0.65 & \text{if } \Delta < 10^{-4} \text{ (smooth)} \\ (29 + 4\log_{10}(\Delta))/20 & \text{if } 10^{-4} < \Delta < 10^{-2} \\ 1.05 & \text{if } \Delta > 10^{-4} \text{ (rough)} \end{cases} \tag{2.3.65}$$

for both regular and irregular wave analysis.

The variation of the drag coefficient as a function of the Keulegan-Carpenter number can be approximated by:

$$c_d = c_{DS}(\Delta) \cdot \psi(K_C) \tag{2.3.66}$$

where $\psi(K_C)$ is the wake amplification factor. For low Keulegan-Carpenter numbers ($K_C < 12$) that value can be taken as:

$$\psi(K_C) = \begin{cases} C_\pi + 0.10(K_c - 12) & \text{if } 2 \leq K_C < 12 \\ C_\pi - 1 & \text{if } 0.75 \leq K_C < 2 \\ C_\pi - 1 - 2(K_C - 0.75) & \text{if } K_C \leq 0.75 \end{cases} \tag{2.3.67}$$

where $C_\pi = 1.5 - 0.024(12/c_{DS} - 10)$.

For combined wave and current action, the current velocity ($v(z)$) must be considered in the estimation of the Keulegan-Carpenter number. When $v(z) > 0.4V_m$, c_d can be taken equal to c_{DS}.

For $K_C < 3$, C_I is independent of K_C and takes the theoretical value $C_I = 2$ for both rough and smooth cylinders. For $K_C > 3$, the mass coefficient becomes

$$C_I = max\left[2 - 0.044(K_C - 3); 1.6 - (c_{DS} - 0.65)\right] \tag{2.3.68}$$

2.3.4.2 Power spectral density of wind waves

Brebbia and Walker (42) defines the spectral density of a random process u as:

$$S_{uu}(\omega) = \lim_{T\to\infty} \frac{1}{T}\{\bar{U}\hat{\mathbf{U}}\} = \lim_{T\to\infty} \frac{1}{T}|\bar{U}|^2 \tag{2.3.69}$$

where $\bar{U}$ is the Fourier transform of u and $\hat{\mathbf{U}}$ is its conjugate. Applying this spectral density to the velocities from eqs. 2.3.38, we obtain:

$$S_{v_x v_x} = \left[\frac{g\kappa}{\omega}\frac{\cosh\left[\kappa(z+d)\right]}{\cosh\kappa d}\right]^2 S_{\eta\eta} \tag{2.3.70}$$

$$S_{v_z v_z} = \left[\frac{g\kappa}{\omega}\frac{\sinh\left[\kappa(z+d)\right]}{\cosh\kappa d}\right]^2 S_{\eta\eta} \tag{2.3.71}$$

and applying the accelerations from eqs. 2.3.39, we obtain:

$$S_{\dot{v}_x \dot{v}_x} = \left[g\kappa\frac{\cosh\left[\kappa(z+d)\right]}{\cosh\kappa d}\right]^2 S_{\eta\eta} \tag{2.3.72}$$

$$S_{\dot{v}_z \dot{v}_z} = \left[g\kappa\frac{\sinh\left[\kappa(z+d)\right]}{\cosh\kappa d}\right]^2 S_{\eta\eta} \tag{2.3.73}$$

where $S_{\dot{v}\dot{v}}(\omega) = \omega^2 S_{vv}(\omega)$. The cross spectral densities of the velocities and accelerations will be equals zero.

Neumann (52) predict wave spectrum for different sea states relating to generate wave. In his work is shown that, for a wind, a certain fetch F and duration T there is a certain cut-off frequency ω_c below which there will be almost no energy content in the waves.

The sea-surface elevation at a specific location is a time-dependent random variable η. A spectral density function of time $S_{\eta\eta}(\omega)$ can well represent this behavior. After estimated the parameters H_s and T_0 there are presented two empirically derived expressions for the spectral density function $S_{\eta\eta}(\omega)$ commonly used: the Pierson-Moskowitz (eq. 2.3.74) and JONSWAP (Joint North Sea Wave Project) (eq. 2.3.76).

Pierson-Moskowitz (PM)

$$S_{\eta\eta}(n) = \frac{\alpha g^2}{n^5}\exp\left[-\beta\left(\frac{g}{nW}\right)^4\right] \tag{2.3.74}$$

where W is the wind speed required, α and β are dimensionless constants dependent on H_s and T_0 and given by the following equations:

$$\alpha = 4\pi^3 \left(\frac{H_s}{gT_0^2}\right)^2, \qquad \beta = 16\pi^3 \left(\frac{W}{gT_0}\right)^4 \tag{2.3.75}$$

The wind speed W is conventionally taken at 19.5 meters above the MSL. For the North Sea α and β are taken as 0.0081 and 0.74 respectively. This spectrum is applicable for a fully developed sea (where low frequencies are presented).

JONSWAP

Unless data indicate otherwise, the spectral density of the sea elevation may be represented by the JONSWAP spectrum (26) (eq. 2.3.76).

$$S_{\eta\eta}(n) = \frac{\alpha g^2}{(2\pi)^4} n^{-5} \exp\left[-\frac{5}{4}\left(\frac{n}{n_p}\right)^{-4}\right] \gamma^{\exp\left[-0.5\left(\frac{n-n_p}{n_p}\right)^2\right]} \tag{2.3.76}$$

where α is now the generalized Phillips' constant, $\alpha = 5(H_S^2 n_p^4/g^2)(1 - 0.287\ln\gamma)\pi^4$, $n = 1/T$ is the wave frequency, T is the wave period, $n_p = (4\beta/5)^{1/4} g/W = 1/T_p$ is the frequency corresponding to maximum energy density given by the PM spectrum, T_p is the peak period, γ is peak-enhancement factor of the maximum spectral energy to the corresponding maximum of the PM spectrum or overshoot parameter, and $\sigma = \sigma_a$ is the left side width (for $n < n_p$) and $\sigma = \sigma_b$ is the right side width (for $n > n_p$).

For the North Sea the overshoot parameter is considered in a range of $1 < \gamma < 7$ as a function of H_s and T_p (and can be extracted from the fig. 2.3.9 from Chakrabarti and Snider (53)) and values of σ_a and σ_b of 0.07 and 0.09 respectively. The overshoot γ parameter can represent some kind of non-linear interactions non considered in the PM spectrum an can be estimated also by eq. 2.3.77.

$$\gamma = \begin{cases} 5 & \text{for } \frac{T_p}{\sqrt{H_S}} \leq 3.6 \\ \exp\left(5.75 - 1.15\frac{T_p}{\sqrt{H_S}}\right) & \text{for } 3.6 < \frac{T_p}{\sqrt{H_S}} \leq 5 \\ 1 & \text{for } 5 < \frac{T_p}{\sqrt{H_S}} \end{cases} \tag{2.3.77}$$

The zero-upcrossing period T_Z depends on the peak period T_p through the relationship of eq. 2.3.78.

$$T_Z = T_p \sqrt{\frac{5+\gamma}{1+\gamma}} \tag{2.3.78}$$

The IEC (25) defines the correlation between the PM (S_{PM}) and JONSWAP(S_{JS}) PSD as:

$$S_{PM} = 0.3125 \cdot H_s^2 \cdot n_p^4 \cdot n^{-5} \cdot \left(-1.25\left(\frac{n_p}{n}\right)^4\right) \tag{2.3.79}$$

$$S_{JS} = C(\gamma) \cdot S_{PM}(n) \cdot \gamma^{\exp\left[-0.5\left(\frac{n-n_p}{n_p}\right)^2\right]} \tag{2.3.80}$$

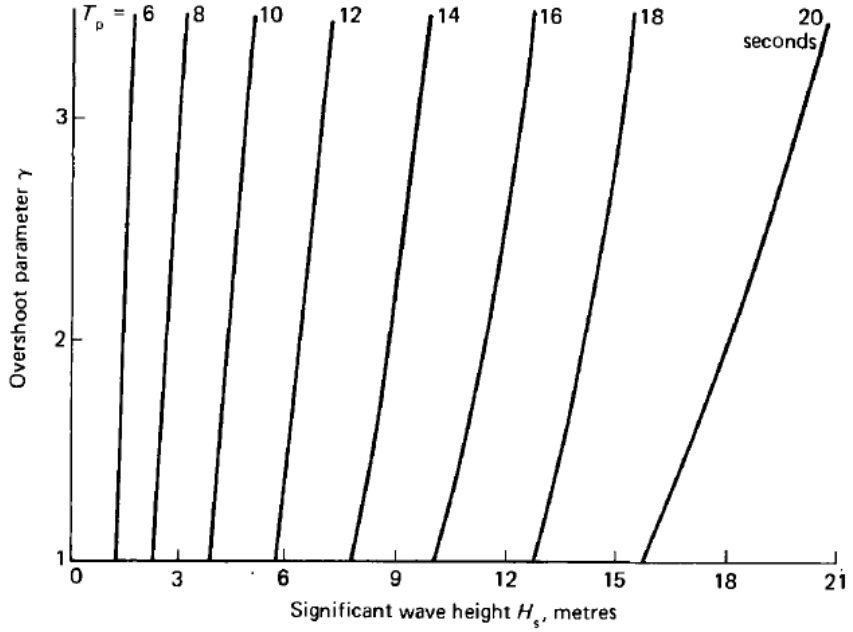

Figure 2.3.9 – Overshoot parameter in function of the wave height and the peak period for the JONSWAP spectrum (53)

where $C(\gamma) = 1 - 0.287 \cdot \ln \gamma$ is the normalizing factor.

Both PM and JONSWAP ($\gamma = 3.3$) spectrum are shown in fig. 2.3.10 for $H_s = 6m$, $T_p = 10s$ (same values used in the 5-MW OWT of Jonkman (34)).

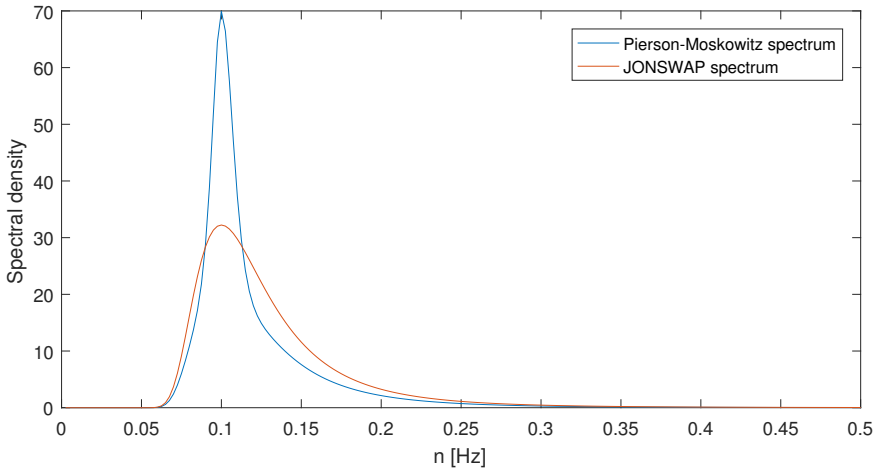

Figure 2.3.10 – Pierson-Moskowitz and JONSWAP spectrum

2.4 Design loads

After selected the basic layout of the OWT and estimate the aerodynamic and hydrodynamic actions, the next step in the design process is to consider in detail the loads related by the turbine. This section shows some international standards used for

modeling wind turbines (and OWT); how to estimate the basis loads as the aerodynamic, gravitational, inertia, operational, ultimate and fatigue loads;

2.4.1 Wind turbine standards

Manwell et al. (29) organizes a variety of relevant standards for the design, testing, and operation of Wind Turbines. The lead in wind turbine standards is being taken by the International Electro-technical Commission (IEC). The most important international standards that are in use today are presented in tab. 2.4.1.

Table 2.4.1 – Some wind turbine-related IEC standards

Source/Number	Title
IEC WT01	IEC System for Conformity Testing and Certification of Wind Turbines Rules and Procedures
IEC 61400-1	Wind Turbines – Part 1: Design Requirements, edition 2
IEC 61400-2	Wind Turbines – Part 2: Safety Requirements for Small Wind Turbines
IEC 61400-3	Wind Turbines – Part 3: Design Requirements for Offshore Wind Turbines
ISO/IEC 81400-4	Wind Turbines – Part 4: Gearboxes for Turbines from 40 kW to 2 MW
IEC 61400-11 TS	Wind Turbines – Part 11: Acoustic Emission Measurement Techniques
IEC 61400-12	Wind Turbines – Part 12: Power Performance Measurements of Electricity Producing Wind Turbines
IEC 61400-13 TS	Wind Turbines – Part 13: Measurement of Mechanical Loads
IEC 61400-14	Wind Turbines – Part 14: Declaration of Apparent Sound Power Levels and Tonality Value of Wind Turbines
IEC 61400-21	Wind Turbines – Part 21: Power Quality Measurements
IEC 61400-22 TS	Wind Turbines – Part 22: Conformity Testing and Certification of Wind Turbines
IEC 61400-23 TS	Wind Turbines – Part 23: Full-scale Structural Testing of Rotor Blades
IEC 61400-24 TR	Wind Turbines – Part 24: Lightning Protection
IEC 61400-25	Wind Turbines – Part 25: Communications for Monitoring and Control of Wind Turbines

Other useful, but non-IEC, standards are listed in tab. 2.4.2. These standards were developed by countries or entities, such as Germanischer Lloyd (GL) or Det Norske Veritas (DNV).

Table 2.4.2 – Other wind turbine-related standards

Source/Number	Title
Germanischer Lloyd	Regulations for the Certification of Wind Energy Conversion Systems
Danish Energy Agency DS-472	Code of Practice for Loads and Safety of Wind Turbine Construction
DNV	Guidelines for the Design of Wind Turbines, 2nd edition
DNV-OS-J101	Design of Offshore Wind Turbine Structures
DNV-OS-J102	Design and Manufacture of Wind Turbine Blades

Petrini et al. (5) adapted the classification of the IEC 61400-3 (28) about environmental conditions in the diagram of fig. 2.4.1.

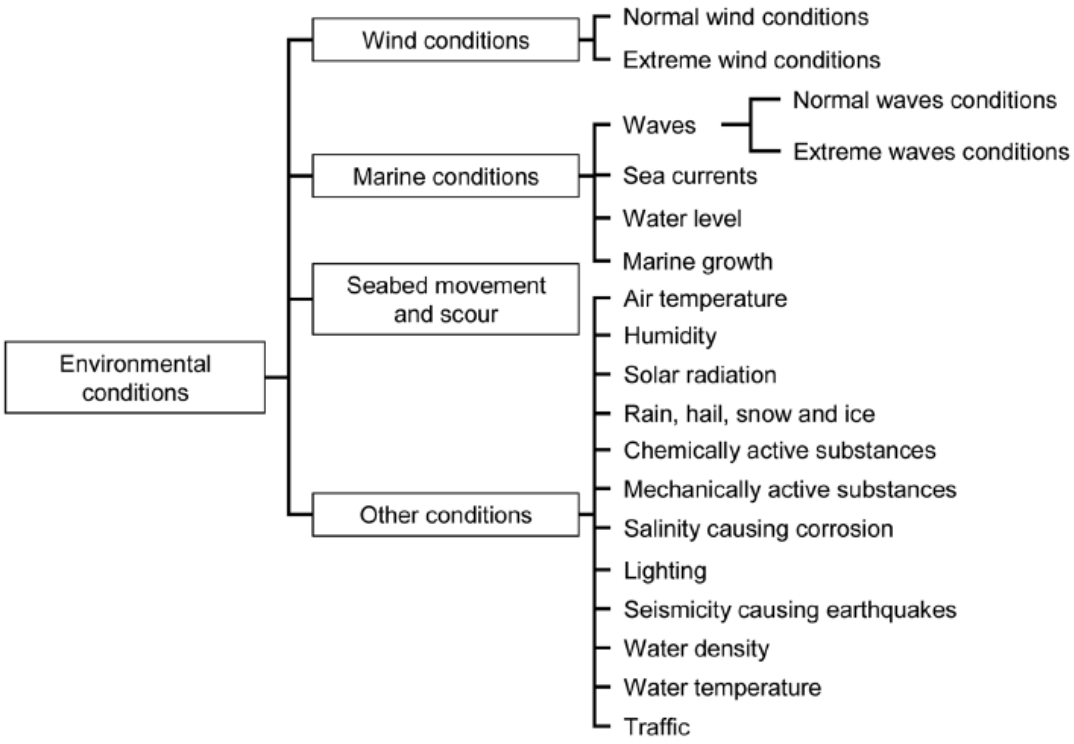

Figure 2.4.1 – Environmental conditions classification

IEC 61400-3 is part of International Standard published by the IEC which rules the requirements to design an OWT, focusing on the engineering integrity of its structural components and also concerning with subsystems such as control and protection mechanisms, internal electrical systems and mechanical systems. Together with appropriated IEC and ISO standards they can properly design an OWT.

2.4.2 Basis for design load

Manwell et al (29) classify onshore wind turbine loads into five categories: steady (including static loads), cyclic, stochastic, transient (including impulsive loads), and resonance-induced loads. Each category relates to the action of the wind turbine elements or by the effects of the environmental action (fig. 2.4.2). For OWTs the effects of marine conditions as waves and sea currents must be added.

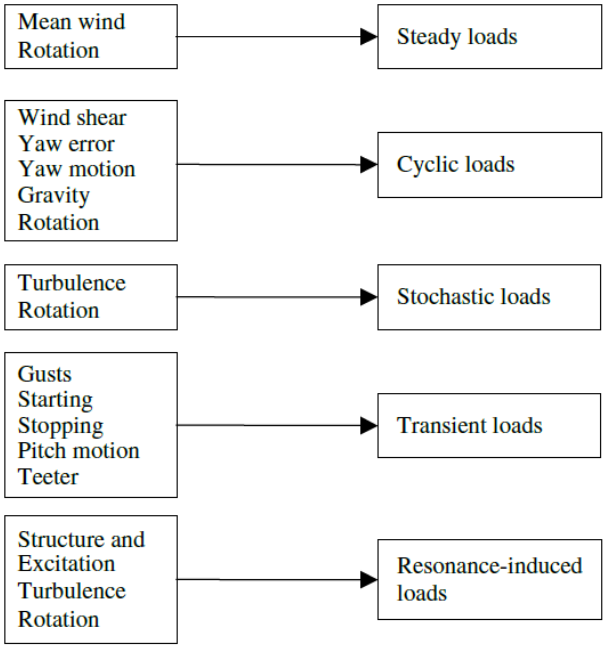

Figure 2.4.2 – Sources of wind turbine loads (29)

To properly model the loads, it is indicated to organize the loads into categories following the standards presented in sec. 2.4.1. Burton et al. (27) categorize sources of loading to be taken into account as:

- aerodynamic loads;
- gravitational loads;
- inertia loads (including centrifugal and gyroscopic effects);
- operational loads arising from actions of the control system.

There are some kind of loads that must be considered in this design process as ultimate and fatigue loads, partial safety factor for loads and functions of the control and safety systems.

Ultimate loads refer to likely maximum loads, multiplied by a safety factor which cover realistic combinations of a wide range of external wind conditions and machine states. Its common distinguish cases between normal and extreme wind conditions and between normal machine states and fault states. The first case are defined in terms of the worst condition occurring for return periods of 50 year for the extreme and 1 year for normal conditions.

The IEC 61400-1 stipulates that the correlation between an extreme condition and a fault state must be considered as a design case. The IEC also provides partial safety factors (tab. 2.4.3) for ultimate loads which have to be properly designed for a limit-state by calculating the sum of the products of each characteristic load and the appropriated partial load factor (27).

Table 2.4.3 – Partial safety factors for loads, γ_f (25)

Unfavourable loads			Favourable loads
Normal (N)	Abnormal (A)	Transport (T)	All design situations
1.35*	1.1	1.5	0.9

For the design load case (DLC) of normal design situations (DLC 1.1 of tab. 2.4.4), the loads are determined using statistical load extrapolation at prescribed wind speeds between cut-in wind speed and cut-out wind speed (V_{in} and V_{out}, respectively), and the partial load factor shall be $\gamma_f = 1.25$.

Fatigue loads refer to the component's ability to withstand an expected number of cycles of possibly varying magnitude. The design fatigue load spectrum should be representative of the loading cycles experienced during power production over the full operational wind speed range taking account the numbers of cycles proportional to the time spent generating at each wind speed.

Control system maintaining the protection of the system by operating the machine parameters following the IEC 61400-1. This way this control is activated by reading critical parameters of the turbine rotational speed, power output, vibration level, and twist of pendant cables running up into nacelle.

2.4.3 Extreme loads

Extreme loads refer to the states of the machine (normal machine state, machine fault state, or loss of load) under operational or non-operational load cases. A non-operational machine state is stationary (i.e. parked, or idling condition), for the cases in which the wind turbine don't generates power (and neither start-up or shut-down).

IEC 61400-1 specifies load cases in function of the wind models, characterized in sec. 2.2.2, as shown tab. 2.4.4 (the following abbreviations are used: $V_r \pm 2m/s$, the sensitivity to all wind speeds; F, Fatigue; U, ultimate strength; N, Normal; A, Abnormal; T, Transport and Erection; $*$, Partial safety for fatigue).

Burton et al. (27) classifies these cases into operational or non-operational states:

- **Operational load cases**: This state taking into account the investigation of several load cases to evaluate the effects of extremes of gust loading, wind direction change and wind shear. The IEC 61400-1 divided this load cases into two distinct types with the wind field can be modeled in deterministic or stochastic terms. IEC 61400-1 specifies for all operational load cases the use of the following requirements: wind shear according to the power law $U(z) \propto z^{0.2}$ (normal wind profile), tower shadow, inclination of the mean air flow up to 8° with respect to the horizontal plane, rotor aerodynamic and rotor mass imbalances, yaw tracking errors, and air density as $1.225kg/m^3$ (27).

Table 2.4.4 – Design load cases (25)

Design situation	DLC	Wind condition	Other conditions	Type of analysis	Partial safety factors
1) Power production	1.1	NTM $V_{in} < V_{hub} < V_{out}$	For extrapolation of extreme events	U	N
	1.2	NTM $V_{in} < V_{hub} < V_{out}$		F	*
	1.3	ETM $V_{in} < V_{hub} < V_{out}$		U	N
	1.4	ECD $V_{hub} = V_r - 2$ m/s, V_r, $V_r + 2$ m/s		U	N
	1.5	EWS $V_{in} < V_{hub} < V_{out}$		U	N
2) Power production plus occurrence of fault	2.1	NTM $V_{in} < V_{hub} < V_{out}$	Control system fault or loss of electrical network	U	N
	2.2	NTM $V_{in} < V_{hub} < V_{out}$	Protection system or preceding internal electrical fault	U	A
	2.3	EOG $V_{hub} = V_r \pm 2$ m/s and V_{out}	External or internal electrical fault including loss of electrical network	U	A
	2.4	NTM $V_{in} < V_{hub} < V_{out}$	Control, protection, or electrical system faults including loss of electrical network	F	*
3) Start up	3.1	NWP $V_{in} < V_{hub} < V_{out}$		F	*
	3.2	EOG $V_{hub} = V_{in}$, $V_r \pm 2$ m/s and V_{out}		U	N
	3.3	EDC $V_{hub} = V_{in}$, $V_r \pm 2$ m/s and V_{out}		U	N
4) Normal shut down	4.1	NWP $V_{in} < V_{hub} < V_{out}$		F	*
	4.2	EOG $V_{hub} = V_r \pm 2$ m/s and V_{out}		U	N
5) Emergency shut down	5.1	NTM $V_{hub} = V_r \pm 2$ m/s and V_{out}		U	N
6) Parked (standing still or idling)	6.1	EWM 50-year recurrence period		U	N
	6.2	EWM 50-year recurrence period	Loss of electrical network connection	U	A
	6.3	EWM 1-year recurrence period	Extreme yaw misalignment	U	N
	6.4	NTM $V_{hub} < 0,7\ V_{ref}$		F	*
7) Parked and fault conditions	7.1	EWM 1-year recurrence period		U	A
8) Transport, assembly, maintenance and repair	8.1	NTM V_{maint} to be stated by the manufacturer		U	T
	8.2	EWM 1-year recurrence period		U	A

- *Power production load cases - normal machine state:* DLC 1.1 involves the operation in turbulent wind field defined by the NTM (normal turbulence model), with wind speeds at $2m/s$ intervals between cut-in wind speed and cut-out wind speed, normal partial load factor, and investigation of the turbine cut-out wind speed U_0. The DLC 1.2 is a fatigue analysis. DLC 1.3 is for an operation in turbulent wind field defined by the ETM (extreme turbulence model). DLCs 1.4 and 1.5 specify

transient cases that have been selected as potentially critical events in the life of a wind turbine.

- *Machine fault state*: Carry out the effects of the occurrence of fault or loss of electrical network while a power production (DLCs 2.1 to 2.4)

- *Start-up and shut-down load cases*: Taking account the transients start-up (DLCs 3.1 to 3.3) and shut-down (DLCs 4.1, 4.2), based on the control system behavior and a emergency shutdown (DLC 5.1).

- **Non-operational load cases (parked)**

  - *Normal machine state:* The design wind speed for this load case is normally taken as the gust speed with a return period of 50 years. This factor depends on the gust duration and the size of the loaded area. For this load case, IEC 61400-1 takes into account the possibility of grid failure, preventing that the yaw system track any subsequent changes in wind direction (in the absence of faults or grid loss cater for varying yaw misalignments, DLCs 6.1 and 6.3; in case of loss of grid connection, DLC 6.2; in case of yaw slippage, DLC 6.4).

  - *Machine fault state:* Involves the failure of the yaw or pich mechanisms. The gust speed for this load case is commonly taken with a return period of 1 year (DLC 7.1).

Other cases involves transportation, installation, maintenance, or repair design situation and appropriate external conditions (DLCs 8.1 and 8.2).

3 Structural modeling and vibration control of OWT

In this chapter are presented the NREL 5-MW OWT reference used in this thesis, a brief review of vibration control techniques applied to wind turbines, focusing on the Pendulum Tuned Mass Damper (PTMD) passive controller type, and three main structural modeling that uses the PTMD for vibration control: the tower+PTMD 2DOF, OWT+FEM, and OWT+SEM models.

3.1 NREL 5-MW OWT definition

The OWT modeled in this thesis belongs to the Offshore Code Comparison Collaboration (OC3) NREL Phase 1 (18), i.e. the NREL 5-MW OWT with a rigid foundation in 20 m of water, represented schematically on the first draw of fig. 3.1.1. This wind turbine is a conventional three-bladed, upwind, variable-speed, variable-blade-pitch-to-feather-controlled turbine. For more details about Phases I to IV see the (55, 56, 57, 58) references.

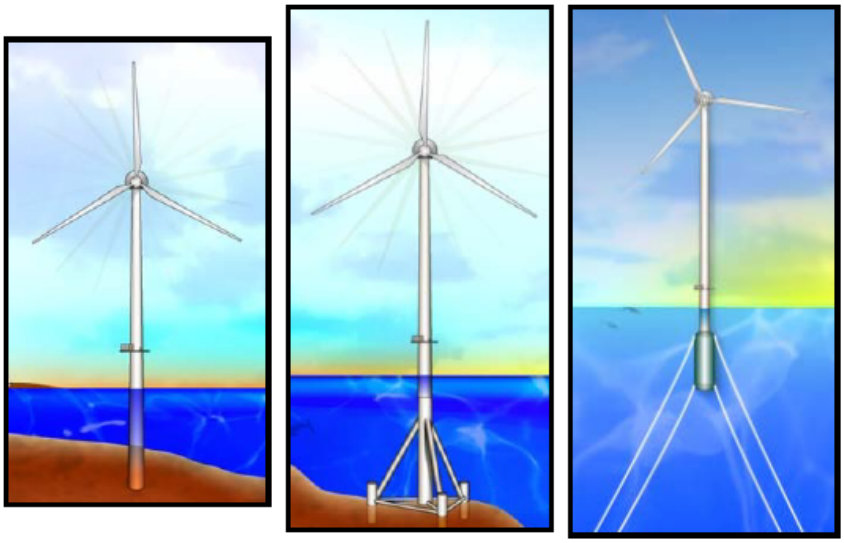

Figure 3.1.1 – Support structure concepts investigated within the OC3 project for the phases I-II, III and IV (which is not modeled here), respectively

Table 3.1.1 – Summary of properties for the NREL 5-MW baseline wind turbine

Rating	5 MW
Rotor orientation, configuration	Upwind, 3 blades
Control	Variable speed, collective pitch
Drivetrain	High speed, multiple-stage gearbox
Rotor, hub diameter	$126m$, $3m$
Hub height	$90m$
Cut-in, rated, cut-out wind speed	$3m/s$, $11.4m/s$, $25m/s$
Cut-in, rated rotor speed	$6.9rpm$, $12.1rpm$
Rated tip speed	$80m/s$
Overhang, shaft tilt, precone	$5m$, 5ž, 2.5ž
Rotor mass	$110,000kg$
Nacelle mass	$240,000kg$
Tower mass	$347,500kg$
Coordinate location of overall center of mass (CM)	$(-0.2m, 0.0m, 64.0m)$

Specifications of the NREL offshore 5-MW baseline wind turbine are summarized in the tab. 3.1. The hydrodynamic and elastic properties of the varying offshore support structures are also controlled. Furthermore, the turbulent full-field wind inflow and regular and irregular wave kinematics are evaluated, including specific turbulence models, wave theories, or stochastic realizations.

The distributed tower properties of the model are based on the base diameter ($6m$) and its thickness ($0.027m$), top diameter ($3.87m$) and its thickness ($0.019m$), and effective mechanical steel properties of the tower used in the DOWEC study, as given in Table 9 on page 31 of (59). The radius and thickness of the tower are assumed to be linearly tapered from base to top. The tower-monopile connection presents a constant diameter and thickness of $6m$ and $0.060m$, respectively. The tower base begins at an elevation of $10m$ above the mean sea level (MSL). The monopile extends from the tower base down to the mud line, which is at $20m$ below MSL. The Young's and shear modulus, and the effective density of the steel are, respectively, $210GPa$, $80.8GPa$, and $8,500kg/m^3$. The $8,500kg/m^3$ is meant to be an increase above steel's typical value of $7,850kg/m^3$ due to the not accounted paint, bolts, welds, and flanges in the thickness data. The support structure incorporates 1% critical structural damping in all modes of the isolated structure (without the top mass present), which corresponds to the values used in the DOWEC study from page 21 of (59).

Jonkman et al. (18) define Phase I-II load-case (LC) simulations including all relevant aerodynamic and hydrodynamic effects (e.g., turbulence, tower shadow, dynamic stall, wind shear, and Wheeler stretching). Individual subsystems are modeled as flexible or rigid depending on the evaluated LC, as follows:

- Load case 1.X: Modal properties in terms of the coupled subsystem eigenfrequencies;
- Load case 2.X: Completely rigid structure;

- Load case 3.X: Flexible onshore wind turbine (rigid substructure), using the land-based version of the NREL offshore 5-MW baseline turbine, as documented in (34);
- Load case 4.X: Flexible offshore structure with tower top mass (rigid nacelle and rotor); also referred to as an "inverted pendulum";
- Load case 5.X: Fully flexible offshore wind turbine;

Load cases 1.1 and 1.2 consists of the eigenanalysis without and with gravity and structural damping, respectively, of the entire system (substructure, tower, drivetrain, blades), and the frequencies are computed as shown fig. 3.1.2 (18).

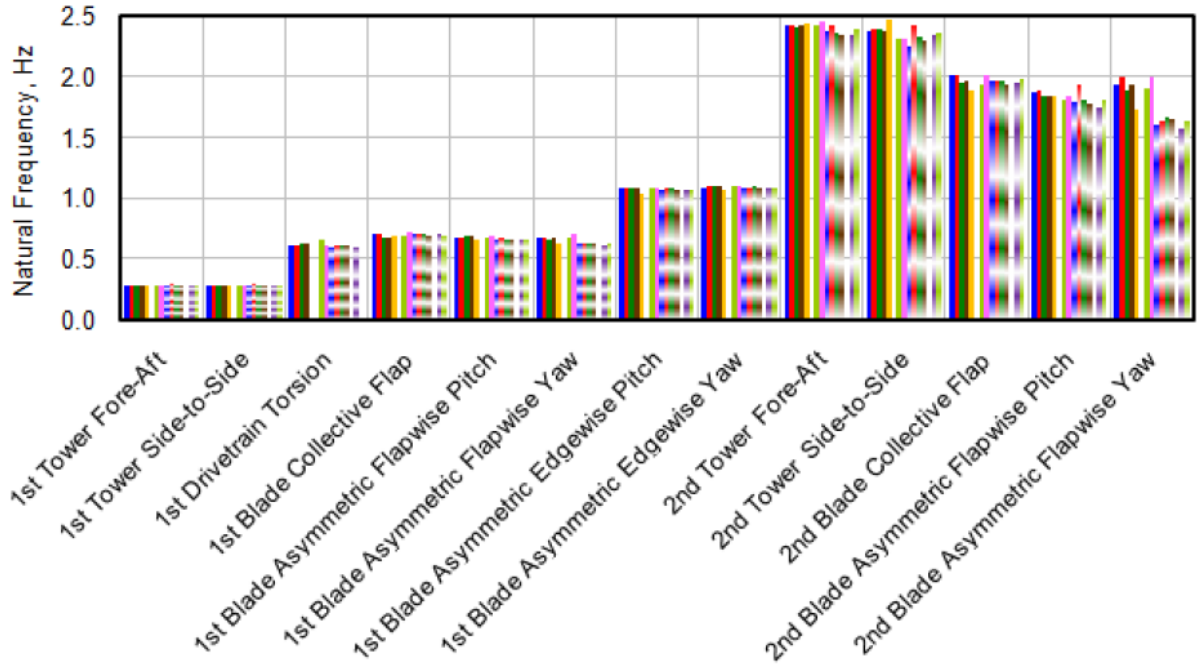

Figure 3.1.2 – Full-system natural frequencies of the phase I fully flexible OWT (18)

In Jonkman et al's (18) report, turbulent wind conditions are considered for LCs with two sets of turbulent wind fields. These turbulence fields are modeled by the International Electrotechnical Commission (IEC) Turbulence Simulator from the WAsP Engineering model, one at $U_{\text{hub}} = U_r = 11.4\ m/s$, i.e., *rated wind speed* and one at $U_{\text{hub}} = 18\ m/s$, i.e., in the *full load range* of the turbine. Both turbulence fields follow the Mann model in conformity with IEC 61400-1 ed.3 (25) using a reference value of $I_{\text{ref}} = 0.14$ for the turbulence intensity (turbine class II of tab. 2.2.2).

3.2 Vibration control strategies

Wind turbines have become one of the most used technologies for power generation. Researchers have been instigating to find its limitations, to improve its productivity and

effectiveness, based on the structural dynamics and control systems (60).

High vibration levels occur in HAWTs and blades due to its height, slenderness, and heavy loads on the tower top (composed of the generator, gearbox, and other components).

Structural control mechanisms have been developed to balance dynamic forces on a wind turbine system, such as earthquake excitation, wind loads, and waves (for offshore turbines). The use of control systems increases wind turbines efficiency by minimizing its vibration and the rotor-nacelle assembly vibration. Damping devices, such as tuned mass dampers, tuned liquid mass dampers, controllable fluid dampers, among others, are commonly used to dissipate the system energy.

3.2.1 Classification of vibration control systems

Structural control systems can be passive, active, hybrid, and semi-active. Passive energy dissipater includes materials and devices which enhancing damping, stiffness, and strength. The other control systems exert external force devices by using sensors, controllers, and signal processing (4).

Several researchers have been studying the use of structural control to help suppress the wind-induced vibrations experienced by Wind Turbines and Offshore Wind Turbines (OWTs), especially the passive controller Tuned Mass Dampers (TMD) (61, 62, 63, 64, 65). Rahmat et al. (60) and Yilmaz (63) present a literature survey about the performance enhancement of wind turbine systems with vibration control following fig. 3.2.1.

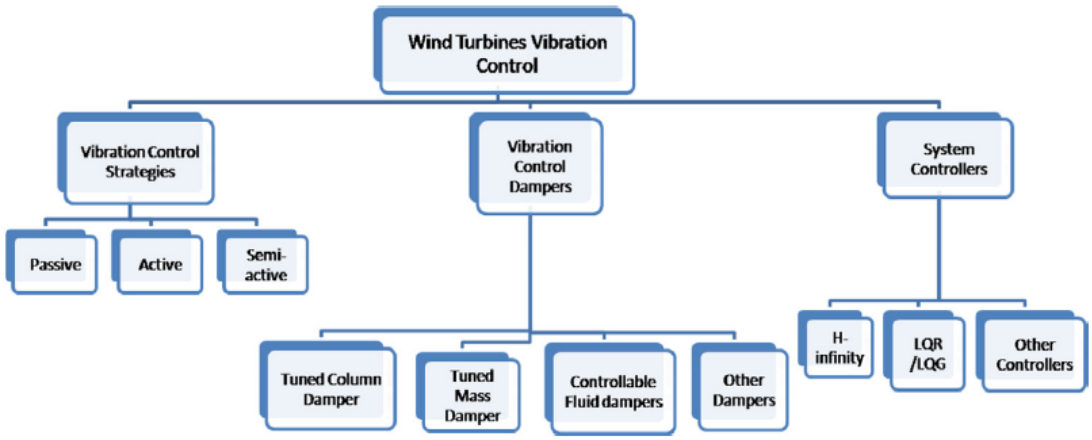

Figure 3.2.1 – Wind turbine vibration control types (63)

Passive control consists of adding one or more devices to the main structure to absorb or transfer part of its energy (65). Passive control typical mechanisms are, for example, mass dampers that control structural response transferring the main structure energy to an auxiliary mass, metallic dampers that dissipate energy while deforming themselves, and base isolation systems that uncouple structure moving from seismic soil vibrations. A passive control system does not require an external power source (66), is

easy to implement and is widely used in wind turbine systems (67). System controllers control the input of forces with the excitation amplitudes measured by sensors.

The active control mitigates the structural vibration of a system with actuators that exert forces or torques to the structure, with real-time data processors and sensors, according to a control law. The forces exerted have the same magnitude as the measure of the forces by real-time processors. Sensors can measure excitation amplitude, structural response amplitudes. Active control is another widely used alternative to control structural vibrations in wind turbines (68, 69). Figure 3.2.2 shows how the structure is controlled by a typical active control (67).

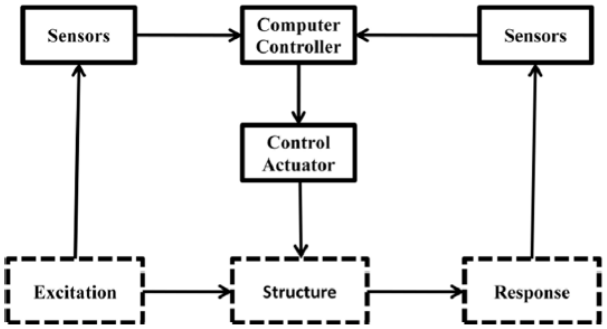

Figure 3.2.2 – Structure with active control (67)

Semi-active controllers combine the best features of active and passive controllers providing better performance. The semi-active approach has become attractive for structural vibration control applications due to controllable damping and low power requirement for operating damping devices. Its operation is similar to the active controller of fig. 3.2.2, but with an addition of a passive energy dissipater in the control actuator. This type of control makes the wind turbine more effective. Many research investigate the use of semi-active controls in wind turbines and OWT with tuned liquid dampers, or controllable fluid dampers like a magnetorheological tuned vibration absorber (70, 71, 72).

3.2.2 Vibration control dampers

A brief review and applications of some classic, pendulum, active, liquid, column-liquid, controllable-fluid tuned mass dampers are presented below:

Tuned mass damper (TMD)

The beginning of the TMD appliance to civil structures was in the sixties on high buildings, bridges, towers, and industrial chimneys to control vibrations caused by wind forces.

Later TMDs were designed for specific construction such as wind turbines. A scheme of a TMD in a wind turbine is illustrated in fig. 3.2.3.

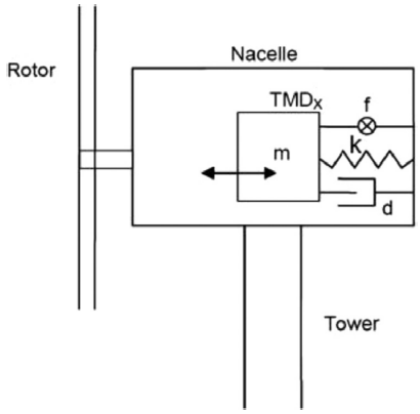

Figure 3.2.3 – Construction of a TMD in a wind turbine (67)

The TMD is a control device composed of a mass-spring-dashpot attached to the structure, aiming to reduce structural vibration response (73). A TMD tuned to the first structure natural frequency reduces substantially the response associated with the first mode vibration while little reducing or even increasing the response associated with higher modes. Moreover, a single TMD is more sensitive to discrepancies on the first natural frequency and/or damping ratio considered on the design. These limitations can be overcome by adding more than one damper, each one of them tuned to a different vibration natural frequency (74).

Extensive applications of passive devices coupled to wind turbines and OWTs have been investigated in the last years (75, 65, 76, 64, 77, 63, 67, 61, 78, 79, 80, 81, 82, 83, 3).

Murthag et al. (84) use a passive to mitigate the vibration level of a simplified wind turbine model which includes the blade/ tower interaction and a rotationally sampled turbulence.

He et al. (61) designed a TMD to suppress the vibration of a barge-type offshore floating wind turbine by using a genetic optimization.

Single (61, 80) and multiple (83) TMDs are applied in many articles in the literature. Other authors (65, 76, 64, 82) present numerical models based on open-source FAST (NREL).

A robust optimal design criterion for a single TMD device analyzing a case of structural vibration control of the main system subject to stochastic dynamic loads was proposed by Marano et al (85). The dynamic input is represented by a random base acceleration, modeled by a stationary filtered white noise process.

Bakre and Jangid (86) search for optimum TMD parameters for different damping ratios of the main system and the mass ratios of the TMD system. The applied excitation of the main system consists of an external force and base acceleration modeled as a Gaussian white-noise random process. Using the numerical searching technique, the optimum damping and tuning frequency ratio of the TMD are obtained for minimization

of various mean square responses such as relative displacement, the velocity of the main mass, and force transmitted to the support.

Lavan et al. (87) reached a multi-objective optimal design of TMDs minimizing simultaneously the structural responses, the TMD mass, and the TMD stroke.

A numerical procedure based on the MinMax method was performed by Tsai et al. (88). The design criteria are obtained through frequency response function minimization searching its minimum-maximum amplitudes. This minimization is achieved by an optimization iterative process.

Some meta-heuristic optimization methods were been used to search optimum TMD design parameters such as Genetic Algorithms (GAs) (89, 90, 91), harmony search algorithms (92), bionic algorithms (93), ant colony optimization (94), particle swarm optimization (95), and hybrid approaches such as an adaptive genetic simulated annealing method (96).

A frequency-based optimization technique (62) finds design variables such as mass, period, and damping ratio of TMD on the top of a structure using a music-inspired algorithm called harmony search.

Mohebbi et al. (97) use GAs for designing optimal Multiple Tuned Mass Dampers (MTMDs) to mitigate the seismic response of structures. They considered the parameters of TMDs as variables and aimed the minimization of the maximum structural response as an objective function while some constraints have been applied to TMDs response and parameters.

Two different optimization criteria of TMDs applied to a slender structure excited by wind load are investigated by Morga et al. (98): the reduction of the maximum displacement at the top of the structure; the reduction of the maximum inertial acceleration at the top of the structure. The wind load is defined by a superposition of the mean wind velocity and filtered white noise.

Pendulum TMD (PTMD)

One of the alternative geometries of the TMD is the PTMD device. The main structure excites the device and part of its energy is transferred by its movement and then it is dissipated by the pendulum damper. In comparison to the TMD, the pendulum length is an extra dimension used for tuning, enabling several optimal PTMD configurations. This type of damper has its vibration period depending on the length of the cable, and can only be considered a linear device when the vibration amplitudes are small.

Figure 3.2.4 shows a schematic description of PTMD. The main PTMD parameters are: the pendulum length (L_p), mass (M_p), torsional stiffness (K_p) and damping (C_p).

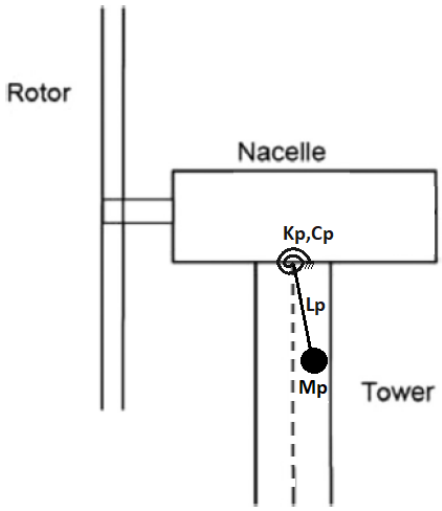

Figure 3.2.4 – Schematic description of the Pendulum-TMD

Pendulum tuned mass dampers (PTMDs) have been investigated in high-rise slender buildings due to the simplicity of installation and maintenance. Murtagh et al. (99) define optimal parameters for a PTMD to control structural vibration of slender towers by reducing the system to two degrees of freedom (2DOF): a mass-spring system with a pendulum attached.

Oliveira et al. (100) proposed a set of general dimensionless optimal parameters for a PTMD, that can be employed in the design to control any tower, subjected to deterministic or random dynamic loads, with different mass and damping ratios.

Deraemaeker and Soltani (101) introduced an analytical formula for the optimum design of the linear Pendulum Tuned Mass Damper (PTMD) coupled to an undamped primary system applying Den Hartog's equal peak method (102) to derive the optimum design. They calculated the optimum length and damping of the pendulum by using the mass ratio between the primary system and the PTMD.

Orlando and Gonçalves (103) modeled a PTMD that controls excessive vibrations in slender towers presenting a parametric analysis of non-linear oscillations of a tower-damper system, searching the best configurations to reduce vibrations and tower construction. The main structure excites the device and part of its energy is transferred by its movement and then it is dissipated by the PTMD.

Xiang and Nishitani (104) performed both experimental and numerical studies to examine the seismic performance of the pendulum-type non-traditional tuned mass damper system (PNTTMD) to control structural vibrations, founding satisfactory control of inter-story drift and floor absolute acceleration, requiring small movement space.

A similar study was presented by Gerges and Vickery (105) using a PTMD to reduce the structure RMS displacement subjected to force and accelerations simulating random excitations such as white noise. A numerical study was performed to obtain optimal parameters to a damped main system subjected to seismic and wind loads.

Guimarães et al. (106) use an inverted PTMD to reduce the vibration of a simplified offshore wind turbine model.

Sun and Jahangiri (79) developed an analytical model of the NREL monopile 5MW OWT (34) coupled with a 3D-PTMD, under the misaligned wind, wave, and seismic loading, showing that unidirectional vibration attenuation is inadequate for real applications.

Active TMD (ATMD)

The ATMD is a hybrid device consisting of a passive TMD supplemented by an actuator parallel to the spring and damper. The active element of the ATMD is controlled by the feedback of the tower top displacement and the relative velocity of the damper mass. The ATMD is a well-known concept in structural control, especially for mitigation of excessive dynamic response of high-rise buildings subjected to strong wind and earthquake loads. Brodersen (107) uses an ATMD for damping offshore wind turbine vibrations, proving that the ATMD yield enhanced damping performance compared with the passive TMD.

Tuned liquid/ column damper (TLD/TLCD)

One common device for vibration control is the TLD. It can be designed to be a passive, active, or semi-active device for structural vibration control. The Tuned Liquid Column Damper (TLCD) is a TLD variation type with a U-shaped tube filled with a volume liquid that acts as a mass of the damper, typically placed on top of the structures. The liquid volume of a TLD or TLCD oscillates by a sloshing fluid-structure interaction re-establishing the system equilibrium.

Mensah (77) uses the TLCD to improve the wind turbine tower reliability. Figure 3.2.5 shows a schematic diagram of a 5-MW wind turbine equipped with two TLCDs.

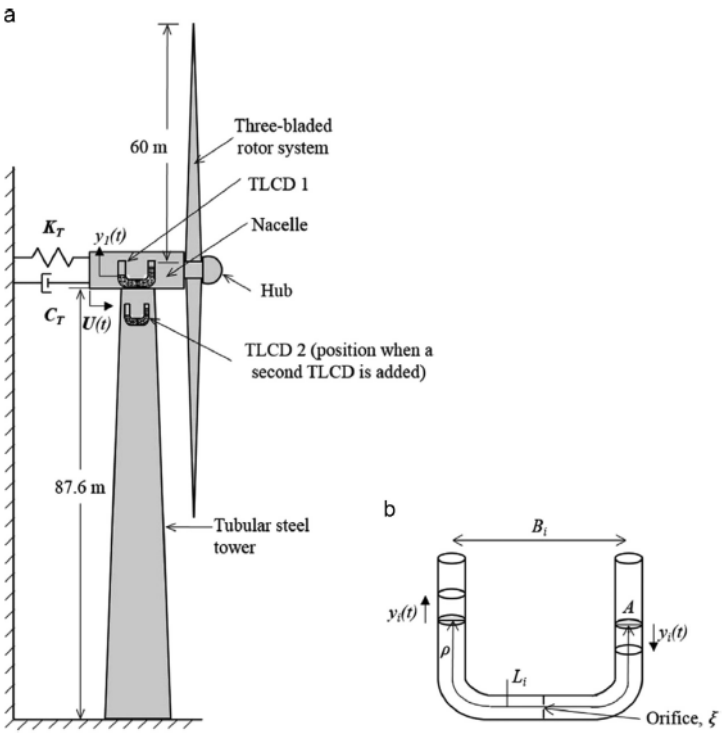

Figure 3.2.5 – (a) A schematic diagram of a 5-MW wind turbine equipped with two TLCDs (b) TLCD model (77)

Controllable fluid damper

The controllable fluid damper is semi-active devices that use controllable fluids, such as Electrorheological (ER) and Magnetorheological (MR), inside a damper for structural vibration control. ER/MR controllable fluids can change from a free-flowing state to a semi-solid state when it comes to an electric (ER) or magnetic (MR) field (67, 70).

3.3 Structural modeling for vibration control

3.3.1 Tower and PTMD 2DOF modeling approach

The equation of motion of a tower with a tip mass subjected to a distributed force $f(z,t)$ is given by

$$[m + M\delta(z-H)]\,\ddot{w}(z,t) + c\dot{w}(z,t) + EIw^{iv}(z,t) = f(z,t) \tag{3.3.1}$$

where $\ddot{w}(z,t)$ is a second partial derivative with respect to time t, $w^{iv}(z,t)$ is a fourth partial derivative with respect to z, EI is the bending stiffness, m and M are the mass per unit length of the beam and the tip mass, respectively, and c is the viscous-damping coefficient. The Dirac delta $\delta(z-H)$ is used to apply the tip mass M at the tower height H, where z is the position along tower axis.

To reduce the tower dynamic system (3.3.1) to a SDOF, we assume the following separated space-time transversal displacement function in terms of $w(z,t) \cong w_h(z,t) =$

$\psi(z)y(t)$, where $y(t)$ is the tip transversal displacement, and $\psi(z) = 1 - \cos(\pi z/2H)$ is the assumed shape function.

Substituting the assumed function shape $w_h(z,t)$ into equation (3.3.1), Avila et al. (108) obtained the equivalent-SDOF dynamic system governed by

$$M_s\ddot{y}(t) + C_s\dot{y}(t) + K_s y(t) = F_s(t) \tag{3.3.2}$$

where the equivalent stiffness K_s, damping C_s and mass M_s of the SDOF are respectively represented by:

$$K_s = \int_0^H EI[\psi''(x)]^2 dx = \int_0^H EI\frac{\pi^4}{16H^4}\cos^2\left(\frac{\pi x}{2H}\right)dx \quad \therefore\ K_s = \frac{EI\pi^4}{32H^3} \tag{3.3.3}$$

$$C_s = \int_0^H c\psi^2(x)dx = \int_0^H c\left[1 - \cos\left(\frac{\pi x}{2L}\right)\right]^2 dx \quad \therefore\ C_s = \frac{cL}{2\pi}(3\pi - 8) \tag{3.3.4}$$

$$M_s = M + \int_0^H m\psi^2(x)dx = M + \int_0^H m\left[1 - \cos\left(\frac{\pi x}{2L}\right)\right]^2 dx$$

$$\therefore\ M_s = \frac{mL}{2\pi}(3\pi - 8) + M \tag{3.3.5}$$

Additionally, the equivalent force representing a discrete harmonic force $f(z,t) = F_0\delta(z - H)\sin(nt)$ on tower top is computed as:

$$F_s(t) = \int_0^L f(z,t)\psi(x)dx \qquad \therefore F_s(t) = F_0 sin(nt)\cdot\psi(H) \tag{3.3.6}$$

The PTMD is attached to the SDOF falling into a 2DOF discrete system described by Fig. 3.3.1 (73).

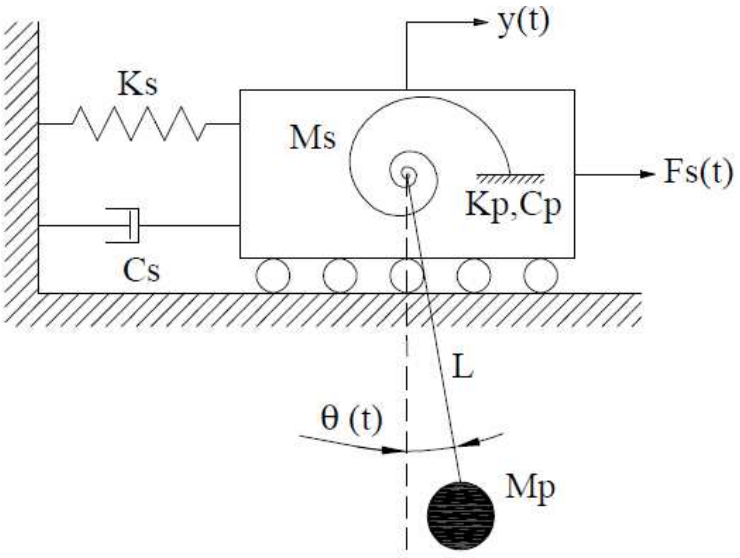

Figure 3.3.1 – Structure with a linear pendulum attached (2DOF) excited by a force $F_s(t)$.

The equations of motion of the 2DOF system are given by

$$\begin{aligned}(M_s + M_p)\ddot{y} + M_p L_p\ddot{\theta} + C_s\dot{y} + K_s y &= F_s(t)\\ M_p L_p\ddot{y} + M_p L_p^2\ddot{\theta} + C_p\dot{\theta} + (K_p + M_p g L_p)\theta &= 0\end{aligned} \tag{3.3.7}$$

These equations can be rewritten in a matrix form as follows.

$$\begin{bmatrix} (M_s + M_p) & M_p L_p \\ M_p L_p & M_p L_p^2 \end{bmatrix} \begin{bmatrix} \ddot{y} \\ \ddot{\theta} \end{bmatrix} + \begin{bmatrix} C_s & 0 \\ 0 & C_p \end{bmatrix} \begin{bmatrix} \dot{y} \\ \dot{\theta} \end{bmatrix} + \\ + \begin{bmatrix} K_s & 0 \\ 0 & (K_p + M_p g L_p) \end{bmatrix} \begin{bmatrix} y \\ \theta \end{bmatrix} = \begin{bmatrix} F_s(t) \\ 0 \end{bmatrix} \tag{3.3.8}$$

where M_s is the main equivalent mass; C_s is the main equivalent damping; K_s is the main equivalent stiffness; M_p is the pendulum mass; C_p is the pendulum damping; K_p is the pendulum stiffness; L is the cable length; g is the gravity acceleration; $F_s(t) = F_{s0}e^{int}$ is the excitation modal force; $y(t)$ is the main system displacement; and $\theta(t)$ is the pendulum angular displacement.

Considering $F_s(t) = e^{int}$, $y(t) = H_y(n)e^{int}$ and $\theta(t) = H_\theta(n)e^{int}$, (3.3.8) can be rewritten by the linear equation system (3.3.9).

$$\begin{bmatrix} A_{11} & A_{12} \\ A_{21} & A_{22} \end{bmatrix} \begin{bmatrix} H_y(n) \\ H_\theta(n) \end{bmatrix} = \begin{bmatrix} 1 \\ 0 \end{bmatrix} \tag{3.3.9}$$

where $H_y(n)$ and $H_\theta(n)$ are respectively the structure and the pendulum frequency transfer function:

$$A_{11} = -(M_s + M_p)n^2 + C_s in + K_s,$$

$$A_{12} = A_{21} = -M_p L_p n^2,$$

$$A_{22} = -M_p L_p^2 n^2 + C_p in + (K_p + M_p g L_p).$$

Oliveira *et al.* (100) solved the linear equation system (3.3.9) given the frequency transfer functions $H_y(n)$ (3.3.10) and $H_\theta(n)$ (3.3.11).

$$H_y(n) = \frac{A_{y0} + A_{y1}n + A_{y2}n^2}{B_0 + B_1 n + B_2 n^2 + B_3 n^3 + B_4 n^4} \tag{3.3.10}$$

$$H_\theta(n) = \frac{A_{\theta 0} + A_{\theta 1}n + A_{\theta 2}n^2}{B_0 + B_1 n + B_2 n^2 + B_3 n^3 + B_4 n^4} \tag{3.3.11}$$

where

$$A_{y0} = L_p M_p g + K_p;\ A_{y1} = iC_p L_p^2;\ A_{y2} = -L_p^2 M_p;$$

$$A_{\theta 0} = 0;\ A_{\theta 1} = 0;\ A_{\theta 2} = L_p M_p;$$

$$B_0 = K_s(K_p + L_p M_p g);\ B_1 = i(C_s K_p + C_p K_s L_p^2 + C_s L_p M_p g);$$

$$B_2 = -(K_p M_p + K_p M_s + C_p C_s L_p^2 + K_s L_p^2 M_p + L_p M_p^2 g + L_p M_p M_s g);$$

$$B_3 = -iL_p^2(C_p M_s + C_s M_p + C_p M_p);\ B_4 = L_p^2 M_p M_s.$$

3.3.2 Offshore wind turbine and PTMD FEM model

This section presents the procedures to obtain the dynamic structural response of the OWT+PTMD model using the FEM following the detailed specifications of Phase I (monopile type) of the NREL 5-MW OWT by Jonkman et al. (34).

3.3.2.1 Dynamic Structural Response

As said before, structural analysis in the frequency domain can be performed to evaluate the dynamic response of OWTs subjected to both the environmental and rotating blade actions. Following Davenport (109), the peak response r_p of the structure is expressed in terms of its mean value (r_m) generated by the mean wind (including the VS effect on the tower) and by sea current, and the response standard deviation (σ_r), which is related to the effects of the turbulent wind and the waves, by making use of the response peak factor g_r, as reported in eq. 3.3.12. The soil-structure interaction is not considered in this paper (the structure is assumed to be fully restrained at the seabed).

$$r_p(h) = r_m + g_r \cdot \sigma_r(h) \tag{3.3.12}$$

where σ_r is the response deviation and the peak factor is computed by

$$g_r = \sqrt{2\ln\left(\eta_{cr} \cdot T_{wind}\right)} + \frac{0.577}{\sqrt{2\ln\left(\eta_{cr} \cdot T_{wind}\right)}} \tag{3.3.13}$$

where η is the cycling rate of effective frequency for the response (taken equal to the first eigenfrequency of the system) and T_{wind} is the time interval over which the maximum value is evaluated.

Operatively, the r_m is computed by a static analysis with the application of the maximum values of the forces or of the displacements evaluated in previous equations for the mean wind (equation 2.2.59), for the vortex shedding effects (eqs. 2.2.80 which directly computes the response, and 2.3.63 by assuming herein $\cos(-) = 1$) and for the sea current (equation 2.3.47), while σ_r can be evaluated by a PSD analysis by applying the power spectra of waves' force (equation 2.3.57) and of turbulent wind components as sampled by rotating blades (eq. 2.2.79), as the area underpinned by the response PSD for the response parameter r (6), which in the following sections will be the displacement at the hub of the OWT.

3.3.2.2 3D OWT+PTMD FEM model

In order to create the FE model, an integrated MATLAB®/ ANSYS® APDL routine create samples of wave and wind rotational spectra, as well the hydrodynamic and aerodynamic loads over the structure. A flowchart represents the ANSYS®/ MATLAB® integrated routines for the global 3D Finite Element analysis of the OWT (eventually provided with the PTMD) is shown in fig. 3.3.2.

Square shapes in the flowchart stand for routines, while rhomboidal shapes stand for input/output data. The flux of the analyzes is represented in the vertical direction, while the flux of the data is represented in the horizontal one.

Initial input (left side column) regards the environmental conditions concerning the wind and the hydrodynamic fields chosen for the analysis, these includes the wind

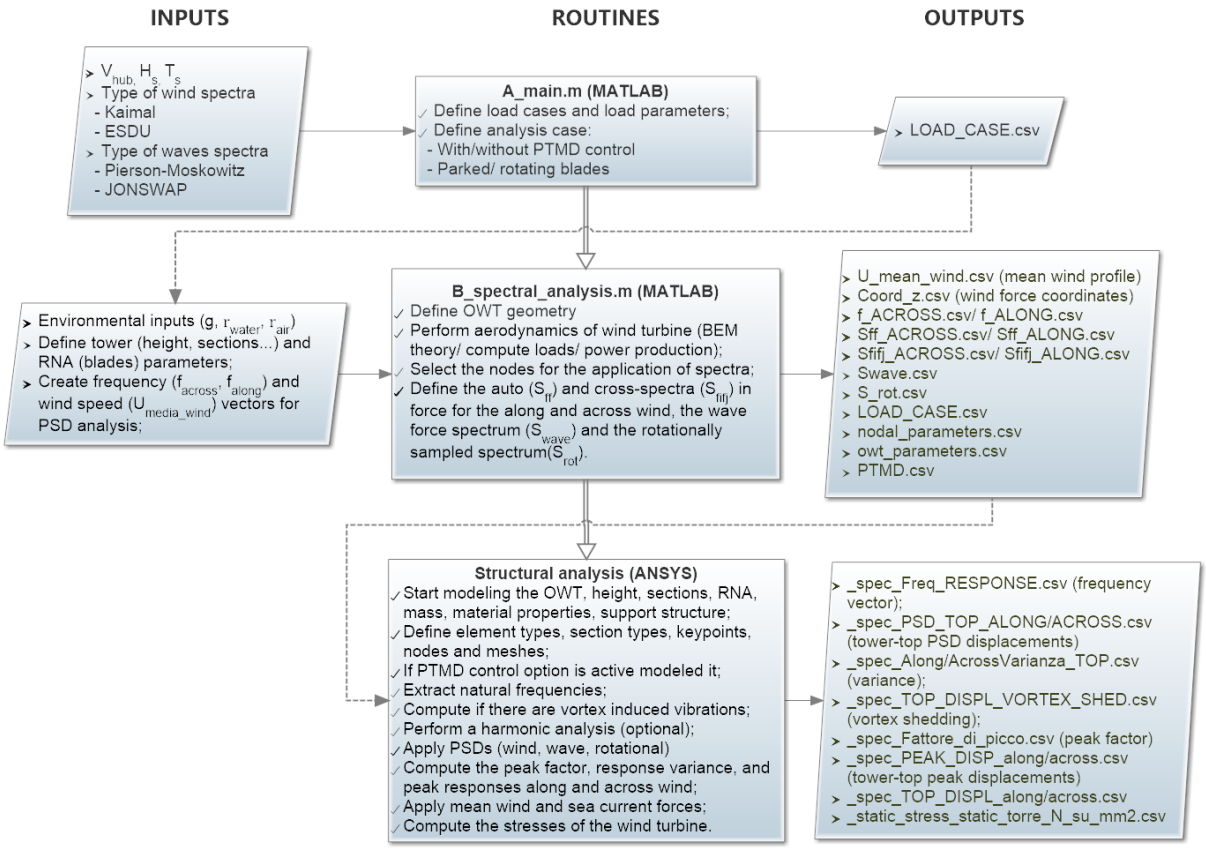

Figure 3.3.2 – Flowchart of the integration between ANSYS and MATLAB routines

velocity at the hub height, the waves height and the waves period. These inputs are passed to a MATLAB® routine defining the load cases first (e.g. parked or rotating blades) and the load spectra later (PSDs of the wind and waves), together with the turbine geometry parameters and saves all these data to a file before launching the ANSYS® routine who performs the structural analyzes (static+modal+PSD) and returns back to MATLAB® the PSD and the mean values of the response parameters for final computation (in MATLAB®) of the peak response.

The gross properties of the NREL baseline OWT modeled are shown in Table 3.1, while a schematic representation of the FE model developed in ANSYS is shown in Figure 3.3.3.

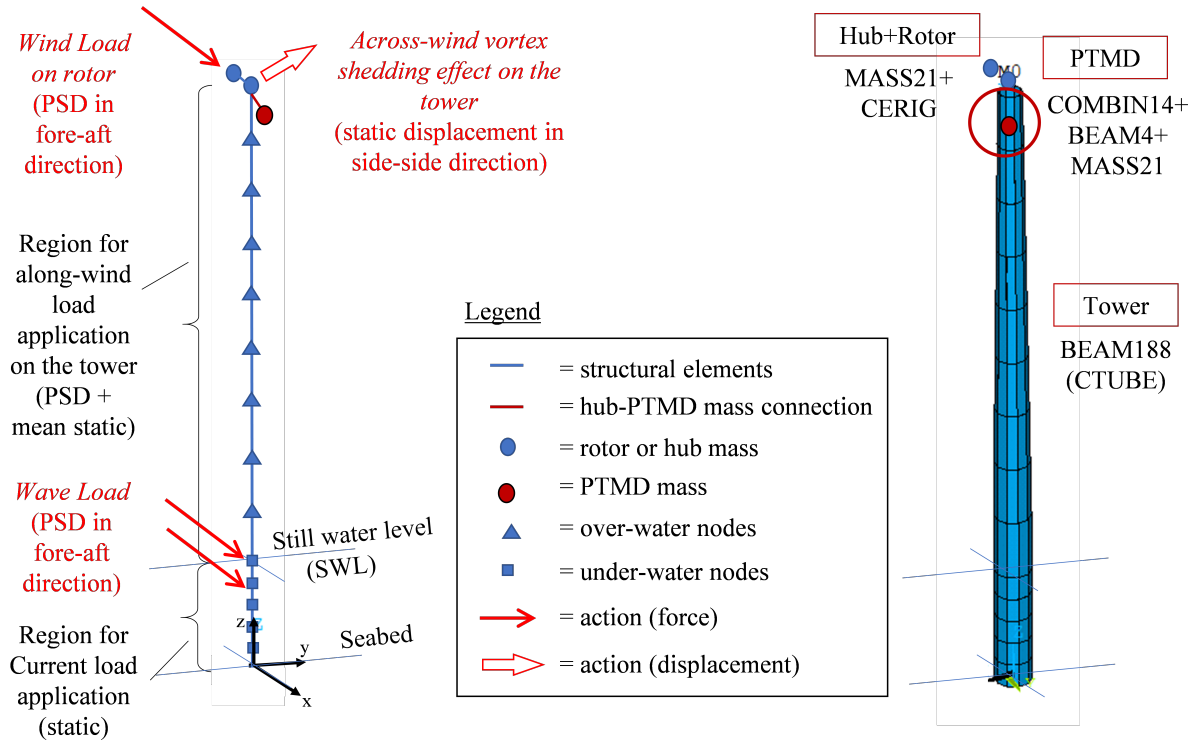

Figure 3.3.3 – Schematic description of the FE model of the OWT developed in ANSYS. Nodes and loads (left); type of FE used (right).

BEAM188 element type is used for the tower and the submerged monopile, and a CTUBE tapered section connects the bottom and the tip of the tower considering the thickness variation along the height. The Rotor-Nacelle Assembly (RNA) is modeled by two MASS21 elements, one for the hub (connected to the tower-top with a rigid CERIG command) and other for the nacelle (with a COMBIN14 connection to a tower-top). The PTMD was modeled using a rigid connector (BEAM4) of length Lp, and a MASS21 connected with a COMBIN14 torsional spring at the tower-top.

To analyze the stochastic aerodynamic loads of blades in the frequency domain, the rotationally sampled spectrum (27) is applied at the hub node. The wind turbulent model along the tower follows the Kaimal spectrum together with its respective coherence, and was applied along the 10 nodes of the tower, while the wind-induced vortex shedding effect r_{across}^{VS} (eq. 2.2.80) was added to the mean value of the peak response in the across-wind (side-side) direction. r_{across}^{VS} was imposed to the node located at the hub height, when the wind velocity V_m herein (U_{hub}) falls within reduced velocity range of $0.8/S_t < V_R < 1.6/S_t$, being V_R the reduced velocity defined as (46):

$$V_R = \frac{U_{hub}}{f_n D} \tag{3.3.14}$$

where f_n is the first natural frequency of the tower in the side-side direction. The waves spectral density S_η is represented by the JONSWAP spectrum. The wave force PSD (eq. 2.3.57) is applied at the two nodes located at- and below- the SWL.

3.3.3 Offshore wind turbine and PTMD spectral element model

The SEM is a practical and accurate technique to analyze the dynamic behaviors of structures. It is formulated in the frequency domain and the structural element interpolation function is the exact analytical solution of the differential equation. Hence, the number of elements required for a spectral model will coincide with the number of discontinuities in the structure. This section presented the use of SEM to model a wind turbine composed of the wind rotor and nacelle supported by a high and slender tower coupled with a PTMD. Therefore, it is also demonstrated in the PTMD spectral model formulation.

3.3.3.1 Beam spectral element

The fundamental equation for the flexural motion in a beam is presented in this section. Figure 3.3.4 shows an elastic two-node beam element with a uniform cross-section.

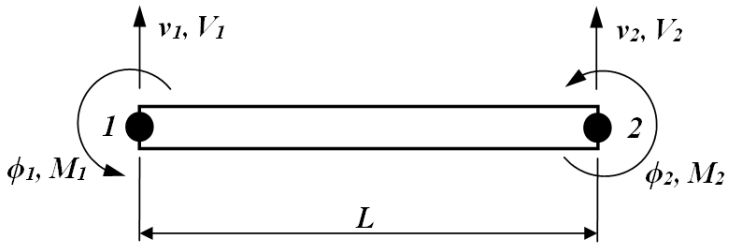

Figure 3.3.4 – Two-node beam spectral element.

The undamped Euler-Bernoulli beam equation of motion under bending vibration is given by

$$EI\frac{\partial^4 v(x,t)}{\partial x^4} + \rho A\frac{\partial^2 v(x,t)}{\partial t^2} = q(x,t) \tag{3.3.15}$$

and spectral representation gives

$$EI\frac{d^4\hat{v}}{dx^4} + n^2\rho A\hat{v} = q(x,t)$$

where E ,I, ρ, A are Young's modulus, inertia moment, mass density per unit length, and cross-section area, respectively; $v(x,t)$ is the transversal displacement and $q(x,t)$ external load. A structural internal damping is introduced into the beam formulation by adding into the variable $(E \cdot I)$ a deterministic part $(E_0 \cdot I_0)$ weighted by a complex damping factor $(i\eta, i = \sqrt{-1})$, to obtain $EI = E \cdot I + (E_0 \cdot I_0)i\eta$. By considering the homogeneous differential equation with constant properties along the beam length, the spectral form of equation (3.3.15) became:

$$\frac{d^4\hat{\mathbf{v}}}{dx^4} - k^4\hat{\mathbf{v}} = 0, \tag{3.3.16}$$

where the wavenumber is

$$k^4 = n^2\frac{\rho A}{EI}. \tag{3.3.17}$$

By considering solutions of the form $e^{-i\beta x}$, the wave number relates with propagating and evanescent waves are $k = \pm\beta$ and $k = \pm i\beta$ respectively. For the spectral Euler-Bernoulli beam element of length L, the general solution of equation. (3.3.16) can be obtained of the form

$$v(x,n) = a_1 e^{-ikx} + a_2 e^{-kx} + a_3 e^{-ik(L-x)} + a_4 e^{-k(L-x)} \tag{3.3.18}$$

$$= \mathbf{s}(x,n)\mathbf{a} \tag{3.3.19}$$

where

$$\mathbf{s}(x,n) = \left\{e^{-ikx}, e^{-kx}, e^{-ik(L-x)}, e^{-k(L-x)}\right\},$$
$$\mathbf{a}(x,n) = \{a_1, a_2, a_3, a_4\}^T \tag{3.3.20}$$

The spectral nodal displacements and slopes of the beam element are related to the displacement field at node 1 ($x = 0$) and node 2 ($x = L$), by

$$\mathbf{d} = \begin{bmatrix} v_1 \\ \phi_1 \\ v_2 \\ \phi_2 \end{bmatrix} = \begin{bmatrix} v(0) \\ v'(0) \\ v(L) \\ v'(L) \end{bmatrix} = \begin{bmatrix} s(0,n) \\ s'(0,n) \\ s(L,n) \\ s'(L,n) \end{bmatrix} \mathbf{a} = \mathbf{G}(n)\mathbf{a} \tag{3.3.21}$$

where

$$\mathbf{G}(n) = \begin{bmatrix} 1 & 1 & e^{-ikL} & e^{-kL} \\ -ik & -k & ie^{-ikL}k & e^{-kL}k \\ e^{-ikL} & e^{-kL} & 1 & 1 \\ -ie^{-ikL}k & -e^{-kL}k & ik & k \end{bmatrix} \tag{3.3.22}$$

The frequency-dependent displacement within an element is interpolated from the nodal displacement vector $\mathbf{d}$ by eliminating the constant vector $\mathbf{a}$ from equation (3.3.21) it is expressed as

$$v(x,n) = \mathbf{g}(x,n)\mathbf{d} \tag{3.3.23}$$

where the shape function is

$$\mathbf{g}(x,n) = \mathbf{s}(x,n)\mathbf{G}^{-1}(n) = \mathbf{s}(x,n)\mathbf{\Gamma}(n) \tag{3.3.24}$$

Considering that $\rho A n^2 = EIk^4$ and substituting in equation. 3.3.15, the weak form can be derived from weight-integral to obtain the dynamic stiffness matrix for the two-nodes beam element by,

$$\mathbf{S}_b(n) = EI\left[\int_0^L \mathbf{g}''(x)^T\mathbf{g}''(x)dx - k^4\int_0^L \mathbf{g}(x)^T\mathbf{g}(x)dx\right] \tag{3.3.25}$$

where $'$ express the spatial partial derivative. Solving the integral the dynamic stiffness matrix.

3.3.3.2 Nodal representation of distributed load

The distributed load was incorporated into the spectral beam formulation as presented in Doyle (8). To determine the contribution of the distributed load to the dynamic stiffness matrix the procedure is to also multiply the force $q(x)$ by the form function $\mathbf{g}(x)$ and integrating over the limits, it has

$$EI\left[\int_0^L \mathbf{g}''(x)^T\mathbf{g}''(x)dx - k^4\int_0^L \mathbf{g}(x)^T\mathbf{g}(x)dx\right] = \int_0^L \widehat{q}(x)\mathbf{g}^T(x)\mathbf{g}(x)dx, \tag{3.3.26}$$

Thus, the stiffness ratio for the beam with a distributed load can be written as

$$\mathbf{S}_b(n)\mathbf{d} = \widehat{\mathbf{F}} + \int_0^L \widehat{q}(x)\mathbf{g}^T(x)\mathbf{g}(x)dx. \tag{3.3.27}$$

where $\widehat{\mathbf{F}}$ represents the externally applied node forces. In SEM a uniform structural element is discretized in case there are discontinues along the structure and the number of an element will follow the number of discontinuities, such as point of loads or damage. Otherwise, it can be modeled by a single spectral element with very accuracy (8). Analogous to FEM, the SEM can be assembled to form a global structure matrix system (9).

3.3.3.3 Wind tower spectral model

The NREL 5MW monopile OWT was adopted in this case of study. The beam spectral element summarized in section 3.3.3.1 was used to model the slender tower and a lumped mass represented the rotor and nacelle, as illustrated in Fig. 3.3.5.

Regarding the traveling waves aspect, the nacelle on the tower top can be considered as an obstruction in the tower traveling waves, which is assumed as a boundary. The incident wave generates a reflected wave in such a way that the two waves superpose at the boundary to satisfy the boundary conditions. To satisfy the boundary conditions associated with the known incident wave and reflected wave (8), the nacelle is modeled by a lumped mass expressed as

$$EI\frac{\partial^3 v(x=L,t)}{\partial x^3} = m_n\frac{\partial^2 v(x=L,t)}{\partial t^2} \tag{3.3.28}$$

The OWT model composed of a beam with a lumped mass m_n connected in one-end. By adding the lumped mass given in eq. 3.3.28 into 3.3.15, the equation of motion that represents the OWT will be,

$$EI\frac{\partial^4 v(x,t)}{\partial x^4} + \rho A\frac{\partial^2 v(x,t)}{\partial t^2} + m_n\frac{\partial^2 v(x=L,t)}{\partial t^2} = q(x,t) \tag{3.3.29}$$

in the spectral representation it has,

$$EI\frac{d^4\hat{v}}{dx^4} + n^2(\rho A + \tilde{m}_n)\hat{v} = q(x,t)$$

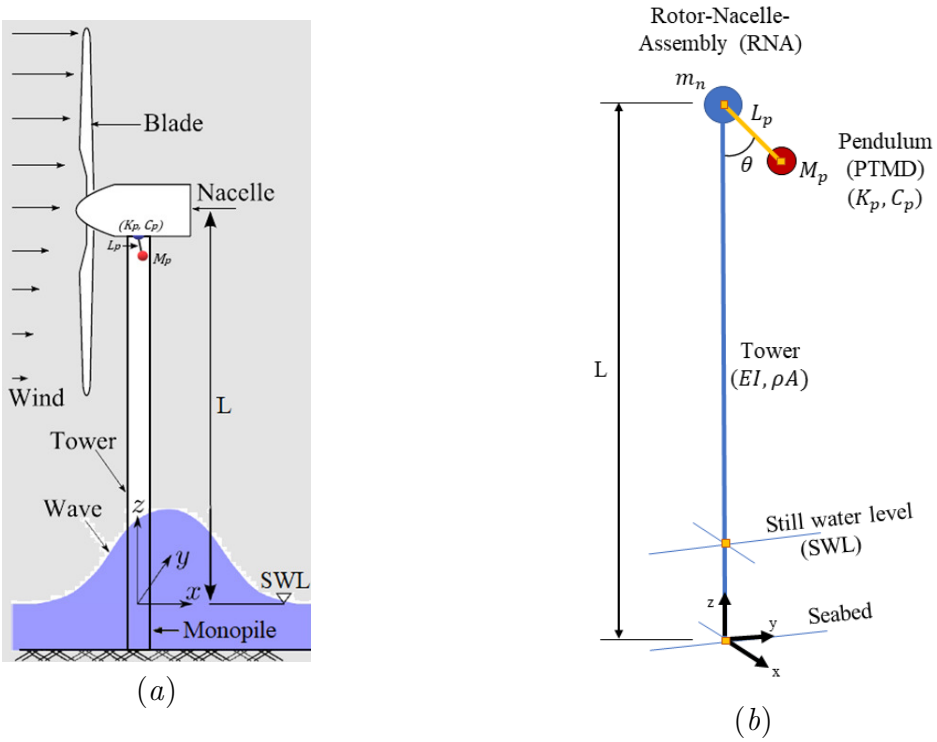

Figure 3.3.5 – OWT representation: a) Draft model (79, adapted); b) Mechanical model.

where $\tilde{m}_n = m_n EI\beta^3$. The presence of the mass makes the reflection and transmission frequency dependent. Therefore, the mass will act as a filter. Low frequencies will not overpass the mass while very high frequency terms will be attenuated. By assembling the OWT it was used a beam and a lumped mass in its end by using the spectral form of each element, which gives the following global OWT spectral matrix:

$$\begin{aligned}\mathbf{S}_{\text{OWT}}(n) &= \mathbf{S}_b(n) + S_{m_n}(x = L, n) \\ &= \begin{bmatrix} S_b(1,1) & S_b(1,2) & S_b(1,3) & S_b(1,4) \\ S_b(2,1) & S_b(2,2) & S_b(2,3) & S_b(2,4) \\ S_b(3,1) & S_b(3,2) & S_b(3,3) + S_{m_n} & S_b(3,4) \\ S_b(4,1) & S_b(4,2) & S_b(4,3) & S_b(4,4) + S_{m_n} \end{bmatrix}\end{aligned} \tag{3.3.30}$$

where $S_{m_n} = -n^2\tilde{m}_n$. Upon, the dynamic properties of the spectral OWT model are introduced regarding the equivalent parameters, the vibration analysis can be easily performed by using the well established spectral element analysis.

3.3.3.4 PTMD coupled to the OWT spectral model

Gerges and Vickery (105) design an optimum PTMD for the vibration mode attached to a primary structure modeled as a single-degree of freedom (SDOF) system with a generalized mass M_s, damping C_s, stiffness K_s, and force F_s. Some authors (110, 111, 73, 112, 108) have modeled the tower with PTMD coupled with an assumed-mode technique where the tower is reduced to a single-degree-of-freedom system (SDOF) by assuming an arbitrary shape function as demonstrated in Fig. 3.3.6.

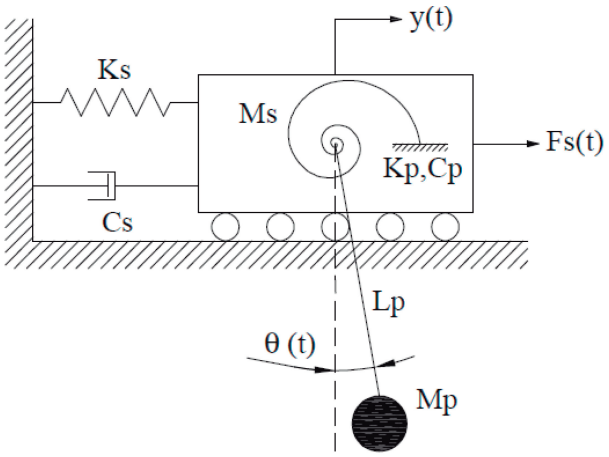

Figure 3.3.6 – Structure with a linear pendulum attached (2DOF) excited by a force $F_s(t)$ (19)

The equation of motion of the pendulum-type tuned mass dampers were formulated by Gerges and Vickery (105) mixing translational and rotational, two-degree of freedom dynamic system with a force applied to the translational degree of freedom. To connect the PTMD with the entire tower it has the following governing equations of motion,

$$\begin{aligned} &EI\frac{\partial^4 v(x,t)}{\partial x^4} + C_s\frac{\partial v(x,t)}{\partial t} + \rho A\frac{\partial^2 v(x,t)}{\partial t^2} + m_n\frac{\partial^2 v(x,t)}{\partial t^2} + L_p M_p\frac{\partial^2 \theta(x,t)}{\partial t^2} = q(x,t) \\ &L_p M_p\frac{\partial^2 v(L,t)}{\partial t^2} + L_p^2 M_p\frac{\partial^2 \theta(x,t)}{\partial t^2} + C_p\frac{\partial \theta(x,t)}{\partial t} + (K_p + M_p g L_p)\theta = 0 \end{aligned} \tag{3.3.31}$$

where v is the vertical displacement and θ is the rotation of the auxiliary system, M_p, C_p, and K_p are the auxiliary system mass moment of inertia, mass, equivalent translational damping and stiffness, respectively, h is the distance between the spring/damper attachment point ant the pivot point, while L_p is the distance between the center of mass and the pivot point. The spectral form of the PTMD coupled to the OWT will be,

$$\begin{aligned} &EI\frac{d^4\hat{v}}{dx^4} - n^2(\rho A + \tilde{m}_n)\hat{v} - n^2 M_p L_p\hat{\theta} = q(x,t) \\ &- n^2 M_p L_p^2\hat{\theta} - n^2 M_p L_p\hat{v} + inC_p\hat{\theta} + (K_p + M_p g L_p)\hat{\theta} = 0 \end{aligned} \tag{3.3.32}$$

For the entire tower with PTMD coupled, the wind tower spectral model presented in section 3.3.3.3 was used. As in the model proposed by Gerges and Vickery (105), the PTMD is coupled at tower node 3, as illustrated in Fig. 3.3.7. The PTMD must be formulated in a spectral form because the tower is modeled using SEM. Hence, the PTMD composed of an adapted torsional stiffness (K_p), damping (C_p), and mass (M_p), can be written in a spectral form as

$$S_{\text{PTMD}}(n) = \begin{bmatrix} -n^2(M_s + M_p) + inC_s + K_s & -n^2 M_p L_p \\ -n^2 M_p L_p & -n^2 M_p L_p^2 + inC_p + (K_p + M_p g L_p) \end{bmatrix} \tag{3.3.33}$$

where $K_s = EI\pi^4/(32L^3)$, $M_s = \rho AL(3\pi - 8)/(2\pi) + m_n$, and $C_s = cL(3\pi - 8)/(2\pi)$ (viscous damping coefficient c) are the structure equivalent rigidity, mass, and damping,

respectively (19). The OWT with active PTMD control in a general spectral form followed the tower model. The PTMD element was attached to the tower in node 3, as showed in Fig. 3.3.7. Analogous to FEM, the SEM can be assembled to form a global structure matrix system. Thus, the global spectral element matrix for the PTMD coupled to the OWT is given by,

$$\mathbf{S}(n) = \mathbf{S}_{\mathrm{OWT}}(n) - \mathbf{S}_{\mathrm{PTMD}}(x = L, n) \tag{3.3.34}$$

where the PTMD is connected on the vertical and rotational tower tip DOF.

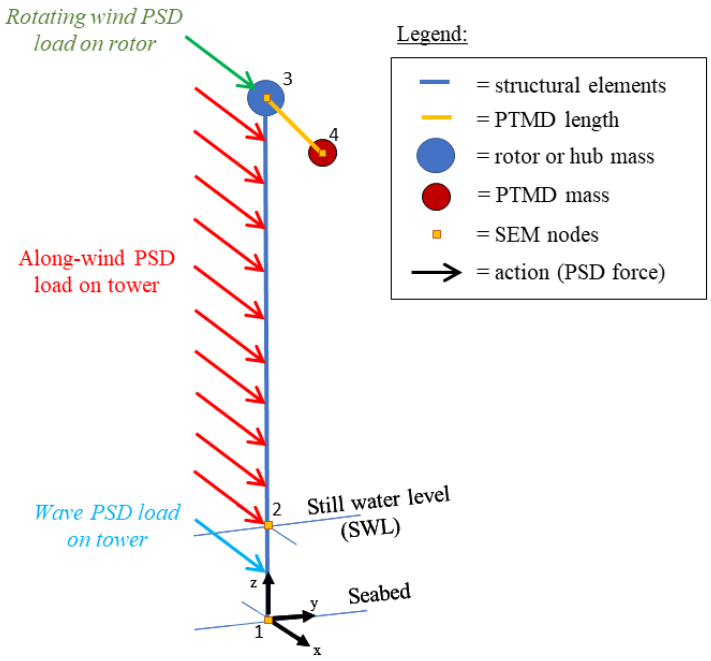

Figure 3.3.7 – Schematic representation of the OWT+PTMD SEM model

To simulate the OWT environment and analyze its dynamic behavior, it included the power spectrum of the stochastic component of actions due to turbulent wind and waves in operating conditions, considering the blade characteristic (including the number of blades, chord, airfoil, and the twist of the rotor geometry) of the 5 MW-NREL OWT model (34), disregarding the soil effects. The PSD due to rotating condition is evaluated at the blade root bending moment following the theory presented by Burton (27). The PSD of environmental action of wind and waves are evaluated regarding Kaimal and JONSWAP spectra, respectively. The rotationally sampled spectrum on blades and the wind and wave spectra analytical background are presented in sec. 2.4.

4 Case studies

In this chapter three case studies (table 4) are presented and compared with models found on literature and also between them. Case study 1 models a simplified tower with a tip mass, and case studies 2 and 3 model the mentioned OWT. All cases presents the amplitude response with and without the PTMD controller.

Table 4.0.1 – Case studies

Case study 1	2DOF model of tower
Case study 2	FEM model of OWT
Case study 3	SEM model of OWT

4.1 Case study 1: 2DOF model of an optimal PTMD design applied to a tower

In this case study, a PTMD is evaluated to obtain the best performance when attached to a tall, flexible, slender tower. Using an assumed-mode technique, the tower (with multiple degrees of freedom - MDOF) is reduced to a single-degree-of-freedom system (SDOF) assuming an arbitrary shape function (sec. 3.3.1) (110, 111, 73, 112, 108). This equivalent SDOF represents the behavior of a dynamic continuous system with distributed mass and stiffness. The analytical background of the 2DOF model is presented on Section 3.3.1.

After obtaining all the optimum parameters, such as pendulum length (L_p), pendulum mass (M_p), pendulum damping (C_p), and pendulum stiffness (K_p), the displacement on the top of tower can be substantially reduced.

Figure 4.1.1 reveals the impact of a PTMD on the Murtagh *et al.* (99) tower. The graphic shows the frequency response of the control and uncontrolled Murtagh *et al.* (99) tower. Previously, Murtagh et al. (99) evaluated a steel tower that had a height of 60 meters, an outer diameter of 3 m and a thickness of 15 mm without control. The authors used a tower with a mass of $M = 66,253.13$ kg, nacelle plus blades represented by a mass of $m = 19,876.00$ kg, and a value of flexural stiffness of $EI = 3.29 \times 10^{10}$ Nm^2. The generalized stiffness $K_s = 463,671.26$ N/m and mass $M_s = 34,899.60$ kg were obtained using equations (3.3.3) and (3.3.5). The tower damping was considered negligible ($C_s \approx 0$).

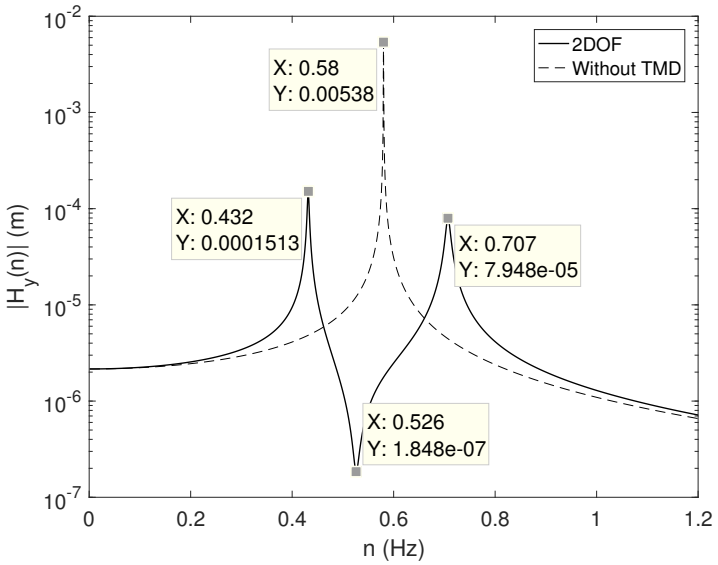

Figure 4.1.1 – Case Example: Tower FRF with and without PTMD

Some PTMDs are based on viscous (101) or friction damping (113), but the current case study is limited to PTMDs with friction dampers. The 2DOF model proposed taking into account the torsional stiffness and damping as $K_p = 1.2479$ MNm/rad and $C_p = 9.0249$ kNms/rad, respectively (114), the mass ratio was $\mu = M_p/M_s = 0.2636$ ($M_p = 9198.6$ kg), and the pendulum length was $L_p = 4$ m.

Five steps toward the PTMD optimum design are suggested as follows:

- 1st step: The system is analyzed first without control (1DOF) and then with the PTMD attached (2DOF) to compare both dynamic responses (fig. 4.1.1);
- 2nd step: The PTMD damping influence is observed by a parametric analysis;
- 3rd step: The PTMD stiffness influence is analyzed by a parametric analysis;
- 4th step: The optimization problem is built to be handled by a toolbox algorithm. The fitness function is the min/max of the frequency response, and the design variables are the pendulum length and mass ratio of PTMD.
- 5th step: The best design of PTMD is identified and compared with Shzu et al.'s results (115), so the toolbox algorithm is validated.

4.1.1 Sensitivity Analysis

To analyze the sensitivity of the torsional damping over the dynamic effects of the structure, two cases $C_p = \{5; 15\}$ kNms/rad are considered using torsional stiffness $K_p = 1.2479$ MNm/rad, mass ratio $\mu = 0.26$ and pendulum length $L_p = 4.38$ m, proposed

by Shzu et al. (115). Both designs presented a similar shape of response map. However, the frequency response increases as damping decreases, as shown in fig. 4.1.2.

- For $C_p = 5$ kNms/rad $\rightarrow H_y = 1.1 \cdot 10^{-4}$ m.
- For $C_p = 15$ kNms/rad $\rightarrow H_y = 0.7 \cdot 10^{-4}$ m.

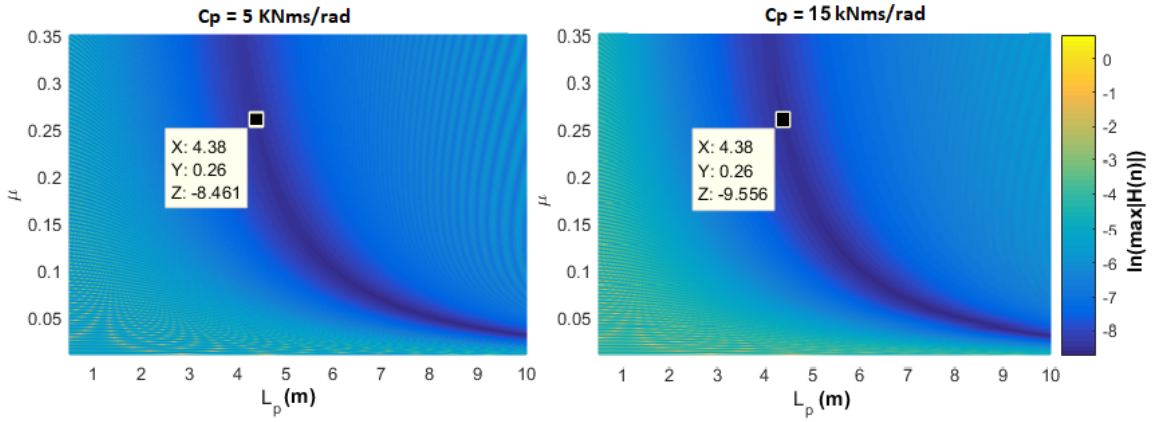

Figure 4.1.2 – Response map for $C_p = \{5; 15\}$ kNms/rad

The torsional stiffness value used is equal to $K_p = \{0.5; 1.5\}$ MNm/rad, and the same damping ($C_p = 9.0249$ kNms/rad) and mass ratio ($\mu = 0.26$) submitted by Shzu et al. are used (115).

- For $K_p = 0.5$ MNm/rad $\rightarrow H_y = 5.5 \cdot 10^{-5}$ m.
- For $K_p = 1.5$ MNm/rad $\rightarrow H_y = 13.8 \cdot 10^{-5}$ m.

It is observed that the geometric valley shifts to the right on the L_p vs. μ plan. When the stiffness K_p increases, the response value peaks $H_y(n)$ also increase, as shown in fig. 4.1.3.

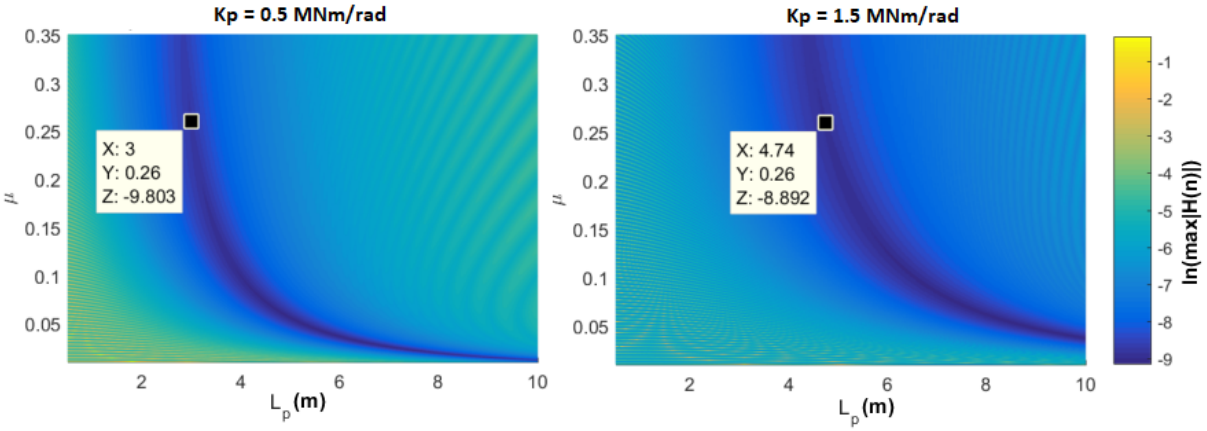

Figure 4.1.3 – Response map for $K_p = \{0.5; 1.5\}$ MNm/rad

4.1.2 GA optimization results

The GA toolbox (19) minimizes the frequency response peaks of the tower described in the analytical 2DOF model (eq. 3.3.10). The fitness function minimizes $H_y(n)$, maximizing its inverse as shown in eq. 4.1.1.

$$f_{\text{fitness}} = \frac{1}{\max H_y(n)_i}, \; i = 1, 2, \ldots, N_{\text{ind}} \tag{4.1.1}$$

where i is the chromosome of the population with N_{ind} individuals.

The pendulum length L_p and the mass ratio μ are defined design variables. This set of numerical inputs is defined by a range of variation from its lower to upper bounds, $0.50 \leq L_p \leq 10.00$ m and $0.1 \leq \mu \leq 0.35$, respectively.

Once the fitness function f_{fitness} was defined, the optimization was performed several times to define the best parameters using the GA toolbox. To find the fastest convergence, the following was established:

- $N_{\text{gen}} = 100$, number of generations;
- $N_{\text{ind}} = 100$, number of individuals in the population;
- $p_{\text{c}} = 60\%$, crossover probability;
- $p_{\text{m}} = 2\%$, mutation probability;
- $p_{\text{elit}} = 2\%$, elitism probability;
- $p_{\text{dec}} = 20\%$, decimation probability;
- $N_{\text{dec}} = 20$, step of generation for the occurrence of decimation (116, 117).

As consequence of the sensitivity analysis (19), a specific set of GA optimizations has been performed varying the pendulum stiffness and maintaining the same damping. As shown in fig. 4.1.4, the GA results are gathered on the μ vs Ł$_p$ plan, and the power regression graphics take a linear form of $\mu = a_i L_p^{b_i} + c_i$.

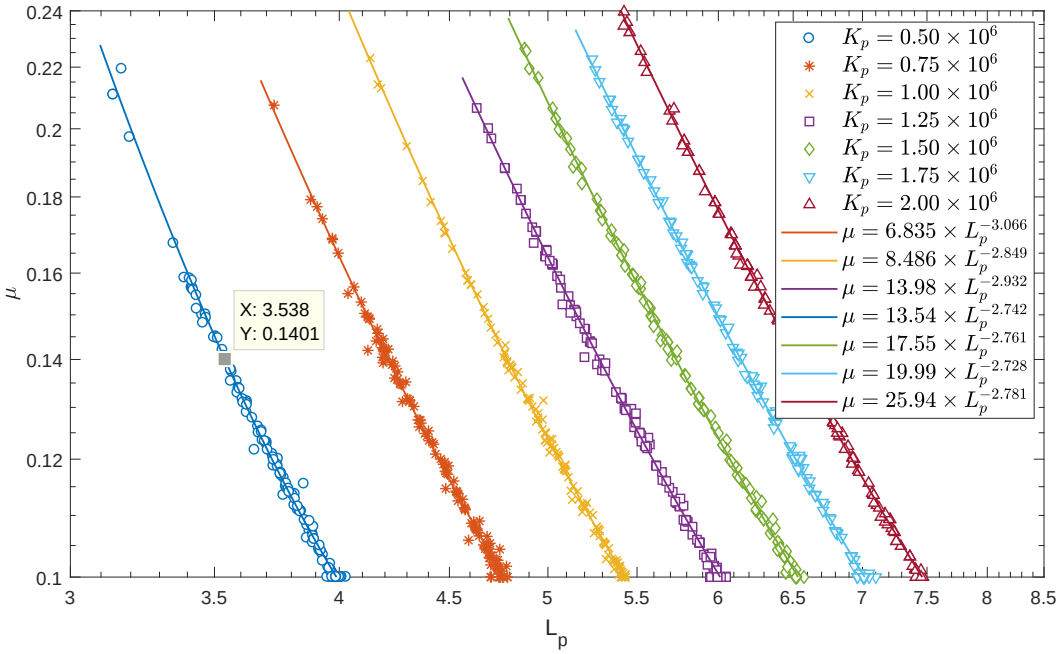

Figure 4.1.4 – Power regression of the $(\mu; L_p)$ optimization results for different values of K_p in log x log scale (L_p in m and K_p in Nm/rad)

These power functions present a certain linearity in *log-log* scale. The designer can easily select the optimal pendulum parameters for L_p, μ and K_p in fig. 4.1.4, since it was observed that the damping C_p does not affect the behavior of these curves. The selection of the pendulum length and the mass ratio is a consequence of the stiffness selected by using the power regression curves. A case example is observed in fig. 4.1.4 with mass ratio $\mu^* = 0.14$ and length $L_p^* = 3.54$ m related to $K_p^* = 0.50$ MNm/rad.

The optimization analysis carried out with a GA toolbox saved a significant amount of time compared to the parametric study and determined the best PTMD according to the problem description. Accordingly, the optimum design consists of $K_p^* = 0.50$ MNm/rad, $C_p^* = 9.0249$ kNms/rad, $\mu^* = 0.14$, and $L_p^* = 3.54$ m.

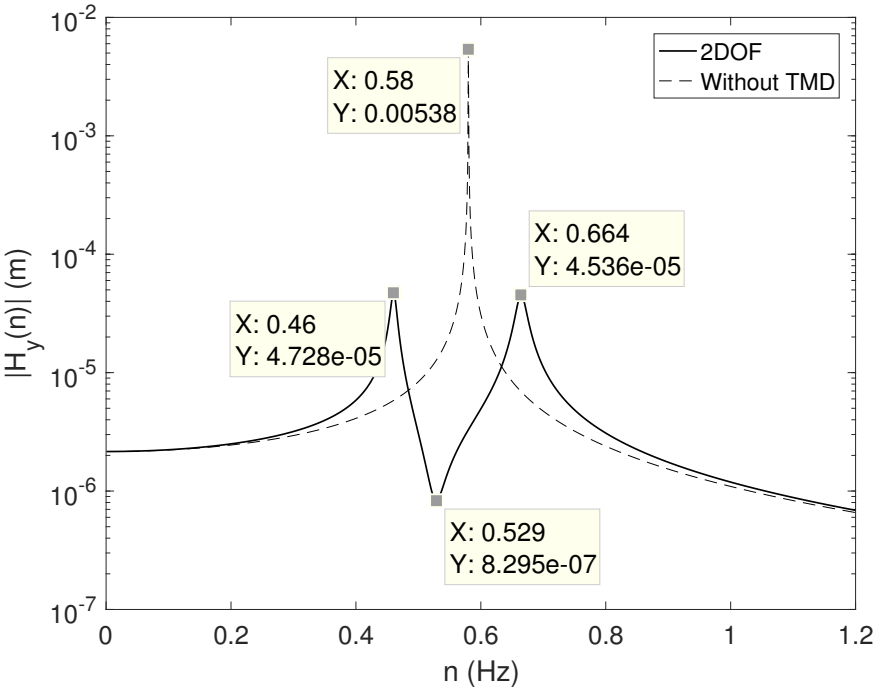

Figure 4.1.5 – Case Study: Tower FRF with and without PTMD

The sensitivity of length L_p and mass ratio μ was evaluated. First, two values of pendulum length were defined: $L_p = 0.8L_p^*$ m and $L_p = 1.2L_p^*$ m. The other optimal values did not change. The comparative study can be observed in fig. 4.1.6. A shift of the peak frequency responses and amplitude changes are observed.

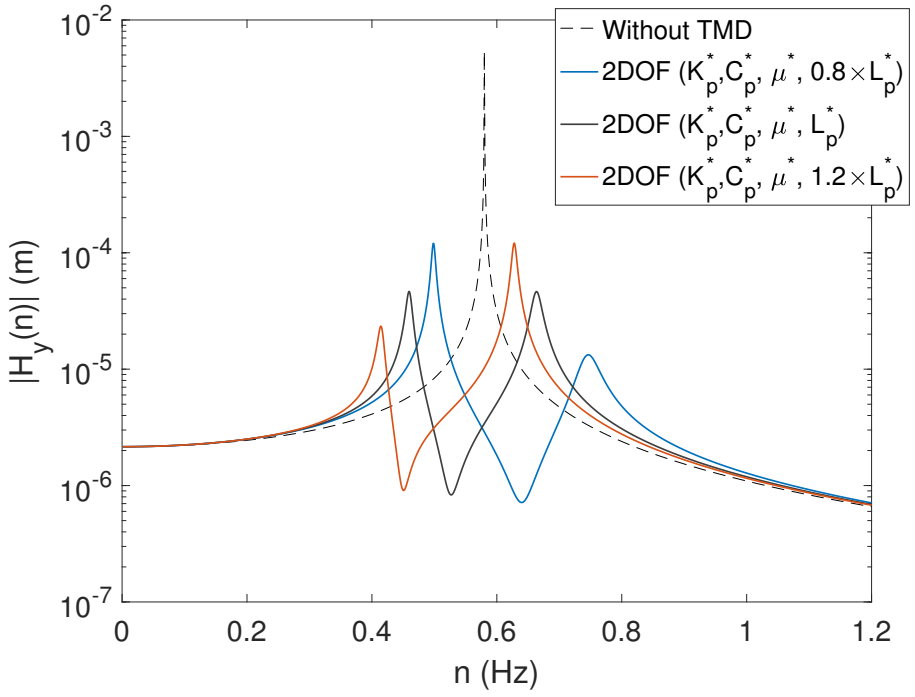

Figure 4.1.6 – Comparison between the case study and pendulum length variations

Then, remaining with the optimum design, but making a slight change in the mass ratio value, that is, $\mu = 0.8\mu^*$ m and $\mu = 1.2\mu^*$ m, it is possible to observe the sensitivity of this parameter over the best design as fig. 4.1.7 shows. Resonance peaks also shift frequency values and amplitudes, but not as significantly as in the previous case.

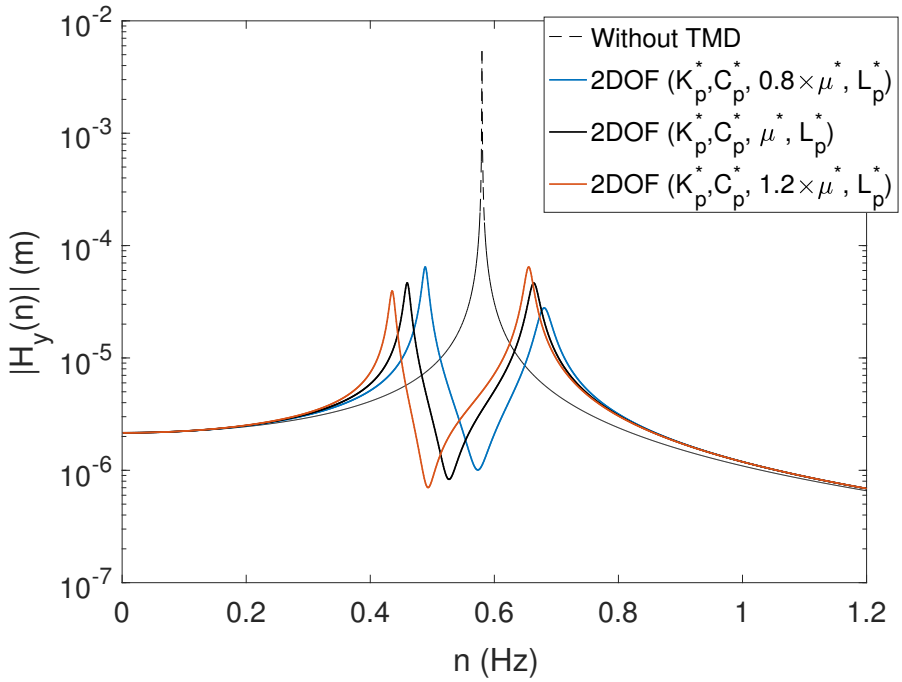

Figure 4.1.7 – Comparison between the case study and mass ratios variations

Figures 4.1.8 and 4.1.9 show the FRFs for some stiffness value ($K_p = [0.50; 0.75; 1.00; 1.25; 1.50; 1.75; 2.00]$ MNm/rad). The first figure was plotted considering the mass ratio value (fig. 4.1.8) $\mu = 0.1$, and the other used $\mu = 0.2$ (fig. 4.1.9).

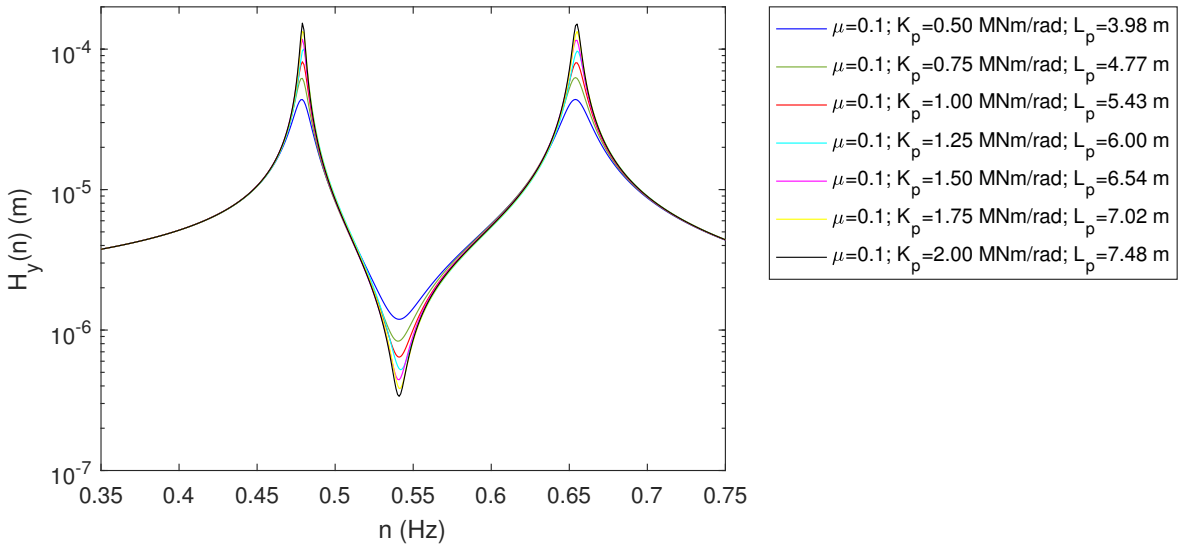

Figure 4.1.8 – Parametric validation: Comparison of the Frequency Response Function for $\mu = 0.1$

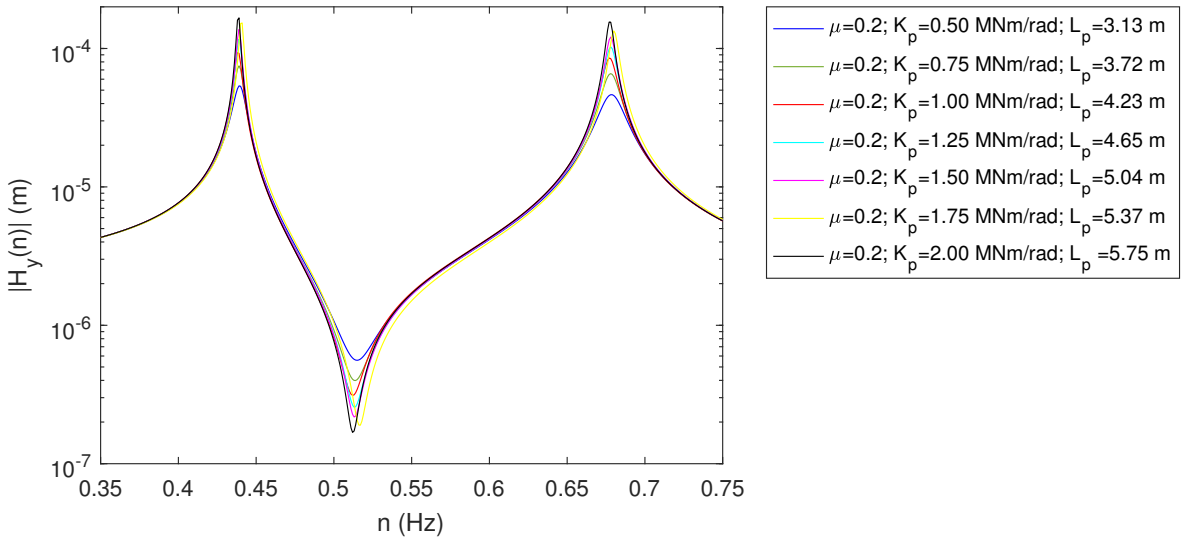

Figure 4.1.9 – Parametric validation: Comparison of the Frequency Response Function for $\mu = 0.2$

Table 4.1.1 shows the amplitude response peaks for the combinations of μ, K_p, and L_p, considering $C_p = 9.0249$ kNms/rad.

Table 4.1.1 – Maximum amplitude responses as a function of the stiffness

K_p (MNm/rad)	**0.50**	**0.75**	**1.00**	**1.25**	**1.50**	**1.75**	**2.00**
$\mu = 0.1$							
$\max \lvert H_y(n) \rvert \times 10^{-5}$ (m)	4.38	6.27	8.13	10.00	11.78	13.35	15.33
L_p (m)	3.98	4.77	5.43	6.00	6.54	7.02	7.48
$\mu = 0.2$							
$\max \lvert H_y(n) \rvert \times 10^{-5}$ (m)	5.37	7.50	9.34	11.67	13.72	15.28	16.65
L_p (m)	3.13	3.72	4.23	4.65	5.04	5.37	5.75

Figures 4.1.8 and 4.1.9 and Tab. 4.1.1 shows that the control frequency range increases when mass ratio μ increases. Moreover, lower values of K_p lead to lower amplitude responses. For each value of μ, taking into account the stiffness variations, the natural frequencies do not change; however, the amplitude response peaks increase when the pendulum stiffness increases.

To observe the performance of optimum PTMD ($K_p = 0.50$ MNm/rad, $C_p = 9.0249$ kNms/rad, $\mu = 0.1$, and Ł$_p = 3.98$ m), a five hour time history was performed with an external white-noise force (random signal with uniform probability distribution) in order to simulate the effects of a simplified wind load. In this particular case, the white-noise spectrum follows the same normal distribution of a constant and unitary force represented in eq. 3.3.9, making it possible to extend these results by performing a structural response using a real record of the wind or simply applying a well representative wind power spectrum density. Figure 4.1.10 shows the time history of a tower with and without control. The effectiveness of the optimal PTMD passive control type can be inferred. PTMD can reduce more than 92% of the effective RMS tip displacement compared to the case without control.

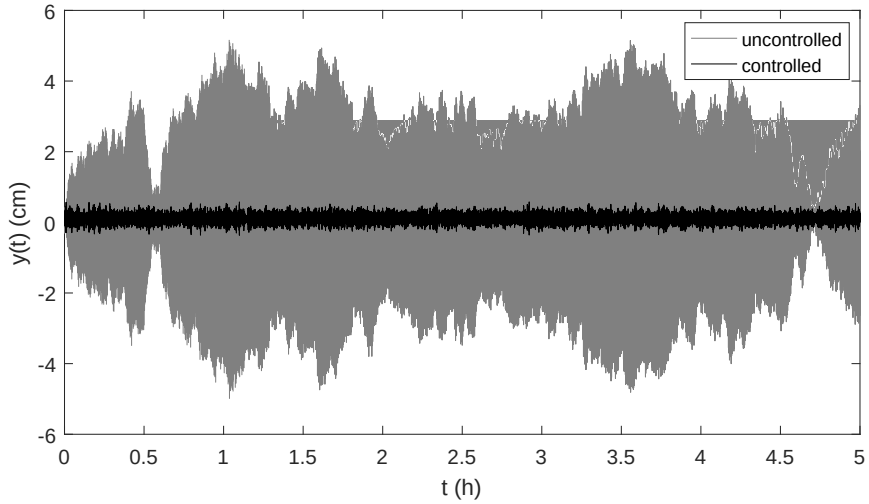

Figure 4.1.10 – Time history of the tower controlled and uncontrolled by a PTMD

4.1.3 Case study 1 conclusions

The GA toolbox enables easy identification of a geometric locus on a map response that contains optimal PTMD parameters using a 2DOF model of a tower with a PTMD. A response map sensitivity study identifies the influence of the stiffness and damping of the pendulum over the frequency response peaks of the tower. Using genetic algorithms, power regression curves comprising optimal data are created as a function of the pendulum stiffness, length and mass.

A design methodology is suggested, allowing the selection of optimal pendulum configurations. We conclude in the parametric validation section that when we increase the mass ratio between the pendulum and tower, the zone control also increases, and increasing the pendulum stiffness maintaining the same mass ratio will increase the FRF response peaks. A time history using a behavior of a white-noise wind effect shows that the PTMD can reduce the tip tower vibration more than 92%. The tower lifetime can be extended by reducing its vibration and, consequently, its fatigue.

4.2 Case Study 2: FE model of an optimal PTMD design applied to a OWT

This case study models the OWT and PTMD by using finite elements following the detailed specifications of Phase I (monopile type) NREL 5-MW OWT baseline defined by Jonkman et al. (18).

4.2.1 Genetic algorithm optimization

The optimization is carried out by hierarchically subdividing the parameters of the PTMD in primary and secondary design variables (DVs). Then couples of values for K_p and C_p (secondary DVs) are fixed, and optimal values of μ and L_p as primary DVs are found. An in-house built Genetic Algorithm (GA) toolbox computes the PTMD optimal parameters of the 2DOF model, following the procedures developed by Colherinhas et al (19) and detailed on sec. B.

The goal of this genetic optimization is to minimize the frequency response peak displacements of the tower described in the analytical 2DOF model, considering the influence of the environment and rotating blade actions as specified in the previous sections. The fitness function f_{fitness} minimizes $|H_y(n)|\sqrt{(S_{F_S}(n))}$ (only in FA direction), maximizing its inverse, as follows

$$(f_{\text{fitness}}) = \frac{1}{\max\left(H_y(n)\sqrt{S_{F_s}(n)}\right)}, \qquad i = 1, 2, \ldots, N_{ind} \tag{4.2.1}$$

where i corresponds to each chromosome evaluated in the population of N_{ind} individuals.

The ranges of variation from $0.10 \leq Lp \leq 10.00$ m and $0.01 \leq \mu_p \leq 0.20$ are chosen for the primary DVs.

4.2.2 Model validation

The modal frequencies in the fore-aft (FA) and side-to-side (SS) directions of the presented FEM model agree with those found in literature for the case study structure (81) 4.2.2.

Table 4.2.1 – Natural frequencies comparison (values in Hz)

	FEM model	Ghassempour's model (81)
1st fore-aft	0.2741	0.2752
1st side-to-side	0.2741	0.2782
2nd fore-aft	2.2783	2.2651
; 2nd side-to-side	2.2916	2.3452

In order to validate the proposed FEM model of the case study when not provided with any control device, a PSD analysis is performed and the resultant tower-top peak displacements are compared with those obtained by the NREL OpenFAST model (Figure 4.2.1).

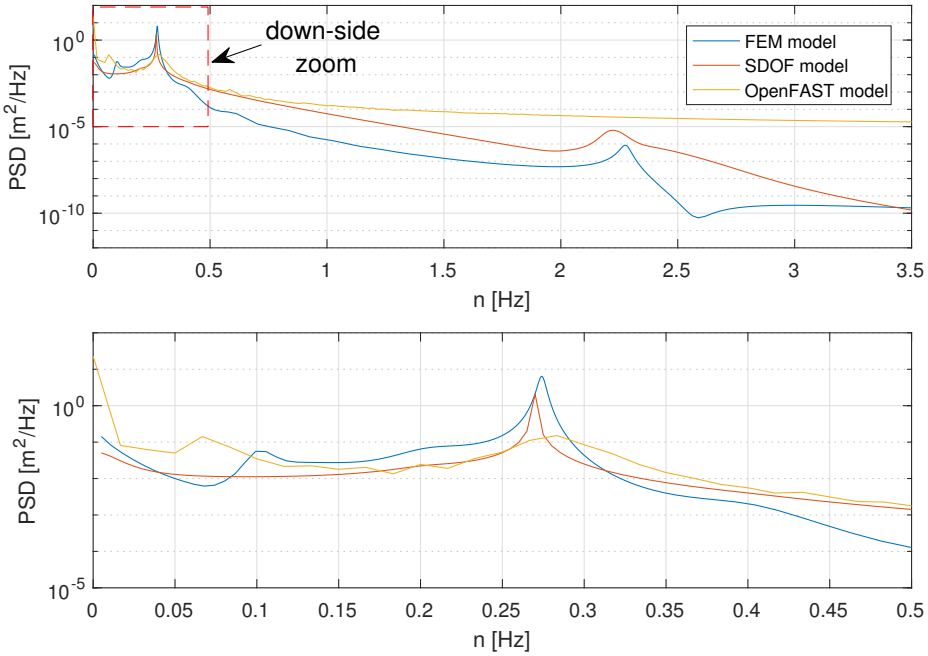

Figure 4.2.1 – PSD for tower-top displacements of the OWT model. Full frequency range (up); first-peak zoom (bottom)

The OpenFAST response PSD is computed as the mean of 20 PSDs produced using the MATLAB Toolbox for OpenFAST (118), from the Discrete Fourier Transform (DFT) of 20 different time-histories obtained by OpenFAST simulations conducted at the same wind intensities. The turbulent stochastic wind velocity fields are generated using the NREL TurbSim software, which works as inputs of the AeroDyn OpenFAST module. The generation of the mean OpenFAST PSD takes a total of 85.52 minutes with the available computational capacity versus 79.32 seconds of the ANSYS FEM analysis in the frequency domain, using the same processor specifications (i.e., the expended simulation time is more than 60 times).

Figure 4.2.1 presents a response PSD comparison of the FEM, SDOF and OpenFAST models for $U_{hub} = 12$ m/s, $H_w = 6$ m, and $T_w = 10$ s for the FA hub displacements.

The FA and SS tower-top peak displacements of the FEM model are, respectively, 1.04 and 0.34 m versus 1.08 and 0.12 m (OpenFAST). The normal peak stress at the tower base is $S_b = 18.16$ MPa as evaluated in FEM analysis, the last one will increase when the PTMD is installed due to the additional weight provided by the PTMD mass.

4.2.3 Optimal PTMD design by the 2 DOFs model

The following parameters are used in the GA-based PTMD optimal design by the 2 DOFs model introduced in previous sections: tower with a mass of 532.60 ton; rotor-nacelle-assembly (RNA) with a mass of $m = 350.00$ ton and flexural stiffness of $EI = 1,036.24\text{GNm}^2$ (value obtained from the FEM model); generalized tower mass and stiffness, respectively, $M_s = 882.60$ ton (eq. 3.3.5) and $K_s = 2,532.07$ kN/m (eq. 3.3.3); the tower damping coefficient was set to 1% (18). For a preliminary investigation, the torsional stiffness and the friction damping of the PTMD are considered, respectively, $K_p = 1.25$ MNm/rad and $C_p = 9.0$ kNms/rad (secondary DVs set No 1) (114), enabling the parametric analysis giving the results shown Figure 4.2.2.

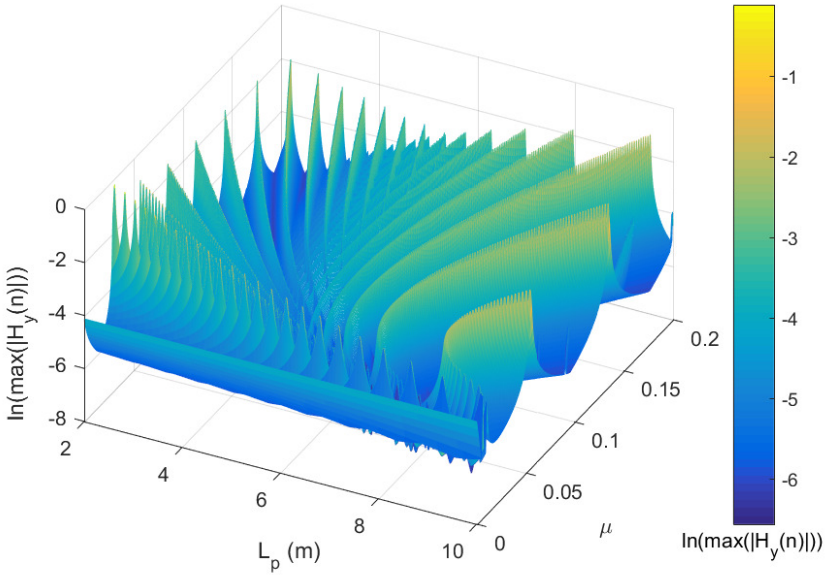

Figure 4.2.2 – Parametric optimization analysis for the secondary DVs set No 1 ($K_p = 1.25$ MNm/rad and $C_p = 9.0$ kNms/rad)

The response surface shown in fig. 4.2.2 has not a simple curvature, but on the contrary it presents multiple geometric valleys, something that is due to the rotor dynamics. The dark regions in the fig. 4.2.2 represent the valleys of this complex surface, i.e. the lower response peak displacements, presenting optimal values of the GA optimization.

To find the fastest convergence of the optimization procedure by the implemented GA, the following parameters were established during the adopted GA optimization:

- $N_{\text{gen}} = 100$, number of generations;
- $N_{\text{ind}} = 100$, number of individuals in the population;
- $p_{\text{c}} = 60\%$, crossover probability;
- $p_{\text{m}} = 2\%$, mutation probability;

- $p_{\text{elit}} = 2\%$, elitism probability;
- $p_{\text{dec}} = 20\%$, decimation probability;
- $N_{\text{dec}} = 20$, step of generation for the occurrence of decimation.

This way, four hundred iteration analyses are carried out by the GA optimization. The results are gathered on the μ vs L_p plane, where the power regression line of the optimal solutions found with the secondary DVs set 1 takes the form of $\mu = aL_p^b + c$, with $a = 1.185 \cdot 10^4$, $b = -7.354$, and $c = 9.249 \cdot 10^{-3}$, as shown in fig. 4.2.3.

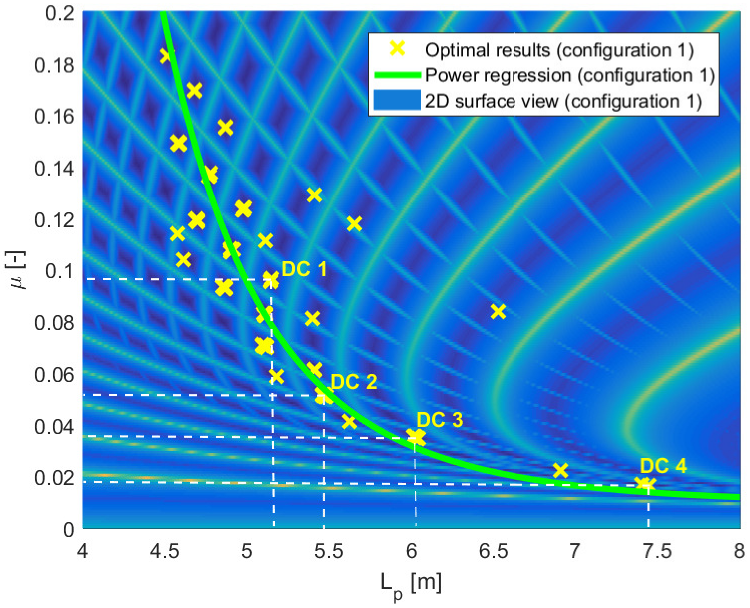

Figure 4.2.3 – Optimal results of L_p and μ obtained with the secondary DVs set No 1 (colours are associated with the same magnitude scale of previous fig. 4.2.2)

Although optimal values fluctuate around the power regression curve of fig. 4.2.3, this regression curve (located in a main valley of the surface) gives a good clue for a pre-design of PTMDs. Four design cases (DC) are selected (DC1 to DC4) from the one obtained considering the secondary DVs set No 1, with $\mu_{DC1} = 0.10$ ($M_p = 85.11$ t), $\mu_{DC2} = 0.05$ ($M_p = 44.88$ t), $\mu_{DC3} = 0.03$ ($M_p = 30.64$ t), $\mu_{DC4} = 0.02$ ($M_p = 14.55$ t). The DC1 to DC4 are also indicated in fig. 4.2.3.

Using the same strategy of (19), the secondary DVs (stiffness K_p, and damping C_p) can be changed to obtain additional sub-optimal configurations, i.e. by increasing K_p the main valley is expected to shift toward the right side on the $L_p \times \mu$ plan, while by increasing C_p the response amplitude is expected to decrease but the surface shape and the valley position are not supposed to be affected. With this in mind, a new set of secondary DVs (set No 2) is selected with $K_p = 0.5$ MN/m and $C_p = 15.0$ kNms/rad, leading to the parametric response surface shown in fig. 4.2.4. For this new set of secondary DVs a

thousand optimizations are performed, expending a total time of 2771.51 seconds (= 2.8 s per optimization).

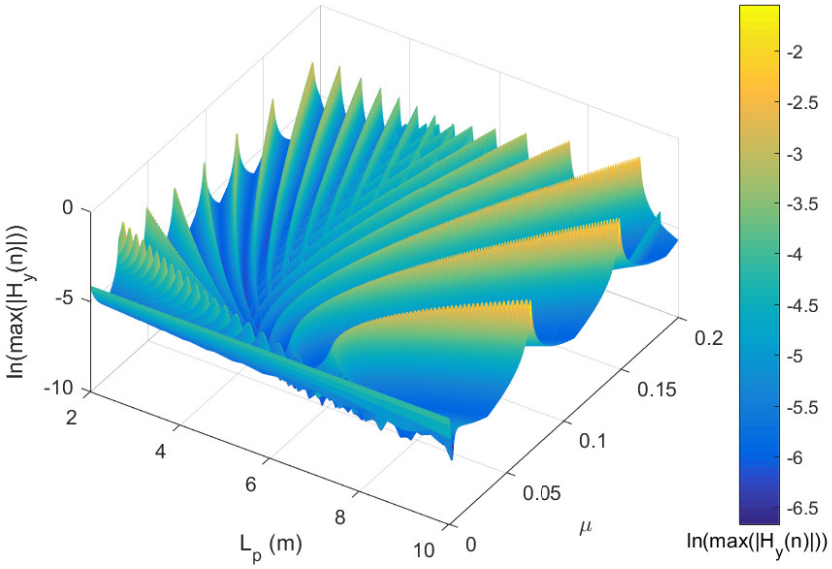

Figure 4.2.4 – Parametric optimization analysis for the secondary DVs set No 2 ($K_p = 0.5$ MNm/rad and $Cp = 15.0$ kNms/rad)

From this new optimization carried out with the DVs set No 2, four additional DCs (DC5 to DC8) are also selected with the criteria of keeping the same mass ratio of the previous DCs ($\mu_{DC5} = 0.10$, $\mu_{DC6} = 0.05$, $\mu_{DC7} = 0.03$, $\mu_{DC8} = 0.02$) as shown in fig. 4.2.5. The power regression for the set No 2 takes the form of $\mu = aL_p^b$, with $a = 300.8$ and $b = -5.629$, as also shown in fig. 4.2.5.

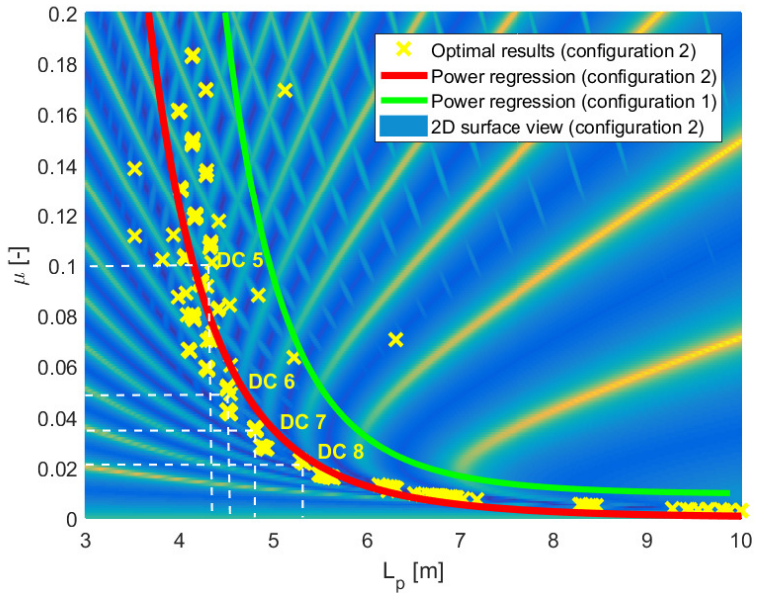

Figure 4.2.5 – Optimal results of L_p and μ obtained with the secondary DVs set No 2 (colours are associated with the same magnitude scale of previous fig. 4.2.4

4.2.4 Optimal PTMD selection of the 3D finite element model

The eight DCs selected above are compared by using the 3D global FEM model. Due to the particular configuration of the system (the PTMD is located inside the tower), as a pre-requisite for a DC to be acceptable, in order to avoid collision of the PTMD mass with the inner surface of the tower, the peak lateral displacements (sway) of the PTMD mass must remain lower than the inner radius of the tubular section of the tower at the location of the PTMD mass. The maximum peak lateral sway experimented by the PTMD mass in the selected DCs is 0.91 m, which is acceptable for avoiding such an event. Figure 4.2.6 shows the peak stresses S_b at the base for the different DCs at different U_{hub} values. The local increasing of the response values obtained for each DC at relatively low velocities, is due to the wind induced vortex shedding effect occurring at the critical velocity range specified above. A cut-off wind speed $V_{out} = 25$ m/s has been set for U_{hub} (i.e. for $U_{hub} \geq V_{out}$ the rotor is parked), resulting in a local drop of the response from V_{out} on.

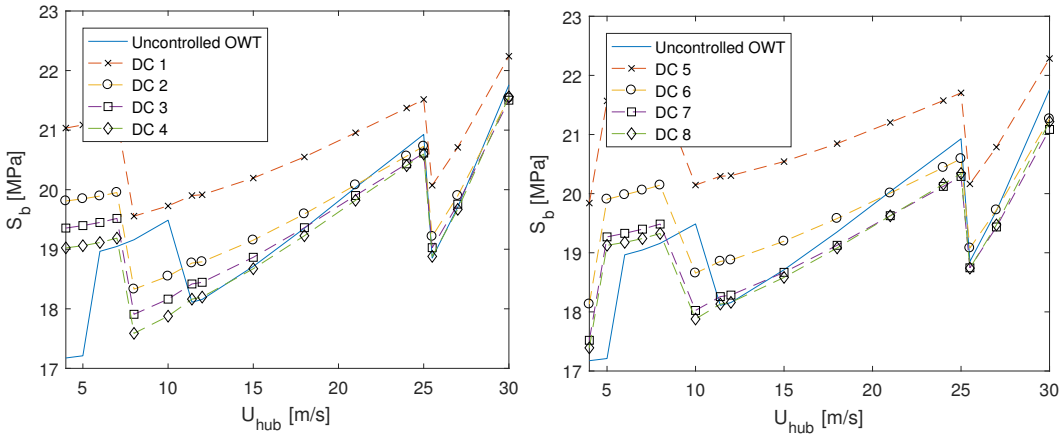

Figure 4.2.6 – Stresses at the base Sb. Secondary DVs set No 1 (left); secondary DVs set No 2 (right)

The decreasing trend of S_b by increasing the DC from 1 to 4 and from 5 to 8 is partially due to the contingent decreasing of the pendulum mass. DCs 1 and 5 present the higher values of stresses at the base, close to 22 N/mm^2 at moderate wind speeds and for $U_{hub} < 8$ m/s, due to vortex induced vibrations.

In Figure 4.2.7 (secondary DVs set No 1) and Figure 4.2.8 (secondary DVs set No 2) the peak response displacements at the hub dp for FA and SS directions are compared for all the considered DCs, and shown as function of U_{hub}, at $H_w = 6$ m, and $T_w = 10$ s, the response of the uncontrolled configuration is also shown for comparison purposes.

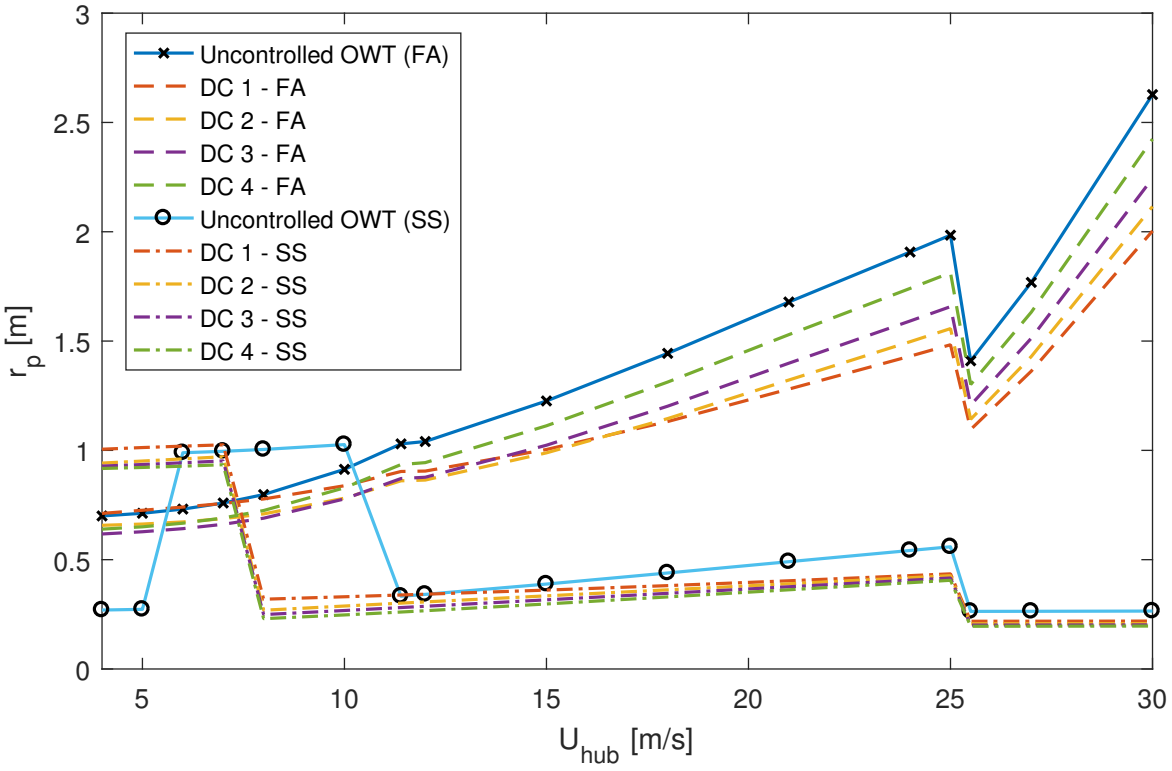

Figure 4.2.7 – Controlled and uncontrolled OWT tower-top peak response displacements for optimal DCs obtained with the secondary DVs set No 1 (DC1 to DC4), in FA and SS directions

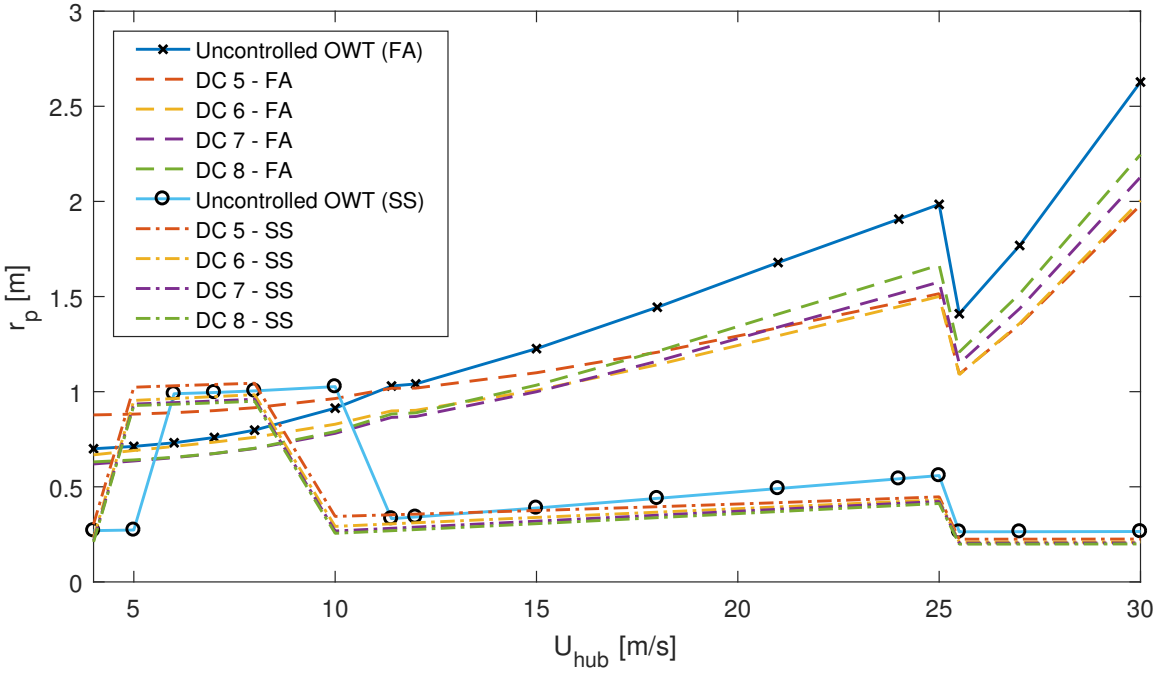

Figure 4.2.8 – Controlled and uncontrolled OWT tower-top peak response displacements for optimal DCs obtained with the secondary DVs set No 2 (DC5 to DC8), in FA and SS directions

For $U_{hub} \geq V_{out} = 25$ m/s, i.e. cut-out speed, the rotational spectrum is set off (i.e. it is replaced by an ordinary Kaimal wind spectra acting of parked blades) and there is a drop of the peak displacement curves. It also can be noticed an increase of the peak displacements at low wind speed in SS direction, due to vortex induced vibrations.

In general, it is graphically shown that the DCs corresponding to the secondary DVs set No 2 presents higher peak response displacement reductions than those of the DVs set No 1. A detailed study for $U_{hub} = 12$ m/s (operating conditions and out from the vortex-shedding velocity range for the uncontrolled case and for all DCs) and 25 m/s (parked conditions) is performed and a comparison summary of the peak displacements reduction and the corresponding stress at the base (SB), is presented in Table 4.2.2 by considering the OWT with and without PTMD for both FA and SS directions. The comparison of results is presented in dB with the purpose of facilitating the understanding of the performances i.e.: for the response peak displacements: $r_p^{dB} = 10 \cdot \log_{10}(r_p^{PTMD}/r_p)$; for the stress at the base: $\sigma_b^{dB} = 10 \cdot \log_{10}(\sigma_b^{PTMD}/\sigma_b)$ (where the superscript PTMD denotes the OWT with the PTMD). By adopting this units, better PTMD performances (larger reduction of the response) corresponds to lower (negative) values.

Table 4.2.2 – Resume of selected optimal DCs (results in dB)

Design Parameters		secondary DVs set No 1				secondary DVs set No 2			
		DC 1	DC 2	DC 3	DC 4	DC 5	DC 6	DC 7	DC 8
μ_p [-]		0.10	0.05	0.03	0.02	0.10	0.05	0.03	0.02
L_p [m]		5.15	5.47	6.04	7.45	4.35	4.51	4.86	5.34
$U_{hub} = 12$ m/s	FA	-1.21	-1.61	-1.49	-0.85	-0.19	-1.24	-1.56	-1.37
	SS	-0.02	-0.93	-1.51	-2.15	0.38	-0.81	-1.47	-1.87
	SB	0.80	0.30	0.14	0.02	0.97	0.34	0.06	0.01
$U_{hub} = 25$ m/s	FA	-2.53	-2.11	-1.56	-0.79	-2.34	-2.43	-2.00	-1.52
	SS	-2.17	-2.34	-2.56	-2.78	-1.94	-2.25	-2.42	-2.64
	SB	0.24	0.08	0.13	0.14	0.32	0.14	0.27	0.25

As expected, due to the variety of conditions explored for performance assessment, there is not a unique optimal DC. For example, in FA direction for $U_{hub} = 25$ m/s, the DC 1 is the best among all explored DCs (-2.53 in reduction). On the contrary, for the wind velocity $U_{hub} = 12$ m/s, DC 2 presents peak displacements reductions higher than DC 1, with reductions of -1.61 and -0.93 dB in FA and SS direction, respectively. On the basis of feasibility considerations, it can be stated that, since the mass of the DC 1 is huge, it's actual implementation is not suggested (the same applies for the DC 5), potentially leading to collateral structural problems in the life-cycle time (e.g. addition of such a mass to the system could increase the vulnerability of the tower to fatigue), the DC 2 is possibly the best optimized design in FA direction among those obtained for secondary DVs set No 1 ($K_p = 1.25$ MNm/rad and $C_p = 9.0$ kNms/rad). In fact, compared to DC 3 and DC 4, the DC 2 presents a reduction of -2.11 versus -1.56 and -0.79 dB respectively in FA direction, at $U_{hub} = 25$ m/s, while DC 2 performs always lower than DC 3 and DC 4 in SS direction.

The DCs obtained by the secondary DVs set No 2 ($K_p = 5.0 \cdot 10^5$ N/m and $C_p = 15.0 \cdot 10^3$ Nms), in FA direction, present, in general, higher peak reductions compared to set No 1, as expected by (19). For $U_{hub} = 25$ m/s there are reductions, in FA direction, in the order of -2.43 dB (DC 6) versus -2.11 dB (DC 2) for $\mu = 0.05$, and -2.00 dB (DC 7) versus -1.56 dB (DC 3) for $\mu = 0.03$. DCs 6 and 7 are selected as the best DCs considering the variation of the wind speed and the feasibility of the optimal pendulum parameters. The hard task to select these optimum DCs proves the following Ghassempour's et al. (81) assumptions: the conventional design of TMDs based on natural frequencies may not be suitable for OWTs due to the fact that the optimal values of the DVs strongly depend on the wind velocity at operational conditions.

Figure 4.2.9 shows a comparison between the tower-top PSD displacements in FA and SS direction for DCs 6 and 7, for wind velocities of $U_{hub} = 24m/s$ (operational condition).

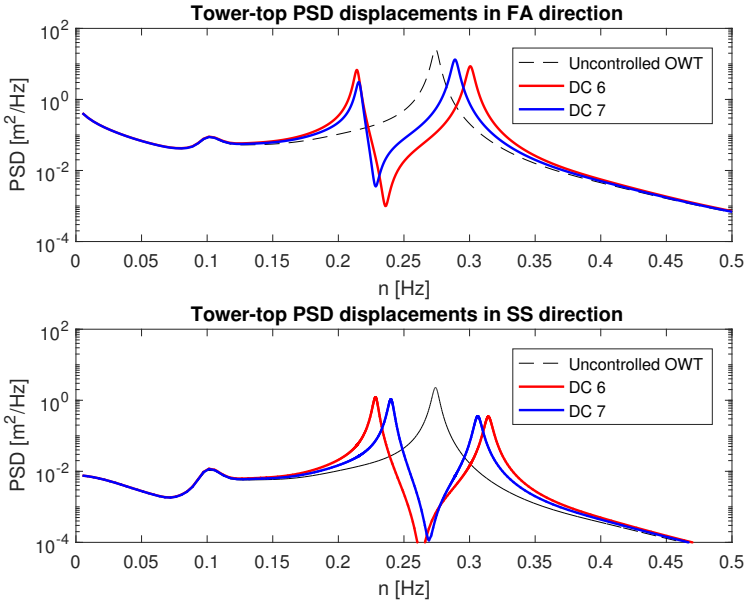

Figure 4.2.9 – PSD of tower-top displacements of DC 6 and 7 for $U_{hub} = 24$ m/s

To further point out on the difficulties in choosing between the two selected DCs, Figure 4.2.10 shows the peak response displacement reduction of DCs 6 and 7 for both FA and SS direction, in function of U_{hub} (in SS, values of $U_{hub} < 11.4$ m/s are neglected for scale purposes). It is clear that (especially in the FA direction, the prevalence of one DC on the other one strongly depends on the wind velocity. Higher reductions happen in operating conditions for wind velocity values close to the cut-off speed $U_{hub} = 25$ m/s.

Finally, regarding the possibility of implementing passive-adaptive control strategies: let us assume that for some reason the PTMD has been set to the DC8, which (from Figure 4.2.8) is shown to work well for both the FA and the SS directions in operating conditions at low wind velocities (e.g. $U_{hub} = 12$ m/s); in the case that strong winds ($U_{hub} \geq 25$ m/s)

are forecast in a certain day with FA direction expected to become critical for ultimate strength for such strong winds, then L_p and μ parameters can be switched in advance to temporary fall in the DC 5, which, for the same K_p and C_p, is more efficient than the DC8 in suppressing the FA vibrations at high wind velocities. This passively-adaptive skill, allowed by the presence of Lp as additional tuning parameter, can be very useful for optimal life-cycle management purposes of the OWT.

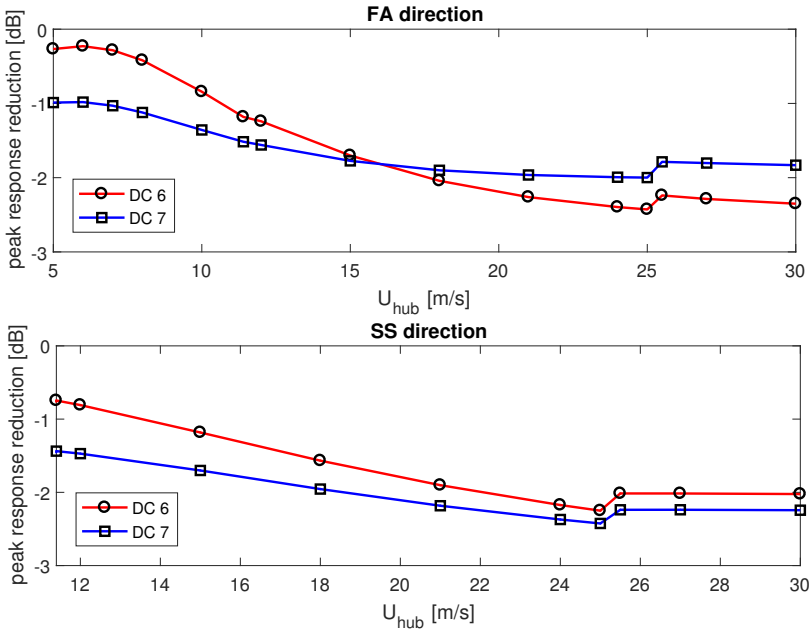

Figure 4.2.10 – Peak response reduction between the control- and uncontrolled OWT

4.2.5 Case study 2 conclusions

Design optimization and performance assessment procedure are presented for PTMDs in OWT systems for the mitigation of the global vibrations of the tower by installing the PTMD inside the tubular tower section and attached to the hub. A simplified 2DOF model is used for optimizing the OWT+PTMD system for different intensities of the actions by a genetic algorithm (GA), which aims to minimize the peak displacement making use of the stochastic dynamic theory and the frequency domain (PSD) analysis, and leading to the identification of some alternative design configurations (DCs). The assessment of the performances and the choice of the best DC among the selected ones are conducted by a global 3D Finite Element model of the turbine still by conducting a PSD frequency domain analysis and by implementing state of art models for the spectra of the wind (as sampled by the rotor in operating conditions) and the wave actions.

Based on the obtained results, the following general conclusions can be provided:

- the PTMD can mitigate wind- and sea- induced global OWT vibrations both in fore-aft and side-side directions.

- it is outlined how the complex shape of the response surface in the primary design variables space, leading to a set of sub-optimal solutions DCs of the optimization problem, which in turn are more or less suitable depending on the operating condition of the system.
- the use of the 2DOFs model during the optimal design phase allows for significant savings in the computational efforts required during the optimization phase;
- the 3D PSD finite element analysis allows for the fast investigation of the performances at different wind velocities, and the individuation of the more suitable DCs for practical realization and passively-adaptive control strategy purposes;
- before choosing the more suitable design configuration, the admissibility of the peak sway of the PTMD mass and the increasing of the peak stress at the base of the tower due to the installation of the PTMD additional mass must be checked;
- moreover, the possibility of passively adapting the pendulum length, if coupled with other passively-adaptive skills (rearrangement of K_p, C_p or μ), allows for the temporary switching from an identified optimal (DC) to different ones, which are more appropriate at different operating conditions (e.g. operating versus parked rotor at different wind intensities)

From the application of the outlined procedure to a case study, a reduction of over 20% of the response peaks for high wind velocities in the fore-aft direction was noticed, which is consistent with the response reduction provided by other semi-active PTMD vibration control systems found in literature (119), but in the device proposed here, there is the advantage of not requiring electric power in operation

This case study contributes to providing advanced tools for the optimal design analysis of the PTMD with the purpose of its installation in OWTs as an initial step toward the implementation of passively adaptive vibration control strategies as a convenient alternative to the active- and semi-active controls, which are complex to calibrate and manage.

4.3 Case study 3: SEM model of an optimal PTMD design applied to OWT

This case study presents the modeling of an optimum pendulum attached to an OWT using a spectral element (SEM) approach. Results are compared with both 2DOF and FEM models. The complete analytical background of the mentioned SEM model is presented in sec. 3.3.3.

Figure 4.3.1 presents the comparison of the frequency response for Murthag et al.'s tower (99), obtained with SEM, FEM as published in (108), modeled as a single-degree of freedom (SDOF) (19), and multi-degree of freedom (MDOF) reduction summarized in C. SEM and MDOF model also estimated the second mode with a good agreement in the resonance frequency and mode shape.

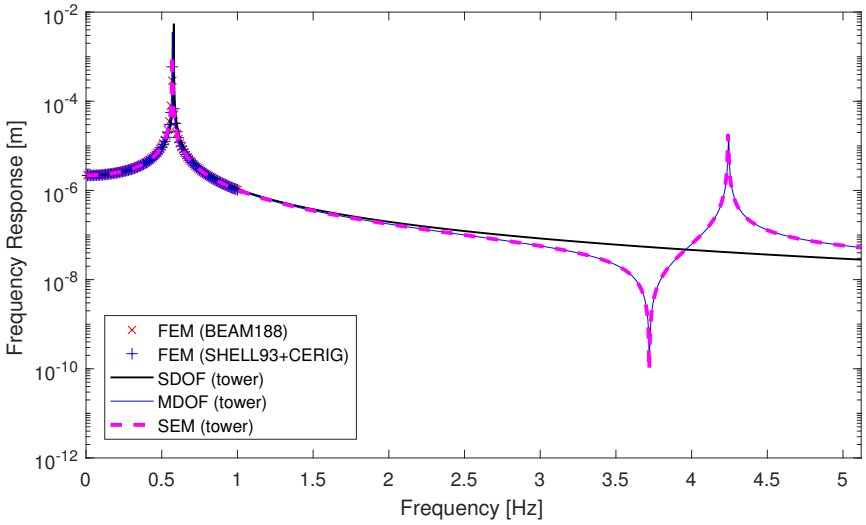

Figure 4.3.1 – Frequency response comparison of the tower for analytical MDOF solution (4 modes), FEM and SEM (108, adapted)

Figure 4.3.2 presents a detailed view of the first mode by comparing the methods. This figure also shows the response of the controlled tower (OWT+PTMD) calculated with SEM and MDOF, which presents a precise match between them. The OWT SEM model proved to be efficient and accurate compared to other techniques. The spectral model of the OWT+PTMD proved to be effective and present a similar behavior in comparison to the 2DOF model.

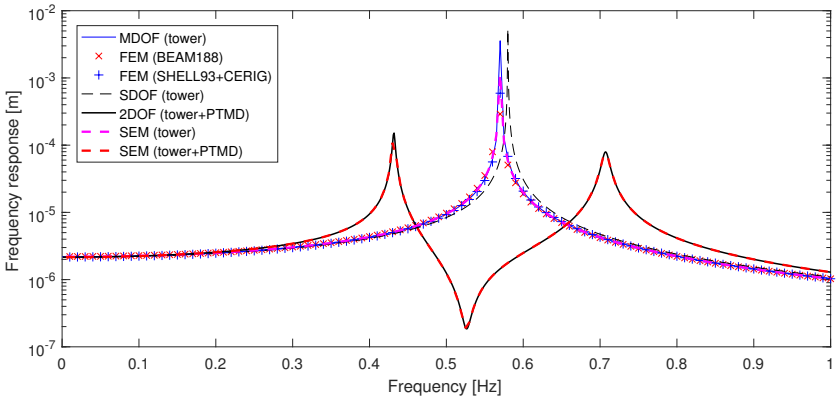

Figure 4.3.2 – Frequency response comparison of the controlled and uncontrolled tower for analytical MDOF solution (4 modes) (108, adapted), FEM, 2DOF (19, adapted) and the presented SEM model

With the OWT and OWT+PTMD SEM models validated, the next analysis will use SEM as the basis model. An optimization study and PTMD design will be presented, in addition to a random excitation analysis.

4.3.1 OWT PSD analysis

A dynamic analysis of the OWT SEM model, with any control device, has been performed for the proposed OWT model taking as input the PSD load models (2.4). Figure 4.3.3 shows the tower-top PSD displacements correspondent to the rotating blades (in blue), waves (orange), and wind (dashed lines), generated by a rotationally sampled spectrum, JONSWAP PSD, and ten equally spaced Kaimal PSDs above the SWL of the OWT, respectively. The resultant PSD (in yellow) is the sum of the rotationally sampled spectrum and all environmental PSD loads.

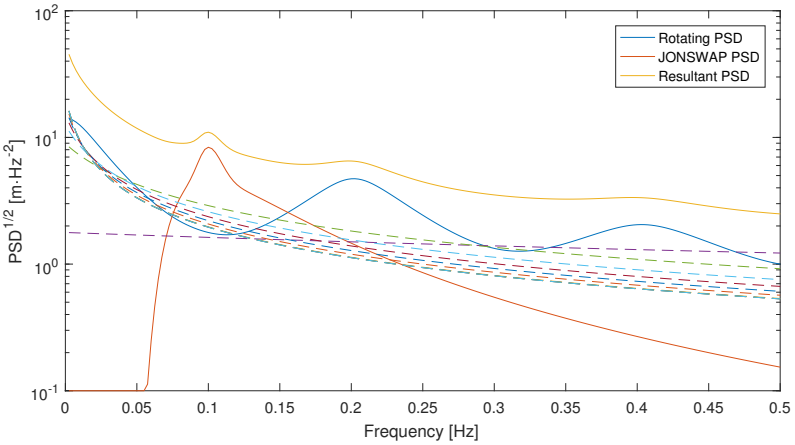

Figure 4.3.3 – PSDs of rotating blades, wave and wind actions, and resultant

All computations were made using an Intel® Core™ i5-6200U CPU with 2.40GHz and 8 GB RAM. By using the SEM model, an enormous reduction in the computational time related to OpenFAST and FEM is achieved. The PSD is compared with those obtained by the NREL OpenFAST model and the FEM of the same NREL 5MW OWT presented in (120) (Fig. 4.3.4). The OpenFAST response PSD is computed through the mean of ten PSDs produced using the MATLAB® Toolbox for OpenFAST (121) from the discrete Fourier transform (DFT) of 20 different time-histories obtained by OpenFAST simulations conducted at the same wind intensities. The turbulent stochastic wind velocity fields generated using the NREL TurbSim software were the inputs of the AeroDyn OpenFAST module. The OpenFAST PSD takes 85.52 minutes to compute the results, in contrast to FEM with 79.32 seconds and SEM using 1.23 seconds.

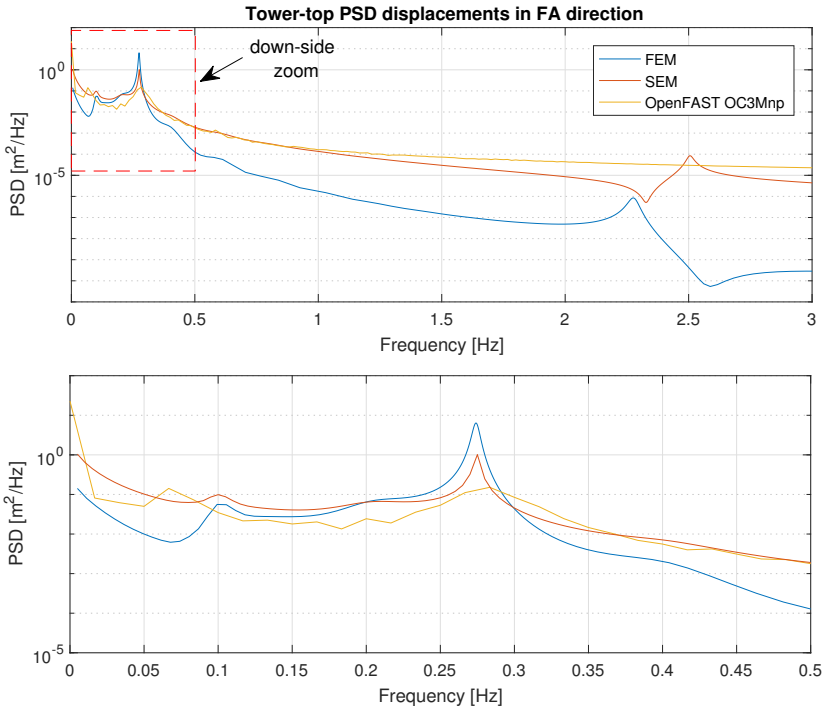

Figure 4.3.4 – PSD comparison for tower-top displacements of FEM, OpenFAST (120, adapted) and SEM OWT models

Figure 4.3.4 shows a PSD comparison of the presented SEM and the FEM and OpenFAST models (120) for $U_{hub} = 12$ m/s, $H_w = 6$ m, and $T_w = 10$ s in the fore-aft (FA) direction. OpenFAST estimated the first mode of the response while FEM and SEM could calculate the first and second modes. The PSD obtained with the three methods showed a good agreement between them.

4.3.2 Optimal PTMD design

The OWT assumed parameters are mass of 522.61 ton, rotor-nacelle-assembly (RNA) with a mass of $m_{tip} = 350$ ton (34). The mean flexural stiffness is $EI = 586.02\text{GNm}^2$. The generalized tower mass and stiffness are: $M_s = 468.51$ ton and $K_s = 1431.94$ kN/m, respectively. Damping coefficient set as 1%, torsional stiffness and the friction damping of the PTMD are considered as $K_p = 0.5$ kNm/rad and $C_p = 15.0$ kNms/rad.

Figures 4.3.5, 4.3.7, and 4.3.9 present an SEM parametric surface shape of the maximum peak response in function of the pendulum length L_p and the mass ratio between the pendulum and the tower mass μ of the monopile 5MW OWT for a white noise, parked, and rotating blade conditions, respectively, revealing a geometric locus with the best design cases. These figures (4.3.5, 4.3.7, 4.3.9) are compared with the 2DOF parametric maps (Figs. 4.3.6, 4.3.8 and 4.3.10) noticing that in some resonant regions the peaks of the 2DOF peaks are more expressive compared to other SEM peaks.

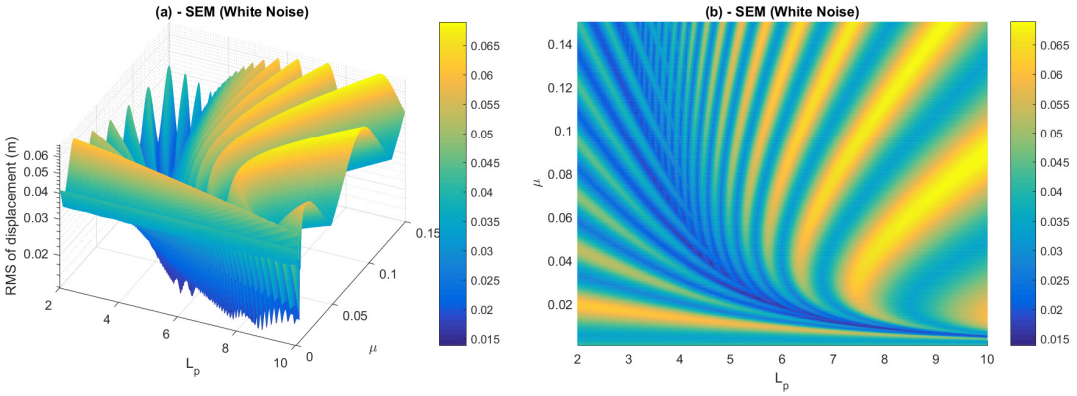

Figure 4.3.5 – SEM Parametric analysis of the OWT+PTMD (white noise)

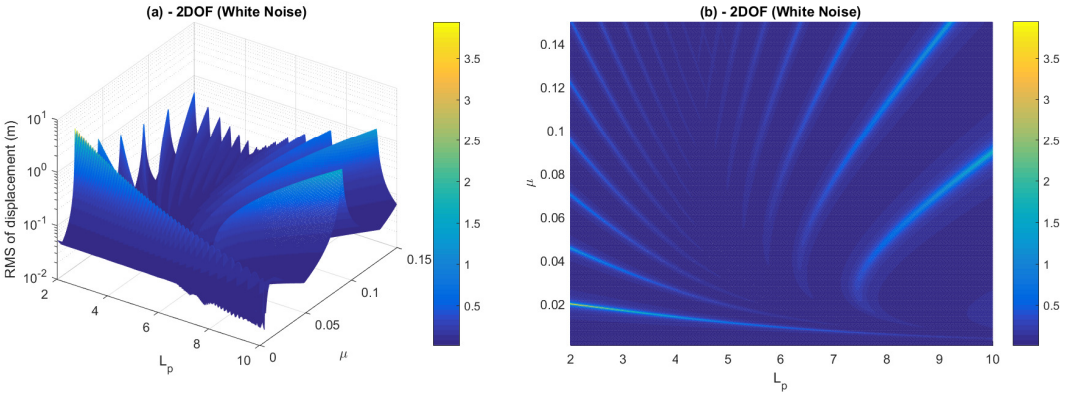

Figure 4.3.6 – 2DOF parametric analysis of the OWT+PTMD (white noise)

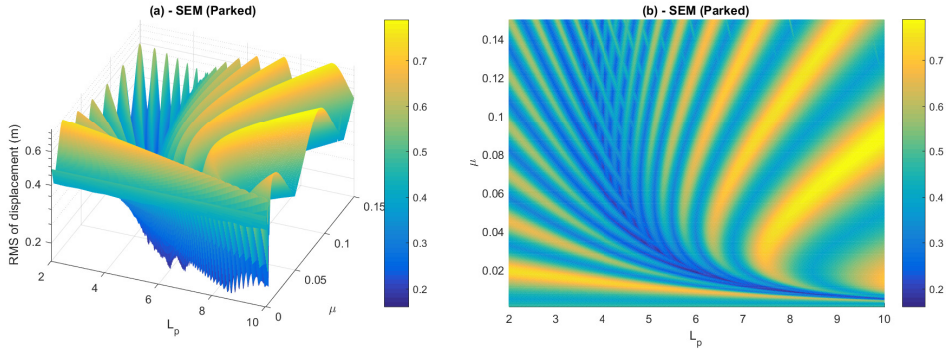

Figure 4.3.7 – SEM parametric analysis of the OWT+PTMD (parked)

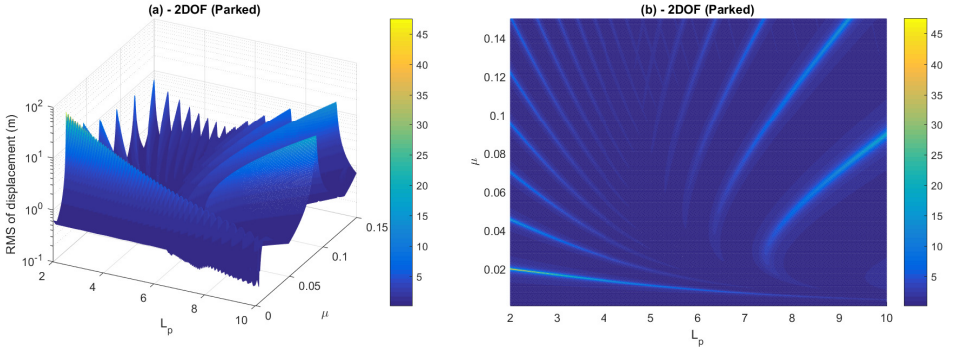

Figure 4.3.8 – 2DOF parametric analysis of the OWT+PTMD (parked)

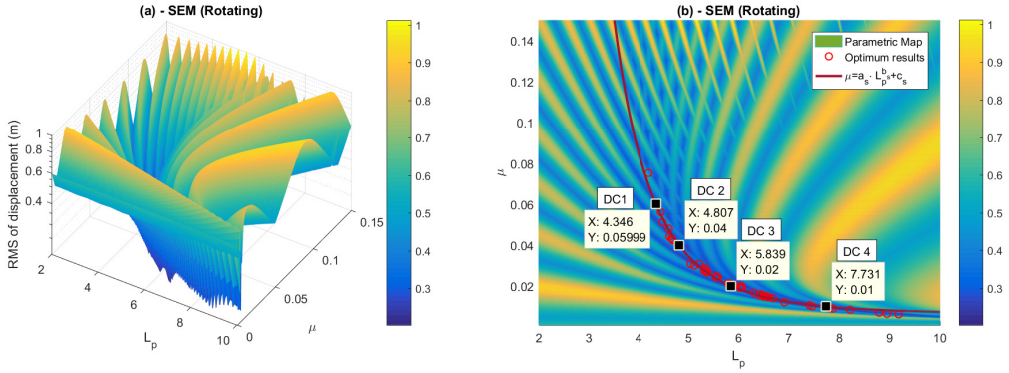

Figure 4.3.9 – SEM parametric analysis of the OWT+PTMD (rotating blades)

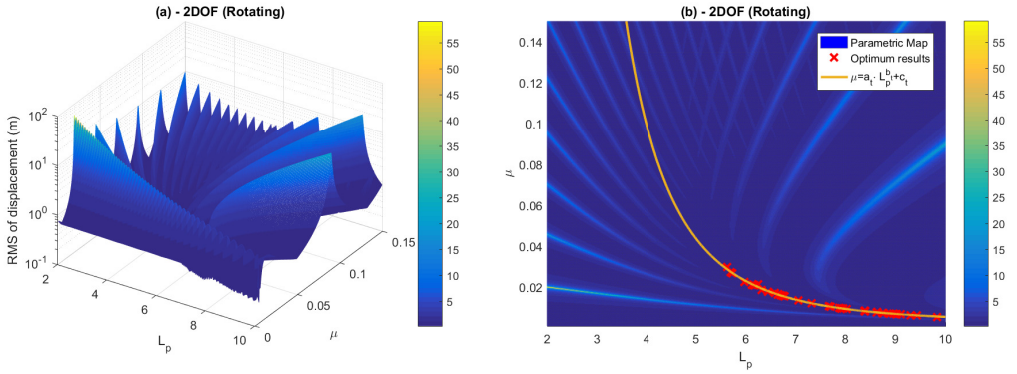

Figure 4.3.10 – 2DOF parametric analysis of the OWT+PTMD (rotating blades)

The optimal PTMD design parameters can be found following the fourth step presented in (19), i.e. implementing an owner GA optimization toolbox, for the rotating blade case. The GA optimization aims as optimum PTMD design the parameters L_p and μ. The fitness function evaluates the maximum peak of the frequency responses obtained by both SEM and 2DOF models. The following was established during the adopted GA optimization:

- $N_{gen} = 50$, number of generations;
- $N_{ind} = 25$, number of individuals in the population;
- $p_c = 60\%$, crossover probability;
- $p_m = 2\%$, mutation probability;
- $p_{elit} = 2\%$, elitism probability;
- $p_{dec} = 20\%$, decimation rate;
- $N_{dec} = 10$, step of generation for the occurrence of decimation.

The fitting curve of the best approximation for both mentioned curves takes a power regression form of $\mu = a \cdot x^b + c$, with $a_s = 47.159$, $b_s = -4.612$ and $c_s = 0.00623$ with R-square of 0.9911 and the sum of squares due to error (SSE) of $1.11 \cdot 10^{-4}$, for the SEM regression and $a_t = 20.176$, $b_t = -3.851$, and $c_t = 0.00260$, with R-square of 0.9972

and SSE of $5.37 \cdot 10^{-6}$ for the 2DOF regression. Figure 4.3.11 shows the power regression comparison of both SEM and 2DOF models presenting a SSE between them of 3.36%.

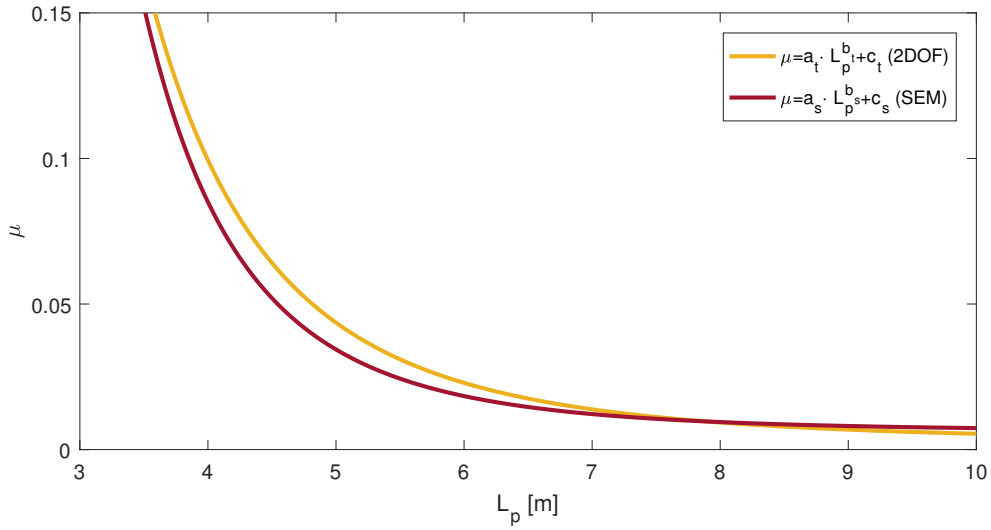

Figure 4.3.11 – Optimization power regression comparison between 2DOF and SEM OWT+PTMD models

Four design cases (DC), shown in Fig. 4.3.9 (b), have been selected for analysis for $\mu \approx [0.02; 0.04; 0.06; 0.08]$. Their frequency responses are compared in Fig. 4.3.12 for the rotating blade condition. As expected, the maximum frequency peaks of each DC presents values near them due to the fitness goal of the optimization. It also can be noticed that the pendulum mass increases the distance between both PSD peaks for the presented frequency range.

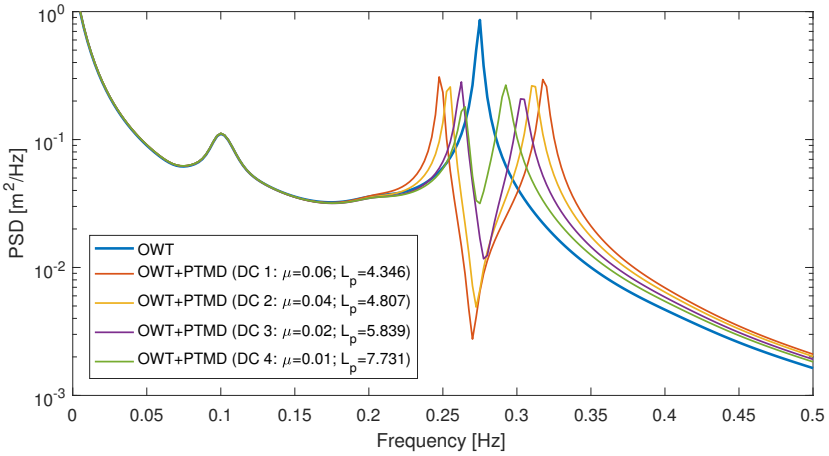

Figure 4.3.12 – PSD of selected DCs for rotating blade conditions

Figures 4.3.13, 4.3.14, 4.3.15, and 4.3.16 present the SEM and 2DOF PSD frequency responses for the DC 1, DC 2, DC 3, and DC 4, respectively, for the white noise, parked, and rotating blade conditions. These figures show how the environmental PSD loads affect the white noise 2DOF model, given a realistic approach.

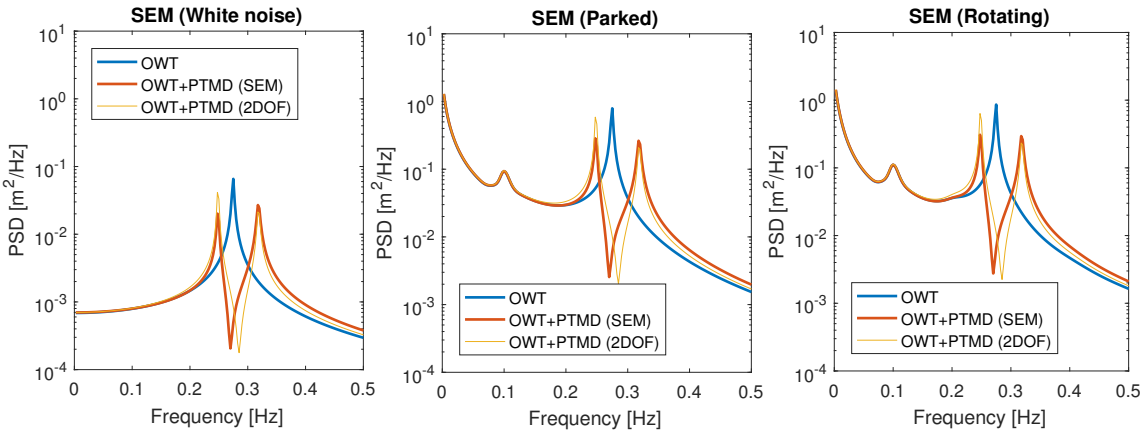

Figure 4.3.13 – PSD of DC 1

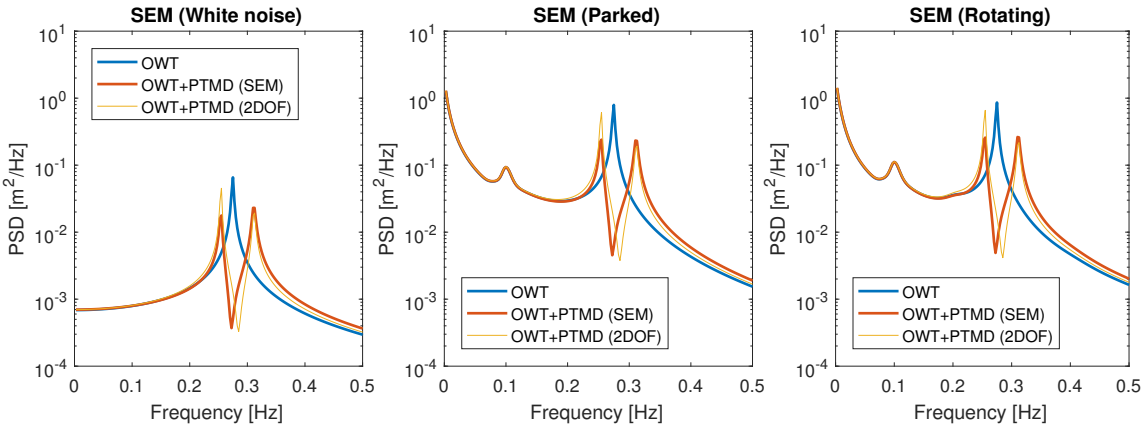

Figure 4.3.14 – PSD DC 2

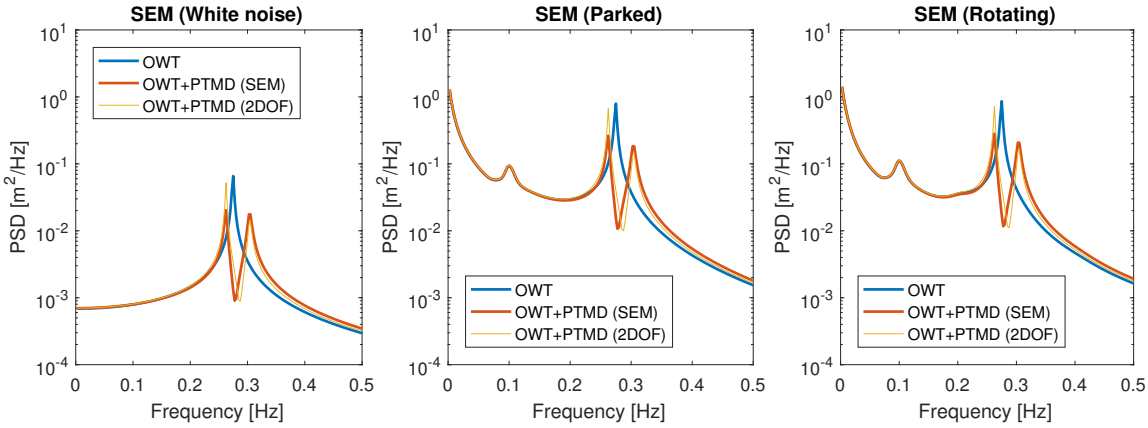

Figure 4.3.15 – PSD of DC 3

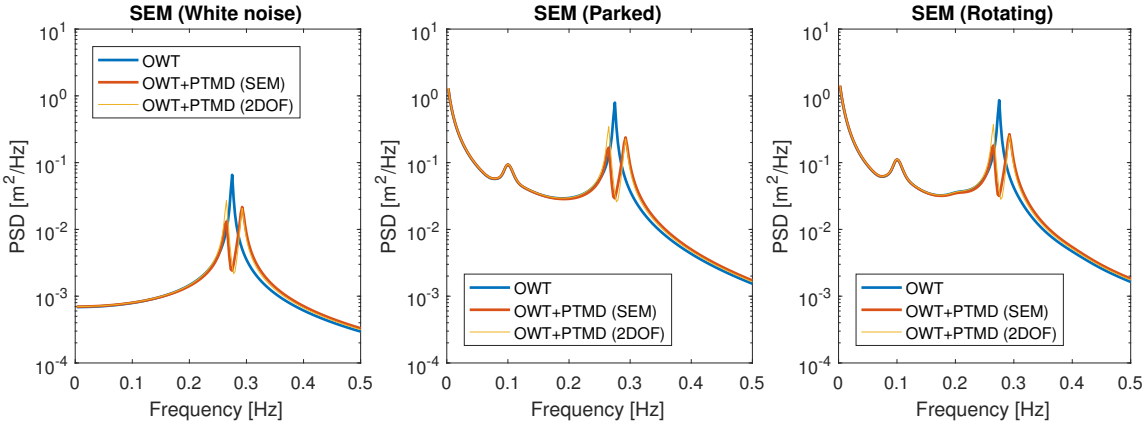

Figure 4.3.16 – PSD of DC 4

The DC 2 is selected and its PSD response for both SEM and FEM models are shown in Figure 4.3.17, for the rotating blade conditions. It can be noticed that while the OWT without control presents frequency response and shapes near between both models, the results between the controlled models are quite different. This can be explained due to the FEM model be a model that uses a three-dimensional PTMD (3D-PTMD) and a detailed geometry model.

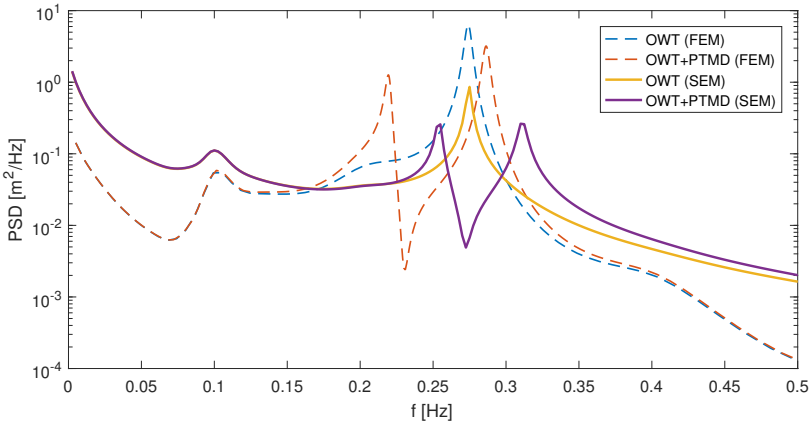

Figure 4.3.17 – PSD comparison between the FEM (120) and SEM models for the OWT coupled to the PTMD

Among the methods presented, the SEM model showed a good relationship between OpenFAST and the numerical models present in the literature. In addition to being the most efficient in computational time, this model presents an accuracy in estimating the dynamic response of OTW and OTW+PTMD, showing an alternative method for studies in wind turbines and a powerful tool when combined with a genetic algorithm optimization.

4.3.3 Case study 3 conclusions

The present case study proposes an optimal PTMD design to mitigate the vibration of OWT in the FA direction in operational condition using spectral elements. The study is conducted in a frequency PSD analysis by implementing the spectra of the wind and wave actions. The PTMD is attached to the end node in the spectral matrix model by adding 2DOF to the system. The SEM tower model is validated by comparing the frequency response of the tower-top with MDOF, beam, and shell FEM models. The SEM OWT model frequency response is also validated with a realistic FEM and simulated OpenFAST models.

A parametric analysis of the SEM and 2DOF models shows that both generated maps of the peak displacements in function of the pendulum length and mass-ratio have similar shapes. A PTMD design procedure is proposed by performing a genetic optimization for both SEM and 2DOF models in operational condition, taken as fitness function the maximum response peaks using the same design parameters. Both models present a residual sum of squares of 3.36%.

Four design cases are selected and their frequency responses are compared for white noise, parked, and operating conditions, revealing the effects of the PSD loads over the OWT. The frequency response of the specific design case 2, in operational condition, presents different natural frequencies in comparison to the FEM model. Despite this, the OWT+PTMD SEM model represents well the magnitude and shape of the response function taking a computational cost 65 times faster, being a powerful tool that enables an efficient way to reach the optimum PTMD design using genetic algorithms.

5 General conclusions

This doctoral thesis proposes a new optimization methodology for a realistic offshore wind turbine capable to compute the offshore environmental loads on the turbine. A genetic optimization is applied to find the optimum PTMD design to minimize the tower-top response. Using genetic optimization allows finding many combinations of optimal mass damper design parameters that reach similar peak response reduction, allowing the temporary switching of different rearrangement of pendulum parameters. This technique can also be applied for the 2DOF, SEM, and FEM models. The tower-top spectrum of the finite and spectral elements were compared to those obtained from the simulated OpenFAST model presenting a good match between them. Three case studies present design cases of optimal PTMD configurations using a 2DOF, FEM, and SEM models:

- Case study 1 consists of modeling a tower using 2DOF. A GA optimization is capable to identify optimal parameters (flexural rigidity, damping, mass-ratio, and pendulum length) of a PTMD, minimizing its peak displacement. Case studies 2 and 3 take the NREL monopile 5-MW OWT as a baseline.

- Case study 2 models a FEM OWT with a PTMD attached. The finite model was performed for realistic characteristics of OWTs and uses the 2DOF model for the fast selection of optimal mass damper configurations. This model allows a fast investigation of the performance at different wind velocities. The PTMD can mitigate wind- and sea-induced global OWT vibrations both in fore-aft and side-side directions. The pendular peak sway and the stress at the tower base were verified due to the additional pendulum mass. It works for parked and operating conditions varying the wind velocity. It was noticed a 20% response peak reduction. The FEM model is 60 times faster than the OpenFAST model.

- Case study 3 design an optimal PTMD+OWT system, using a spectral element approach, mitigating wind- and sea- induced global OWT vibrations in the fore-aft direction. A simplified tower with tip mass was modeled using spectral elements finding a perfect match when compared to the finite element, multi-, single-, and two-degrees-of-freedom models. A parametric and a GA optimization analysis are conduct finding optimal DCs for both PTMD+OWT 2DOF and SEM models. The spectral model is 4000 times faster than the OpenFAST model

The frequency response of the specific DC 2 of the SEM model (case study 3), in operational condition, presents a slight difference of natural frequencies in comparison to the FEM model (case study 2). Despite this, the OWT+PTMD SEM model represents well the magnitude and shape of the response function taking a computational cost 65 times faster, being a powerful tool that enables an efficient way to reach the optimum PTMD design using GA.

Bibliography

1 GWEC. *Global wind report annual market update 2019*. [S.l.], 2020. Quoted 2 times on pages 1 and 2.

2 KANG, N.; PARK, S. C.; PARK, J.; ATLURI, S. N. Dynamics of flexible tower-blade and rigid nacelle system: dynamic instability due to their interactions in wind turbine. *Journal of Vibration and Control*, v. 22, n. 3, p. 826–836, 2016. Available from Internet: <http://dx.doi.org/10.1177/1077546314532119>. Quoted on page 2.

3 ZUO, H.; BI, K.; HAO, H. A state-of-the-art review on the vibration mitigation of wind turbines. *Renewable and Sustainable Energy Reviews*, Pergamon, v. 121, p. 109710, 2020. ISSN 18790690. Available from Internet: <https://www.sciencedirect.com/science/article/pii/S1364032120300083>. Quoted 2 times on pages 2 and 65.

4 SOONG, T.; SPENCER, B. Supplemental energy dissipation: state-of-the-art and state-of-the-practice. *Engineering Structures*, v. 24, n. 3, p. 243 – 259, 2002. ISSN 0141-0296. Available from Internet: <http://www.sciencedirect.com/science/article/pii/S014102960100092X>. Quoted 2 times on pages 2 and 63.

5 PETRINI, F.; LI, H.; BONTEMPI, F. Basis of design and numerical modeling of offshore wind turbines. v. 36, p. 599–624, 11 2010. Quoted 3 times on pages 2, 16, and 55.

6 MANENTI, S.; PETRINI, F. Dynamic analysis of an offshore wind turbine: Wind-waves nonlinear interaction. In: _____. *Earth and Space*. [s.n.], 2010. p. 2014–2026. Available from Internet: <https://ascelibrary.org/doi/abs/10.1061/41096%28366%29184>. Quoted 3 times on pages 2, 6, and 72.

7 ZIENKIEWICZ, O. C.; TAYLOR, R. L. *The Finite Element Method*. fourth. London: McGraw-Hill, 1991. Quoted on page 2.

8 DOYLE, J. F. *Wave propagation in structures : spectral analysis using fast discrete Fourier transforms*. Second. New York: Springer-Verlag New York, Inc., 1997. (Mechanical engineering). Quoted 2 times on pages 2 and 77.

9 LEE, U. *Spectral Element Method in Structural Dynamics*. John Wiley & Sons, Ltd, 2009. ISBN 9780470823767. Available from Internet: <https://onlinelibrary.wiley.com/doi/abs/10.1002/9780470823767.fmatter>. Quoted 2 times on pages 2 and 77.

10 SONG, Y.; KIM, T.; LEE, U. Vibration of a beam subjected to a moving force: Frequency-domain spectral element modeling and analysis. *International Journal of Mechanical Sciences*, v. 113, p. 162 – 174, 2016. ISSN 0020-7403. Available from Internet: <http://www.sciencedirect.com/science/article/pii/S0020740316300431>. Quoted on page 2.

11 GOPALAKRISHNAN, S. *Wave propagation in materials and structures*. CRC Press, 2016. ISBN 9781315354897. Available from Internet: <https://books.google.com.br/books?id=s5-KDQAAQBAJ>. Quoted on page 2.

12 DUTKIEWICZ, M.; MACHADO, M. Spectral element method in the analysis of vibrations of overhead transmission line in damping environment. *Structural Engineering and Mechanics*, v. 71(3), p. 291–303, 2019. Available from Internet: <https://doi.org/10.12989/sem.2019.71.3.291>. Quoted on page 2.

13 MACHADO, M.; DUTKIEWICZ, M.; MATT, C.; CASTELLO, D. Spectral model and experimental validation of hysteretic and aerodynamic damping in dynamic analysis of overhead transmission conductor. *Mechanical Systems and Signal Processing*, v. 136, p. 106483, 2020. ISSN 0888-3270. Available from Internet: <http://www.sciencedirect.com/science/article/pii/S0888327019307046>. Quoted on page 2.

14 DUTKIEWICZ, M.; M.R.MACHADO. Spectral approach in vibrations of overhead transmission lines. *IOP Conference Series: Materials Science and Engineering*, v. 471, p. Session 4, 2019. Available from Internet: <https://doi.org/10.1088/1757-899x/471/5/052029>. Quoted on page 2.

15 DUTKIEWICZ, M.; M.R.MACHADO. Dynamic response of overhead transmission line in turbulent wind flow with application of the spectral element method. *IOP Conference Series: Materials Science and Engineering*, v. 471, p. Session 5, 2019. Available from Internet: <https://doi.org/10.1088/1757-899x/471/5/052031>. Quoted on page 2.

16 KIM, T.; LEE, U. Modified one-element method for exact dynamic responses of a beam by using the frequency domain spectral element method. *International Journal of Mechanical Sciences*, v. 119, p. 333 – 342, 2016. ISSN 0020-7403. Available from Internet: <http://www.sciencedirect.com/science/article/pii/S0020740316306014>. Quoted on page 2.

17 KIM, T.; LEE, B.; LEE, U. State-vector equation method for the frequency domain spectral element modeling of non-uniform one-dimensional structures. *International Journal of Mechanical Sciences*, v. 157-158, p. 75 – 86, 2019. ISSN 0020-7403. Available from Internet: <http://www.sciencedirect.com/science/article/pii/S0020740318328522>. Quoted on page 2.

18 JONKMAN, J. M.; MUSIAL, W. Book, Online. *Offshore Code Comparison Collaboration (OC3) for IEA Task 23 Offshore Wind Technology and Deployment [electronic resource]*. National Renewable Energy Laboratory, 2010. v, 70 p. Available from Internet: <https://www.nrel.gov/docs/fy11osti/48191.pdf>. Quoted 7 times on pages ix, 3, 60, 61, 62, 91, and 93.

19 COLHERINHAS, G. B.; MORAIS, M. V. G. de; SHZU, M. A. M.; AVILA, S. M. Optimal pendulum tuned mass damper design applied to high towers using genetic algorithms: Two-dof modeling. *International Journal of Structural Stability and Dynamics*, v. 19, n. 10, p. 1950125, 2019. Available from Internet: <https://doi.org/10.1142/S0219455419501256>. Quoted 12 times on pages ix, x, 3, 79, 80, 84, 91, 94, 99, 102, 106, and 128.

20 LI, J.; CHEN, J. *Stochastic Dynamics of Structures*. [S.l.]: John Wiley and Sons (Asia), 2009. ISBN 978-0-470-82424-5. Quoted 2 times on pages 5 and 48.

21 PETRINI, F.; GIARALIS, A.; WANG, Z. Optimal tuned mass-damper-inerter (tmdi) design in wind-excited tall buildings for occupants' comfort serviceability performance and energy harvesting. *Engineering Structures*, v. 204, p. 109904, 2020. ISSN 0141-0296. Available from Internet: <http://www.sciencedirect.com/science/article/pii/S0141029619310983>. Quoted on page 6.

22 CIAMPOLI, M.; PETRINI, F. Performance-based design of offshore wind turbines. In: _____. *Earth and Space*. [S.l.: s.n.], 2010. Quoted 2 times on pages 6 and 16.

23 ABNT. *ABNT NBR 6123 - Forças devidas ao vento em edificações*. Rio de Janeiro: Comissão de Estudo de Forças Devidas ao Vento em Edificações, 1988. Quoted on page 7.

24 CNR. *CNR DT 207/2008 - Istruzioni per la valutazione delle azioni e degli effetti del vento sulle costruzioni*. Roma: Commissione di studio per la predisposizione e l'analisi di norme tecniche relative alle costruzioni, 2009. Quoted 3 times on pages 7, 9, and 13.

25 IEC. *Wind turbines - Part 1: Design requirements*. International Standard: International Electrotechnical Commission (IEC) 61400-1, 2005. Quoted 9 times on pages 8, 11, 12, 14, 17, 52, 57, 58, and 62.

26 DNV. *Design of Offshore Wind Turbine Structures*. Det Norske Veritas AS: DNV-OS-J101 - Offshore Standard, 2014. Quoted 6 times on pages 9, 10, 16, 17, 38, and 52.

27 BURTON, T.; DAVID, S.; JENKINS, N.; BOSSANYI, E. *Wind energy: handbook*. J. Wiley, 2001. ISBN 9780471489979. Available from Internet: <https://books.google.it/books?id=m9dSAAAAMAAJ>. Quoted 21 times on pages 10, 11, 13, 14, 15, 18, 20, 22, 25, 26, 27, 28, 29, 30, 31, 32, 33, 56, 57, 74, and 80.

28 IEC. *Wind turbines - Part 3: Design requirements for offshore wind turbines*. International Standard: International Electrotechnical Commission (IEC) 61400-3, 2009. Quoted 3 times on pages 14, 30, and 55.

29 MANWELL J. G. MCGOWAN, A. L. R. J. F. *Wind Energy Explained: Theory, Design and Application*. Second edition. [S.l.]: John Wiley & Sons, 2009. ISBN 978-0-470-01500-1. Quoted 4 times on pages 15, 54, 55, and 56.

30 KARMAN, T. V. Progress in the statistical theory of turbulence. *Proceedings of the National Academy of Sciences*, National Acad Sciences, v. 34, n. 11, p. 530–539, 1948. Quoted on page 15.

31 ESDU. *Characteristics of atmospheric turbulence near the ground. Part II: single point data for strong winds (neutral atmosphere)*. [S.l.]: EDSU 85020, Engineering Sciences Data Unit, 1993. Quoted on page 16.

32 SOLARI, G.; PICCARDO, G. Probabilistic 3-d turbulence modeling for gust buffeting of structures. *Probabilistic Engineering Mechanics*, v. 16, n. 1, p. 73 – 86, 2001. ISSN 0266-8920. Available from Internet: <http://www.sciencedirect.com/science/article/pii/S0266892000000102>. Quoted on page 16.

33 ESDU. *Characteristics of atmospheric turbulence near the ground. Part III: Variations in space and time for strong winds (neutral atmosphere)*. [S.l.]: ESDU 75001, Engineering Sciences Data Unit, 1975. Quoted on page 16.

34 JONKMAN, J. M.; BUTTERFIELD, S.; MUSIAL, W.; SCOTT, G. Book, Online. *Definition of a 5-MW reference Wind Turbine for Offshore System Development [electronic resource]*. National Renewable Energy Laboratory, 2009. x, 63 p. Available from Internet: <https://www.nrel.gov/docs/fy09osti/38060.pdf>. Quoted 9 times on pages 17, 23, 24, 53, 62, 68, 71, 80, and 104.

35 HANSEN, M. *Aerodynamics of Wind Turbines*. Earthscan, 2013. ISBN 9781849770408. Available from Internet: <https://books.google.it/books?id=GVD_HDPix6YC>. Quoted 5 times on pages 18, 21, 22, 25, and 26.

36 E., W. R.; LISSAMAN, P. B. S. Applied aerodynamics of wind power-machines. NTIS: PB-238-595, Oregon State University, Oregon, 1974. Quoted on page 22.

37 DOWEC 6 MW Pre-Design: Aero-elastic modeling of the DOWEC 6 MW pre-design in PHATAS", author =. Quoted on page 23.

38 GLAUERT, H. Airplane propellers. In: _____. *Aerodynamic Theory: A General Review of Progress Under a Grant of the Guggenheim Fund for the Promotion of Aeronautics*. Berlin, Heidelberg: Springer Berlin Heidelberg, 1935. ISBN 978-3-642-91487-4. Available from Internet: <https://doi.org/10.1007/978-3-642-91487-4_3>. Quoted on page 26.

39 BATCHELOR, G. *The Theory of Homogeneous Turbulence*. Cambridge University Press, 1953. (Cambridge Science Classics). ISBN 9780521041171. Available from Internet: <https://books.google.it/books?id=POG-LSUgYckC>. Quoted on page 29.

40 BORRI, C.; PASTò. *Lezioni di ingegneria del vento*. [S.l.]: Firenze: Universit Press (in italian), 2006. Quoted on page 34.

41 SIMIU, E.; SCANLAN, R. H. *Wind effects on structures : fundamentals and applications to design*. 3rd. ed. [S.l.]: New York: John Wiley, 1996. Quoted on page 34.

42 BREBBIA, C.; WALKER, S. *Dynamic Analysis of Offshore Structures*. Newnes, 1979. ISBN 978-0-408-00393-3. Available from Internet: <http://www.sciencedirect.com/science/article/pii/B9780408003933500035>. Quoted 9 times on pages 34, 36, 42, 44, 45, 46, 47, 48, and 51.

43 CHANDRASEKARAN, S. *Dynamic Analysis and Design of Offshore Structures*. [S.l.]: Springer India, 2015. 1-287 p. Quoted on page 37.

44 SARPKAYA, T.; ISAACSON, M. *Mechanics of wave forces on offshore structures*. Van Nostrand Reinhold Co., 1981. ISBN 9780442254025. Available from Internet: <https://books.google.it/books?id=CVG6AAAAIAAJ>. Quoted on page 37.

45 LEMÉHAUTÉ, B. *An introduction to hydrodynamics and water waves*. Springer-Verlag, 1976. ISBN 9783540072324. Available from Internet: <https://books.google.it/books?id=Rn8pAQAAMAAJ>. Quoted 2 times on pages 37 and 38.

46 DNVGL. *Recommended practice: environmental conditions and environmental loads*. [S.l.]: DNV-GL-RP-C205, 2017. Quoted 5 times on pages 39, 41, 42, 50, and 74.

47 CHAKRABARTI, S. *Hadbook of Offshore Engineering - Volume 1*. [S.l.]: Elsevier, 2005. Quoted on page 41.

48 RICE, S. O. Mathematical analysis of random noise. *The Bell System Technical Journal*, v. 24, n. 1, p. 46–156, Jan 1945. ISSN 0005-8580. Quoted on page 43.

49 MORISON, J.; CALIFORNIA, B. F. M. L. University of. *The Force Exerted by Surface Waves on Piles*. University of California, Department of Engineering, Fluid Mechanics Laboratory, 1949. (Technical report ser. H-116). Available from Internet: <https://books.google.it/books?id=pZkRHQAACAAJ>. Quoted on page 46.

50 KEULEGAN, G. H.; CARPENTER, L.; RESEARCH, U. S. O. of N. *Forces on Cylinders and Plates in an Oscillating Fluid*. U.S. Department of Commerce, National Bureau of Standards, 1956. (NBS report). Available from Internet: <https://books.google.it/books?id=cnJRAQAAMAAJ>. Quoted on page 49.

51 CHAKRABARTI, S. *Hydrodynamics of Offshore Structures*. Computational Mechanics, 1987. ISBN 9780905451664. Available from Internet: <https://books.google.it/books?id=RNGW9CucxQsC>. Quoted on page 49.

52 NEUMANN, G.; METEOROLOGY, N. Y. U. D. of; OCEANOGRAPHY. *On Ocean Wave Spectra and a New Method of Forecasting Wind-generated Sea*. U.S. Beach Erosion Board, 1953. (Technical memorandum - Beach Erosion Board). Available from Internet: <https://books.google.it/books?id=_lIrnQEACAAJ>. Quoted on page 51.

53 CHAKRABARTI, S.; SNIDER, R. *Modelling of wind waves with JONSWAP spectra*. [S.l.]: Proc. Modelling, 1975. Quoted 2 times on pages 52 and 53.

54 GL. Renewables Certification, *Guideline for the Certification of Offshore Wind Turbines*. 2012. Nenhuma citação no texto.

55 PASSON, P.; KüHN, M.; BUTTERFIELD, S.; JONKMAN, J.; CAMP, T.; LARSEN, T. J. Oc3—benchmark exercise of aero-elastic offshore wind turbine codes. *Journal of Physics: Conference Series*, v. 75, n. 1, p. 012071, 2007. Available from Internet: <http://stacks.iop.org/1742-6596/75/i=1/a=012071>. Quoted on page 60.

56 JONKMAN, J.; BUTTERFIELD, S.; PASSON, P.; LARSEN, T.; CAMP, T.; NICHOLS, J.; AZCONA, J.; MARTINEZ, A. *Offshore code comparison collaboration within IEA wind annex XXIII: Phase II results regarding monopile foundation modeling*. [S.l.]: National Renewable Energy Laboratory (NREL), 2008. Quoted on page 60.

57 NICHOLS, J. A.; (U.S.), N. R. E. L. Book, Online. *Offshore code comparison collaboration within IEA Wind Annex XXIII. phase III, results regarding tripod support structure modeling [electronic resource] / J. Nichols ... [et al.]*. [S.l.]: National Renewable Energy Laboratory Golden, CO, 2009. 1 online resource (21 p.) : p. Quoted on page 60.

58 JONKMAN, J.; LARSEN, T.; HANSEN, A.; NYGAARD, T.; MAUS, K.; KARIMIRAD, M.; GAO, Z.; MOAN, T.; FYLLING, I.; NICHOLS, J.; KOHLMEIER, M.; VERGARA, J.; MERINO, D.; SHI, W.; PARK, H. Offshore code comparison collaboration within iea wind task 23:phase iv results regarding floating wind turbine modeling: 2010 european wind energy conference (ewec) 20-23 april 2010, warsaw, poland, april 2010. In: . [s.n.], 2010. European Wind Energy Conference : EWEC2010, EWEC2010 ; Conference date: 20-04-2010 Through 23-04-2010. Available from Internet: <http://www.ewea.org/ewec2010/conference/conference-proceedings/>. Quoted on page 60.

59 HJT, K.; C, L.; D, W.; EL van der H. Dowec 6 mw pre-design: Aero-elastic modeling of the dowec 6 mw pre-design in phatas. ecn-cx–01-135, dowec 10046009. Energy Research Center of the Netherlands, 2003. Quoted on page 61.

60 RAHMAT-SAMII, Y.; MICHIELSSEN, E. *Electromagnetic Optimization by Genetic Algorithms*. Wiley, 1999. (Wiley Series in Microwave and Optical Engineering). ISBN 9780471295457. Available from Internet: <https://books.google.com.br/books?id=0x5TAAAAMAAJ>. Quoted on page 63.

61 HE, E.-M.; HU, Y.-Q.; ZHANG, Y. Optimization design of tuned mass damper for vibration suppression of a barge-type offshore floating wind turbine. *Proceedings of the Institution of Mechanical Engineers, Part M: Journal of Engineering for the Maritime Environment*, v. 231, n. 1, p. 302–315, 2017. Available from Internet: <https://doi.org/10.1177/1475090216642466>. Quoted 2 times on pages 63 and 65.

62 NIGDELI, S. M.; BEKDAŞ, G. Optimum tuned mass damper design in frequency domain for structures. *KSCE Journal of Civil Engineering*, v. 21, n. 3, p. 912–922, Mar 2017. ISSN 1976-3808. Available from Internet: <https://doi.org/10.1007/s12205-016-0829-2>. Quoted 2 times on pages 63 and 66.

63 YILMAZ, O. C. *The Optimization of Offshore Wind Turbine Towers Using Passive Tuned Mass Dampers*. 2014. Master thesis of Science in Mechanical Engineering. Quoted 2 times on pages 63 and 65.

64 STEWART, G. M.; LACKNER, M. A. The impact of passive tuned mass dampers and wind–wave misalignment on offshore wind turbine loads. *Engineering Structures*, v. 73, p. 54 – 61, 2014. ISSN 0141-0296. Available from Internet: <http://www.sciencedirect.com/science/article/pii/S0141029614002673>. Quoted 2 times on pages 63 and 65.

65 LACKNER, M. A.; ROTEA, M. A. Passive structural control of offshore wind turbines. *Wind Energy*, John Wiley & Sons, Ltd., v. 14, n. 3, p. 373–388, 2011. ISSN 1099-1824. Available from Internet: <http://dx.doi.org/10.1002/we.426>. Quoted 2 times on pages 63 and 65.

66 HOUSNER, G. W.; BERGMAN, L. A.; CAUGHEY, T. K.; CHASSIAKOS, A. G.; CLAUS, R. O.; MASRI, S. F.; SKELTON, R. E.; SOONG, T. T.; SPENCER, B. F.; YAO, J. T. P. Structural control: Past, present, and future. *Journal of Engineering Mechanics*, v. 123, n. 9, p. 897–971, 1997. Quoted on page 63.

67 RAHMAN, M.; ONG, Z. C.; CHONG, W. T.; JULAI, S.; KHOO, S. Y. Performance enhancement of wind turbine systems with vibration control: A review. *Renewable and Sustainable Energy Reviews*, v. 51, p. 43 – 54, 2015. ISSN 1364-0321. Available from Internet: <https://www.sciencedirect.com/science/article/pii/S1364032115005602>. Quoted 3 times on pages 64, 65, and 69.

68 STAINO, A.; BASU, B. Dynamics and control of vibrations in wind turbines with variable rotor speed. *Engineering Structures*, v. 56, p. 58 – 67, 2013. ISSN 0141-0296. Available from Internet: <http://www.sciencedirect.com/science/article/pii/S0141029613001375>. Quoted on page 64.

69 KRENK, S.; SVENDSEN, M. N.; HØGSBERG, J. Resonant vibration control of three-bladed wind turbine rotors. *AIAA journal*, v. 50, n. 1, p. 148–161, 2012. Quoted on page 64.

70 MARTYNOWICZ, P. Control of a magnetorheological tuned vibration absorber for wind turbine application utilising the refined force tracking algorithm. *Journal of Low Frequency Noise, Vibration and Active Control*, v. 36, n. 4, p. 339–353, 2017. Available

from Internet: <https://doi.org/10.1177/1461348417744299>. Quoted 2 times on pages 64 and 69.

71 KARIMI, H. R.; ZAPATEIRO, M.; LUO, N. Semiactive vibration control of offshore wind turbine towers with tuned liquid column dampers using hinfty output feedback control. In: *2010 IEEE International Conference on Control Applications*. [S.l.: s.n.], 2010. p. 2245–2249. ISSN 1085-1992. Quoted on page 64.

72 WEBER, F. Semi-active vibration absorber based on real-time controlled mr damper. *Mechanical Systems and Signal Processing*, v. 46, n. 2, p. 272 – 288, 2014. ISSN 0888-3270. Available from Internet: <http://www.sciencedirect.com/science/article/pii/S0888327014000508>. Quoted on page 64.

73 SOONG, T.; DARGUSH, G. *Passive Energy Dissipation Systems in Structural Engineering*. Wiley, 1997. ISBN 9780471968214. Available from Internet: <https://books.google.com.br/books?id=OxBmQgAACAAJ>. Quoted 4 times on pages 65, 70, 78, and 81.

74 CARNEIRO, R. B.; AVILA, S. M.; BRITO, J. L. V. de. Parametric study on multiple tuned mass dampers using interconnected masses. *International Journal of Structural Stability and Dynamics*, v. 08, n. 01, p. 187–202, 2008. Available from Internet: <http://www.worldscientific.com/doi/abs/10.1142/S0219455408002600>. Quoted on page 65.

75 MURTAGH, P. J.; GHOSH, A.; BASU, B.; BRODERICK, B. M. Passive control of wind turbine vibrations including blade/tower interaction and rotationally sampled turbulence. *Wind Energy*, v. 11, n. 4, p. 305–317, 2007. Available from Internet: <https://onlinelibrary.wiley.com/doi/abs/10.1002/we.249>. Quoted on page 65.

76 STEWART, G. M. Load reduction of floating wind turbines using tuned mass dampers. 2012. Quoted on page 65.

77 MENSAH, A. F.; DUEñAS-OSORIO, L. Improved reliability of wind turbine towers with tuned liquid column dampers (tlcds). *Structural Safety*, v. 47, p. 78 – 86, 2014. ISSN 0167-4730. Available from Internet: <http://www.sciencedirect.com/science/article/pii/S0167473013000593>. Quoted 3 times on pages 65, 68, and 69.

78 HUSSAN, M.; RAHMAN, M. S.; SHARMIN, F.; KIM, D.; DO, J. Multiple tuned mass damper for multi-mode vibration reduction of offshore wind turbine under seismic excitation. *Ocean Engineering*, v. 160, p. 449 – 460, 2018. ISSN 0029-8018. Available from Internet: <http://www.sciencedirect.com/science/article/pii/S0029801818305237>. Quoted on page 65.

79 SUN, C.; JAHANGIRI, V. Bi-directional vibration control of offshore wind turbines using a 3d pendulum tuned mass damper. *Mechanical Systems and Signal Processing*, v. 105, p. 338 – 360, 2018. ISSN 0888-3270. Available from Internet: <http://www.sciencedirect.com/science/article/pii/S0888327017306465>. Quoted 4 times on pages ix, 65, 68, and 78.

80 ZHAO, B.; GAO, H.; WANG, Z.; LU, Z. Shaking table test on vibration control effects of a monopile offshore wind turbine with a tuned mass damper. *Wind Energy*, v. 21, n. 12, p. 1309–1328, 2018. ISSN 10991824. Available from Internet: <https://onlinelibrary.wiley.com/doi/abs/10.1002/we.2256>. Quoted on page 65.

81 GHASSEMPOUR, M.; FAILLA, G.; ARENA, F. Vibration mitigation in offshore wind turbines via tuned mass damper. *Engineering Structures*, v. 183, p. 610 – 636, 2019. ISSN 0141-0296. Available from Internet: <http://www.sciencedirect.com/science/article/pii/S0141029618315220>. Quoted 3 times on pages 65, 91, and 99.

82 PARK, S.; LACKNER, M. A.; POURAZARM, P.; Rodríguez Tsouroukdissian, A.; CROSS-WHITER, J. An investigation on the impacts of passive and semiactive structural control on a fixed bottom and a floating offshore wind turbine. *Wind Energy*, John Wiley & Sons, Ltd, v. 22, n. 11, p. 1451–1471, nov 2019. ISSN 1095-4244. Available from Internet: <https://doi.org/10.1002/we.2381>. Quoted on page 65.

83 JU, S. H.; HUANG, Y. C. Mtmd to increase fatigue life for owt jacket structures using powell's method. *Marine Structures*, p. 102726, 2020. ISSN 09518339. Available from Internet: <https://www.sciencedirect.com/science/article/pii/S0951833920300204?via%3Dihub>. Quoted on page 65.

84 MURTAGH, P. J.; GHOSH, A.; BASU, B.; BRODERICK, B. M. Passive control of wind turbine vibrations including blade/tower interaction and rotationally sampled turbulence. *Wind Energy*, v. 11, n. 4, p. 305–317. Available from Internet: <https://onlinelibrary.wiley.com/doi/abs/10.1002/we.249>. Quoted on page 65.

85 MARANO, G. C.; SGOBBA, S.; GRECO, R.; MEZZINA, M. Robust optimum design of tuned mass dampers devices in random vibrations mitigation. *Journal of Sound and Vibration*, v. 313, n. 3, p. 472 – 492, 2008. ISSN 0022-460X. Available from Internet: <http://www.sciencedirect.com/science/article/pii/S0022460X07009868>. Quoted on page 65.

86 BAKRE, S. V.; JANGID, R. S. Optimum parameters of tuned mass damper for damped main system. *Structural Control and Health Monitoring*, John Wiley & Sons, Ltd., v. 14, n. 3, p. 448–470, 2007. ISSN 1545-2263. Available from Internet: <http://dx.doi.org/10.1002/stc.166>. Quoted on page 65.

87 LAVAN, O. Multi-objective optimal design of tuned mass dampers. *Structural Control and Health Monitoring*, v. 24, n. 11, p. e2008–n/a, 2017. ISSN 1545-2263. E2008 stc.2008. Available from Internet: <http://dx.doi.org/10.1002/stc.2008>. Quoted on page 66.

88 TSAI, H.-C.; LIN, G.-C. Optimum tuned-mass dampers for minimizing steady-state response of support-excited and damped systems. *Earthquake Engineering & Structural Dynamics*, John Wiley & Sons, Ltd, v. 22, n. 11, p. 957–973, 1993. ISSN 1096-9845. Available from Internet: <http://dx.doi.org/10.1002/eqe.4290221104>. Quoted on page 66.

89 DESU, N. B.; DEB, S. K.; DUTTA, A. Coupled tuned mass dampers for control of coupled vibrations in asymmetric buildings. *Structural Control and Health Monitoring*, John Wiley & Sons, Ltd., v. 13, n. 5, p. 897–916, 2006. ISSN 1545-2263. Available from Internet: <http://dx.doi.org/10.1002/stc.64>. Quoted 2 times on pages 66 and 131.

90 MARANO, G. C.; GRECO, R.; CHIAIA, B. A comparison between different optimization criteria for tuned mass dampers design. *Journal of Sound and Vibration*, v. 329, n. 23, p. 4880 – 4890, 2010. ISSN 0022-460X. Available from Internet: <http://www.sciencedirect.com/science/article/pii/S0022460X1000341X>. Quoted 2 times on pages 66 and 131.

91 FRANS, R.; ARFIADI, Y. Designing optimum locations and properties of mtmd systems. *Procedia Engineering*, v. 125, n. Supplement C, p. 892 – 898, 2015. ISSN 1877-7058. Civil Engineering Innovation for a Sustainable. Available from Internet: <http://www.sciencedirect.com/science/article/pii/S1877705815033962>. Quoted 2 times on pages 66 and 131.

92 ZHANG, H.; ZHANG, L. Tuned mass damper system of high-rise intake towers optimized by improved harmony search algorithm. *Engineering Structures*, v. 138, n. Supplement C, p. 270 – 282, 2017. ISSN 0141-0296. Available from Internet: <http://www.sciencedirect.com/science/article/pii/S0141029617303917>. Quoted 2 times on pages 66 and 131.

93 STEINBUCH, R. Bionic optimisation of the earthquake resistance of high buildings by tuned mass dampers. *Journal of Bionic Engineering*, v. 8, n. 3, p. 335 – 344, 2011. ISSN 1672-6529. Available from Internet: <http://www.sciencedirect.com/science/article/pii/S167265291160036X>. Quoted 2 times on pages 66 and 131.

94 FARSHIDIANFAR, A.; SOHEILI, S. Ant colony optimization of tuned mass dampers for earthquake oscillations of high-rise structures including soil–structure interaction. *Soil Dynamics and Earthquake Engineering*, v. 51, n. Supplement C, p. 14 – 22, 2013. ISSN 0267-7261. Available from Internet: <http://www.sciencedirect.com/science/article/pii/S0267726113001048>. Quoted 2 times on pages 66 and 131.

95 LEUNG, A.; ZHANG, H. Particle swarm optimization of tuned mass dampers. *Engineering Structures*, v. 31, n. 3, p. 715 – 728, 2009. ISSN 0141-0296. Available from Internet: <http://www.sciencedirect.com/science/article/pii/S0141029608003817>. Quoted 2 times on pages 66 and 131.

96 XU, R.; CHEN, J.; ZHU, X. A hybrid approach for parameter optimization of multiple tuned mass dampers in reducing floor vibrations due to occupant walking: Theory and parametric studies. *Advances in Structural Engineering*, v. 20, n. 8, p. 1232–1246, 2017. Available from Internet: <https://doi.org/10.1177/1369433216684351>. Quoted 2 times on pages 66 and 131.

97 MOHEBBI, M.; SHAKERI, K.; GHANBARPOUR, Y.; MAJZOUB, H. Designing optimal multiple tuned mass dampers using genetic algorithms (gas) for mitigating the seismic response of structures. *Journal of Vibration and Control*, v. 19, n. 4, p. 605–625, 2013. Available from Internet: <https://doi.org/10.1177/1077546311434520>. Quoted 2 times on pages 66 and 131.

98 MORGA, M.; MARANO, G. C. Optimization criteria of tmd to reduce vibrations generated by the wind in a slender structure. *Journal of Vibration and Control*, v. 20, n. 16, p. 2404–2416, 2014. Available from Internet: <https://doi.org/10.1177/1077546313478296>. Quoted on page 66.

99 MURTAGH, P. J.; BASU, B.; BRODERICK, B. M. *Simple models for natural frequencies and mode shapes of towers supporting utilities*. [S.l.: s.n.], 2004. Quoted 3 times on pages 67, 81, and 102.

100 OLIVEIRA, F. d. S.; GOMEZ, A.; AVILA, S. M.; BRITO, J. Design criteria for a pendulum absorber to control high building vibrations. *International Journal od Innovations in Material Science and Engineering (IMSE)*, v. 1, n. 2, p. 82–89, 2014. Quoted 2 times on pages 67 and 71.

101 DERAEMAEKER, A.; SOLTANI, P. A short note on equal peak design for the pendulum tuned mass dampers. *Proceedings of the Institution of Mechanical Engineers, Part K: Journal of Multi-body Dynamics*, v. 231, n. 1, p. 285–291, 2017. Available from Internet: <https://doi.org/10.1177/1464419316652558>. Quoted 2 times on pages 67 and 82.

102 DEN, H. J. P. Mechanical vibrations. fourth edition. mcgraw-hill, new york, 1956. 67s. 6d. *The Journal of the Royal Aeronautical Society*, Cambridge University Press, v. 61, n. 554, p. 139–139, 1957. Available from Internet: <https://doi.org/10.1017/S0368393100131049>. Quoted on page 67.

103 ORLANDO, D.; GONçALVES, P. B. Hybrid nonlinear control of a tall tower with a pendulum absorber. *Structural Engineering and Mechanics*, Techno-Press, v. 46, n. 2, p. 153–177, 2013. Available from Internet: <http://dx.doi.org/10.12989/sem.2013.46.2.153>. Quoted on page 67.

104 XIANG, P.; NISHITANI, A. Structural vibration control with the implementation of a pendulum-type nontraditional tuned mass damper system. *Journal of Vibration and Control*, v. 23, n. 19, p. 3128–3146, 2017. Available from Internet: <https://doi.org/10.1177/1077546315626821>. Quoted on page 67.

105 GERGES, R. R.; VICKERY, B. J. Optimum design of pendulum-type tuned mass dampers. *The Structural Design of Tall and Special Buildings*, John Wiley & Sons, Ltd., v. 14, n. 4, p. 353–368, 2005. ISSN 1541-7808. Available from Internet: <http://dx.doi.org/10.1002/tal.273>. Quoted 3 times on pages 67, 78, and 79.

106 GUIMARÃES, P.; MORAIS, M. de; AVILA, S. Tuned mass damper inverted pendulum to reduce offshore wind turbine vibrations. *Vibration Engineering and Technology of Machinery*, Springer International Publishing, p. 379–388, 2015. Quoted on page 68.

107 BRODERSEN, M. L.; BJøRKE, A.-S.; HøGSBERG, J. Active tuned mass damper for damping of offshore wind turbine vibrations. *Wind Energy*, v. 20, n. 5, p. 783–796. Available from Internet: <https://onlinelibrary.wiley.com/doi/abs/10.1002/we.2063>. Quoted on page 68.

108 AVILA, S. M.; SHZU, M. A. M.; PEREIRA, W. M.; SANTOS, L. S.; MORAIS, M. V. G.; PRADO, Z. J. G. Numerical modeling of the dynamic behavior of a wind turbine tower. Article in Advances in Vibration Engineering, 2016. Quoted 6 times on pages x, 70, 78, 81, 102, and 143.

109 DAVENPORT, A. G. Probabilistic methods in wind engineering for long span bridges. *Proceedings of the International Symposium on Advances in Bridge Aerodynamics*. Quoted on page 72.

110 MEIROVITCH, L. *Analytical methods in vibrations*. Macmillan, 1967. (Macmillan series in advanced mathematics and theoretical physics). Available from Internet: <https://books.google.com.br/books?id=sf1QAAAAMAAJ>. Quoted 2 times on pages 78 and 81.

111 CRAIG, R. R.; KURDILA, A. J. *Fundamentals of structural dynamics*. [S.l.]: John Wiley & Sons, 2006. Quoted 2 times on pages 78 and 81.

112 MORAIS, M. V. G.; BARCELOS, M.; ÁVILA, S. M.; SHZU, M. A. M.; SILVA, R. de C. Dynamic ehavior analysis of wind turbine towers. Congreso de Métodos Numéricos en Ingeniería, Barcelona, 29 junio al 2 de julio, SEMNI, España, 2009. Quoted 2 times on pages 78 and 81.

113 CHUNG, L. L.; WU, L. Y.; LIEN, K. H.; CHEN, H. H.; HUANG, H. H. Optimal design of friction pendulum tuned mass damper with varying friction coefficient. *Structural Control and Health Monitoring*, v. 20, n. 4, p. 544–559, 2012. Available from Internet: <https://onlinelibrary.wiley.com/doi/abs/10.1002/stc.514>. Quoted on page 82.

114 ZULUAGA, A. L. Controle de vibrações em edifícios submetidos à ação de cargas dinâmicas utilizando amortecedor de massa sintonizado na forma de pêendulo. Master's dissertation in Structures and Civil Construction, Universidade de Brasília, p. 22–64, 2007. Quoted 2 times on pages 82 and 93.

115 SHZU, M. A. M.; MORAIS, M. V. G.; PRADO, Z. J. G. del; ÁVILA, S. M. Finite element analysis of a wind turbine tower with a pendulum tuned mass damper. DINAME 2015 - XVII International Symposium on Dynamic Problems of Mechanics, ABCM, RN, Brazil, Frebruary 22-27, 2015. Quoted 2 times on pages 82 and 83.

116 GOLDBERG, D. E. *Genetic Algorithms in Search, Optimization and Machine Learning*. 1st. ed. Boston, MA, USA: Addison-Wesley Longman Publishing Co., Inc., 1989. ISBN 0201157675. Quoted 4 times on pages 84, 132, 138, and 140.

117 GOLDBERG, D. E. Real-coded genetic algorithms, virtual alphabets, and blocking. Complex Systems, v. 5, n. 2, p. 139–168, 1991. Quoted 2 times on pages 84 and 139.

118 NREL. *Collection of Matlab tools developed for use with OpenFAST*. 2020. Available from Internet: <https://github.com/OpenFAST/MATLAB-mbc>. Quoted on page 92.

119 LIAN, J.; ZHAO, Y.; LIAN, C.; WANG, H.; DONG, X.; JIANG, Q.; ZHOU, H.; JIANG, J. Application of an eddy current-tuned mass damper to vibration mitigation of offshore wind turbines. *Energies*, MDPI AG, v. 11, n. 12, p. 3319, Nov 2018. ISSN 1996-1073. Available from Internet: <http://dx.doi.org/10.3390/en11123319>. Quoted on page 101.

120 COLHERINHAS, G. B.; PETRINI, F.; MORAIS, M. V. G. de; BONTEMPI, F. Optimal design of passive-adaptive pendulum tuned mass damper for the global vibration control of offshore wind turbines. *Wind Energy*, n/a, n. n/a. Available from Internet: <https://onlinelibrary.wiley.com/doi/abs/10.1002/we.2590>. Quoted 5 times on pages x, 103, 104, 109, and 128.

121 OPENFAST. *GitHub repository*. 2019. Available from Internet: <https://github.com/OpenFAST/matlab-toolbox>. Quoted on page 103.

122 COLHERINHAS, G. B.; SHZU, M. A. M.; ÁVILA, S. M.; MORAIS, M. V. G. Genetic optimization of tower vibrations with pendulum tmd. 5th ECCOMAS Thematic Conference on Computational Methods in Structural Dynamics and Earthquake Engineering, COMPDYN 2015, 2015. Quoted on page 128.

123 COLHERINHAS, G. B.; MORAIS, M. V. G.; SHZU, M. A. M.; ÁVILA, S. M. Genetic optimization analysis of wind tower vibrations controlled by a pendulum tmd. *Revista Interdisciplinar De Pesquisa Em Engenharia*, v. 2, n. 13, p. 103–119, 2017. XXXVII Ibero-Latin American Congress on Computational Methods in Engineering,

CILAMCE 2016. Available from Internet: <https://doi.org/10.26512/ripe.v2i13.21637>. Quoted on page 128.

124 COLHERINHAS, G. B.; SHZU, M. A.; AVILA, S. M.; MORAIS, M. V. de. Wind tower vibration controlled by a pendulum tmd using genetic optimization: Beam modelling. *Procedia Engineering*, v. 199, p. 1623 – 1628, 2017. ISSN 1877-7058. X International Conference on Structural Dynamics, EURODYN 2017. Available from Internet: <https://doi.org/10.1016/j.proeng.2017.09.080>. Quoted on page 128.

125 COLHERINHAS, G. B.; MORAIS, M. V. G. de; MACHADO, M. R. Offshore wind turbines with pendulum tuned mass dampers design for vibration control using spectral element method. *Manuscript submitted for publication*, 2020. Quoted on page 128.

126 FERREIRA, Á. C.; COLHERINHAS, G. B.; ALBUQUERQUE, É. L. de; MACHADO, M. R.; MORAIS, M. V. G. de. $\mathcal{H}$-matrix acoustics bem for vocal tract configuration optimization using genetic algorithms. *Journal of the Brazilian Society of Mechanical Sciences and Engineering*, v. 42, n. 9, p. 476, Aug 2020. ISSN 1806-3691. Available from Internet: <https://doi.org/10.1007/s40430-020-02545-6>. Quoted on page 129.

127 BIONDI, L.; BECCENERI, J. C.; SILVA, J. D. S.; LUZ, E. F. P.; NETO, A. J. S. *Técnicas de Inteligência Computacional Inspiradas na Natureza - Aplicação em Problemas Inversos em Transferência Radiativa*. [S.l.]: São Carlos: SBMAC, 2009. v. 41. 35-42 p. Quoted on page 130.

128 BEZDEK, J. C. What is computational itelligence? computational intelligence imitating life. IEEE Press, Piscataway, 112, Reprinted in: DOE Proc. Adaptive Control Systems Tech. Symp, 1993. Quoted on page 130.

129 COELHO, L. d. S.; MARIANI, V. C. Sistema híbrido neuro-evolutivo aplicado ao controle de um processo multivariável. *Sba: Controle & Automação Sociedade Brasileira de Automática*, scielo, v. 17, p. 32 – 48, 2006. ISSN 0103-1759. Available from Internet: <http://www.scielo.br/scielo.php?script=sci_arttext&pid=S0103-17592006000100004&nrm=iso>. Quoted on page 130.

130 SUCUPIRA, I. R. *Métodos Heurísticos Genéricos: Meta-heurísticas e hiper-heurísticas*. [S.l.]: Universidade de São Paulo, 2004. Quoted on page 130.

131 IZMAILOV, A.; SOLODOV, M. *Otimização, Volume II - Métodos Computacionais*. Rio de Janeiro: IMPA, 2010. 2ª edição. ISBN 978-85-244-0268-5. Quoted on page 131.

132 IZMAILOV, A.; SOLODOV, M. *Otimização, Volume I - Métodos Computacionais*. Rio de Janeiro: IMPA, 2014. 3ª edição. ISBN 978-85-244-0238-8. Quoted on page 131.

133 SOUZA, G. S. C. *OTIMIZAÇÃO GENÉTICA DE VIGAS DE PAREDES FINAS COMPÓSITAS: UMA ABORDAGEM FENOMENOLÓGICA*. Undergraduate dissertation in Mechanical Sciences of the University of Brasilia, 2017. Available from Internet: <http://bdm.unb.br/handle/10483/19863>. Quoted on page 131.

134 HOLLAND, J. *Adaptation in natural and artificial systems: an introductory analysis with applications to biology, control, and artificial intelligence*. University of Michigan Press, 1975. ISBN 9780472084609. Available from Internet: <https://books.google.com.br/books?id=JE5RAAAAMAAJ>. Quoted 2 times on pages 132 and 134.

135 MITCHELL, M. *An Introduction to Genetic Algorithms*. Bradford Books, 1998. (A Bradford book). ISBN 9780262631853. Available from Internet: <https://books.google.com.br/books?id=0eznlz0TF-IC>. Quoted 3 times on pages 132, 135, and 137.

136 ERBATUR, F.; HASANçEBI, O.; TüTüNCü İlker; KıLıç, H. Optimal design of planar and space structures with genetic algorithms. *Computers & Structures*, v. 75, n. 2, p. 209 – 224, 2000. ISSN 0045-7949. Available from Internet: <http://www.sciencedirect.com/science/article/pii/S004579499900084X>. Quoted on page 132.

137 BAUMAL, A.; MCPHEE, J.; CALAMAI, P. Application of genetic algorithms to the design optimization of an active vehicle suspension system. *Computer Methods in Applied Mechanics and Engineering*, v. 163, n. 1, p. 87 – 94, 1998. ISSN 0045-7825. Available from Internet: <http://www.sciencedirect.com/science/article/pii/S0045782598000048>. Quoted on page 132.

138 GRADY, S.; HUSSAINI, M.; ABDULLAH, M. Placement of wind turbines using genetic algorithms. *Renewable Energy*, v. 30, n. 2, p. 259 – 270, 2005. ISSN 0960-1481. Available from Internet: <http://www.sciencedirect.com/science/article/pii/S0960148104001867>. Quoted on page 132.

139 RODRIGUES, A. P. de S. P. Dissertação de mestrado em ciências mecânicas: Parametrização e simulação numérica da turbina hidrocinética - otimização via algoritmos genéticos. ENM.DM - 119 A/07. Universidade de Brasília, Faculdade de Tecnologia, Departamento de engenharia mecânica, 2007. Quoted on page 132.

140 SILVA, A. J. M. Implementação de um algoritmo genético utilizando o modelo de ilhas. Dissertação de mestrado em Engenharia da Universidade Federal do Rio de Janeiro, 2005. Quoted on page 132.

141 MICHALEWICZ, Z. *Genetic Algorithms + Data Structures = Evolution Programs (3rd Ed.)*. London, UK, UK: Springer-Verlag, 1996. ISBN 3-540-60676-9. Quoted on page 134.

142 ALBUQUERQUE, A. C. M. L. de. Algoritmos genéticos e processamento paralelo aplicados à definição e treinamento de redes neurais perceprton de múltiplas camadas. Dissertação de Mestrado em Engenharia Elétrica da Universidade Federal do Rio Grande do Norte, 2005. Quoted on page 134.

143 MOLE, V. L. D. Algoritmos genéticos - uma abordagem paralela baseada em populações cooperantes. Dissertação de Mestrado em Ciência da Computação da Universidade Federal de Santa Catarina, 2002. Quoted on page 134.

144 COLHERINHAS, G. B.; DIAS, P. H. C. Projeto de graduação: Otimização paramétrica via algoritmos genéticos da cadeia cinemática automotiva por meio de investigação das razões de transmissão. Universidade de Brasília, Faculdade de Tecnologia, Departamento de engenharia mecânica, 2014. Quoted on page 134.

145 BAKER, J. E. Adaptive selection methods for genetic algorithms. In: *Proceedings of the 1st International Conference on Genetic Algorithms*. Hillsdale, NJ, USA: L. Erlbaum Associates Inc., 1985. p. 101–111. ISBN 0-8058-0426-9. Available from Internet: <http://dl.acm.org/citation.cfm?id=645511.657075>. Quoted on page 137.

146 MOGNON, V. R. Algoritmos genéticos aplicados na otimização de antenas. Dissertação de Mestrado em Engenharia Elétrica da Universidade Federal do Paraná, 2004. Quoted 2 times on pages 138 and 141.

147 GABRIEL, P. H. R.; DELBEM, A. C. B. Fundamentos de algoritmos evolutivos. Instituto de Ciências Matemáticas e de Computação da Universidade de São Paulo, 2008. Quoted 2 times on pages 139 and 141.

148 MICHALEWICZ, Z.; JANIKOW, C. Z. Handling constraints in genetic algorithms. In: *Proc. of the Fourth International Conference on Genetic Algorithms*. San Diego, CA: [s.n.], 1991. p. 151–157. Quoted on page 139.

149 DEEP, K.; THAKUR, M. A. A new crossover operator for real coded genetic algorithms. Applied Mathematics and Computation, 2007. Quoted on page 139.

150 ESHELMAN, L. J.; SCHAFFER, J. D. Real-coded genetic algorithms and interval-schemata. Foundations of Genetic Algorithms 2 (FOGA-2), p. 187–202, 1993. Quoted 2 times on pages 139 and 140.

151 LIM, S. M.; SULAIMAN, M. N.; SULTAN, A. B. M.; MUSTAPHA, N.; TEJO, B. A. A new real coded genetic aldorithm crossover: Rayleigh crossover. Journal of Theoretical and Applied Information Technology, 2014. Quoted on page 140.

Appendix

A List of publications

The following publications on international congress (122), Brazilian journal (123), international journals (124, 19, 120), and a paper submitted for publication (125) form the scope of this thesis, respectively:

- COLHERINHAS, G. B.; SHZU, M. A. M.; ÁVILA, S. M.; MORAIS, M. V. G. Genetic optimization of tower vibrations with pendulum tmd. *COMPDYN 2015, 5th ECCOMAS Thematic Conference on Computational Methods in Structural Dynamics and Earthquake Engineering*, 2015.

- COLHERINHAS, G. B.; MORAIS, M. V. G.; SHZU, M. A. M.; ÁVILA, S. M. Genetic optimization analysis of wind tower vibrations controlled by a pendulum tmd. *Revista Interdisciplinar De Pesquisa Em Engenharia*, v. 2, n. 13, 103-119, 2017. XXXVII Ibero-Latin American Congress on Computational Methods in Engineering, CILAMCE 2016. Available from Internet: <https://doi.org/10.26512/ripe.v2i13.21637>.

- COLHERINHAS, G. B.; SHZU, M. A. M.; ÁVILA, S. M.; MORAIS, M. V. G. Wind tower vibration controlled by a pendulum tmd using genetic optimization: Beam modeling. *Procedia Engineering*, v. 199, p. 1623-1628, 2017. ISSN 1877-7058. X International Conference on Structural Dynamics, EURODYN 2017. Available from Internet: <https://doi.org/10.1016/j.proeng.2017.09.080>.

- **Case study 1:** COLHERINHAS, G. B.; MORAIS, M. V. G.; SHZU, M. A. M.; ÁVILA, S. M. Optimal Pendulum Tuned Mass Damper Design Applied to High Towers Using Genetic Algorithms: Two-DOF Modeling. *International Journal of Structural Stability and Dynamics*, v. 19, n. 10, p. 1950125, 2019. Available from Internet: <https://doi.org/10.1142/S0219455419501256>.

- **Case study 2:** COLHERINHAS, G. B.; PETRINI, F.; MORAIS, M. V. G; BONTEMPI, F. Optimal design of passive-adaptative pendulum TMD for the global vibration control of offshore wind turbines. *Wind Energy (Early view)*, 2020. Available from Internet: <https://doi.org/10.1002/we.2590>

- **Case study 3:** COLHERINHAS, G. B.; MORAIS, M. V. G; MACHADO, M. R. Offshore wind turbines with pendulum tuned mass dampers design for vibration control using spectral element method. *Manuscript submitted for publication*, 2020.

The following paper is related to the work with $\mathcal{H}$-matrix acoustics BEM for vocal tract configuration using genetic algorithms (126) but is not included as a part of this thesis because it falls outside of the main topic of the thesis.

- FERREIRA, Á. C.; COLHERINHAS, G. B.; de ALBUQUERQUE, É. L; MACHADO, M. R.; de MORAIS, M. V. G. $\mathcal{H}$-matrix acoustics BEM for vocal tract configuration optimization using genetic algorithms. *Journal of the Brazilian Society of Mechanical Sciences and Engineering*, v. 42, n. 9, p. 476, Aug 2020. ISSN 1806-3691. Available from Internet: <https://doi.org/10.1007/s40430-020-02545-6>.

B Genetic Optimization

The technology evolution in the last few decades have been motivate the engineer to find new optimized solutions for complex problems. Although methodologies to solve some type of problems are not well defined at all, a little variation of the parameters can drastically affect the results. The manipulation of these parameters induced the creation of many numerical techniques that, with the development of computational sources and processing, integrated even more the relation between the human race and the computers.

Stochastic methods were developed to reduce the number of solutions to give more "intelligence" to these machines. In practice is easier and more efficient to find local solutions instead of a global, because the last one require a high computational cost. In this way a lot of heuristic formulations have been developed to solve problems with a lot of complexity and been also capable to vary many variables. This heuristics are techniques inspired in intuitive processes that find satisfactory solutions near to the optimal global.

Since 1980s, many studies were developed to evaluate heuristic procedures by using a broad theoretical structure. The merge of concepts between the optimization and Computational Intelligence (CI) made viable the construction of flexible strategies, known by meta-heuristics. This technique explore efficiently the viable space of problem solutions, escaping from the confinement of local maxima and minima. How more we apply these specific acknowledgements in an heuristic form, the algorithm converges closer to the global solution (127).

This interface introduced a new concept of algorithms based on CI. Bezdek (128) attribute to CI a collection of methodologies that explores the uncertainty, imprecision and tolerance to failures, given robustness to low cost solutions. Between the mainly CI methods are the Artificial Neural Network (ANN), Evolutionary Computation (EC), Fuzzy Logic, Probabilistic Methods, and hybrid systems (combinations between two or more CI methods) (129). The optimization use CI techniques to find the best maxima or minima values of a fitness function, subject to a set of constraints.

Meta-heuristics are mostly bio-inspired algorithms in logical process of nature, based on behavioural, evolutionary, or from well defined strategies, such as Particle Swarm Optimization (PSO), Ant Colonies Optimization (ACO), Simulated Annealing (SA), (ANN), Genetic Algorithms (GA), Memetic Algorithms (130), among others.

Some meta-heuristic optimization methods were been used to search optimum TMD design parameters such as the GA (89, 90, 97, 91), PSO (95), ACO (94), harmony search algorithm (92), bionic algorithm (93), and hybrid approaches such as an adaptive GA-SA method (96).

B.1 Optimization

Mathematically, a set $D \subset \mathbb{R}^n$ and a function $f : \Omega \to \mathbb{R}$, where $D \subset \Omega$ such that a minimizer must be found for the **fitness function** f in a viable set D. The points belonging to D are named viable points . This situation can be write as (131, 132):

$$\min f(x) \text{ subject to } x \in D \tag{B.1.1}$$

this way, the point $\bar{x} \in D$ is a **global minimizer** of f if:

$$f(\bar{x}) \leq f(x), \ \forall x \in D \tag{B.1.2}$$

and a **local minimizer** of f if exist a neighbourhood U, such that:

$$f(\bar{x}) \leq f(x), \ \forall x \in D \cap U \tag{B.1.3}$$

In other words, $\bar{x} \in D$ is a local minimizer if exists $\epsilon > 0$, such that:

$$\forall x \in D \Rightarrow \|x - \bar{x}\| \leq \epsilon \tag{B.1.4}$$

The **optimum value** $\bar{v} \in [-\infty, +\infty]$ of a fitness function of the Eq. B.1.1 is defined as:

$$\bar{v} = \inf f(x) : x \in D \tag{B.1.5}$$

It is noticed that a function may assume many global minimizers but the optimum value is the same for all of them. In addition, all global minimizers are also local but the reciprocal does not apply. Sales (133) show in fig. B.1.1 an example that illustrate this case, extracted from Izmailov and Solodov (132).

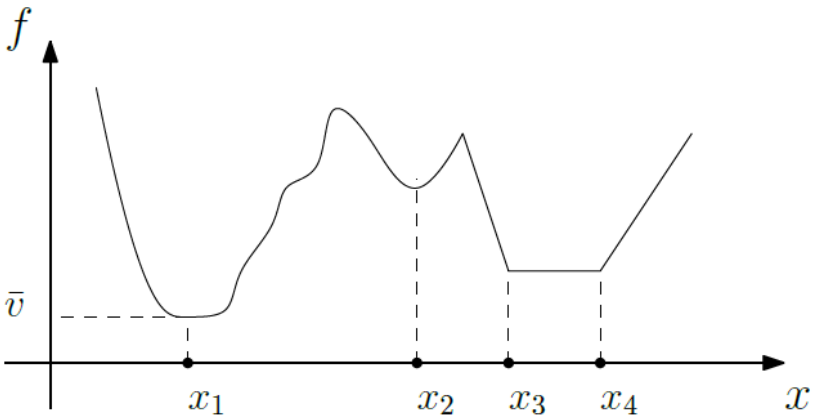

Figure B.1.1 – The minimization problem of f, where x_1 is the global minimizer and $\bar{v}$ the optimal value.

B.2 Genetic Algorithms

Inspired on the Darwin natural adaptation principle, Holland (134) and their students and friends from the University of Michigan (135), in the 60's and 70's, implemented the natural evolution mechanism in an algorithm to create the GA. The development of this optimization technique reverberated in the academic community and now the GA is a classic method of EC used in many different areas (engineering, computation sciences, geology...).

Holland presented the GAs in his book *Adaptation in Natural and Artificial Systems* and his student Goldberg (116) advanced the GAs studies as a optimization technique in his book *Genetic Algorithms in Search, Optimization and Machine Learning*, through simulations of genetic systems.

These algorithms expanded through academic community in a role of many non conventional applications, as examples: solution problems, machine learning, strategies to find mathematical formulae, economic model analysis, engineering problems by modelling space structures (136), vehicle systems (137), turbines (138, 139) and in biology by simulating the bacteria, immunologic systems, ecosystems, organic molecules. These wide range of applications also contributed in the development of commercial software such as the *Evolver* and *ModeFrontier*, and a lot of similar ways to reach the same object.

In theory, each *chromosome* or individual of the population associates to a solution and each *gene* associate to a variable. One allele correspond to a value that the gene can assume (fig. B.2.1). Through each sequence of interaction of logical steps, the population evolves in each generation until arise an optimal chromosome.

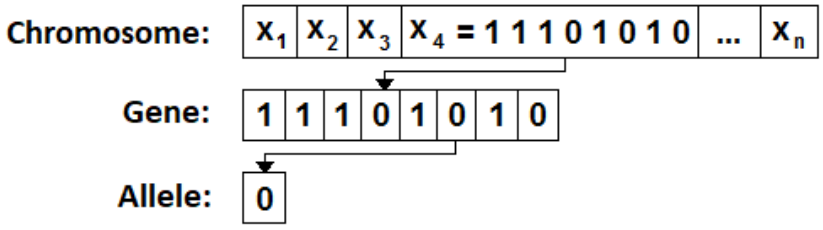

Figure B.2.1 – Definition of the components of a chromosome

A set of chromosomes are defined as genotypes organized in data structures of binary or real vectors that defines the genetic constitution of each individual. Evolutionary strategies - such as selection, crossover, mutation, elitism, decimation - are applied over these chromosomes to generate new individuals (140).

An **initial population** is created with chromosomes presenting uniform random values over defined restrictions. Each chromosome is evaluated through a score by a **fitness function**. The chromosome participate in a **selection** process where the fittest have the greatest ability to transfer their characteristics to the next generations through

a **crossover**. A minimal portion of the population may have their genetic information altered in a process of **mutation**. Deterministic methods such as **elitism** can ensure that a percentage of the best individuals will always survive for subsequent generations. And a **decimation** can eliminate a portion of the worst individuals in the population.

Figure B.2.2 shows how the GA is defined in this thesis. The variable i is a logical counter of the evolution of generations. If $i = 0$, the GA is initialized. If $i_n = n_{ger}$, it ends. If i is a integer multiple of the decimation step n_{diz}, decimation occurs.

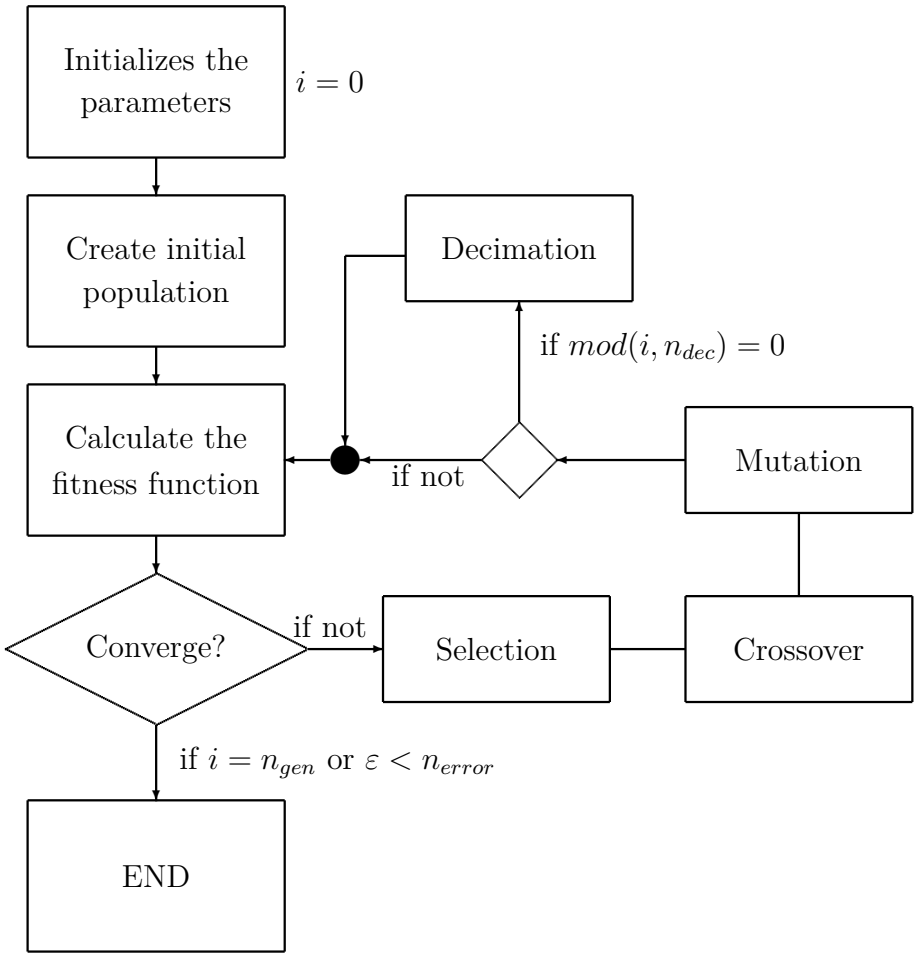

Figure B.2.2 – GA Flowchart implemented

In sequence, each operator is explained and how the parameters definition may be setted.

Initial Parameters

When initializing the parameters ($i = 0$), essential information about how the AG works may be included, such as:

- the encoding type used (binary or real);
- the constraints that limit the chromosomes within a range of possible solutions;

- which evolutionary strategies will be applied and their respective rates (probability of individuals crossing, mutation, elitism and decimation)
- the population size and in how many generations the GA will end (or an error can also be defined).

Binary or real enconding?

In the original work of Holland (134), binary coding was the first to be developed. It is widely used because of its easy implementation, manipulation, and is simple to analyse theoretically.

For problems with optimization parameters with variables over continuous domains, real (or floating-point) coding genes are used, having their own genetic operators. Michalewicz (141) compares the computational time for both implementations by varying the chromosome numbers of the elements, for specific examples. He comes to the conclusion that coding via floating points can achieve convergence faster than binary implementation. For large and/or high-precision domains the total length of the chromosomes increases, increasing the computational cost.

Initial Population

After the optimization parameters have been defined, the initial population assigns to each chromosome a value from a random distribution. These chromosomes are restricted to a range of constrains assigned in the initial parameters.

Often some optimizations require a high computational cost and not converges on the pre-established number of generations. The selection of some chromosomes trapped at local maxima can be inserted into a new optimization reducing the processing time and evolution of this new simulation.

Some approaches present the use of parallel processing where multiple populations are generated simultaneously in several processing cores (142, 143). These cores share information produced through a central node.

Fitness function

The fitness function is a very important step and depends on the objectives of the optimization, subject to a set of constraints. This is a decisive step for the correct functioning of the algorithm. The conjunction between the fitness function and the constraints assigns a final score on a given individual. Each case has a distinct logic for assigning this note. In order to define multi-objective problems, a combination of the evaluated factors is performed. You can also weigh each goal with different weights.

For example, in (144) it was optimized the transmission ratios of a powertrain system in order to obtain the best fuel consumption and acceleration ratio. For this case, three distinct fitness functions have been defined. The first one optimizes two parameters simultaneously (acceleration and consumption). The second one prioritizes fuel economy.

And the latter, determines the optimum point for only the vehicle acceleration. Since the acceleration and fuel consumption have different objectives, when weighing each one it is possible to assign transmission reasons for a touring car (prioritizing the fuel economy) or a sport model (prioritizing the vehicle acceleration). Giving priority to an fitness function does not mean disregarding others.

B.2.1 Selection

After the evaluation, a specialized algorithm selects best genetic characteristics of the chromosomes with stochastic and/or deterministic choices. The selection depends on the grade assigned to each chromosome. Some well-known selection strategies are described in the following items (135):

Deterministic selection: elistism and decimation

Elitism is a method that holds a small portion of the individuals with the highest fitness of the population. As a deterministic method, this value should be small so that the population does not lose genetic variability when passing through generations.

Similarly, decimation is a strategy that removes a fixed number of individuals of low fitness. The simplicity of this method faces the disadvantage of eliminating potential genetic characteristics. Some of these characteristics may be relevant despite their low aptitude while, in stochastic methods, individuals with low fitness have the chance of being selected.

This elimination usually occurs from a step of n_{dec}. A strategy to skip the decimation selection at all generations must be applied to increase the genetic variability of the population.

Roulette-wheel method

The roulette-wheel is a classical proportional selection method in which each chromosome assigned a slice over a circular area of the roulette wheel. The size of this slice is based on the fitness of each chromosome relative to the sum of all scores of the population. The roulette (fig. B.2.3) is rotated N times, where N is the number of individuals in the population. Each time the roulette wheel stops, the individual is selected for the next generation. These selected individuals will be able to participate in the evolutionary strategies of crossover and mutation.

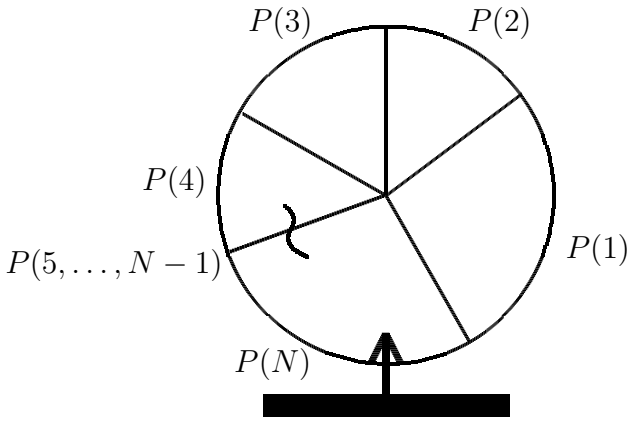

Figure B.2.3 – Roulette-wheel method and its probabilities

The probability P_i that an individual i has to be selected as a function of his fitness $f_{fit}(i)$, is expressed by Eq. B.2.1.

$$P_i = \frac{f_{fit}(i)}{\sum_{i=1}^{N} f_{fit}(i)} \tag{B.2.1}$$

P_i represents a portion of the roulette that individual i has to be selected. A chromosome with higher fitness score has a greater chance of being chosen.

The cumulative probability q_i represents the sum of the probabilities P_k, expressed by Eq. B.2.2.

$$q_i = \sum_{k=1}^{i} P_k \tag{B.2.2}$$

where $k = 1, \ldots, i$.

The algorithm 1 presents the roulette-wheel method.

Algorithm 1: Roulette-wheel method

input : individuals of population
output : selection of the fittest individuals

$i \leftarrow 1$: start counting individuals to be selected;
$N \leftarrow$ number of individuals in the population;
repeat
  $P_i \leftarrow$ Eq. B.2.1;
  generate r with random value between 0 e 1;
  $q_i \leftarrow$ Eq. B.2.2;
  if $r < q_i$ **then**
    select i;
    $i \leftarrow i + 1$;
  end
until $i = N$;

Rank selection

Rank selection is an alternative method that avoids the rapid convergence of the GA. Individuals of the population are classified according to their fitness and the expected values of each individual depends on their rank, rather than their brute fitness.

Linear rank selection is a method proposed by Baker in 1985 (145) where each individual of the population is ranked in increasing order of fitness. The worst guy gets 1 and the best N. The rest of the selection is made in the same way as the roulette wheel.

Discarding absolute fitness informations can have advantages and disadvantages. Rank selection avoids giving to the offspring a small group of individuals with high aptitude. This avoids selective pressure when the fitness variance is too high. It is also observed that when the variance of fitness is small, the ratio of the expected values of the individuals of the rank selection i and $i+1$ will be the same if the difference of their brute fitness is high or low (135). Figure B.2.4 compares the roulette method with the rank selection.

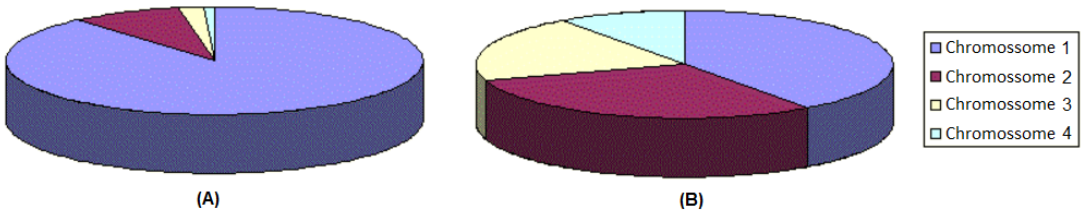

Figure B.2.4 – (A) Roulette-wheel method x (B) Rank Selection

Tournament selection

The tournament selection is a method where a portion of individuals from the population is randomly chosen. This portions competes one each other, based on their skills. The one with the best score is selected. A tournament size parameter k, defines the number of individuals selected for the competition.

Figure B.2.5 shows how the best individual in the population is selected through the tournament.

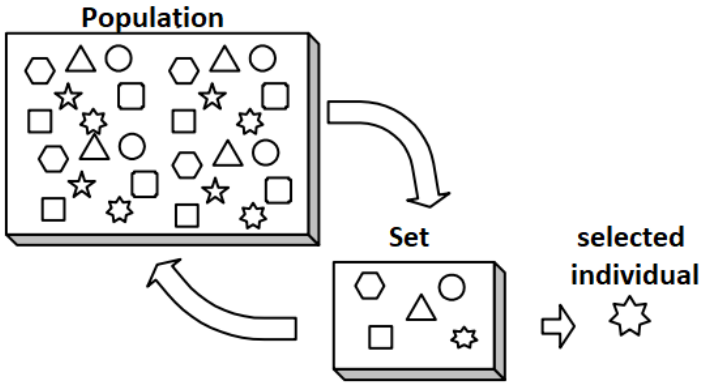

Figure B.2.5 – Representation of the Tournament Method with $k = 5$

The minimum value of k is two, since only the competition exists. If $k = N$ (population size), the winner is always the same. If k is a high value, the $N-k$ chromosomes will predominate, since they will always have a higher probability of being chosen.

Algorithm 2 presents the pseudo-code corresponding to this method.

Algorithm 2: Tournament selection

input : individuals of population
output : selection of the fittest individuals

$N \leftarrow$ number of individuals in the population;
$k \leftarrow$ parameters between 2 and N of individuals to be selected;
for $i \leftarrow 1$ **to** N **do**
    for $j \leftarrow 1$ **to** k **do**
        generate r_j with random values between 1 and k;
    end
    select $i(\max(f_{obj}(r_j)))$;
end

B.2.2 Crossover

The crossover is responsible for exchange genetic information between two selected chromosomes. From this exchange, new descendants are generated. Goldberg (116) suggests that the crossover probability must be $P_c \geq 60\%$. This simulates a natural occurrence in which most couples have children. With this high probability, the crossover becomes a fundamental operator for the new generations.

Crossover in binary coding

Crossover can be accomplished in different ways. A simple way is the random selection of a gene from the chromosome where parents exchange genetic material in any position (fig. B.2.6, (146)).

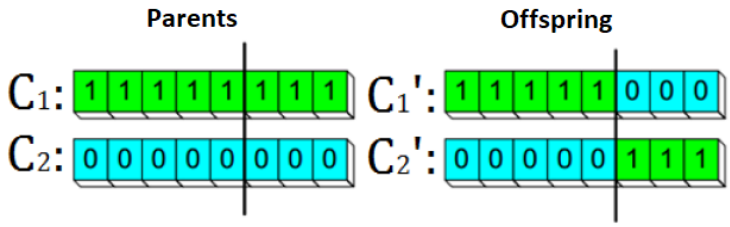

Figure B.2.6 – Crossover in a single point

There are some variations of this method: random two points or more (fig. B.2.7) and there is also the possibility of crossover into random alleles (fig. B.2.8) (146).

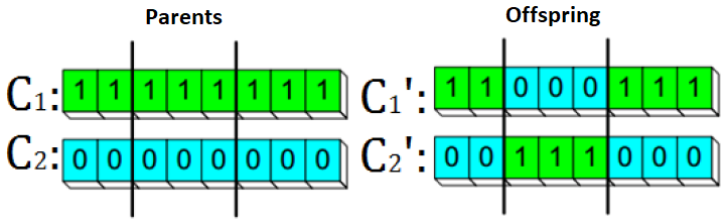

Figure B.2.7 – Crossover in two points

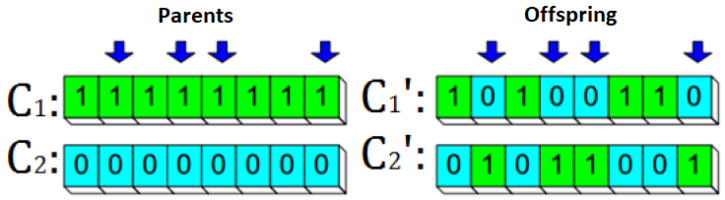

Figure B.2.8 – Crossover in random points

Arithmetic crossover

Arithmetic crossover (or intermediary) seeks an analogy of binary representation. The chromosomes are represented by real numbers (147). The arithmetic crossover proposed by Michalewicz (148) creates new alleles in the offspring with intermediate values to those of the parents.

A linear combination between two chromosomes x and y generates an offspring z can be computed in Eq. B.2.3.

$$z = y + \beta(x - y) \tag{B.2.3}$$

where β is a random number belonging to the range $[0, 1]$. β can be considered fixed (for example $\beta = 0.5$), characterizing a uniform crossover.

Heuristic crossover (HX)

The Heuristic crossover (HX) evaluates fitness information to prevent arithmetic crossover takes the genes to the center of the range, as show Eq. B.2.4 (149).

$$z = y + \beta(x - y) \tag{B.2.4}$$

where $f(y) > f(x)$ and $\beta \sim U(0, 1)$. U represents a uniform distribution.

Blend crossover (BLX-α)

Another approach (that is the used in this thesis) is the Blend crossover (BLX-α) (150, 117). Given two chromosomes x and y, a chromosome z is produced as follow Eq. B.2.5.

$$z = x + \beta(y - x) \tag{B.2.5}$$

where $\beta \sim U(-\alpha, 1+\alpha)$. In the literature it is suggested $\alpha = 0,5$ or $0,25$.

This operator allows to extrapolate the region of crossover of the parents. For this reason, it attributes greater genetic variability during the evolution of the generations. fig. B.2.9 (150) shows a representation of how the space of BLX-α works in this evolutionary strategy. It is interesting to see that by adding the α parameter, new solutions are added to the search space.

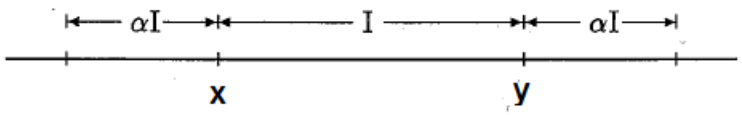

Figure B.2.9 – Blend crossover - BLX-α

***Rayleigh crossover* (RX)**

Rayleigh crossover (RX) uses the Rayleigh distribution. This is a continuous probability distribution that generates random descendants at floating points. The Rayleigh density function is defined in Eq. B.2.6.

$$f(x;s) = \frac{x}{s^2} e^{-x^2/2s^2}, x \geq 0 \tag{B.2.6}$$

where $s > 0$ the scale parameter of the distribution. Lim et al. (151) experimentally defines the best value of $s = 3$.

To use this distribution, two parents p_1 and p_2 produce two offspring y_1 and y_2 from the following equations:

$$y_1 = p_1 \log(x) + p_2(1 - \log(x)) \tag{B.2.7}$$

$$y_2 = p_2 \log(x) + p_1(1 - \log(x)) \tag{B.2.8}$$

The offspring y_1 (B.2.7) is defined closer to the parent p_1, while the offspring y_2 (B.2.8) of the parent p_2. The logarithm defines the contour x, where $0 < x < 1$. The number of the Rayleigh distribution x is generated by the inversion of the Rayleigh distribution function (B.2.9).

$$|x| = \sqrt{-2s^2 \log_e (1-U)} \tag{B.2.9}$$

being assigned to x only the positive values. Therefore:

$$x = |-s(2\ln(1-U))^{1/2}| \tag{B.2.10}$$

B.2.3 Mutation

The mutation operator randomly modifies one or more genes of a chromosome through a mutation rate of P_m. Goldberg (116) suggests a mutation rate of 5%. Generally,

small values are assigned for this rate, since this operator can generate an individual much worse than the original. Through mutation, however, new information is introduced or perhaps lost in iterations. The mutation seeks to escape of local maxima by increasing the probability of finding a global maximum.

The most common mutation operators for floating points are the uniform mutation and the Gaussian mutation.

Mutation in binary coding

Mutation is a very simple genetic operator in binary algorithms. It is only necessary to reverse the value of one or more random alleles of the chromosome. fig. B.2.10 (146) illustrates the mutation in a single allele.

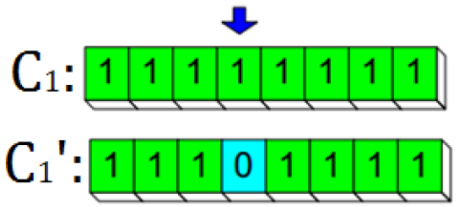

Figure B.2.10 – Mutation in a single point

Uniform mutation

For this type of mutation, the operator selects random genes $k \in \{1, 2, \ldots, n\}$ of chromosome $C = [x_1, \ldots, x_k, \ldots, x_n]$. A new gene x'_k is generated through a uniform random distribution $U(L_i, L_s)$, , respectively, the lower limits L_i an higher L_s of the gene restriction x_k (147).

Contour mutation

In this type of mutation, a random gene j is selected. This gene is replaced by one of the limits of the range $[L_i, L_s]$, explicit in Eq. B.2.11.

$$x'_k = \begin{cases} L_i, & \text{if} \quad r < 0,5 \quad \text{and} \quad k = j \\ L_s, & \text{if} \quad r \geq 0,5 \quad \text{and} \quad k = j \\ x_k, & \text{otherwise} \end{cases} \tag{B.2.11}$$

where $r \in U(0, 1)$.

This operator prevents the chromosome inducing genes to the center of the feasible range $[L_i, L_s]$.

Gaussian mutation

This operator adds a random value to the chromosome according to a Gaussian distribution as follows:

$$x'_k = \begin{cases} N(x_k, \sigma), & \text{if} \quad k = j \\ x_k, & \text{otherwise} \end{cases} \tag{B.2.12}$$

where $N(x_k, \sigma)$ is the normal distribution with mean x_k and standard deviation σ.

This procedure generates great genetic variability in the solutions, making it difficult to converge the solution to a minimum (local or global). One strategy in order to decrease this variability is to progressively reduce the standard deviation σ as the number of generations

Uniform creep mutation

This operator adds a small random number to the gene x_k or multiplies it by a number closer to 1.

This is a less destructive operator used to locally search the space. Small disturbances in the genes are made in order to move them faster to convergence. It applies at a higher rate than other mutation operators ($P_m \approx 10\%$).

Non-uniform creep mutation

This type of mutation replaces the gene with a number extracted from a non-uniform distribution (Eq. B.2.13).

$$x'_k = \begin{cases} x_k + \Delta(i, L_s - x_k), & \text{se } z = 0 \\ x_k - \Delta(i, x_k - L_i), & \text{se } z = 1 \end{cases} \tag{B.2.13}$$

where z is a random binary digit (0 ou 1), L_i and L_s the upper and lower limits of the parameter x'_k. The function $\Delta(i, y)$ returns a value in the range $[0, y]$ such that the probability of $\Delta(i, y)$ it starts at zero and is incremented according to the number of generations i, such that:

$$\Delta(i, y) = y.r \left(1 - \frac{i}{N_{ger}}\right)^b \tag{B.2.14}$$

where r is a number generated randomly in the interval $[0, 1]$, N_{ger} is the maximum number of generations and b a parameter chosen by the user, which determines the degree of dependence with the number of generations.

This property instigates the operator to perform a uniform search in the initial space (when i is small) and a more local search as the i increases.

C Multi degree of freedom (MDOF) reduction

The MDOF reduction consists in reducing the continuous system of a beam with a tip mass, subject to a distributed force $F(x,t)$ in a discrete numbers of temporal ordinary differential equations (ODEs) depending of the test functions, taking the matricial form

$$\mathbf{M}\ddot{\mathbf{q}} + \mathbf{C}\dot{\mathbf{q}} + \mathbf{K}\mathbf{q} = \mathbf{f} \tag{C.0.1}$$

where $\mathbf{M}$, $\mathbf{C}$ and $\mathbf{K}$ are, respectively, the mass, damping and stiffness matrices, $\mathbf{q}$ is the vector of generalized coordinates, and $\mathbf{f}$ is the vector of imposed forces; the overdot denotes differentiation with time. Using three-mode approximation ($N = 3$), the Eq. C.0.1 may be written in the following matrix form (108):

$$\begin{bmatrix} mL + M_e\psi_1^2(L) & M_e\psi_1(L)\psi_2(L) & M_e\psi_1(L)\psi_3(L) \\ M_e\psi_2(L)\psi_1(L) & mL + M_e\psi_2^2(L) & M_e\psi_2(L)\psi_3(L) \\ M_e\psi_3(L)\psi_1(L) & M_e\psi_3(L)\psi_2(L) & mL + M_e\psi_3^2(L) \end{bmatrix} \begin{Bmatrix} \ddot{q}_1 \\ \ddot{q}_2 \\ \ddot{q}_3 \end{Bmatrix} + \begin{bmatrix} c_1 & 0 & 0 \\ 0 & c_2 & 0 \\ 0 & 0 & c_3 \end{bmatrix} \begin{Bmatrix} \dot{q}_1 \\ \dot{q}_2 \\ \dot{q}_3 \end{Bmatrix}$$
$$+EI \begin{bmatrix} \lambda_1^4 & 0 & 0 \\ 0 & \lambda_2^4 & 0 \\ 0 & 0 & \lambda_3^4 \end{bmatrix} \begin{Bmatrix} q_1 \\ q_2 \\ q_3 \end{Bmatrix} = F_0 \sin\omega_f t \cdot \begin{Bmatrix} \psi_1(L) \\ \psi_2(L) \\ \psi_3(L) \end{Bmatrix} \tag{C.0.2}$$

where $\psi_j(x)$ are test functions in domain $\mathbb{D} = [0, L]$ that satisfies the boundary conditions. The following eigenfunctions is used as basis function

$$\psi_j(x) = \cosh\lambda_j x - \cos\lambda_j x - \sigma_j(\sinh\lambda_j x - \sin\lambda_j x) \tag{C.0.3}$$

where $\sigma_j = (\sinh\lambda_j L - \sin\lambda_j L) \div (\cosh\lambda_j L - \cos\lambda_j L)$ and $\lambda_j L$ are the roots of transcendental equation $\cos\lambda_j L \cdot \cosh\lambda_j L + 1 = 0$ that yields a set of the eigenvalues. The pair $(\lambda, \psi)_j$ are the natural frequencies and modal shapes of a clamped beam (108).

The Eq. C.0.2 is solved by using the Runge-Kutta ode45 command in MATLAB®.